THE UNIVERSITY OF HULL

PHOTOCHEMICAL AND EVAPORATION BEHAVIOUR OF SUNSCREEN FORMULATIONS

being a Thesis submitted for the Degree of Doctor of Philosophy

in the University of Hull

by

Ioannis Marinopoulos

MSc (University of York)

BSc (University of Hull)

June 2016

ACKNOWLEDGEMENTS

I am grateful to my academic supervisors Prof. Bernard P. Binks and Prof. Paul D.I. Fletcher whose patience and watchful support took me successfully through this exciting project.

I would like to thank GlaxoSmithKline (GSK) for financial support in sponsoring this research project.

Many thanks to my industrial supervisors Dr. Jonathan M. Crowther and Dr. Michael A. Thompson as well as to Dr. Tirma Herranz and Dr. Andrew J. Johnson for their involvement in the project from a post-doctoral position.

I would also like to thank the two 4th Year MChem students I have co-supervised and whose undergraduate projects are summarised and presented within this study: i) Jonathan Brown for obtaining the experimental results on the evaporation of dispersions containing nanoparticles (Section 4.4) and ii) Lucy R. Dignan for obtaining the experimental results on the photochemical behaviour of dispersions containing nanoparticles (Section 6.7).

Θα ήθελα να ευχαριστήσω και τους γονείς μου Παναγιώτη Μαρινόπουλο και Βασιλική Μαρινοπούλου για την ανιδιοτελή τους αγάπη και στήριξη σε κάθε μου απόφαση. Είμαι βαθύτατα ευγνώμων.

LIST OF PUBLICATIONS AND PRESENTATIONS

The work contained in this thesis has been published or will be submitted for publication and contributed to the following presentations.

1. "Evaporation of sunscreen films: how the UV protection properties change". B.P. Binks, J. Brown, P.D.I. Fletcher, A.J. Johnson, I. Marinopoulos, J.M. Crowther and M.A. Thompson, *ACS Appl. Mater. Interfaces*, **8**, 13270-13281, (2016).
2. "Evaporation of particle-stabilized emulsion sunscreen films". B.P. Binks, P.D.I. Fletcher, A.J. Johnson, I. Marinopoulos, J.M. Crowther and M.A. Thompson, *ACS Appl. Mater. Interfaces*, submitted (2016).
3. "How the sun protection factor (SPF) of sunscreen films change during solar irradiation". B.P. Binks, P.D.I. Fletcher, A.J. Johnson, I. Marinopoulos, J.M. Crowther and M.A. Thompson, *J. Photochem. Photobiol. A*, to be submitted (2016).
4. "Spectrophotometry of thin films of light absorbing particles". B.P. Binks, P.D.I. Fletcher, A.J. Johnson, I. Marinopoulos, J.M. Crowther and M.A. Thompson, *Phys. Chem. Chem. Phys.*, to be submitted (2016).
5. Oral presentation 1st prize: "Sunscreen formulations and their behaviour upon thin film evaporation" University of Hull, Postgraduate Research Colloquium, 15 – 16 June 2015.
6. Poster presentation 1st prize: "Photochemical studies of a common sunscreen UV filter – avobenzone" University of Hull, Postgraduate Research Colloquium, 18 – 19 June 2014.
7. Conference presentation: "Sunscreen formulations and their behaviour upon thin film evaporation", 29th Conference of the European Colloid and Interface (ECIS), Bordeaux, France, 6 - 11 September 2015.

ABSTRACT

Sunscreens ensure protection of the human skin against the harmful effects of the UV radiation in the UVB (290 – 320 nm) and UVA (320 – 400 nm) wavelength ranges. They commonly contain one or more organic UV absorbers that absorb light in the wavelength range of interest and/or inorganic particles, such as metal oxide semiconductors that absorb, scatter and reflect light. The efficiency of these formulations is measured by introducing the Sun Protection Factor (SPF). Currently, SPF is estimated from *in vivo* measurements, which is a time-consuming and expensive process. For a validated method, however, SPF can also be determined *in vitro* by measuring the diffuse optical transmittance as a function of wavelength. In this study, we show how *in vitro* SPF changes as a function of time upon i) evaporation of volatile components and ii) exposure under UV irradiation.

We start by investigating the evaporation of solution films containing a selection of UV absorbers. We show that during solvent evaporation, an initial film, which is deposited on a smooth quartz plate, progressively dewets. The solvent loss causes an increase in the solute concentration until its solubility limit is reached. From that point onwards, solute precipitation is expected to occur. Hence, the combined effect of dewetting and solute precipitation during evaporation leads to a decrease in the absorbance and thus to the *in vitro* SPF values. We model the evolution of film spectra and we compare it with experiment. Results confirm that both are in reasonable agreement.

The addition of either inorganic particulates in the nm size or polymer was also pursued. Our data confirm that their use aid film pinning at its base edge and suppressed dewetting. However, it did not tackle the problem of precipitation during solvent evaporation. Throughout our experimental procedure, the solvent of choice was the slow evaporating propane-1,2-diol (PG). We show that the same behaviour is observed when a fast-evaporating solvent, such as *n*-decane is used. Dewetting is also suppressed when alternative substrates such as Vitro Skin and keratin-lipid film are used.

We have extended our investigation to the evaporation of particle-stabilised emulsion films, consisting of equal volumes of involatile squalane (SQ) and slow-evaporating PG and stabilised by partially hydrophobised silica particles. We show for these

emulsions that the loss in the absorbance is due to the loss of light scattering. The loss of the latter results from the collapse of the emulsion structure during evaporation.

We also examine how the *in vitro* SPF of solutions containing UV absorbers varies with standard solar irradiation. With the use of chemical actinometry, we have determined the overall quantum yields of the photochemical processes of photolabile UV absorbers. Using the obtained parameters, we have developed models to calculate the evolution of the film spectra and derived SPF values for both non-scattering films consisting of solutions of multiple UV absorbers and for highly scattering emulsion films. Finally, we are able to predict the SPF changes as a result of the photochemical processes upon “standard” sunlight exposure.

CONTENTS

CHAPTER 1 INTRODUCTION 12

1.1 Introduction to sunscreen products 12

1.2 Sunscreen actives 12

1.2.1 Dibenzoyl methanes 12

1.2.2 Cinnamates 13

1.2.3 Bis-Ethylhexyloxyphenol Methoxyphenyl Triazine (BEMT, Tinosorb S) 14

1.2.4 Diethylamino Hydroxybenzoyl Hexyl Benzoate (DHHB, Uvinul A Plus Granular) 14

1.2.5 Inorganic particulates 15

1.3 Sun Protection Factor (SPF) 17

1.3.1 *In vivo* SPF measurements 17

1.3.2 *In vitro* SPF measurements 17

1.3.3 Beer- Lambert Law 20

1.4 Photochemistry of sunscreen ingredients 21

1.4.1 Physical deactivation pathways 21

1.4.2 Photochemistry of dibenzoyl methanes 22

1.4.3 Photochemistry of cinnamates 24

1.4.4 Chemical actinometry 25

1.5 Emulsions 26

1.5.1 Solid particles as emulsifiers 26

1.6 Evaporation of droplets / thin films 28

1.6.1 Contact angle and wetting phenomena 29

1.7 Aims of current research 31

1.8 Presentation of thesis 31

1.9 References 33

CHAPTER 2 EXPERIMENTAL 37

2.1 Materials 37

2.1.1 Solvents 37

2.1.2 UV absorber molecules 37

2.1.3 Metal oxide nanoparticles 38

2.1.4 Vitro Skin 39

2.1.5 Other materials 39

2.2 Methods 40

2.2.1 UV/vis absorption spectroscopy 40

2.2.2 Diffuse transmittance spectroscopy 41

2.2.3 Experimental setup of evaporation 42

2.2.4 Preparation of Vitro Skin film 44

2.2.5 Preparation of keratin – lipid dispersion film 45

2.2.6 Preparation of solutions and films containing poly-DADMAC 46

2.2.7 Portable UV lamp 46

2.2.8 Solar simulator 47

2.2.9 Actinometry measurements 49

2.2.10 Experimental setup of photochemical measurements 49

2.2.11 Preparation of particle-stabilised emulsions 52

2.2.12 Characterisation of particle-stabilised emulsions 52

2.2.12.1 Drop test 52

2.2.12.2 Optical microscopy 52

2.2.12.3 Stability measurements 53

2.2.13 Preparation of nanoparticle dispersions 54

2.2.14 Transmission electron microscopy (TEM) 54

2.2.15 Solubility measurements 56

2.2.16 Contact angle measurements 57

2.3 References 58

CHAPTER 3 DETERMINATION OF INITIAL *IN VITRO* SPF FOR SOLUTIONS AND DISPERSIONS CONTAINING UV FILTERS 59

3.1 Introduction 59

3.2 Organic UV absorbers 60

3.2.1 Determination of molar extinction coefficients of UV absorbers in solvents of different polarity 60

3.3 Inorganic particulates 64

3.3.1 Determination of apparent extinction coefficient of dispersions containing metal oxides 64

3.4 Predicted initial in vitro SPF values of UV filters in solvents of different polarity 66

3.4.1 Predicted initial in vitro SPF values of solutions containing UV absorbers 67

3.4.2 Predicted initial *in vitro* SPF values of dispersions containing inorganic particles 71

3.4.3 Predicted *in vitro* SPF for a combination of UV absorbers 75

3.4.4 Comparison of predicted initial *in vitro* SPF of all UV filters 76

3.5 Conclusions 77

3.6 References 79

CHAPTER 4 EVAPORATION OF SOLUTION AND DISPERSION FILMS CONTAINING UV FILTERS 80

4.1 Introduction 80

4.2 Evaporation of solutions of UV absorbers in PG 81

4.2.1 Evaporation of AVB in PG 82

4.2.2 Absorbance measurements of AVB in PG during evaporation 87

4.2.3 Evaporation of DHHB and MC in PG 92

4.2.4 Absorbance measurements of MC and DHHB in PG during evaporation.. 94

4.2.5 *In vitro* SPF determination of UV absorbers.................................... 97

4.3 *Comparison of solutions containing solvents with slow and fast evaporating rate….* 99

4.4 Evaporation of nanoparticle dispersions containing UV absorber.......... 103

4.4.1 Evaporation of 1.0 wt.% nanoparticle dispersions containing UV absorber. 103

4.4.2 Evaporation of 0.1 wt.% nanoparticle dispersions containing UV absorber. 106

4.4.3 Absorbance measurements of 0.1 wt.% TiO_2 dispersion containing 8.0 mM AVB in PG 108

4.5 Evaporation of solutions containing UV absorber molecules in the presence of polymer.. 111

4.6 Evaporation of solutions containing UV absorbers on other substrates.. 115

4.6.1 Vitro Skin as an alternative substrate 115

4.6.2 Keratin – lipid film as an alternative substrate................................ 119

4.7 Conclusions 123

4.8 References 125

CHAPTER 5 EVAPORATION OF PARTICLE-STABILISED EMULSION FILMS……….. 126

5.1 Introduction... 126

5.2 Evaporation evolution of AVB in solvents of different polarity 127

5.2.1 Evaporation evolution of AVB in SQ and PG 127

5.2.2 Absorbance measurements of AVB in SQ and PG 130

5.3 Evaporation evolution of SQ-in-PG and PG-in-SQ emulsion films......... 131

5.4 Optical microscopy measurements of SQ-in-PG and PG-in-SQ emulsion films… 137

5.4.1 Optical microscopy measurements of PG-in-SQ emulsion film....... 137

5.4.2 Optical microscopy measurements of SQ-in-PG emulsion film....... 139

5.5 Absorbance measurements of SQ-in-PG and PG-in-SQ emulsions during evaporation 141

5.5.1 Theoretical considerations 141

5.5.2 Determination of measured and calculated absorbance values of PG-in-SQ and SQ-in-PG emulsion films containing 4.0 mM AVB overall 149

5.5.3 Determination of measured and calculated absorbance values of PG-in-SQ and SQ-in-PG emulsion films containing 4.19 mM MC overall 153

5.6 In vitro SPF determination of UV absorbers 156

5.7 Comparison of emulsions containing solvents with slow and fast evaporating rate…. 159

5.7.1 Optical microscopy measurements of *n*-decane-in-PG emulsion film…... 163

5.7.2 Absorbance measurements of *n*-decane-in-PG emulsion film 164

5.8 Conclusions 167

5.9 References 168

CHAPTER 6 IRRADIATION OF SOLUTIONS, DISPERSIONS AND EMULSIONS CONTAINING UV FILTERS 169

6.1 Introduction 169

6.2 Theoretical considerations 170

6.3 Determination of the absolute spectral irradiances of the light sources .. 171

6.4 Photochemical kinetics of solutions of a single UV absorber 174

6.4.1 Photochemical kinetics of solutions containing AVB 176

6.4.2 Photochemical kinetics of solutions containing MC 189

6.5 Photochemical kinetics of solutions containing a combination of UV absorbers 197

6.6 Photochemical kinetics of emulsions containing UV absorbers 200

6.6.1 Photochemical kinetics of AVB in emulsions 202

6.6.2 Photochemical kinetics of MC in emulsions 207

6.6.3 Varying the volume fraction of PG 210

6.7 Photochemical kinetics of dispersions containing nanoparticles and a single UV absorber 213

6.8 Prediction of the in vitro SPF changes during solar irradiation 217

6.9 Conclusions 221

6.10 References.. 223

CHAPTER 7 SUMMARY OF CONCLUSIONS AND FUTURE WORK.... 225

7.1 Conclusions 225

7.2 Future work 228

APPENDIX A - ^{1}H-NMR DATA OF AVB AND MC.................................229

APPENDIX B - EQUATIONS RELATED TO DETERMINING REACTION RATES..231

CHAPTER 1 INTRODUCTION

1.1 Introduction to sunscreen products

The role of sunscreens is to provide protection against the detrimental short-term and long-term effects that UV radiation can cause to the human skin, such as sunburn, photoaging and photocarcinogenesis.[1] Sunscreen formulation types include solutions, dispersions and emulsions (either oil-in-water or water-in-oil).[2,3] The active ingredients within a sunscreen formulation are commonly a combination of organic UV absorbers and inorganic particulates, both of which can provide optimal performance in the UVA and UVB region of the electromagnetic spectrum.[4,5]

1.2 Sunscreen actives

Desirable properties of an ideal sunscreen active include primarily its photochemical stability under UV light as well as its high effectiveness within low dosage.[6,7] For the latter case, in particular, the concentrations of individual UV absorbers can be limited due to a number of factors including low solubility, regulatory reasons or even patent restrictions.[6,8] In order to tackle these problems, fine metal oxide nanoparticles have also been used to enhance the overall sunscreen performance.[6]

Currently, there are about 55 approved UV absorbers for use in the sunscreen industry.[9] All organic UV absorbers contain aromatic moieties with an electron donating group such as hydroxyl, methoxy or amine in an *ortho*- or *para*- position conjugated next to a carbonyl group.[6,10] Examples of organic molecules that absorb in the UVB region include *para*-amino benzoic acid (PABA) derivatives such as padimate O, salicylates and cinnamates. On the contrary, dibenzoyl methanes and benzophenones exhibit protection against UVA radiation.[11] In this study, we selectively investigate compounds that belong to some of the classes of UV absorbers such as the dibenzoyl methanes, cinnamates and aminobenzoates. In addition, we also present a class of the newly introduced broader UV absorbers.

1.2.1 Dibenzoyl methanes

Dibenzoyl methanes are a representative group of many β-dicarbonyl compounds, which exhibit a major absorbance in the UVA region.[12] From this group, the most widely used is 4-*tert*-butyl-4'-methoxy dibenzoyl methane also known as avobenzone.[13] Avobenzone (other tradenames Parsol 1789 or Eusolex 9020), which is shown in Figure 1.1, has an exceptionally high molar extinction coefficient in the UVA-I region[9] and a maximum absorption at a wavelength in the range of 350 to 365 nm depending on the solvent used.[14] The maximum allowed concentration is 3 wt.%.[2]

Figure 1.1. Structure of the predominant enol form of avobenzone (AVB).

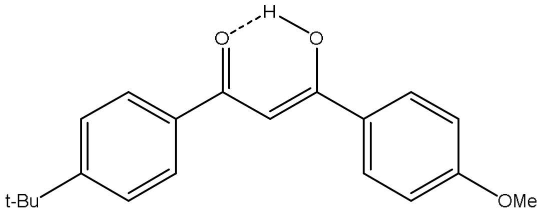

1.2.2 Cinnamates

In general, cinnamates are used in the cosmetic industry due to their excellent ability to act as UVB absorbers. Among these, 2-ethylhexyl-4-methoxycinnamate (octyl methoxycinnamate, EHMC) is the most common representative used in sunscreen formulations. In this group of UV absorbing molecules, isopentyl *p*-methoxycinnamate (isoamyl 4-methoxycinnamate, MC) can also be found. Tradename of MC is Univul MC 80 and its maximum allowed concentration in EU is 10 wt.%. MC is a good solvent for other ingredients of suncare products.[2] The chemical structures of both compounds are shown in Figure 1.2.

Figure 1.2. Structures of (upper) *trans*-ethyl hexyl methoxycinnamate (EHMC) and (lower) isopentyl *p*-methoxycinnamate (Neo Heliopan E-1000).

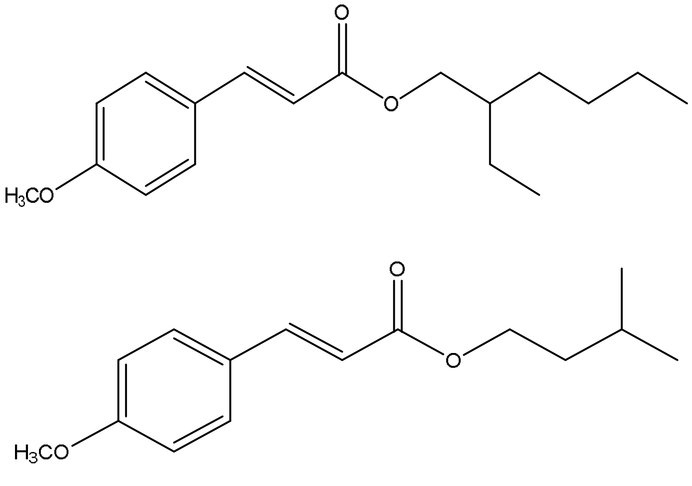

1.2.3 Bis-Ethylhexyloxyphenol Methoxyphenyl Triazine (BEMT, Tinosorb S)

Bis-ethylhexyloxyphenol methoxyphenyl triazine (BEMT) (tradename Tinosorb S) is an oil-soluble UV filter with a strong absorption in both UVA and UVB regions of the UV spectra as depicted in Figure 1.3. Its strong absorption properties can be attributed to the extended resonance delocalisation as a result of the π-π^* character of the tri-phenyl-triazines present. The photostabilising mechanism is enhanced by the presence of the hydroxy substituents in the *ortho*- position which extend the electron transfer through hydrogen bonding.[15] BEMT shows two maximum absorbance peaks around 310 and 350 nm with an extinction coefficient of 46,800 M^{-1} cm^{-1} and of 51,900 $M^{-1}cm^{-1}$ respectively measured in ethanol.[15] Its maximum allowed concentration in sunscreen formulations in EU is equal to 10 wt.%.[2]

Figure 1.3. Structure of bis-ethylhexyloxyphenol methoxyphenyl triazine (BEMT).

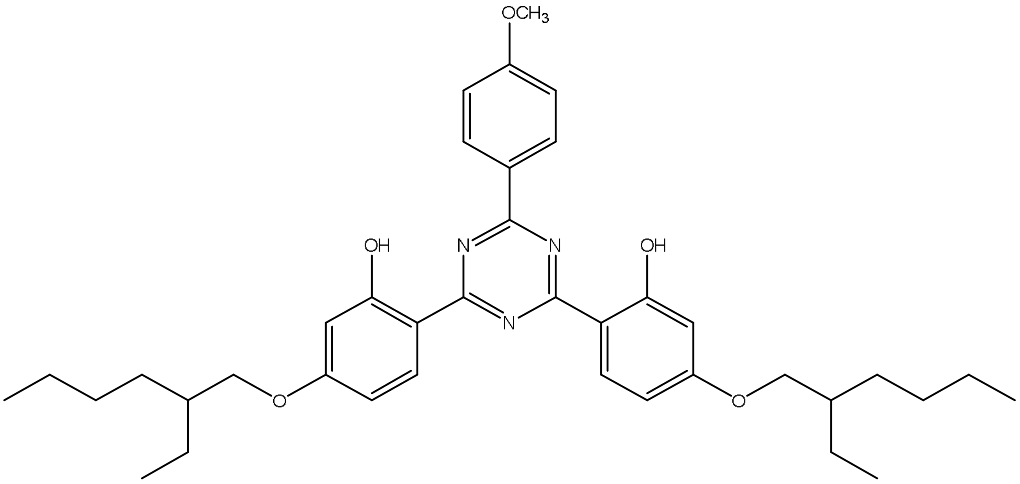

1.2.4 Diethylamino Hydroxybenzoyl Hexyl Benzoate (DHHB, Uvinul A Plus Granular)

Diethylamino hydroxybenzoyl hexyl benzoate (DHHB) is an efficient UVA-I absorber with a maximum absorbance peak around 350 nm and a high extinction coefficient of an approximate value of 35,900 M^{-1} cm^{-1} as illustrated in Figure 1.4. As a result of its high molar extinction coefficient in the UVA-I region of the electromagnetic spectrum, DHHB has been considered as an alternative UV absorber to avobenzone.[3] DHHB comes with other tradenames such as Uvinul A Plus Granular and its maximum allowed concentration in sunscreen formulations is equal to 10 wt.%.[2]

Figure 1.4. Structure of diethylamino hydroxybenzoyl hexyl benzoate (DHHB).

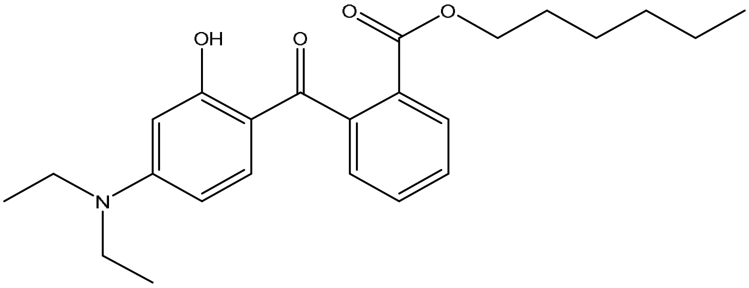

1.2.5 Inorganic particulates

Sunscreen formulations also contain inorganic particles, which attenuate UV irradiation by a contribution of absorption, scattering and reflection. Suitable candidates are materials known as semiconductors.[8] The electronic state of the semiconductors contains regions where no energy levels are present. This void energy region is termed band gap and it is extended in the area between the filled valence and the vacant conduction band as shown in Figure 1.5.[16] For the electronic excitation from the valence to the conduction band, the photon energy is expected to be equal or greater than the band gap.

Since the energy gap corresponds to wavelengths between 380 and 420 nm, only light with equal or shorter wavelength (termed as critical wavelength), will have enough energy for electronic excitation. Light with longer wavelengths than the band gap will not be absorbed by the semiconductor.[6] It is also important to note that for semiconductors, the relationship between the band gap and the particle size is inversely proportional. As such, the maximum absorbance peak will shift to shorter wavelengths as the particle size decreases.[17,18]

Figure 1.5. Conceptual diagram showing the excitation of an electron (e^-) from the valence band to the conduction band upon irradiation of a semiconductor. The vacancy left in the valence band is known as hole (h^+).[19]

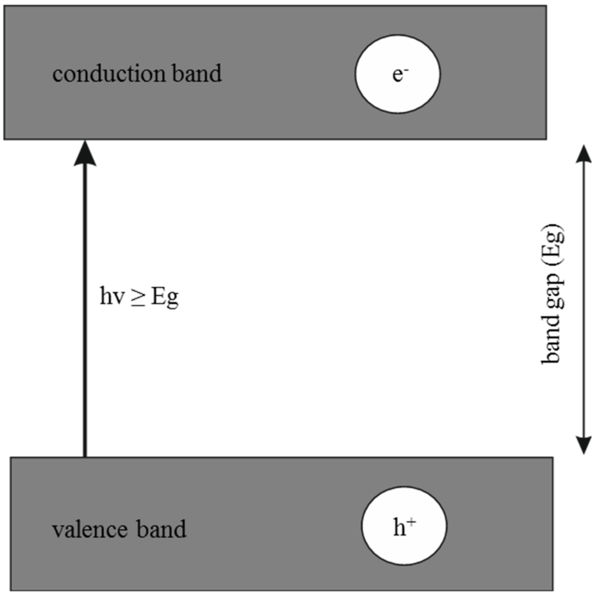

Recently, Zhang et al. have determined the band gap energies for numerous metal oxide semiconductors using diffuse reflectance spectroscopy.[20] Within this study, we are concerned with the investigation of TiO_2, ZnO, CeO_2 and WO_3 nanoparticles and their band gap energies and critical wavelengths are shown in the Table 1.1 below.

Table 1.1. Band gap energies and critical wavelengths of metal oxide nanoparticles.[20]

Semiconductor type	**Band gap energy/eV**	**Critical wavelength λ_c/nm**
TiO_2 (anatase)	3.33	373
ZnO	3.31	375
WO_3	3.05	407
CeO_2	3.65	340

In order to achieve the "cosmetically acceptable" transparency, the particles introduced in the sunscreen formulations are of nm size and particularly in the range between 100 – 200 nm. For these sizes, the particles remain deposited on the stratum corneum surface and do not penetrate to the lower viable layers of the skin.[21]

1.3 Sun Protection Factor (SPF)

1.3.1 *In vivo* SPF measurements

The official accepted method for the efficacy of sunscreen products is the *in vivo* Sun Protection Factor (SPF) method based on the European Cosmetic Association (COLIPA) standard.[22] The *in vivo* SPF is described by the equation below[22,23]

$$in\ vivo\ SPF = \frac{MED\ of\ skin\ protected\ with\ sunscreen}{MED\ of\ unprotected\ skin} \tag{1.1}$$

where minimal erythemal dose (MED) corresponds to the lowest possible UV dose that produces the first unambiguous erythema within 16 - 24 h after exposure.[22] With the term erythema, it is defined the development of an inflammation reaction of the human skin as a result of its overexposure to UV radiation.[24] The source of UV irradiation is artificial (Xe or Hg arc lamp with appropriate filters) of defined and known output, which simulates solar sunlight.[22] The test is restricted to the back of the same volunteer and the determination of the *in vivo* SPF is expressed as the arithmetic mean that was derived from a panel of human subjects (between 10 - 20) with different skin types.[22,24] Based on equation 1.1, the *in vivo* SPF is an established metric to measure sunscreen protection against erythema/sunburn alone. It is important to note, however, that *in vivo* SPF cannot be used as a metric for protection against photoaging and skin cancer.[6]

1.3.2 *In vitro* SPF measurements

In vivo SPF measurements, though reliable, are time-consuming and invasive processes on human volunteer subjects. *In vitro* SPF measurements, on the contrary, based on spectrophotometric data are considered to be a fast, inexpensive and convenient approach, which lacks accuracy however. For this reason, a validated method is required, which can control several parameters, including choice of i) substrate, ii) instrumentation, iii) product application and/or iv) technique variations.[25,26]

The determination of the *in vitro* SPF of a thin sunscreen film, which is applied on a suitable UV transparent substrate, is based on the measurement of the diffuse transmittance.[27,28] The estimated *in vitro* SPF is derived according to equation below[29]

$$in\ vitro\ SPF = \frac{\int_{\lambda=290\ nm}^{\lambda=400\ nm} E(\lambda)S(\lambda)d\lambda}{\int_{\lambda=290nm}^{\lambda=400nm} E(\lambda)S(\lambda)\ T(\lambda)\ d\lambda} \qquad (1.2)$$

where *E(λ)* is the erythema action spectrum and *S(λ)* is the spectral irradiance from the UV source (simulating for SPF testing) as a function of wavelength (W m^{-2} nm^{-1}). The inverse of the transmission T(λ) corresponds to the factor by which the intensity of the UV radiation is attenuated at a certain wavelength and it is termed as monochromatic protection factor (MPF).[29,30]

The erythema action spectrum *E(λ)* is defined as the relative effectiveness of UV radiation to cause erythema in human skin.[31] It is used in a normalised form based on experimental data and it is strongly dependent on wavelength.[24,32] In addition, it is the basis of UV index, which is globally used in weather forecasting and in public health information.[32] From Figure 1.6 it can be seen that the higher the value of the erythemal action spectrum, the more sensitive the human skin is against the respective type of UV radiation.[24] The highest values are observed in the UVC (200 – 290 nm) region, which are blocked, however, by the stratospheric ozone layer and do not penetrate in earth's atmosphere.[33] A steep decrease is observed in the UVB region between 290 – 320 nm, followed by a further decrease in the UVA range between 320 – 400 nm. Since energy is inversely proportional to wavelength, it can be seen that the former obtains higher values and thus is more damaging at short wavelengths.[6,24]

The spectral irradiance *S(λ)* describes the intensity of solar irradiation that hits earth's surface at each spectral wavelength.[3,34] For our investigation, the values of spectral irradiance correspond to defined conditions such as midday midsummer sunlight for latitude 40°N, solar zenith angle 20° and ozone layer thickness equal to 0.305 cm.[35] From Figure 1.6, it can also be seen that the spectral irradiance values exponentially increase within the UVB region. The highest values of the spectral irradiance, however, are measured in the UVA region of the electromagnetic spectrum.[30]

The product of the two curves of erythemal action spectrum and spectral irradiance results in the erythemal effectiveness spectrum, which spreads over the whole range of UV irradiation.[6,30] The maximum value of the erythemal effectiveness is expected to appear at 308 nm, in the UVB range.[24] It is important to note that equation 1.2 describes the wavelength integration limit, for the combined UVA and UVB range.

However, other wavelength ranges can be used accordingly to estimate alternative SPF values corresponding to the UVB or the UVA region of the electromagnetic spectrum alone.

Figure 1.6. Erythema action spectrum (black solid line) and spectral irradiance of terrestrial sunlight (white dots) corresponding to midday midsummer sunlight for latitude 40°N, solar zenith angle 20° and ozone layer thickness equal to 0.305 cm. Vertical dashed lines indicate the UV regions of the electromagnetic spectrum: UVC (200 – 290 nm), UVB (290 – 320 nm) and UVA (320 – 400 nm).[35]

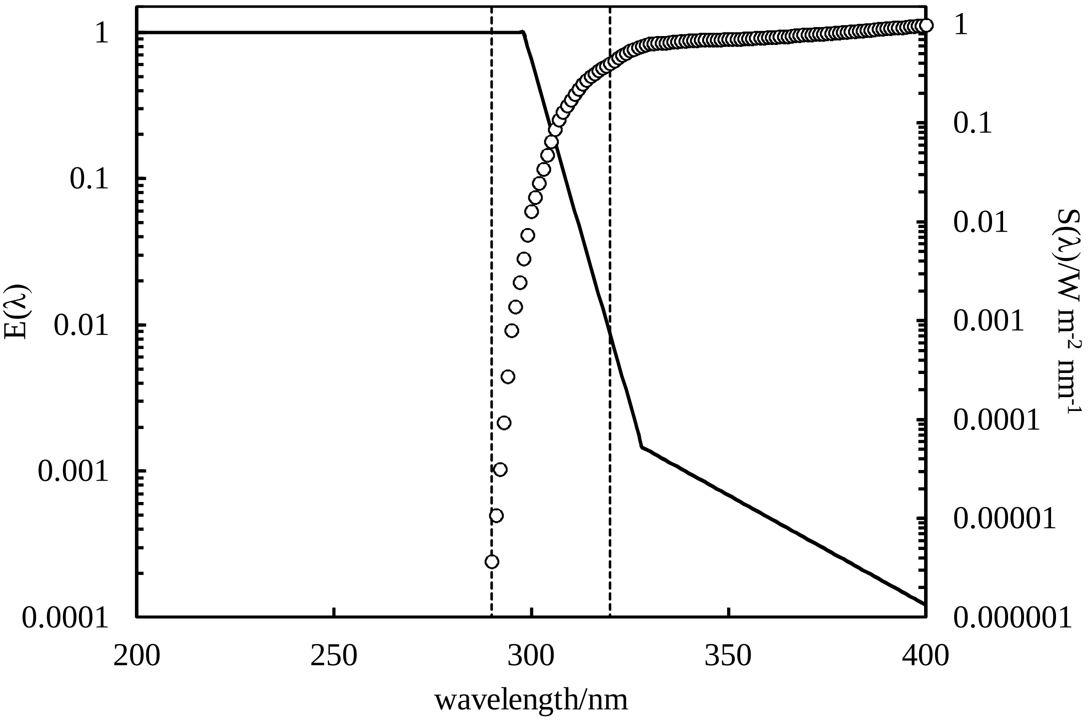

The amount of test product applied to skin for the *in vivo* SPF measurement is 2.0 mg cm^{-2}.[22] This value is equal to a uniform film of approximately 20 μm thickness deposited on a smooth surface. In reality, however, film deposition on human skin is usually irregular and it does not follow skin's outer surface resulting in "valleys" with coverage and "peaks" with very thin or even no sunscreen coverage at all.[3,30] For this reason, model calculations have been introduced in order to account for these film irregularities in an attempt to correctly determine the optical transmittance and thus the *in vitro* SPF .[36]

Despite these discrepancies, however, *in vitro* SPF calculations are still advantageous because they can be used to assess as a function of time[9,21,25,37] i) the photochemical behaviour of the active ingredients within sunscreen films, ii) the evaporation behaviour of their volatile components[38] and iii) the film's resistance upon its water immersion. Within this study, we are concerned with the investigation of the first two processes only.

1.3.3 Beer- Lambert Law

Consider the case where light passes through a solution containing an absorbing solute. It is expected that part of the light will be absorbed by the solute and the light intensity will decrease exponentially. The ratio of the transmitted (I) over the incident light intensity (I_o) is described as transmittance T. The relationship between absorbance A and transmittance is shown with the equation below.

$$A = -log_{10}T = log_{10}\left(\frac{I_o}{I}\right) \tag{1.3}$$

where I_o, I are the incident and the transmitted light intensity respectively.

Empirically, it was found that at a particular wavelength and for a specific solute, the absorbance of a solution is proportional to its concentration c and its path length d, as shown below

$$A = \varepsilon cd \tag{1.4}$$

where ε is the molar extinction coefficient, which indicates how strongly the solute absorbs at a particular wavelength. Equation 1.4 is known as the Beer-Lambert Law and it is used throughout for the determination of the absorbance measurements. For solutions containing a mixture of UV absorbing solutes, at each wavelength the absorbance of the solution is described below

$$A = (\varepsilon_1 c_1 + \varepsilon_2 c_2 + \varepsilon_3 c_3 + \cdots)d \tag{1.5}$$

where ε and c are the molar extinction coefficient and the concentrations respectively for each UV absorber as indicated by the subscript. Equation 1.5 is used for our investigation of sunscreen films containing a combination of UV absorbers.

1.4 Photochemistry of sunscreen ingredients

1.4.1 Physical deactivation pathways

Organic molecules contain group of atoms, termed as chromophore groups, which are responsible for light absorption of the UV region of the electromagnetic spectrum[24] and its conversion to electronic excited energy.[19] These organic molecules can be classified, depending on the protection they provide within the UV range, as UVA or UVB absorbers.[11]

Absorption of photons by the chromophore group increases the energy of the molecule promoting the latter from a ground electronic state to an excited electronic state (either singlet or triplet). Physical deactivation pathways, however, allow the molecule to return to its ground state configuration with the energy of either of the excited states dissipated as heat, light or transferred to other molecules.[15] In this study, we will be mostly concerned with radiationless transitions such as internal conversion and intersystem crossing. Internal conversion is a process which corresponds to relaxation from an upper excited electronic state to a lower excited electronic state with the same spin quantum number. Intersystem crossing however is the radiationless transition that occurs between states with different spin quantum number.[19,39] The electronic transitions within the ground and the excited electronic states are represented by the Jablonski diagram as illustrated below in Figure 1.7.

Figure 1.7. Simplified Jablonski diagram presenting the properties of the excited states and their relaxation processes that may occur after excitation.

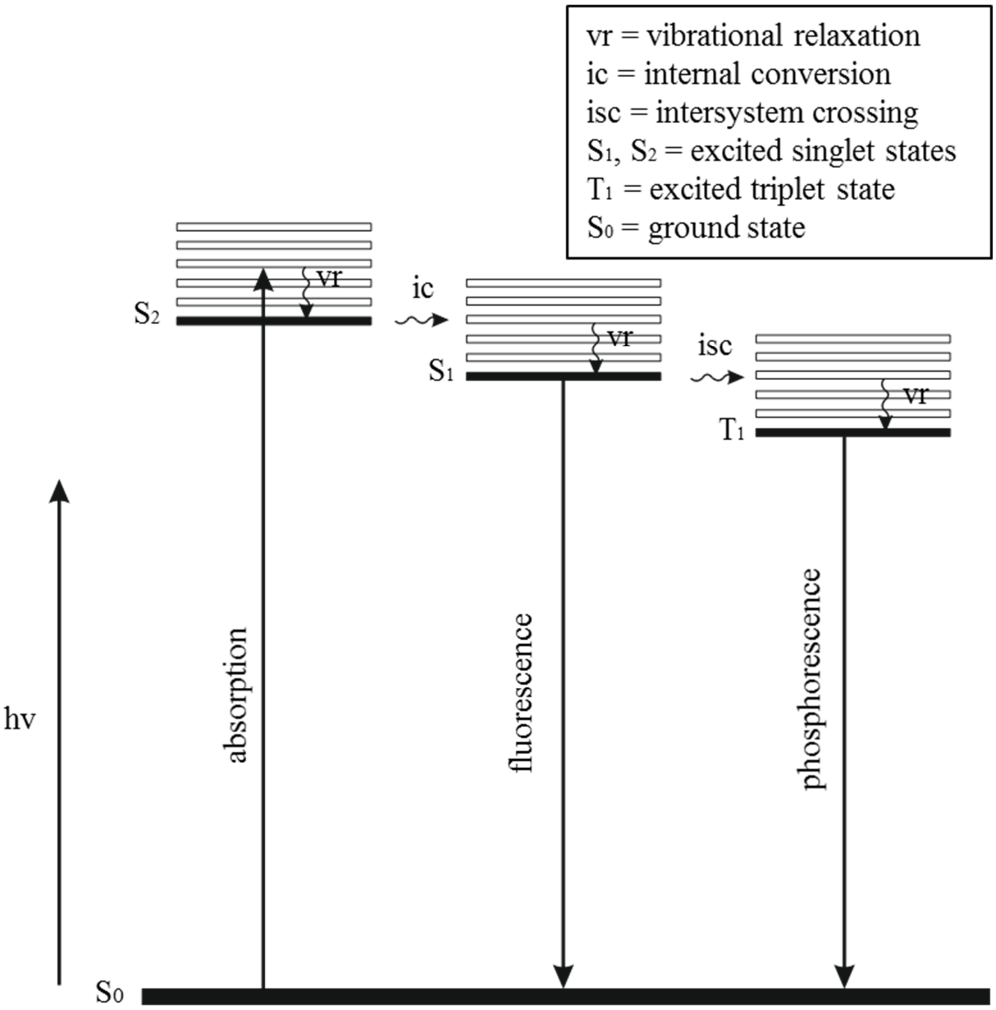

1.4.2 Photochemistry of dibenzoyl methanes

It is known that avobenzone exists in two tautomeric forms named as the enol- and the keto- tautomer.[40] The latter occurs in one geometric form whereas the former has been found in many geometric configurations as shown in Figure 1.8.[41] It was also suggested that the transient enol- species of avobenzone were a result of either a fast rotation over the single bond or as an isomerisation at the double bond[41] with a very short lifetime.[7]

Figure 1.8. Tautomeric and geometric configurations of AVB in equilibrium. Di-keto- form (left), enol- form (middle) and possible rotamer of the enol- form (right).

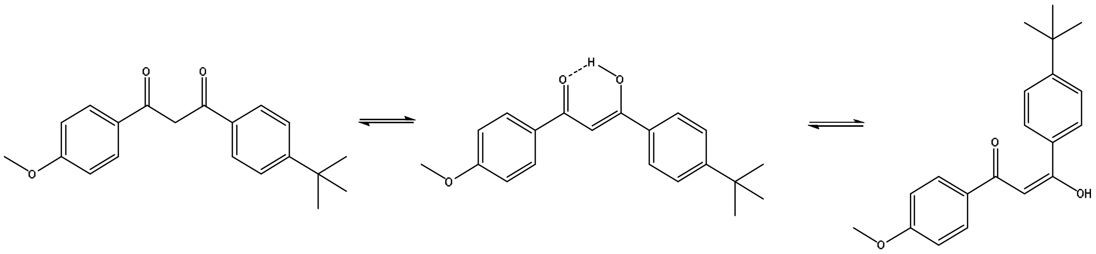

The predominant enol- form in the ground state is due to intramolecular H-bonding and it shows a significant absorbance in the UVA-I wavelength region. Under UV radiation, the enol form is photoisomerised to the keto form absorbing in the UVC wavelength region and particularly in the range from 260 to 280 nm as illustrated in Figure 1.9.[41]

Figure 1.9. Simplified schematic diagram to present keto – enol tautomerism in AVB.

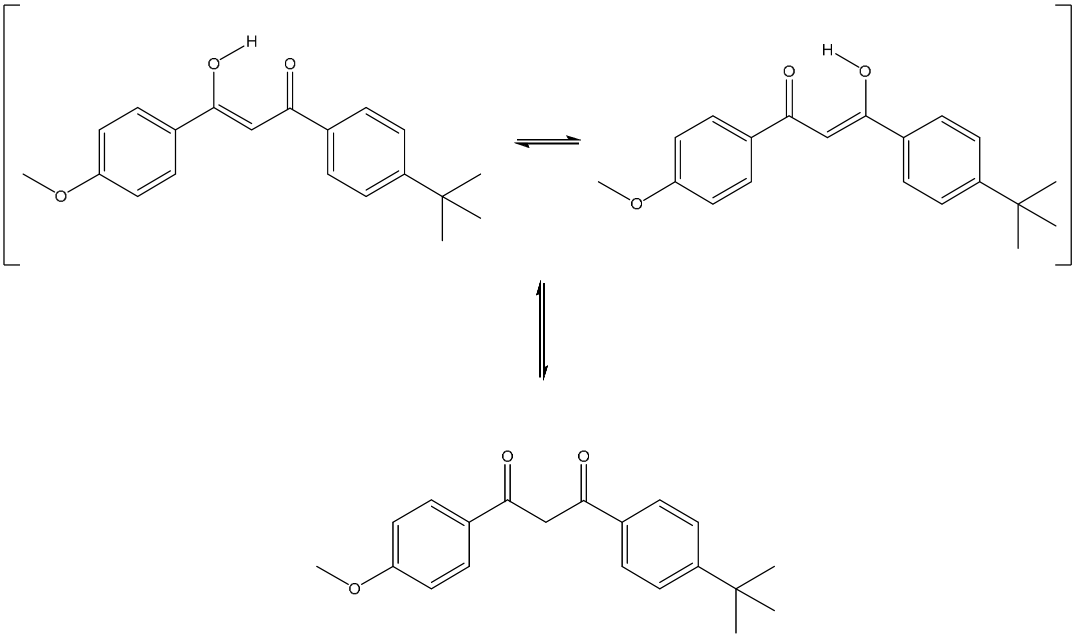

The mechanism proposed occurs via the conversion of the excited singlet state of the di-keto form to its lower excited triplet state.[7] It is the latter species which either gives rise to the photodegradation products or reacts with oxygen resulting in the formation of singlet oxygen.[21] The highly reactive oxygen species react with the enol- form of avobenzone leading to the formation of different photodegradation products as shown schematically in Figure 1.10.[21]

Figure 1.10. Keto – enol tautomerism of AVB and schematic representation of the photochemical paths after UV irradiation.

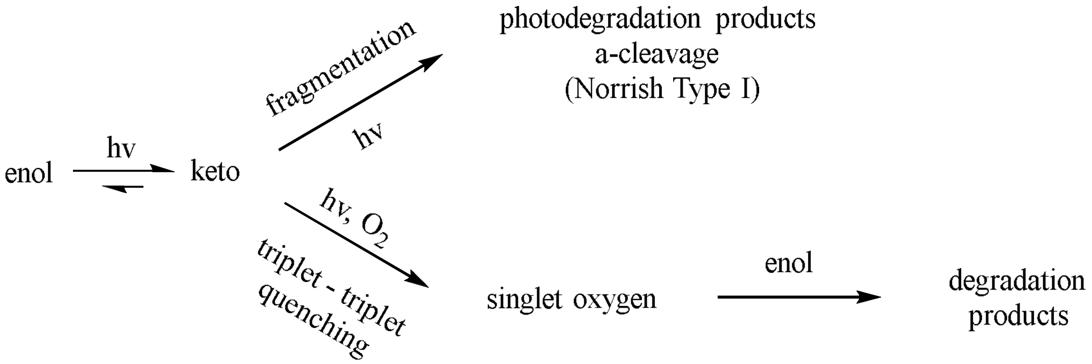

Irreversible photodegradation of avobenzone has been observed and related to an α-cleavage (or otherwise stated as Norrish Type I process) occurring from the di-keto triplet state.[7] By the term α-cleavage it is implied the cleavage of one of the bonds in the α-position adjacent to C=O group leading to the formation of radicals.[19] Schwack et al. have investigated the photochemistry of dibenzoyl methanes under solar simulated irradiation and they have identified with the use of gas chromatography/mass spectrometry techniques, several groups of photodegradation products.[41] Mturi et al. have suggested that the photostability of avobenzone is solvent dependent with the latter being photostable when dissolved within a polar protic solvent as opposed to a non-polar.[40] A plausible mechanism that has been proposed is based on the formation of an adduct between the enol- tautomer and the polar protic solvent *via* intermolecular H-bonding.[40]

1.4.3 Photochemistry of cinnamates

Though cinnamates are classified as excellent UVB absorbers with a maximum absorbance peak around 310 nm, they are also efficient in the UVA-II region of the electromagnetic spectrum.[42,43] In their ground state, it is the *trans* isomer that is the dominant form. Under UV irradiation, however, cinnamates undergo *trans* to *cis* isomerisation in solutions as shown in Figure 1.11.

Figure 1.11. *Trans*- to *cis*- isomerisation of EHMC when UV irradiation is present.

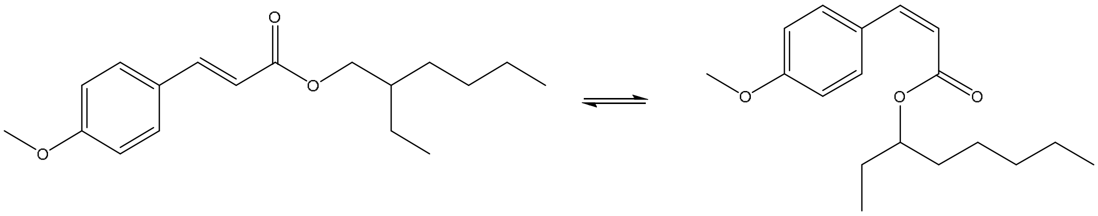

In terms of EHMC, Pattanaargson et al. have investigated its photoisomerisation under natural sunlight exposure.[44] Their results have indicated that the equilibrium of the photoisomerisation of EHMC depends upon concentration and the polarity of the solvent used. In their work, they have also determined the extinction coefficients of the *trans* and the *cis* isomer, both of which are observed in the UVB region.[44] Less attention has been paid to the formation of other photoproducts. Relative studies have shown that two molecules of EHMC can undergo a [2+2] cycloaddition reaction or they can also react with avobenzone molecules leading to photo cycloaddition reactions.[37,43]

1.4.4 Chemical actinometry

By the term chemical actinometer, it is implied a chemical system that undergoes a photochemical reaction for a known quantum yield. The rates of this photochemical process can be used in order to determine the absorbed photon flow.[45] The quantum yield is defined as the number of molecules changed, formed or destroyed over the number of absorbed photons for the same period of time as shown

$$\phi = \frac{number\ of\ events}{number\ of\ photons\ absorbed} \tag{1.6}$$

For conditions where one molecule is excited by a single quantum or photon (known as Stark-Einstein Law) the quantum yield should be equal to 1. However, the Stark-Einstein Law is not always obeyed and the values of the quantum yield are significantly less than one. In this study, the selected chemical actinometer was 9, 10 – dimethylanthracene (DMA) in 1,1,2 – trichloro – 1,2,2 – trifluoro ethane (Freon 113) solution with a known quantum yield.[46]

1.5 Emulsions

Emulsions are used as “vehicles” for photoprotection. An emulsion can be defined as a thermodynamically unstable mixture of two immiscible liquids (for example oil and water) where one of the phases is dispersed into the other.[47] In the case where oil drops are dispersed in water, the emulsion is named as oil-in-water (o/w) whereas when water drops are dispersed in oil, the emulsion is named as water-in-oil (w/o). Mixing of the heterogeneous system between two immiscible liquids results in the formation of an unstable emulsion which undergoes complete phase separation within seconds due to the large amount of disfavoured oil and water interfacial area. This is evident based on the free energy of emulsion formation ΔG from two separate immiscible phases as shown in the equation below

$$\Delta G = \gamma \Delta A - T\Delta S \tag{1.7}$$

where γ is the interfacial tension between the two immiscible liquids, ΔA is the change in the interfacial area between the two immiscible liquids, ΔS the change in the entropy of the system and T the temperature of the system. For a high value of interfacial tension between water and oil, it is evident that the ΔG will be positive and thus the system is thermodynamically unstable.

Since emulsions made by agitation are very unstable and break, a surface active material is required and this is termed as an emulsifier. As such, the role of the emulsifier is to lower the interfacial tension of the two immiscible liquids by adsorbing between them[48] and thus rendering them stable against creaming, flocculation, Ostwald ripening and coalescence.[49] Types of emulsifiers that can be used include low molar mass surface active agents (termed as surfactants), polymers, proteins and solid particles.[48]

1.5.1 Solid particles as emulsifiers

Emulsions can also be prepared and stabilised with the use of solid particles alone.[50] Emulsions of this type are named Pickering emulsions after the work of S.U. Pickering who described the phenomenon.[51] An earlier independent study was also made by W. Ramsden.[52] Particle-stabilised emulsions show enhanced stability, which is attributed to the high energy barrier required to remove the particles from the interface and to drop coalescence.[53] During the emulsification process, a layer is formed around the droplets, which can act as a steric barrier that inhibits coalescence.[54] A wide variety of solid particles has been used as stabilisers for the formation of either oil-in-water or water-in-oil emulsions such as hydrophilic and hydrophobic silica, barium sulfate, clay, and calcium carbonate.[55]

A key factor of solid-stabilised emulsions is the contact angle that the particles make with the oil-water interface.[48] Thus, the type of the emulsion formed is dependent upon the wettability (contact angle) of the individual particles when adsorbed at the liquid interface.[56] For a spherical particle residing at a two liquid interface, the contact angle is measured by convention through the aqueous phase as shown in Figure 1.12.[57] For conditions such that the contact angle is less than 90°, particles stabilise o/w emulsions. On the contrary, when a contact angle is more than 90°, particles stabilise w/o emulsions. An important note is that if the solid particles were completely wetted by either phase, they become dispersed and are incapable of stabilising an emulsion.[58]

Figure 1.12. Upper: Location of a particle at the oil-water interface is determined by the contact angle θ measured through the aqueous phase, which in turn dictates (lower) the emulsion type produced.[48]

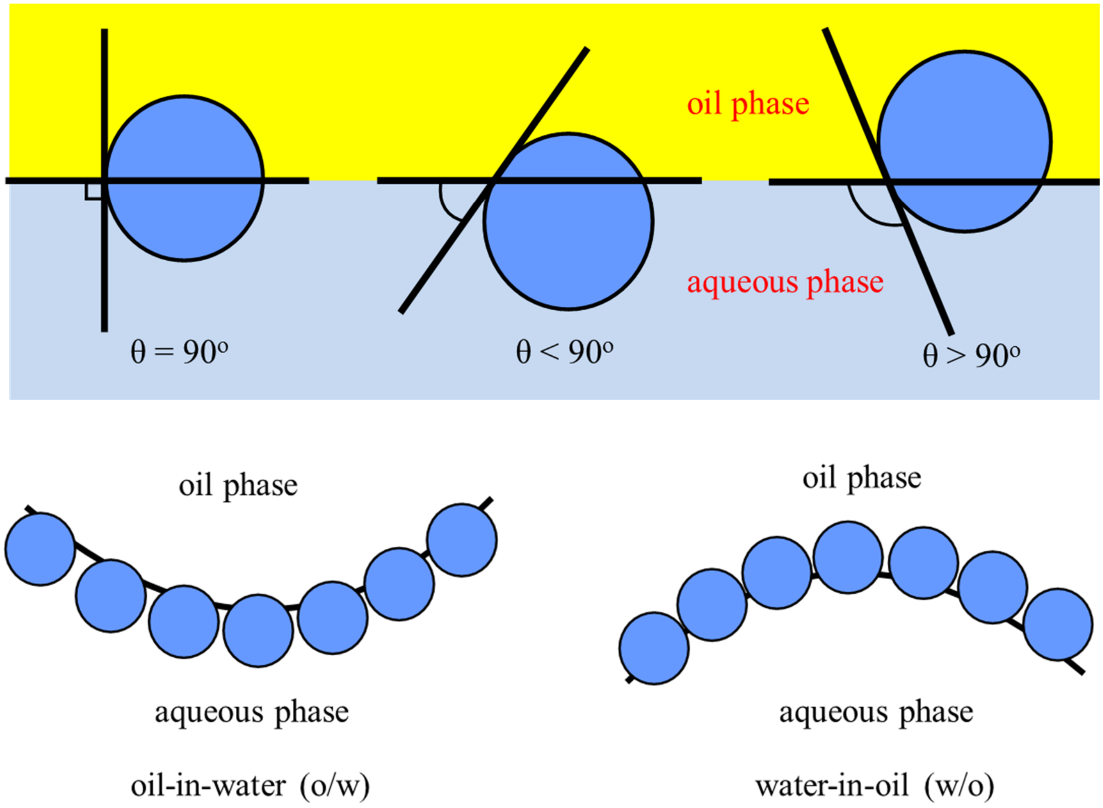

The energy of detachment required to remove a particle from the interface to the continuous phase is given by the following equation[48]

$$E_{detach} = \pi r^2 \gamma (1 \pm cos\theta)^2 \tag{1.8}$$

where E_{detach} corresponds to the detachment energy (J), γ is the interfacial tension between two immiscible liquids (oil-water) (N m^{-1}), r is the particle radius (m) and θ is the contact angle (degrees). The sign within the bracket corresponds to particle adsorption either from the aqueous phase (negative sign) or from the non-aqueous phase (positive sign). From equation 1.8, it can also be seen that the energy of detachment is proportional to the square of the radius of the particle. Hence, the bigger the particle, the larger the energy of the detachment required.[48]

In the present work, particular attention was given to particle-stabilised emulsions where the aqueous phase has been replaced with another polar liquid such as propane-1,2-diol.[59] Merits of the use of propane-1,2-diol instead of water, include its ability to solubilise the sunscreen actives and its slow evaporation rate.

1.6 Evaporation of droplets / thin films

The evaporation mechanism results from a combination of heat and mass transfer at the liquid/vapour interface.[60] Heat is transferred by conduction and convection from the vapour present in the immediate vicinity of the liquid film, to the liquid surface whereas mass is transferred by diffusion and convection from the liquid surface back into the vapour.[60,61] Under conditions where the partial vapour pressure of the surrounding gas is lower than its saturated vapour pressure, evaporation of the liquid molecules is favoured into the air as shown in Figure 1.13.[62] For conditions, however, that the saturated vapour pressure has been reached, an equilibrium has been established where the rate of evaporation of the molecules leaving the liquid phase is equal to the rate of condensation of the vapour molecules entering the liquid phase as illustrated in Figure 1.13.[61]

Figure 1.13. Schematic representation of the evaporation of a liquid into a gas phase in an open (left) and in a sealed (right) container.

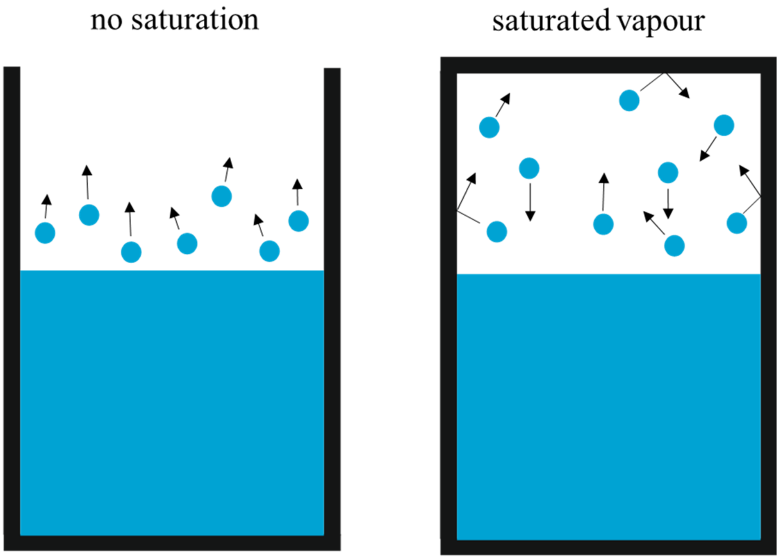

1.6.1 Contact angle and wetting phenomena

For a circular drop deposited on a solid substrate, a quantitative description of wetting phenomena can be provided. At the three-phase contact line, which is formed between the solid substrate, the deposited liquid and the gaseous environment/vapour, the contact angle can be determined based on equation below, known as Young's equation.

$$\gamma_{LV}\, cos\theta = \gamma_{SV} - \gamma_{SL} \tag{1.9}$$

where γ_{LV}, γ_{SV} and γ_{SL} correspond to the interfacial tensions between the liquid/vapour, solid/vapour and solid/liquid interfaces respectively. If the three interfacial tensions are known, the wetting state can be directly determined.[63] As shown in Figure 1.14, for conditions where the solid/vapour interfacial tension is higher than that of the solid/liquid tension, the $cos\theta$ is expected to be positive. This implies that the contact angle is smaller than 90° and thus the liquid partially wets the solid substrate. For conditions, however, where the solid/liquid tension is higher than the solid/vapour interfacial tension, the $cos\theta$ will be negative. As such, it is expected that the contact angle will be higher than 90° and the liquid dewets the solid substrate.[63] It is important to note that Young's equation is valid assuming thermodynamic equilibrium (*i.e.* mechanical, chemical and thermal equilibrium).[63]

Figure 1.14. Cross-section diagram of the three-phase contact angle between a sessile droplet of liquid deposited on a solid substrate.

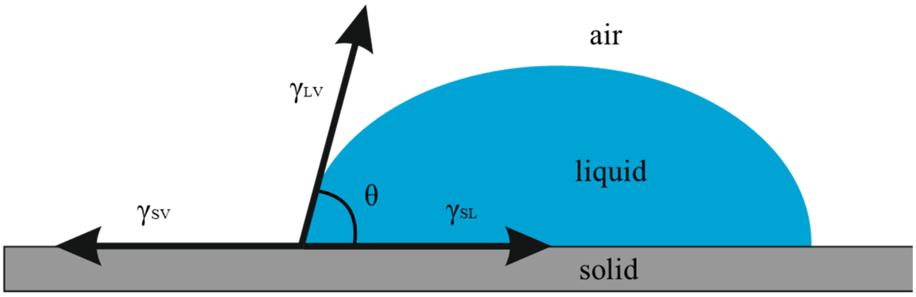

Two possible mechanisms have been proposed in order to describe the evaporation evolution of a droplet.[60] The first scenario assumes that the droplet contact area remains constant but the height of the droplet progressively decreases as evaporation proceeds. It is evident that for this mechanism to be observed, the droplet has to be pinned at the three-phase contact line. Pinning of the droplet can be achieved either with the addition of particles or the use of a rough substrate.

The second scenario assumes that the contact angle at the base edge remains constant but the droplet surface area progressively recedes. For the latter case to occur, it is implied that there is no pinning of the droplet. In reality, however, both mechanisms are observed in a combined fashion. A critical contact angle is initially reached followed by droplet area shrinkage and this is repeatedly observed until complete droplet evaporation. Both evaporation mechanisms are schematically shown in Figure 1.15.[60]

Figure 1.15. Cross-section of the flow regimes within the droplet during its evaporation. The solid black line indicates the constant contact area regime whereas the dashed line illustrates the constant contact angle regime.

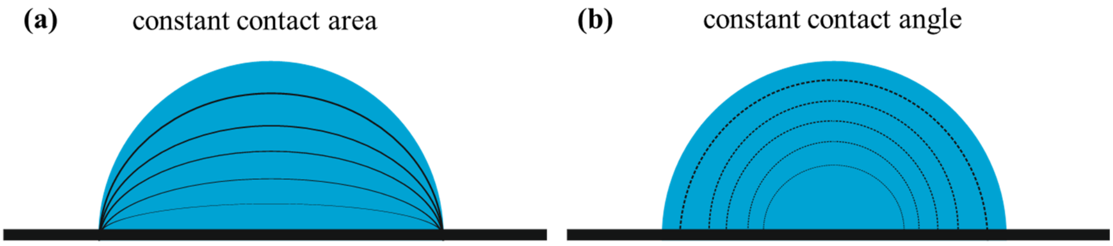

There is extensive literature on the particle deposition and the formation of the so-called coffee-ring effect from evaporating colloidal droplets and films.[60,64,65]

However, in this study, we are not concerned with the physics and the relevant fluid mechanisms of colloidal suspensions.

1.7 Aims of current research

The aim of the work presented in this study is to understand and optimise sunscreen formulations. The efficacy of these formulations is determined by introducing the Sun Protection Factor (SPF). It is expected that the higher the SPF value, the better the human skin protection will be against solar irradiation. In this study, we show with simple measurements that the two primary mechanisms for the loss of SPF in sunscreens correspond to i) the evaporation of the volatile components present in the formulation and ii) to the photochemical changes that UV filters undergo upon exposure to solar irradiation.

From the obtained *in vitro* measurements with regards to the relevant photochemical and evaporation processes, we have developed validated models that allows us to predict how sunscreen film SPF varies with time. This information provides useful guidance about the impact that both mechanisms have on these formulations when monitored with respect to time. This can be an important step for formulators in the sunscreen industry to design more effective sunscreens.

1.8 Presentation of thesis

Following up a concise introduction describing the area of sunscreens, Chapter 2 presents the experimental techniques used throughout this study. In addition, there is an extensive description of the evaporation and photochemical experimental setup. In Chapter 3, we present the initial estimated *in vitro* SPF values for solutions and dispersions containing sunscreen actives close to their solubility limit at a fixed temperature of 32^{o}C.

In Chapter 4, we discuss the evaporation of solution and dispersion films. Results have shown how the evaporation process affects the loss in the absorbance and how this behaviour is depicted in the *in vitro* SPF calculations. In Chapter 5, our investigation is extended to particle-stabilised emulsion films, which were prepared from equal volumes of a polar PG phase and a non-polar squalane phase. Our data have confirmed that for these systems, the loss in the transmittance is directly related to the collapse of the emulsion structure upon complete evaporation of the PG phase alone. Chapter 6 is concerned with the relevant photochemical mechanisms that occur upon irradiation of solutions, dispersions and emulsions containing UV absorbers. Conclusions and suggestions for future work are described in Chapter 7. Appendix A presents the ^{1}H-NMR data of AVB and MC that were extensively investigated within this study. Finally, Appendix B contains the derivation of the equation related to the reaction rates presented in Chapter 6.

1.9 References

1. A. Fourtanier, D. Moyal and S. Seite, *Photochem. Photobiol. Sci.*, 2012, **11**, 81-89.
2. H. W. Lim and Z. D. Draelos, *Clinical Guide to Sunscreens and Photoprotection*, Informa Healthcare, New York, 1st edition, 2009.
3. N. A. Shaath, *Sunscreens – Regulations and Commercial Development*, Taylor and Francis, Boca Raton, 3rd edition, 2005.
4. K. Morabito, N. C. Shapley, K. G. Steely and A. Tripathi, *Int. J. Cosmetic Sci.*, 2011, **33**, 385-390.
5. S. González, M. Fernández-Lorente and Y. Gilaberte-Calzada, *Clin. Dermatol.*, 2008, **26**, 614–626.
6. U. Osterwalder, M. Sohn and B. Herzog, *Photodermatol. Photoimunol.& Photomed.*, 2014, **30**, 62-80.
7. V. Lhiaubet-Vallet, M. Marin, O. Jimenez, O. Gorchs, C. Trullas and M. A. Miranda, *Photochem. Photobiol. Sci.*, 2010, **9**, 552–558.
8. B. Herzog and F. Sengun, *Photochem. Photobiol. Sci.*, 2015, **14**, 2054-2063.
9. N. A. Shaath, *Photochem. Photobiol. Sci.*, 2010, **9**, 464-469.
10. L. Beyere, S. Yarasi and G. R. Loppnow, *J. Raman Spectrosc.*, 2003, **34**, 743–750.
11. N. Serpone, D. Dondi and A. Albini, *Inorganica Chim. Acta*, 2007, **360**, 794–802.
12. C. Paris, V. Lhiaubet-vallet, O. Jiménez, C. Trullas and M. A. Miranda, *Photochem. Photobiol.*, 2009, **85**, 178–184.
13. S. Tobita, J. Ohba, K. Nakagawa and H. Shizuka, *J. Photochem. Photobiol.*, 1995, **92**, 61–67.
14. A. Cantrell and D. J. McGarvey, *J. Photochem. Photobiol.*, 2001, **64**, 117–122.
15. E. Chatelain and B. Gabard, *Photochem. Photobiol.*, 2001, **74**, 401–406.
16. A. L. Linsebigler, G. Lu and J. T. Yates Jr., *Chem. Rev.*, 1995, **95**, 735-758.
17. J. P. Wilcoxon, R. L. Williamson and R. Baughman, *J. Chem. Phys.*, 1993, **98**, 9933-9950.
18. J. D. Aiken III, R. G. Finke, *J. Mol. Catal. A-Chem.*, 1999, **145**, 1-44.
19. B. Wardle, *Principles and Applications of Photochemistry*, Wiley, Chichester, 1st edition, 2009.

20. H. Zhang, Z. Ji, T. Xia, H. Meng, C. Low-Kam, R. Liu, S. Pokhrel, S. Lin, X. Wang, Y. Liao, M. Wang, L. Li, R. Rallo, R. Damoiseaux, D. Telesca, L. Madler, Y. Cohen, J. I. Zink and A. E. Nel, *ACS Nano*, 2012, **5**, 4349–4368.
21. J. Kockler, M. Oelgemoller, S. Robertson and B. D. Glass, *J. Photochem. Photobiol. C*, 2012, 13, 91-110.
22. The European Cosmetic Toiletry and Perfumery Association - COLIPA, *International Sun Protection Factor (SPF) Test Method*, COLIPA, Bruxelles, 2006.
23. P. U. Giacomoni, L. Teta and L. Najdek, *Photochem. Photobiol. Sci.*, 2010, **9**, 524–529.
24. A. Albini, *Photochemistry Volume 40*, RSC Publishing, Cambridge, 2012.
25. J. Stanfield, U. Osterwalder and B. Herzog, *Photochem. Photobiol. Sci.*, 2010, **9**, 489-494.
26. Y. Miura, T. Hirao and M. Hatao, *Photochem. Photobiol.*, 2012, **88**, 475-482.
27. L. Ferrero, M. Pissavini and O. Doucet, *Photochem. Photobiol. Sci.*, 2010, **9**, 540–551.
28. D. Garoli, M. G. Pelizzo, B. Bernardini, P. Nicolosi and M. Alaibac, *J. Dermatol. Sci.*, 2008, **52**, 193–204.
29. R. M. Sayre, P. P. Agin, G. J. LeVee and E. Marlowe, *Photochem. Photobiol.*, 1979, **29**, 559-566.
30. B. Herzog and U. Osterwalder, *Pure & Appl. Chem.*, 2015, **87**, 937-951.
31. SCCP, Opinion on biological effects of ultraviolet radiation relevant to health with particular reference to sunbeds for cosmetic purposes, SCCP/0949/05, 2006.
32. A. R. Webb, H. Slaper, P. Koepke and A. W. Schmalwieser, *Photochem. Photobiol.*, 2011, **87**, 483–486.
33. P. E. Hockberger, *Photochem. Photobiol.*, 2002, **76**, 561-579.
34. B. L. Diffey, *Methods*, 2002, **28**, 4-13.
35. B. L. Diffey and J. Robson, *J. Soc. Cosmet. Chem.*, 1989, **40**, 127-133.
36. J. J. O'Neill, *J. Pharm. Sci.*, 1984, **73**, 888-891.
37. B. Herzog, M. Wehrle and K. Quass, *Photochem. Photobiol.*, 2009, **85**, 869-878.
38. D. M. Beyer, A. Faurschou, P. A. Philipsen, M. Hoedersdal and H. C. Wulf, *Photodermatol. Photoimmunol & Photomed.*, 2010, **26**, 22-27.

39. D. C. Harris, *Quantitative chemical analysis*, W.H. Freeman and Company, New York, 7th edition, 2007.
40. G. J. Mturi and B. S. Martincigh, *J. Photochem. Photobiol.*, 2008, **200**, 410–420.
41. W. Schwack and T. Rudolph, *J. Photochem. Photobiol.*, 1995, **28**, 229–234.
42. E. M. M. Tan, M. Hilbers and W. J. Buma, *J. Phys. Chem. Lett.*, 2014, **5**, 2464–2468.
43. L. A. MacManus-Spencer, M. L. Tse, J. L. Klein and A. E. Kracunas, *Environ. Sci. Technol.*, 2011, **45**, 3931–3937.
44. S. Pattanaargson, T. Munhapol, P. Hirunsupachot and P. Luangthongaram, *J. Photochem. Photobiol. A*, 2004, **161**, 269–274.
45. H. J. Kuhn, S. E. Braslavsky and R. Schmidt, *Pure Appl. Chem.*, 2004, **76**, 2105-2146.
46. H. J. Adick, R. Schmidt and H. D. Brauer, *J. Photochem. Photobiol. A*, 1988, **45**, 89-96.
47. F. Leal-Calderon, *OCL*, 2012, **19**, 111–119.
48. B. P. Binks, *Cur. Opin. Colloid Interface Sci.*, 2002, **7**, 21–41.
49. B. P. Binks, P. D. I. Fletcher, M. A. Thompson and R. P. Elliott, *Colloids Surf. A*, 2011, **390**, 67-73.
50. B. P. Binks and J. H. Clint, *Langmuir*, 2002, **18**, 1270–1273.
51. S. U. Pickering, *J. Chem. Soc.*, 1907, **91**, 2001-2021.
52. W. Ramsden, *Proc. R. Soc. Lond.*, 1903, **72**, 156-164.
53. J. O. Zoppe, R. A. Venditti and O. J. Rojas, *J. Colloid Interface Sci.*, 2012, **369**, 202–209.
54. T. S. Horozov and B. P. Binks, *Angew. Chem.*, 2006, **118**, 787–790.
55. B. P. Binks and S. O. Lumsdon, *Langmuir*, 2000, **16**, 3748–3756.
56. V. N. Paunov, O. J. Cayre, P. F. Noble, S. D. Stoyanov, K. P. Velikov and M. Golding, *J. Colloid Interface Sci.*, 2007, **312**, 381–389.
57. B. P. Binks, P. D. I. Fletcher, B. L. Holt, J. Parker, P. Beaussoubre and K. Wong, *Phys. Chem. Chem. Phys.*, 2010, **12**, 11967–11974.
58. B. P. Binks and S. O. Lumsdon, *Phys. Chem. Chem. Phys.*, 1999, **1**, 3007–3016.
59. B. P. Binks, P. D. I. Fletcher, M. A. Thompson and R. P. Elliott, *Langmuir*, 2013, **29**, 5723-5733.

60. K. Sefiane, *Adv. Colloid Interface Sci.*, 2014, **206**, 372-381.
61. H. Y. Erbil, *Adv. Colloid Interface Sci.*, 2012, **170**, 67-86.
62. D. Brutin, *Droplet wetting and evaporation*, Elsevier, New York, 1st edition, 2015.
63. D. Bonn, J. Eggers, J. Indekeu, J. Meunier and E. Rolley, *Rev. Mod. Phys.*, 2009, **81**, 739-804.
64. A. F. Routh, *Rep. Prog. Phys.*, 2013, **76**, 1-30.
65. R. D. Deegan, O. Bakajin, T. F. Dupont, G. Huber, S. R. Nagel and T. A. Witten, *Nature*, 1997, **389**, 827-829.

CHAPTER 2 EXPERIMENTAL

2.1 Materials

2.1.1 Solvents

Squalane (Sigma-Aldrich, 99% purity) was purified by column chromatography over acidic aluminium oxide (Merck). The process was repeated several times in order to remove polar impurities and the purity of the squalane was determined with the use of UV/vis measurements. Propane-1,2-diol (also called propylene glycol (PG)) (Sigma-Aldrich, > 99%) and *n*-decane (TCI Europe, > 99%) were used as received.

Water was purified by passing through an Elgastat Prima Reverse Osmosis Unit followed by a Millipore Milli-Q reagent water system consisting of one carbon filter and two ion-exchange filters. Its resistivity at 25°C was ~ 16 MΩ cm^{-1}, which is in good agreement with literature value.[1]

2.1.2 UV absorber molecules

Two types of 4-*tert*-butyl-4'-methoxy dibenzoyl methane (tradename avobenzone AVB) were used as received: i) a pharmaceutical secondary standard (Sigma-Aldrich, traceable to USP) and ii) an analytical standard (Sigma-Aldrich, > 99%). GC – MS measurements, shown in Table 2.1, confirmed that the pharmaceutical secondary standard of AVB did not contain any impurities compared to its analytical standard. As such, the denoted AVB corresponds to the pharmaceutical secondary standard, which was the preferred material of choice.

The GC - MS instrument consisted of an Agilent 6890 Series GC, an Agilent 7683 injector and an Agilent 5973N MS detector. Solutions of AVB were dissolved in ethyl acetate with a 1 μl injection with a 50:1 split. The injector temperature was set at 260°C. The GC analyses were performed on an Agilent HP-1 column with 12 m x 0.2 mm (0.33 μm film thickness) dimensions. Helium gas served as the mobile phase with a flow rate of 1 ml min^{-1}. The following temperature program was set: 40°C initial for 2 min, an increase of 20°C min^{-1} to 300°C, 300°C held for 10 min with a 25 min total run time. The MS detector operated in electron ionization (EI) method. It scanned from m/z 30 to 600 with 2.6 scans s^{-1} with a solvent delay of 1.7 min.

Table 2.1. GC retention time R_T and fragmentation pattern of MS spectra of pharmaceutical secondary standard (PSS) and analytical standard (AS) of AVB in ethyl acetate prior to UV irradiation.

Substance	**R_T/min**	**MS (EI)**
PSS	12.57	310 (M^+ +1) (100%), 295 (43), 267 (3), 253 (13), 177 (12), 161 (33), 147 (6), 135 (74), 121 (9), 108 (25), 91 (7), 77 (12), 69 (13), 55 (2), 41 (3)
AS	12.58	310 (M^+ +1) (100%), 295 (44), 267 (3), 253 (12), 177 (11), 161 (37), 147 (5), 135 (82), 121 (11), 108 (27), 91 (10), 77 (15), 69 (15), 57 (4), 41 (3)

Iso-pentyl *p*-methoxycinnamate (MC, Neo Heliopan E1000), bis-ethylhexyloxyphenol methoxyphenyl triazine (BEMT, Tinosorb S) and diethylamino hydroxybenzoyl hexyl benzoate (DHHB, Uvinul A Plus Granular) were kindly donated by the industrial sponsor (GSK) and used as received.

The structures of AVB and MC were also determined by ^1H NMR spectroscopy using a JEOL JNM-ECP FT NMR spectrometer (400 MHz). For AVB, it was confirmed that the dominant form present is the enol form (approx. 91% present). For the case of MC, it is *trans*-isomer present in the starting material. All samples were dissolved in $CDCl_3$. An internal standard of tetramethylsilane (TMS) was used. Abbreviations used to describe the splitting patterns: s - singlet, d - doublet, t – triplet. All results are presented in Appendix A.

2.1.3 Metal oxide nanoparticles

Titanium dioxide (Sigma-Aldrich, Aeroxide P25, a mixture of rutile 20 wt.% and anatase 80 wt.%, 21 nm particle size), cerium oxide (Sigma-Aldrich, nanopowder, < 25 nm particle size), zinc oxide (Sigma-Aldrich) and tungsten oxide (US Research Nanomaterials Inc., 60 nm particle size) were also used as received.

Fumed silica particles grafted to different extents by chemical reaction of the surface silanol groups with dichlorodimethylsilane (DCDMS), were provided by Wacker-Chemie (Germany). Two silica particle samples with different hydrophobicity (containing 23% and 35% unmodified SiOH present) were used as received. A third type of silica particles, unmodified silica with 100% surface SiOH groups was also used as received without additional purification.

The preparation of the modified silica particles is a two-step process. Firstly, the hydrophilic silica particles with a surface area of 200 m^2 g^{-1} were produced by the hydrolysis of silicon tetrachloride in an oxygen-hydrogen flame under high temperature conditions, leading to the formation of spherical primary particles of 10 – 30 nm in diameter. These particles may collide and fuse at lower temperatures, resulting in stable aggregates with dimensions in the range of 100 – 500 nm. Secondly, the silica particles were hydrophobised by their reaction with DCDMS in the presence of water followed by drying at 300°C for 1 h. This resulted in the formation of dimethylsiloxy groups on the particle surface and their characterisation can be achieved by acid-base titration with sodium hydroxide. The relative content of the silanol groups is determined as the ratio of the modified silica over the unmodified silica (100% SiOH).[2]

2.1.4 Vitro Skin

Vitro Skin (IMS Inc.) is a rough, homogeneous, semi-transparent synthetic (non-biological) membrane that exhibits similar surface properties to human skin. It is designed to mimic the topography, pH, elasticity, surface tension and ionic strength of the human skin. Its surface roughness was measured using Bruker DektakXT stylus profiler with a 12.5 mm radius stylus and it was found to be equal to 12 μm. Vitro Skin is used as an *in vitro* testing medium for skin care applications[3] and it was used as received.

2.1.5 Other materials

As part of this work, materials other than those already defined have been used. These chemicals along with supplier’s name and their purity are given in Table 2.2. All these chemicals were used as received.

Table 2.2. Supplier and purity of chemicals used as received as part of this work.

Chemical	**Supplier**	**Purity/%**
Keratin from wool	TCI Europe	
Cholesterol	Sigma – Aldrich	> 99
Lignoceric acid	TCI Europe	> 96
N-acylphytosphingosine C18:1 Ceramide III	Evonik	
Poly-diallyldimethylammonium chloride (Poly-DADMAC) Average relative molar mass 200 – 350 kDa	Sigma – Aldrich	20% vol. (aq), > 99.5
Chloroform	VWR Chemicals	99.1
9, 10 – dimethylanthracene (DMA)	Sigma - Aldrich	> 99
1,1,2 – trichloro – 1,2,2 – trifluoro ethane (Freon 113)	Sigma – Aldrich	> 99.7

2.2 Methods

2.2.1 UV/vis absorption spectroscopy

UV/vis spectroscopy records the absorbance derived from the measured specular transmittance. The specular absorbance of the organic UV absorbers in both solutions and emulsions was measured, for a range of concentrations and path lengths producing UV spectra from 200 to 400 nm after each irradiation period. The experiments were carried out on two UV/visible spectrophotometers: i) a double beam PerkinElmer Lambda 25 equipped with UV WinLab v.6.0.4 software and ii) a double beam UNICAM UV3 UV/visible spectrophotometer equipped with Vision 32 v.1.22 software for spectral acquisition and elaboration. The spectra were obtained using rectangular quartz plates and cuvettes with path lengths of 0.001, 0.01, 0.1 and 1 cm, all purchased from Hellma Analytics. Both instruments monitor specular optical transmittance over a narrow angular range with respect to the direction of the incident light, as shown in Figure 2.1. The angular range of the instrument detector is estimated to be in the range of ± < 5°.

2.2.2 Diffuse transmittance spectroscopy

In order to determine the transmittance over a scattering angular range ± 90°, we introduce diffuse transmittance. The diffuse absorbance is derived as the negative logarithm of the diffuse transmittance. For samples that only absorb and do not scatter light significantly, the diffuse absorbance is equal to the specular absorbance.

Diffuse transmittance measurements were recorded with the use of a modified Scientific Fluoromax 4 instrument (Horiba Jobin Yvon) equipped with a 2-inch in diameter integrating sphere accessory (Thorlabs). The integrated sphere is located directly underneath the sample and connected to the silicon detector of the instrument as shown in Figure 2.1. FluorEssence software was used for spectral acquisition and elaboration.

Two 1-inch diameter fused silica plano-convex lenses with focal lengths of 50.0 mm and 100.0 mm were used in order to focus the light into the integrated sphere. A 1-inch diameter UV-enhanced aluminium mirror is also used to reflect the light into the integrated sphere. The latter is made from PTFE based high reflective bulk material to scatter the light and to allow the light intensity to be equal at all points inside the sphere. All samples (either solutions of AVB in SQ or PG-in-SQ emulsions) with a fixed path length of 0.01 cm were placed on top of the integrated sphere. Diffuse transmittance data and thus the corresponding absorbance were collected for wavelengths between 200 – 400 nm from the sample detector with an angular range of ± 60° with respect to the incident light direction. For all our measurements, a dark correction was subtracted from the background signal.

Figure 2.1. Detection of specular transmittance (left) and of diffuse transmittance (right) of a sample exposed to incident light. Redrawn from ref. 4.

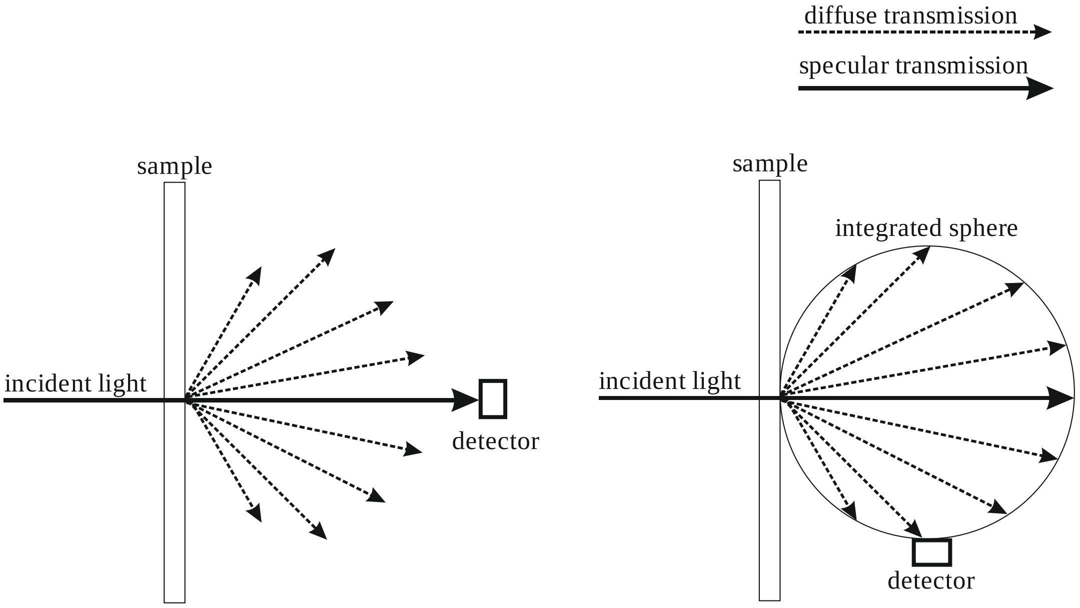

2.2.3 Experimental setup of evaporation

An initial volume of 11.25 μl of the sample (solution, dispersion or emulsion) was deposited on top of a quartz plate with dimensions of 4.5 x 1.25 cm with the aid of an automated Eppendorf pipette. The sample was spread as evenly as possible to produce a uniform film of thickness approximately equal to 20 μm, which corresponds to the standard application of 2.0 mg cm^{-2} for the determination of the *in vivo* SPF.[5]

The substrate plus film were placed on a Linkam Peltier heating stage as shown in Figure 2.2 and allowed to evaporate in the open lab air. The temperature was set at 32°C, which corresponds to skin’s surface temperature. The evaporation process was monitored at frequent timed intervals with the use of a Denver instruments mass balance (accurate to ± 0.2 mg). During the evaporation, digital photos were taken and processed with the use of ImageJ software in order to determine the film perimeter and to define the total film area. The presence and the appearance of any precipitated crystals of the UV filters were recorded by optical microscopy.

For all samples, the specular absorbance was also measured at timed intervals with the aid of the UNICAM UV3 UV/vis double beam spectrophotometer, which was oriented vertically to enable the samples (substrate plus film) to be placed horizontally in fixed measurement positions. The software Vision 32 v.1.22 was used for spectral acquisition and elaboration. The position and the area of the illuminated region on the sample (substrate plus film) were measured and found to be equal to 0.32 cm^2 (dimensions 1.6 cm x 0.2 cm). This corresponds to the area where the beam of the UV/vis spectrophotometer passes through for sample detection.

All samples (solutions, dispersions or emulsions) were measured *versus* air as a reference. The absorbance spectra were determined as follows. Firstly, the absorbance of the reference sample was recorded. The latter consisted of the substrate plus the film without containing any UV absorber. Secondly, the absorbance of the sample was measured. This included the substrate plus the film containing a concentration of a UV absorber. The actual absorbance value due to the UV absorber resulted from the subtraction of the absorbance data of the sample minus the absorbance data of the reference.

For a PG film deposited on a smooth quartz plate, the absorbance values of the substrate reference spectrum were small (around 0.05) relative to the absorbance values of the sunscreen film (around 0 – 2) and hence subtraction of the substrate reference spectrum was a relatively small correction. For the Vitro Skin and the keratin – lipid dispersion film, the substrate absorbance values were significantly higher and of similar magnitude to the film absorbance spectra. In these cases, subtraction of the substrate reference spectrum was a large correction leading to a reduced precision of the final spectrum of the film alone. The absorbance per wavelength of all organic UV absorbers were deduced from this procedure.

Figure 2.2. Experimental setup of evaporation. Left: quartz plates with the deposited film were placed on a heating stage at a temperature of 32ºC. Right: Schematic representation of the digital photographs, which were taken at timed intervals.

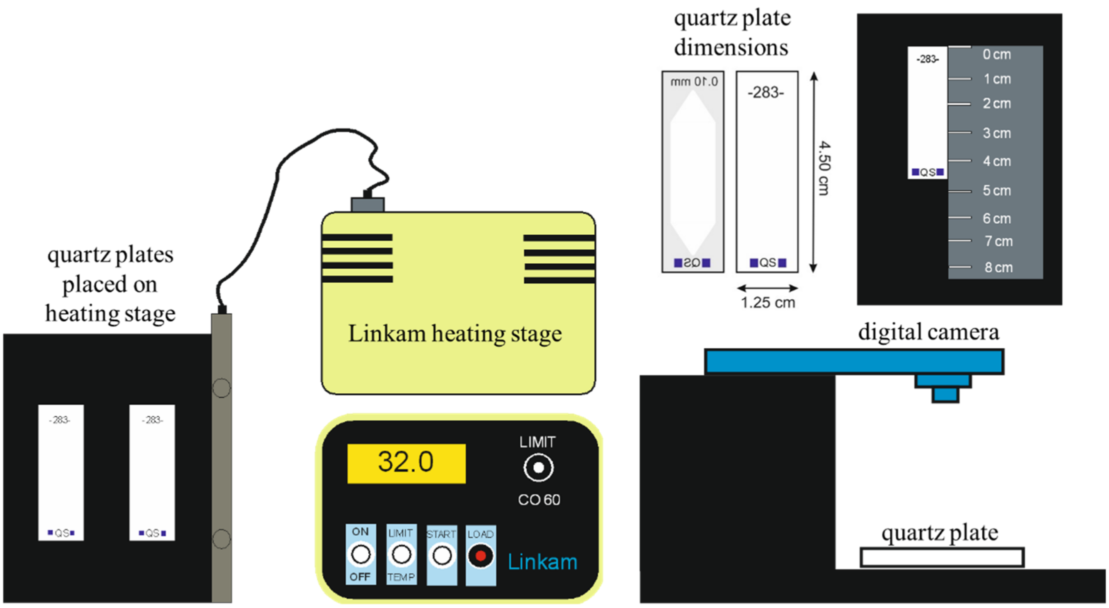

During the evaporation process, the film behaviour was investigated with the aid of optical micrographs by using an Olympus BX51 microscope equipped with an Olympus DP70 camera. Seven consecutive optical micrographs were taken in order to determine the crystal formation from which the beam of the UV/vis spectrometer passed through.

2.2.4 Preparation of Vitro Skin film

Samples of Vitro Skin sheet were cut into rectangular pieces of 4.50 x 1.25 cm to exactly fit on the dimensions of the quartz plate as shown in Figure 2.3. This was made not only for convenience (*i.e.* handling) but also to ensure that the Vitro Skin will appropriately fit in the slot of the UV/vis spectrophotometer for the relevant absorbance measurements. As such, the top and bottom edges were carefully selotaped leaving an area of 4.2 cm^2 available for spreading the thin solution film on top of the Vitro Skin surface.

Figure 2.3. Left: digital photo of a Vitro Skin sample cut in dimensions of a quartz plate. Right: optical micrograph of the surface of Vitro Skin indicating its morphology. Black spots appear to be the pores of Vitro Skin.

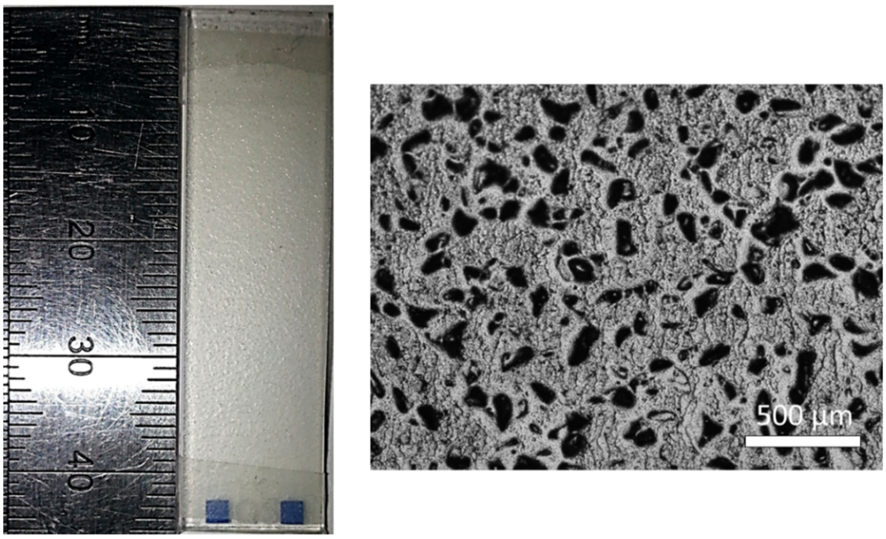

2.2.5 Preparation of keratin – lipid dispersion film

Keratin – lipid films containing keratin 80 wt.%, cholesterol 6.7 wt.%, lignoceric acid 6.7 wt/% and ceramide III 6.7 wt.% in the final dry film were made as follows in order to mimic the surface of the stratum corneum.[6-8] 0.16 g total mass of the three lipids (cholesterol, lignoceric acid and ceramide III) were initially added to 5 ml of chloroform at 50°C and the solution was left under stirring until all lipids were fully dissolved. 0.64 g total mass of keratin powder with particle diameter size in the range of 2 – 5 μm was added and the dispersion was left to stir for a further 30 min at 50°C to give an opaque dispersion of keratin particles in a solution of the mixed lipids.

Volumes of 15 μl of the above keratin – lipid dispersion were deposited on top of the quartz plate. Evaporation of chloroform occurred within approximately 1 min, leaving an opaque film residue of the dispersion with a mass equal to 0.003 g as illustrated in Figure 2.4. The application of the keratin – lipid dispersion film on top of a quartz plate was achieved with the aid of an Eppendorf pipette tip. The deposited keratin – lipid mass plus the quartz plate were the substrate upon which the AVB in PG solution was placed. The initial area of the keratin – lipid dispersion film measured with ImageJ software was found to be 2.06 cm^2. From the film mass and area, the average thickness of the keratin – lipid dispersion film was found to be approximately equal to 15 μm.

Figure 2.4. Digital photo (left) of a deposited 15 μl of the keratin – lipid film on top of a smooth quartz plate. SEM image (right) of the keratin as received and used for the film preparation.

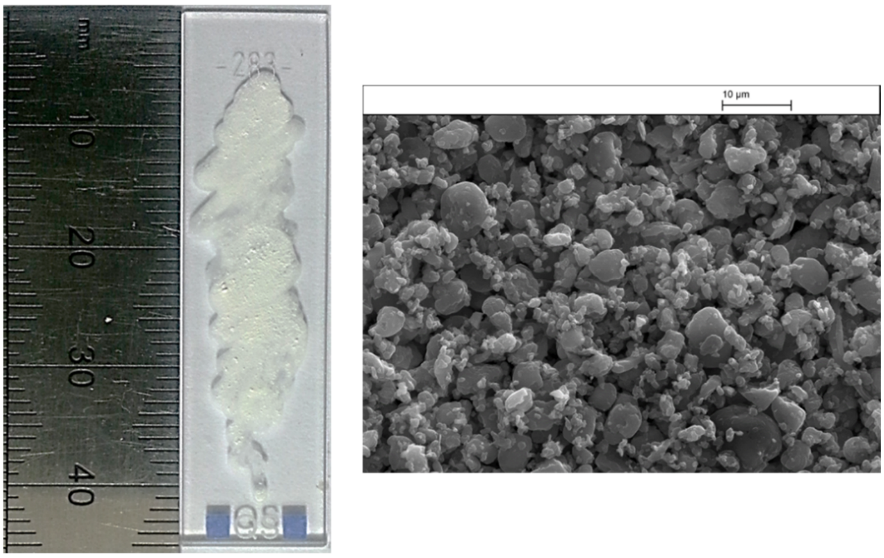

2.2.6 Preparation of solutions and films containing poly-DADMAC

The addition of a polymer into films containing solutions of AVB in PG was also pursued. The reason was to investigate how the film formation is affected by the presence of a polymer additive during evaporation. The choice of poly-DADMAC was made, based on the fact that it does not absorb in the wavelength region of interest.

Solutions containing poly-DADMAC were prepared by addition of 5.0 wt.% and 1.0 wt.% of a poly-DADMAC aqueous stock solution to a solution containing both PG and the dissolved UV absorber followed by stirring at 800 rpm for 24 h, until a final transparent solution was obtained. Again, the films containing poly-DADMAC were deposited on top of a quartz plate with the use of an Eppendorf pipette and they were left to evaporate in the open lab air. It should be noted that PG films containing poly-DADMAC also contained minor amounts of water originating from the polymer stock solution.

2.2.7 Portable UV lamp

The irradiance spectrum of a portable UV lamp B7960 (Agar Scientific) equipped with two cylindrical 6 Watt Hg tubes was measured with an Ocean Optics HR 2000 spectrometer with integration time set at 100 ms. Light was introduced straight into the spectrometer without the use of a fibre optic. Dark spectra were subtracted to remove the influence of the laboratory light. Spectroscopic data were recorded in the range 200 – 850 nm. The UV lamp was emitting at a main wavelength of 368 as shown in Figure 2.5 below.

Figure 2.5. Emission spectrum of portable UV lamp B7960.

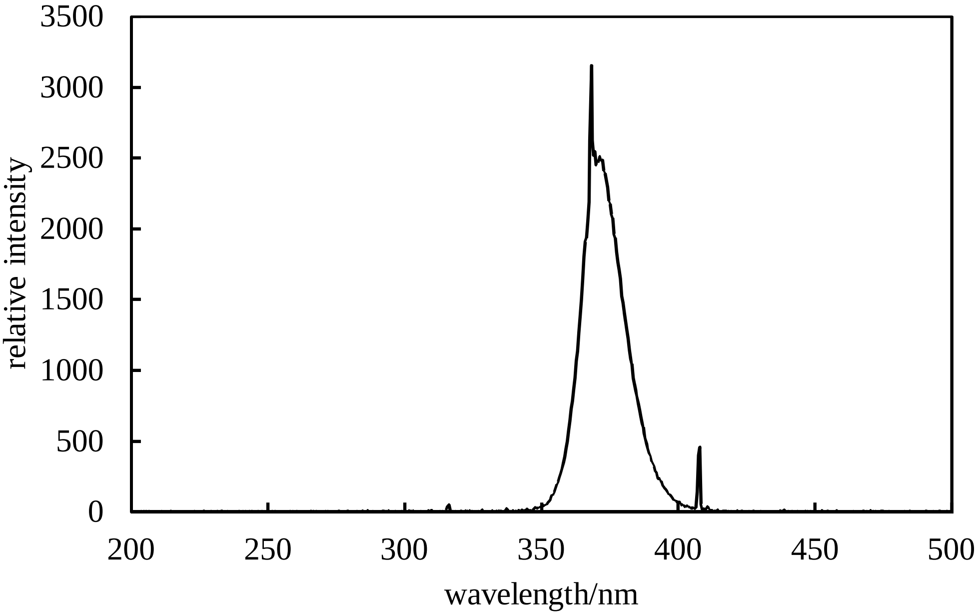

2.2.8 Solar simulator

The irradiance spectrum of a 1000 W Oriel Solar Simulator (Model 81291) with 4 x 4 inch (102 x 102 mm) collimated beam, shown in Figure 2.6, was measured with the aid of an Ocean Optics HR 2000 spectrometer with integration time 5 ms. Light was introduced into the spectrometer without the use of a fibre optic. Dark spectra were subtracted to remove the influence of the laboratory light. The spectrometer was set at a fixed distance of 55 cm from the solar simulator. The light output intensity was also checked and it was found to be independent of the sample location distance from the light exit lens. Three types of filters were compared, named as i) the Atmospheric Attenuation Filter (No 81017), ii) the UG 11 to block the visible light and iii) the UVB/C filter (No 81050). In addition, the spectrometer was used to measure the intensity without the use of any additional filters (Base unit). Throughout our investigation, the selected output of the Oriel Solar Simulator was set at 200W/10A and the Atmospheric Attenuation Filter (No 81017) was the only filter used.

Figure 2.6. Upper plot: Emission spectra of Oriel Solar Simulator with and without any additional filters for the wavelength range between 190 – 1100 nm. Lower plot: Comparison of all the emission spectra for the UV region of the electromagnetic spectrum between 190 – 400 nm alone.

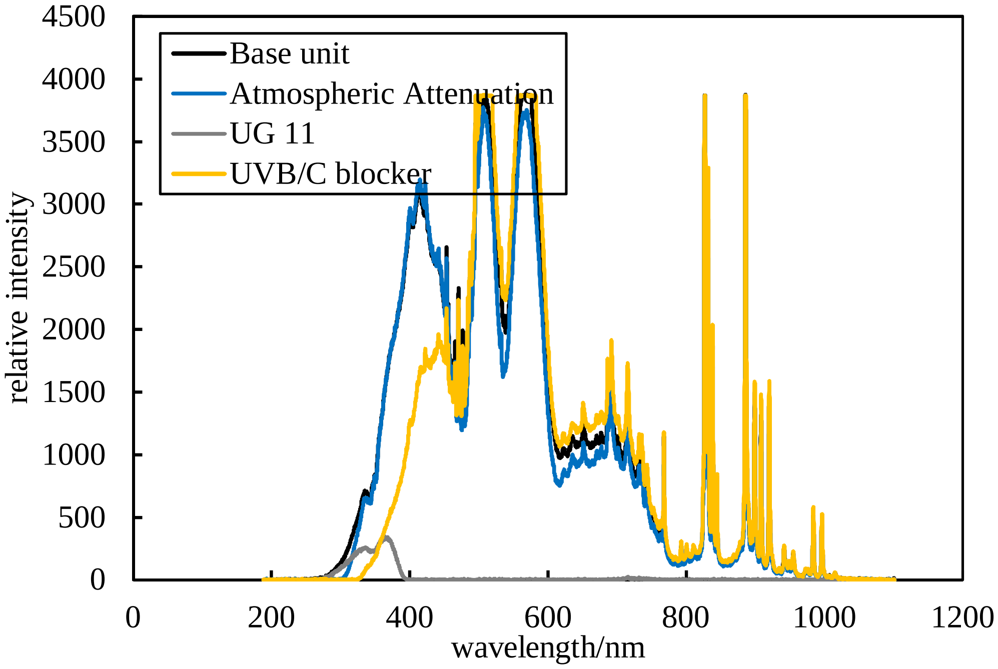

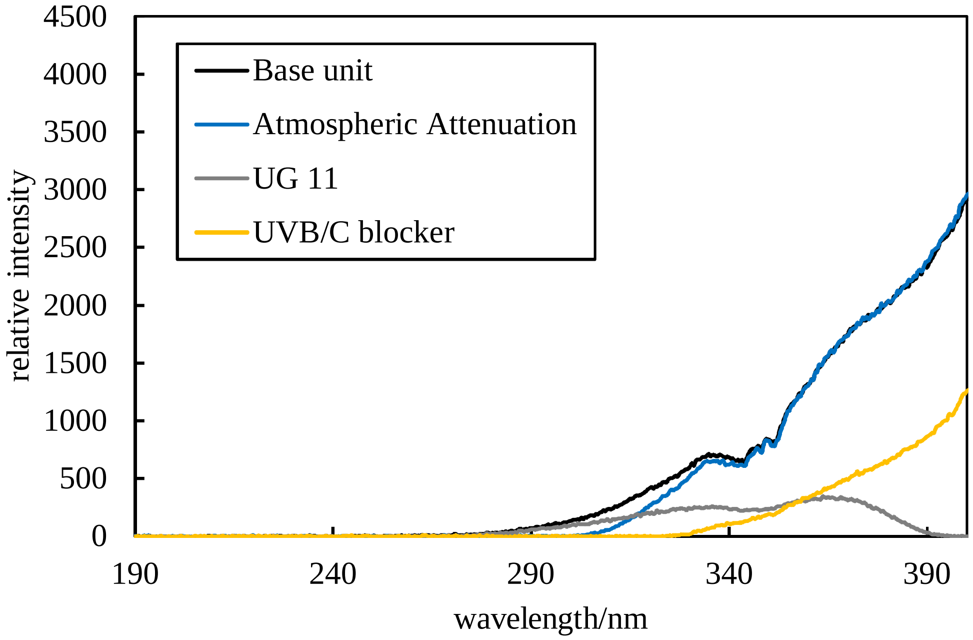

2.2.9 Actinometry measurements

The determination of the quantum yield of a known actinometer (DMA) was made as follows. A fresh solution of DMA in Freon 113 equal to 0.47 mM was prepared at room temperature. Samples of DMA in Freon 113 (volume = 3.5 ml, path length 1 cm) were UV irradiated at timed intervals and the absorption spectra (200 – 400 nm) were recorded accordingly for both sources of irradiation: i) portable UV lamp at three fixed distances (3.6, 7.2 and 14.4 cm) and ii) solar simulator at a fixed distance of 55 cm. All measurements were made at 32^{o}C.

2.2.10 Experimental setup of photochemical measurements

The behaviour of the organic molecules under UV light was investigated for samples (solutions, dispersions or emulsions) consisting of different concentrations and path lengths. For this purpose, a UV lamp B7960 (Agar Scientific) having two cylindrical 6 Watt Hg tubes emitting at a wavelength around 360 nm was used to provide the necessary source. The UV lamp was set initially at a fixed distance from the samples, which was equal to 7.2 cm. Only air interfered between the UV lamp and the investigated samples. In order to vary the light intensity, the distance of the UV lamp from the samples was either halved (3.6 cm) or doubled (14.4 cm). For all our experiments, two fixed positions underneath the UV lamp were used for sample irradiation.

A rectangular opaque box was placed in a water bath to ensure constant temperature conditions. The UV lamp B7960 (Agar Scientific) was set on top of the box as shown in Figure 2.7. The temperature inside the box was set at 32^{o}C and it was monitored with a Brannan England thermostat probe. Deviations in the temperature inside the box were recorded upon removal of the samples during measurement. These deviations, however, were only temporary and did not exceed 0.5^{o}C. Each sample was placed at one of the two specific positions within the box and it was irradiated perpendicular to the UV light for better exposure. The side of the cuvette that was UV irradiated was always the one that faced the beam of the UV/vis spectrophotometer. In order to ensure good sealing, the stoppers of the quartz cuvettes were covered with Teflon. In the case of the quartz plates (volume = 26 μl), the application of a uniform thin film was achieved with the introduction of an excess volume of 50 μl provided by an Eppendorf pipette.

Figure 2.7. Top view (left) and cross-sectional view (right) sketch of the experimental setup. Arrows indicate the orientation of UV light which is perpendicular to the cuvettes. Portable UV lamp set at 7.2 cm distance from samples. Fixed positions of cuvettes within the box. Only air is interfering between the UV lamp and the cuvettes.

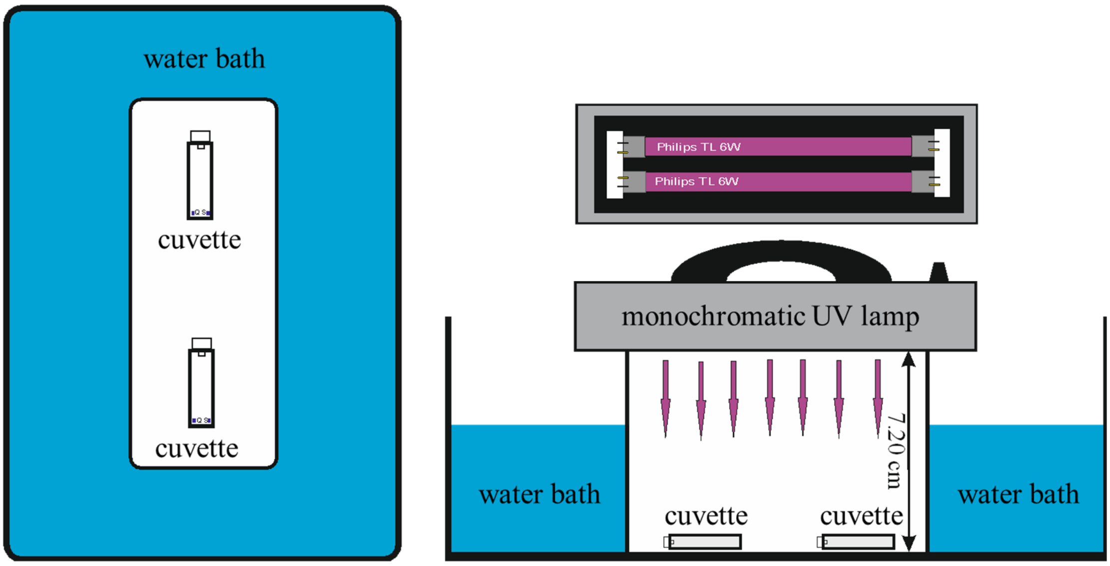

Similarly, the photochemical behaviour of all organic compounds under UV light was also investigated for different concentrations and path lengths under the use of an alternative source of UV irradiation. As such, a 1000 W Oriel Solar Simulator (Model 81291) with 4 x 4 inch (102 x 102 mm) collimated beam was used to provide the necessary source as shown in Figure 2.8. Throughout our investigation, the selected output of the Oriel Solar Simulator was set at 200W/10A and the Atmospheric Attenuation Filter (No 81017) was the only filter used.

Samples were placed underneath and parallel to the Solar Simulator's uniform beam at a fixed distance of 55 cm. Only air interfered between the beam source and the samples of interest. The temperature was monitored at 32°C with the aid of a Brannan England thermostat probe. As in the case of the portable UV lamp, slight deviations in the temperature inside the water bath were recorded upon removal of the samples during measurements. Since the beam of the UV source was uniform throughout, each sample was placed randomly. However, the side of the cuvette that was UV irradiated was again always the one that faced the beam of the UV/vis spectrophotometer.

Figure 2.8. Experimental setup of 1000 W Oriel Solar Simulator (Model 81291) with 4 x 4 inch (102 x 102 mm) collimated beam. Cuvettes were placed at a fixed distance of 55 cm from the irradiation source. Arrows indicate the orientation of the UV light which is perpendicular to cuvettes. Only air interfered between the cuvettes and the source of irradiation.

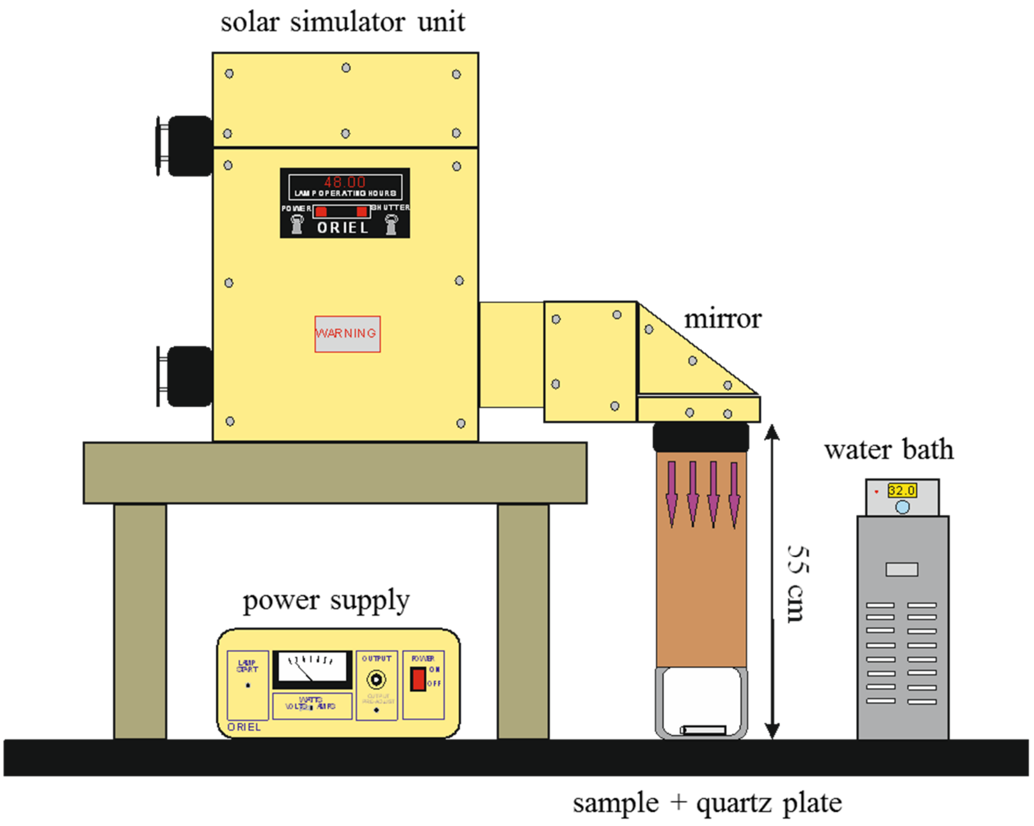

For the irradiated samples, the specular absorbance was recorded at timed intervals with the aid of a double beam PerkinElmer Lambda 25. The software UV WinLab v.6.0.4 was used for spectral acquisition and elaboration.

The absorbance spectra were determined as follows. Firstly, absorbance spectra of the neat solvent-filled cuvette *versus* air were separately measured as a reference sample. Secondly, absorbance spectra of all samples (solutions, dispersions or emulsions) were measured *versus* air. The absorbance spectra of the UV filters alone were obtained by subtraction of the reference spectrum from the sample spectrum.

2.2.11 Preparation of particle-stabilised emulsions

Silica particle-stabilised emulsions containing SQ and PG were prepared as follows. Mixtures of various volume fractions of SQ (oil phase) and of PG (polar phase) ranging between 0.2 of up to 0.8 with respect to the polar phase, were treated with various wt.% of DCDMS modified silica particles. The latter were added with respect to the entire mass of the two immiscible liquids. The masses of the two liquids and the silica particles were equal to an approximate volume of 10 cm^3 of emulsion. The required concentration of the UV absorber was dissolved in either one or both phases prior to emulsification. The two immiscible liquids with and without UV absorbers plus the modified silica particles were emulsified in glass vessels of 28 mm in diameter by 72 mm in height at room temperature conditions (21^{o}C).

Each mixture was emulsified with the use of an IKA Ultra – Turax T25 homogeniser device equipped with a metal head of diameter of 18 mm which was immersed in the mixture prior to homogenization. Intense shear forces at 13,000 rpm for 2 minutes led to the breakdown of both bulk phases and to the formation of emulsion droplets within a continuous phase in the presence of the modified silica particles, which act as the emulsifying agent.

2.2.12 Characterisation of particle-stabilised emulsions

2.2.12.1 Drop test

The continuous phase of an emulsion was determined by observing whether the drop of the prepared emulsion was dispersed or not when added to either the polar PG or the oil phase. As such, the emulsion continuous phase can be described as PG-continuous when the emulsion is dispersed within the polar PG phase as opposed to oil-continuous when it is dispersed in SQ. Drop tests were taken shortly after the emulsion preparation.

2.2.12.2 Optical microscopy

Emulsion droplets were visualized under optical microscopy with the use of an Olympus BX51 microscope equipped with an Olympus DP70 camera. The emulsion droplets were placed within a dimple cell microscope slide with a coverslip on top. 8-

bit grey scale images of 1360 pixels x 1024 pixels resolution with a 4 and 20 x long distance objectives, were taken and edited with ImageJ software providing images of a scale of 500 and 100 μm respectively. The mean droplet diameter of each emulsion was calculated from an average of 150 individual droplets. The size distribution was characterized in terms of the surface average diameter by application of equation 2.1 below.

$$D[3,2] = \frac{\sum_i N_i D_i^3}{\sum_i N_i D_i^2} \qquad (2.1)$$

where

- $D[3,2]$ is the area-volume mean diameter of droplets
- N_i is the total number of droplets with diameter D_i.

Optical microscopy pictures were taken immediately after the emulsion preparation.

2.2.12.3 Stability measurements

Emulsions were stored in dark at room temperature. The stability of the emulsions to creaming or coalescence was assessed by monitoring the change of the position of the clear polar liquid-emulsion or oil-emulsion interfaces, as a function of time as illustrated schematically in Figure 2.9.

Figure 2.9. Determination of PG and SQ resolved from an emulsion.

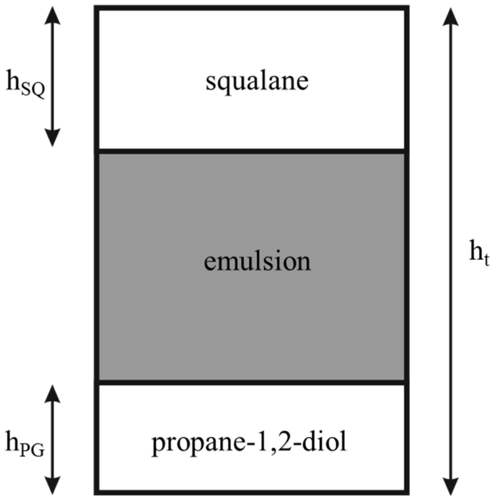

The relevant equations for the determination of the emulsion stability are shown below

$$f_{PG} = \frac{h_{PG}}{h_t \times \Phi_{PG}} \tag{2.2}$$

$$f_{SQ} = \frac{h_{SQ}}{h_t \times \Phi_{SQ}} \tag{2.3}$$

where h_{PG} and h_{SQ} correspond to the height of PG and SQ resolved respectively, Φ_{PG} and Φ_{SQ} correspond to the volume fraction of PG and SQ initially respectively and h_t is the total height of the emulsion plus PG and SQ resolved.

2.2.13 Preparation of nanoparticle dispersions

0.1 and 1.0 wt.% of dry particles (CeO_2, TiO_2, WO_3 and ZnO) with respect to the total mass were added in 5 ml of the solution containing the solvent and the dissolved UV absorber. The particles were dispersed by sonication using a Branson Digital Sonifier 450 (400W). The experiments were conducted by immersing the standard ultrasonic probe of length 150 mm and diameter of 5 mm in a 5 ml sample dispersion within glass vessels of dimensions of 28 mm in diameter by 72 mm in height. The providing power was set at an amplitude of 40% with 1 sec pause every 2 sec for a total run time of 5 min.

For the photostability measurements, the dispersions were placed in quartz plates of path length of 0.01 cm and UV irradiated for an investigating period of 6 h with measurements taken every 1 h. For the evaporation measurements, the dispersions were deposited on top of the quartz plates and were left to evaporate in the open lab air.

2.2.14 Transmission electron microscopy (TEM)

All particles were analysed by a JEOL 2010 High Resolution Transmission Electron Microscopy (TEM) operated at 200 kV. Figures 2.10 – 2.11 show the collected images with the aid of a Gatan 64 megapixel US4000 camera operated by Digital Micrograph software. The samples were dispersed in ethanol prior to their deposition on carbon-supported copper grids and they were left to evaporate in the open lab air under ambient temperature conditions. The determination of the particle size distribution resulted from the measurement of 200 individual particles with the use of ImageJ software. This corresponded to 50 individual measurements within a set of 4 micrographs per metal oxide.

Figure 2.10. TEM images and particle size distribution based on the measurement of 200 individual particles of the investigated CeO_2 and TiO_2 dispersions respectively.

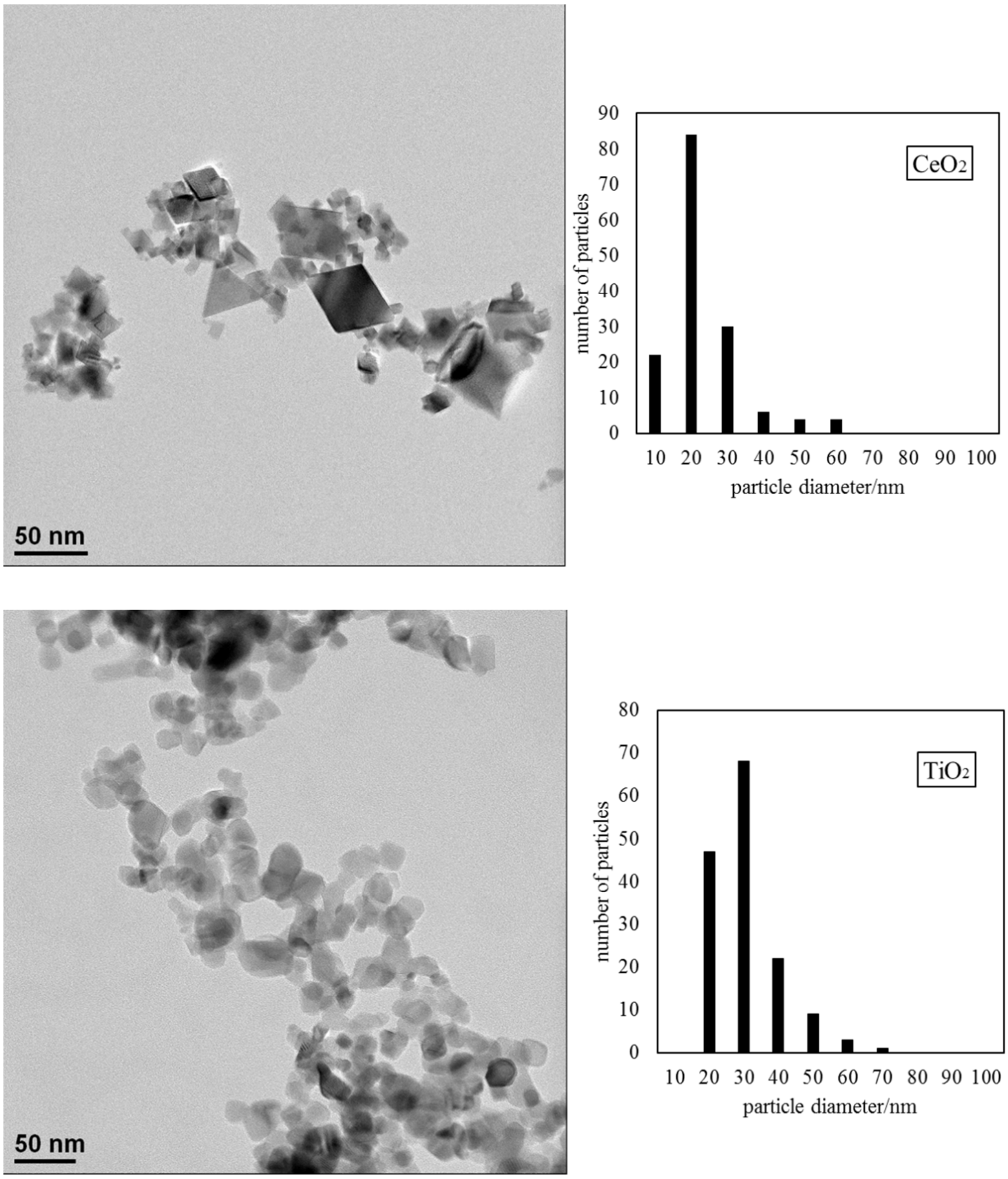

Figure 2.11. TEM images and particle size distribution based on the measurement of 200 individual particles of the investigated WO_3 and ZnO dispersions respectively.

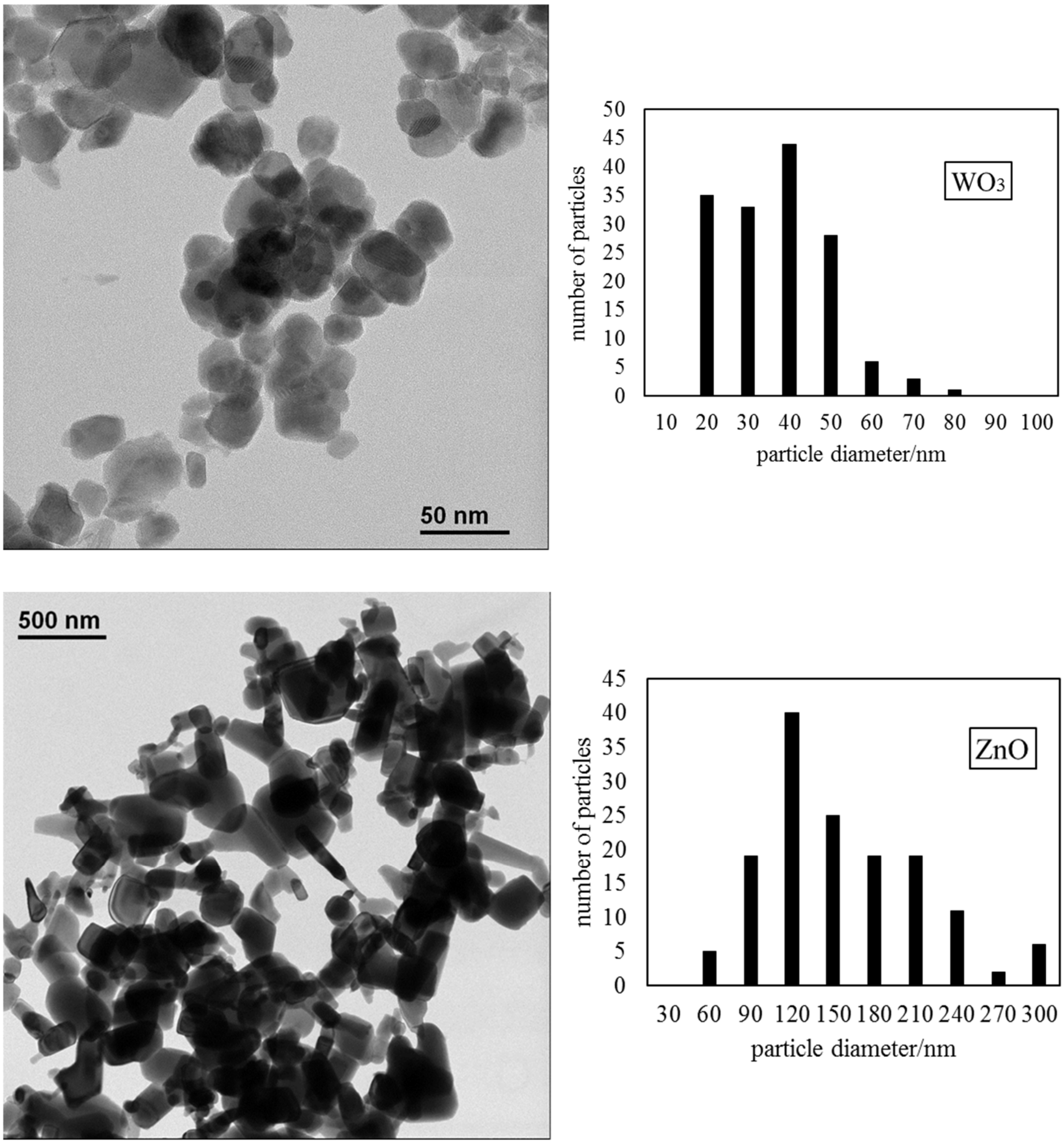

2.2.15 Solubility measurements

The determination of the equilibrium solubilities was made as follows. An excess of each of the UV absorbers was added to 10 ml of the selected solvents sealed in a glass vessel and they were left to equilibrate under stirring conditions within a thermostated water bath at the temperature of 32°C for seven days. The stirring was stopped and the excess solute phase was allowed to separate under gravity for 3 hours. Samples of the saturated supernatant phase of the solution were removed and accurately diluted with fixed known volumes of the solvent. The solubility limit of each of the UV absorber in all solvents, as summarised in Table 2.3, was determined from absorption measurements and corresponds to the average of four repeats. These values are estimated to be accurate within approximately ± 10%.

Table 2.3. Solubility data of all UV filters measured in both SQ and PG at 32^{o}C.

UV absorbers	Solvent	Solubility/mM	Solubility/wt.%
AVB	squalane	38	1.45
AVB	propane-1,2-diol	14	0.42
AVB	*n*-decane	54	2.29
BEMT	squalane	16	1.24
BEMT	propane-1,2-diol	< 3	< 0.19
DHHB	squalane	20	0.98
DHHB	propane-1,2-diol	28	1.07
MC	squalane	1300	39.80
MC	propane-1,2-diol	435	10.41

2.2.16 Contact angle measurements

Contact angles (static, advanced) of drops of *n*-decane, squalane, propane-1,2-diol and *iso*-pentyl *p*-methoxycinnamate were measured as follows. A 0.2 – 0.5 μl sessile drop of the solvent was injected on top of the quartz plate with the use of a BAS MD-0250 syringe. All measurements were made at 32^{o}C by using a Kruss DSA 10 instrument resulting in the capture of optical micrographs. The latter were analysed with the use of a drop shape analyser software v.1.90.0.11 and the contact angles were determined by forming a tangent between the liquid drop and the quartz substrate.

2.3 References

1. *CRC Handbook of Chemistry and Physics,* CRC Press/Taylor and Francis, Boca Raton, 89th edn., 2008.
2. H. Barthel, *Colloids Surf. A*, 1995, **101**, 217–226.
3. D. Garoli, M. G. Pelizzo, P. Nicolosi, A. Peserico, E. Tonin and M. Alaibac, *J. Dermatol. Sci.*, 2009, **56**, 89–98.
4. B. Herzog and F. Sengün, *Photochem. Photobiol. Sci.*, 2015, **14**, 2054-2063.
5. Y. Miura, T. Hirao and M. Hatao, *Photochem. Photobiol.*, 2012, **88**, 475–482.
6. P. W. Wertz, *Adv. Drug Deliv. Rev.*, 1996, **18**, 283–294.
7. P. W. Wertz and B. Van Den Bergh, *Chem. Phys. Lipids*, 1998, **91**, 85–96.
8. M. Boncheva, *Int. J. Cosmet. Sci.*, 2014, **36**, 505–515

CHAPTER 3 DETERMINATION OF INITIAL *IN VITRO* SPF FOR SOLUTIONS AND DISPERSIONS CONTAINING UV FILTERS

3.1 Introduction

We have already discussed in the Introduction section, the limitations of the derived *in vitro* SPF compared to the *in vivo* process. However, for solution films at their initial state the *in vitro* SPF is a valid approach that can be used to estimate their efficiency. In this chapter, we present the *in vitro* SPF at time t = 0 min (termed as initial *in vitro* SPF) of solution films containing a single UV absorber. In particular, we show that the initial *in vitro* SPF for any concentration of the UV absorber can be estimated from calculated absorbance measurements based on the Beer-Lambert Law. For this reason, we determine the molar extinction coefficient values for each UV absorber. The selected path length was 20 μm, which is approximately equal to the recommended standard application of 2.0 mg cm^{-2} described in the *in vivo* process. The UV absorbers of choice included i) UVA absorbers such as avobenzone (AVB) and diethylamino hydroxybenzoyl hexyl benzoate (DHHB), ii) UVB absorbers such as *iso*-pentyl *p*-methoxycinnamate (MC) and iii) a broad UV absorber named bis-ethylhexyloxyphenol methoxyphenyl triazine (BEMT).

Similarly, the determination of the initial *in vitro* SPF was also pursued for dispersions containing a selection of semiconductor oxide nanoparticles, such as TiO_2, ZnO, CeO_2 and WO_3. Results have indicated variations in their estimated initial *in vitro* SPF values, which can be attributed to differences in particle size and/or solvent type. It is important to note, however, that these dispersions, unlike the investigated solutions, do not fully obey the Beer-Lambert Law since the measured absorbance spectra are a combined result of absorption, scattering and reflection by the semiconductor oxide nanoparticles. These measurements provide, however, an approximation of the efficiency of the dispersions. Throughout our investigation, two types of solvents were used based on their polarity and these were squalane (SQ) and propane-1,2-diol (PG).

We also demonstrate that for solutions containing mixtures of the selected UV absorbers, the overall absorbance is additive. In our study, a solution consisting of a combination of similar concentrations of AVB and BEMT in SQ was investigated. From the determined molar extinction coefficient values of AVB and BEMT and for a fixed path length of 100 μm, the calculated absorbance data when compared with measured absorbance spectra show very good agreement.

3.2 Organic UV absorbers

Organic UV filters are classified as UVA or UVB absorbers depending on the ability of their chromophore group to absorb light in a narrow wavelength range of the electromagnetic spectrum. In general, the absorbance of a solution containing a solute concentration c, with a molar extinction coefficient ε applied to a uniform film with thickness d, can be calculated based on the Beer – Lambert Law using equation 1.4.

3.2.1 Determination of molar extinction coefficients of UV absorbers in solvents of different polarity

The upper plot of Figure 3.1 shows the absorbance measurements at time t = 0 min for a range of concentrations and path lengths of AVB in SQ solutions. All samples and reference absorbance spectra were measured separately *versus* air. For each sample, the actual spectra resulted from the subtraction of the sample spectrum minus the reference spectrum. The latter corresponded to a SQ filled cuvette. All measurements were made at a fixed temperature of 32°C, which corresponds to skin's outer temperature.

Overall, for solutions that obey the Beer-Lambert Law, the molar extinction coefficient can be derived for each wavelength based on equation 1.4. This is illustrated in the lower plot of Figure 3.1, where the molar extinction coefficient is shown for all sample solutions of AVB in SQ. The solid black line corresponds to their average value. As expected, the values of the molar extinction coefficients in the range 230 – 400 nm are in very good agreement.

Following the same experimental procedure, the average molar extinction coefficient values were derived for all UV absorbers for both solvent types (*i.e.* SQ and PG) and these are shown in Figure 3.2. Throughout our photochemical and evaporative investigation, the determination of the calculated absorbance spectra was made based on the use of average molar extinction coefficient values.

Figure 3.1. Upper plot: Absorbance spectra for different concentrations and path lengths of AVB in SQ solutions. Lower plot: Molar extinction coefficient values of AVB in SQ solutions. The solid black line corresponds to the average value of the extinction coefficient.

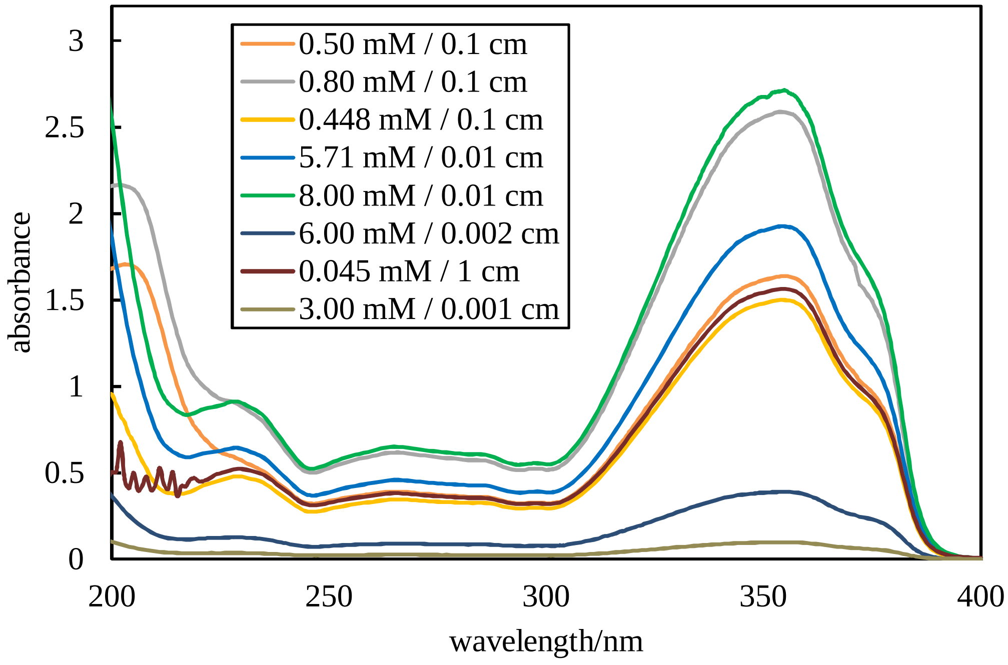

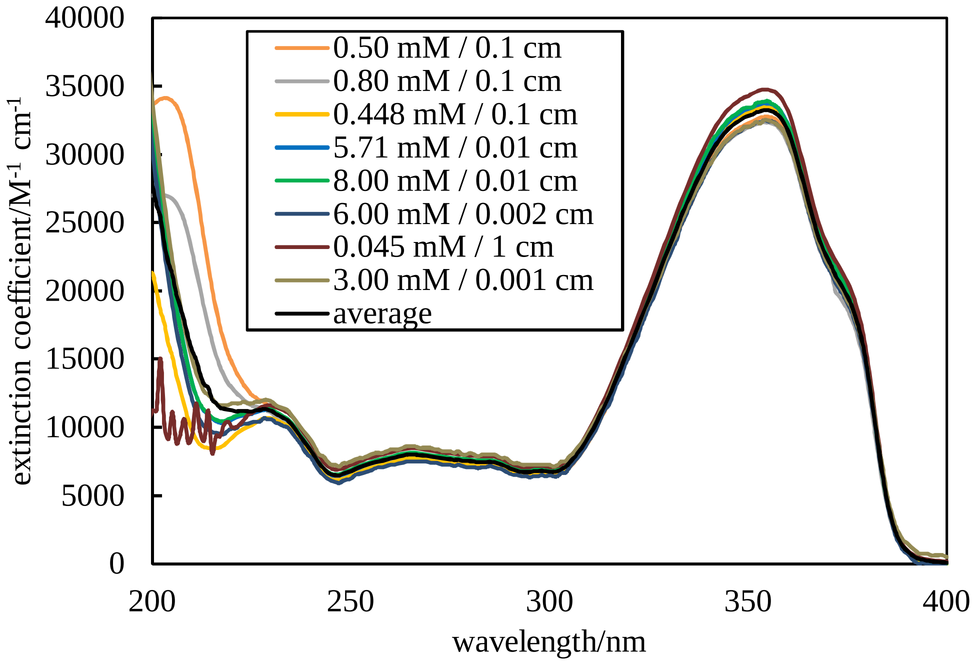

Figure 3.2. Upper plot: Average molar extinction coefficient values of AVB, BEMT, DHHB and MC in SQ. Lower plot: Average extinction coefficient values for AVB, DHHB and MC in PG. No data are presented for BEMT due to its significantly low solubility in PG.

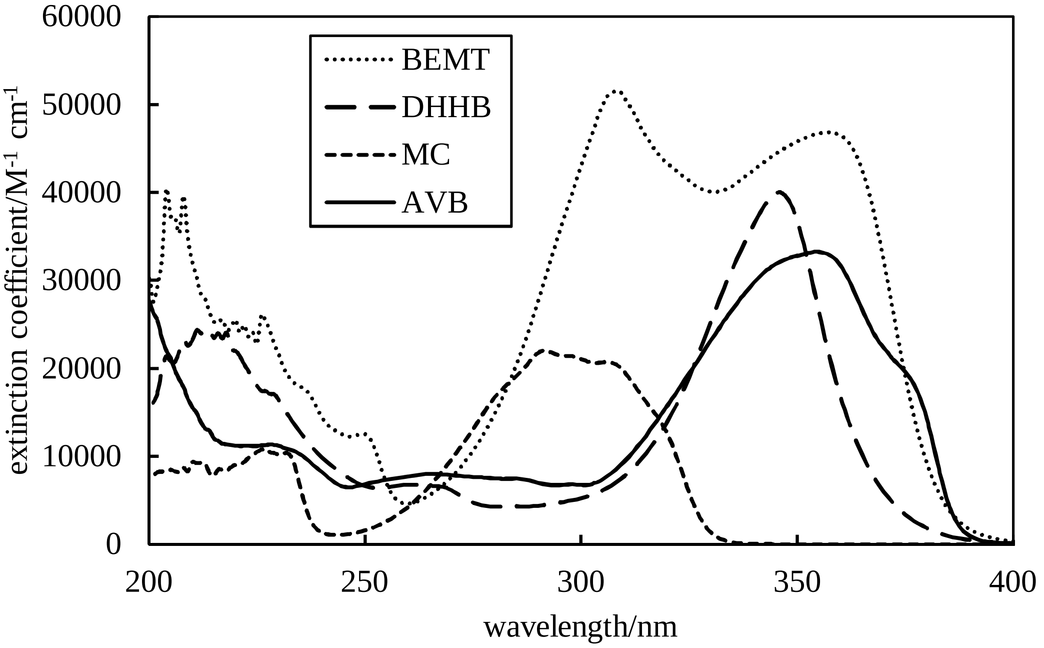

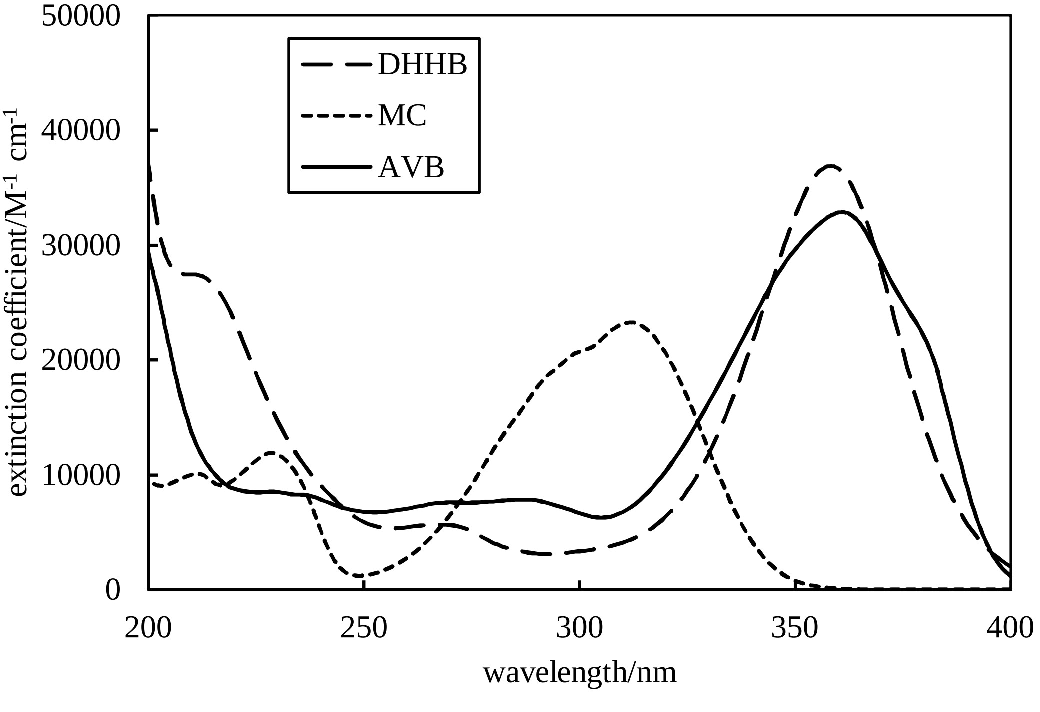

Table 3.1 summarises i) the wavelength where the peak absorbance of all UV absorbers, is observed in the solvents of interest and ii) their corresponding molar extinction coefficient values at this particular wavelength. For each UV absorber, a comparison of its molar extinction coefficient values in both SQ and PG indicates that they are approximately the same within the estimated errors despite the significant difference in the solvent polarity.

It is important to note, however, the solvent dependent shift of the maximum absorbance peak of each solute to longer wavelengths (termed as red or bathochromic shift). Previous work in the field of sunscreens has investigated this behaviour within a range of UV absorbers and solvents. It has been reported that polar solvents shifted the maximum absorbance peak of i) less polar UV absorbers to longer wavelengths and that of ii) polar UV absorbers to shorter wavelengths.[4] A plausible explanation can be attributed to the presence of a carbonyl group as part of a conjugated system of double bonds, which can cause both the n-π* and the π-π* transition bands to shift to longer wavelengths. In particular, for extensively conjugated systems such as aromatic rings, the n-π* is “buried” under the more intense π-π* band, which is the only one observed.[5] For solutes in polar solvents, this behaviour can also be favoured due to the intermolecular hydrogen bonding that can be formed between them. In the case of the extensively studied AVB, for example, it has been confirmed the bathochromic shift to longer wavelength with an increase in the solvent polarity as a result of the π-π* transition in the C=O conjugated system of the enol form.[6–8]

Table 3.1. Tabulated values of molar extinction coefficients for each of the UV absorber molecules in both solvents of interest.

UV absorbers	Solvent	Wavelength of peak(s) absorbance /nm	Molar extinction coefficient/M^{-1} cm^{-1}
AVB	SQ	354	35,000
AVB	PG	361	32,000
BEMT	SQ	357 / 308	46,800 / 51,488
DHHB	SQ	346	40,000
DHHB	PG	358	36,900
MC	SQ	291	22,000
MC	PG	312	24,300

3.3 Inorganic particulates

Sunscreen formulations also contain inorganic particles, which attenuate UV irradiation by a contribution of absorption, scattering and reflection. Suitable candidates are materials known as semiconductors, with void energy regions termed band gap between the filled valence and the vacant conduction band.[10] The selection of the semiconductor particles included TiO_2, ZnO, CeO_2 and WO_3 with typical band gap energies of 3.33, 3.31, 3.65 and 3.05 eV respectively.[11]

3.3.1 Determination of apparent extinction coefficient of dispersions containing metal oxides

The preparation of dispersions containing 0.1 wt.% of nanoparticles in both SQ and PG is described in the experimental section and it was achieved with the use of sonication. Attempts to measure the specular absorbance at a higher particle loading (equal to 1 wt.%) were unsuccessful as the strong light absorption and scattering by the particles exceeded the reliable range of the UV/vis spectrophotometer. For this reason, the absorbance of a dispersion consisting of 0.1 wt.% of nanoparticles in either SQ or PG, at a fixed path length of 100 μm was only investigated. From these set of data, the molar extinction coefficient was derived using equation 1.4.

It is important to note, however, that these dispersions do not fully obey the Beer-Lambert Law, since these absorbance measurements contain contributions not only from absorption but also from reflection and scattering by the particles. As such, the derived calculations with the use of equation 1.4 correspond to the determination of the apparent extinction coefficient instead and these values are presented below in Figure 3.3. It is evident that the apparent extinction coefficient values of WO_3 and ZnO in both solvents, are rather low and practically flat compared to those presented for CeO_2 and TiO_2 particles. Since all dispersions were prepared by a particular method (*i.e.* sonication), a possible explanation to account for the differences in the apparent extinction coefficient values can be attributed to their particle size.

Figure 3.3. Apparent extinction coefficient values of 0.1 wt.% of CeO_2, WO_3, TiO_2 and ZnO nanoparticles in SQ (upper plot) and in PG (lower plot) respectively.

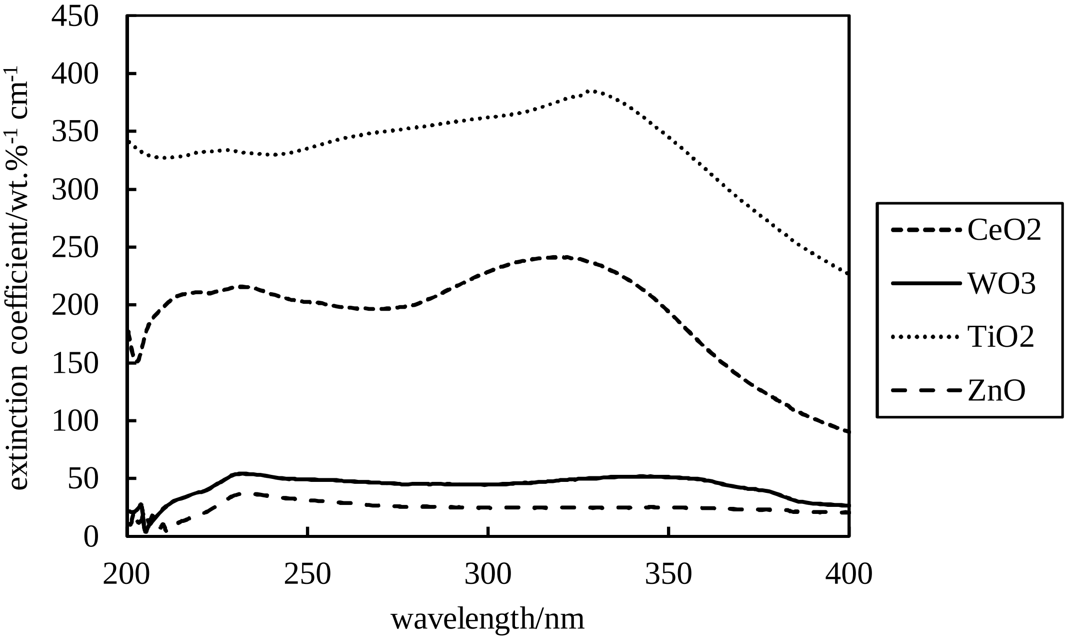

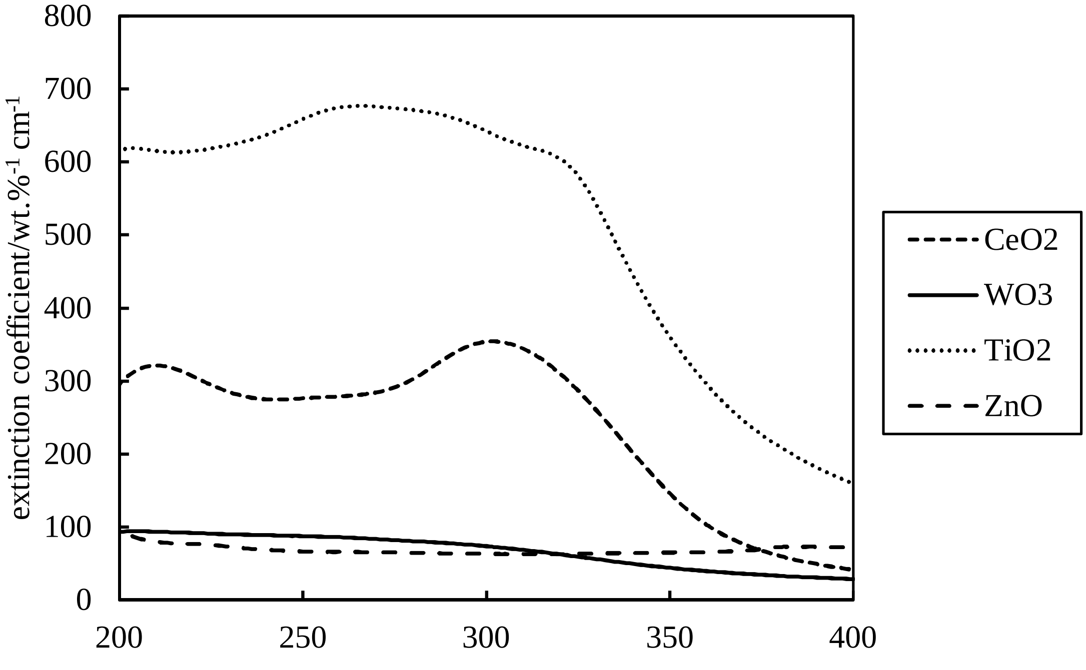

3.4 *Predicted initial in vitro SPF values of UV filters in solvents of different polarity*

For our investigated systems, the derived average values of the molar extinction coefficients will be used for the determination of the calculated absorbance for each of the UV filters, using the Beer-Lambert Law. From the calculated absorbances, the initial *in vitro* SPF, can be derived for any concentration assuming a uniform film thickness/path length equal to the recommended standard application of 2.0 mg cm^{-2}.

The volume of a film mass of a solution equal to 2.0 mg can be derived as follows

$$V = \frac{m}{\rho} \tag{3.1}$$

where V is the volume expressed in cm^3 and ρ is the density of the solution expressed in g cm^{-3}. For diluted solutions, it can be argued that the density of the solution is approximately equal to the density of the solvent. For the solvents of interest, the densities of SQ and that of PG are 0.81 and 1.027 g cm^{-3} respectively. The film thickness can be derived by the equation below

$$film\ thickness = \frac{V}{Area} \tag{3.2}$$

where film thickness is calculated in cm but is preferably expressed in µm. As such, the thickness of a film of SQ solution is approximately 24.7 µm whereas the thickness of a film of PG is equal to 19.5 µm. For convenience, the selected path length of choice for the determination of the calculated absorbance will be considered equal to 20 µm or 0.002 cm.

Having obtained the molar extinction coefficient values of all UV filters and the path length of choice, we can determine the calculated absorbance and thus the derived initial *in vitro* SPF based on equation 1.2. The functions E(λ) and S(λ) correspond to the erythema action spectrum (erythema inducing effectiveness) and the spectral irradiance of terrestrial sunlight under defined conditions respectively. These are documented experimental values available in the literature.[9]

It is important to note that depending on the UV region of interest, the wavelength integration limit as expressed in equation 1.2 can be varied accordingly. As such, three possible interpretations of *in vitro* SPF derivations can be presented. These can be defined as shown below

- SPF (290 – 400 nm), which covers the integration limit between 290 – 400 nm and represents both UVA and UVB region of the electromagnetic spectrum
- SPF (290 – 320 nm), which covers the integration limit between 290 – 320 nm and represents only the UVB region of the electromagnetic spectrum
- SPF (320 – 400 nm), which covers the integration limit between 320 – 400 nm and represents only the UVA region of the electromagnetic spectrum.

Based on the selection of the wavelength integration limit, variations in the *in vitro* SPF values are expected. These are primarily a result of the type of the UV absorbers. In this study, particular attention will be given to the combined SPF (290 – 400 nm).

3.4.1 Predicted initial in vitro SPF values of solutions containing UV absorbers

Figures 3.4 – 3.6 show the predicted initial *in vitro* SPF values for all UV absorbers in SQ and PG respectively. Since AVB and DHHB are UVA absorbers, it is expected to show significant higher SPF (320 – 400 nm) values as opposed to MC and BEMT, which show higher SPF (290 – 320 nm) values. For the overall performance in both the UVA and UVB region, however, the predicted initial *in vitro* SPF (290 – 400 nm) indicates that MC and BEMT are the most efficient UV absorbers. In addition, MC obtains high SPF (290 – 400 nm) values in both solvents.

Figure 3.4. Predicted initial *in vitro* SPF values of AVB (upper plot) and DHHB (lower plot) in SQ. The dashed line corresponds to the solubility limit for each of the UV absorbers at 32ºC.

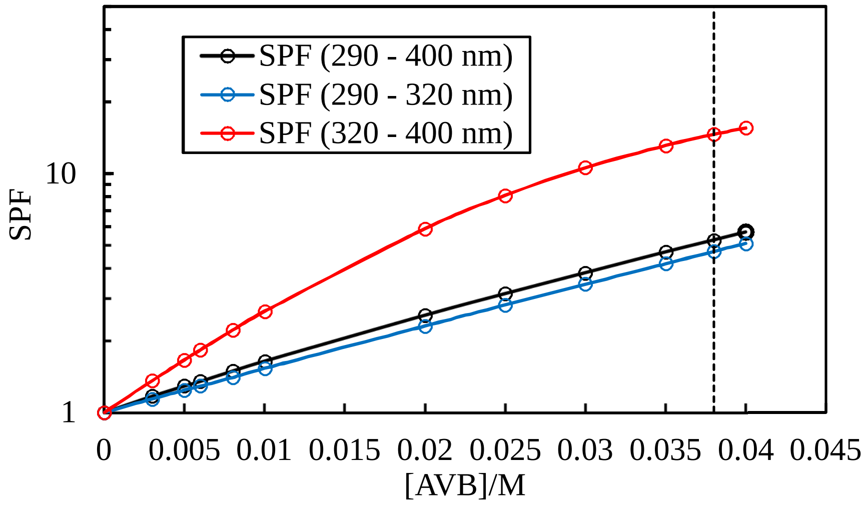

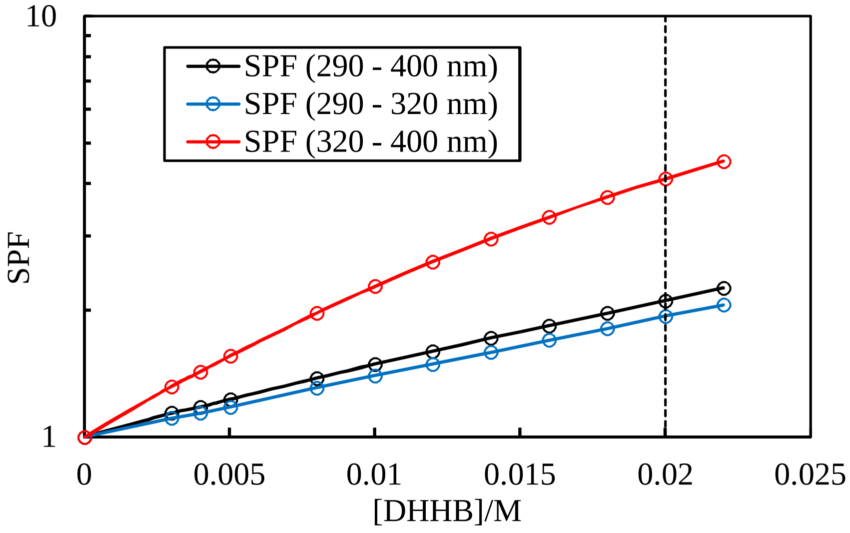

Figure 3.5. Predicted initial *in vitro* SPF values of MC (upper plot) and BEMT (lower plot) in SQ. The dashed line corresponds to the solubility limit for each of UV filters at 32^{o}C. For MC, we note that is completely miscible in SQ.

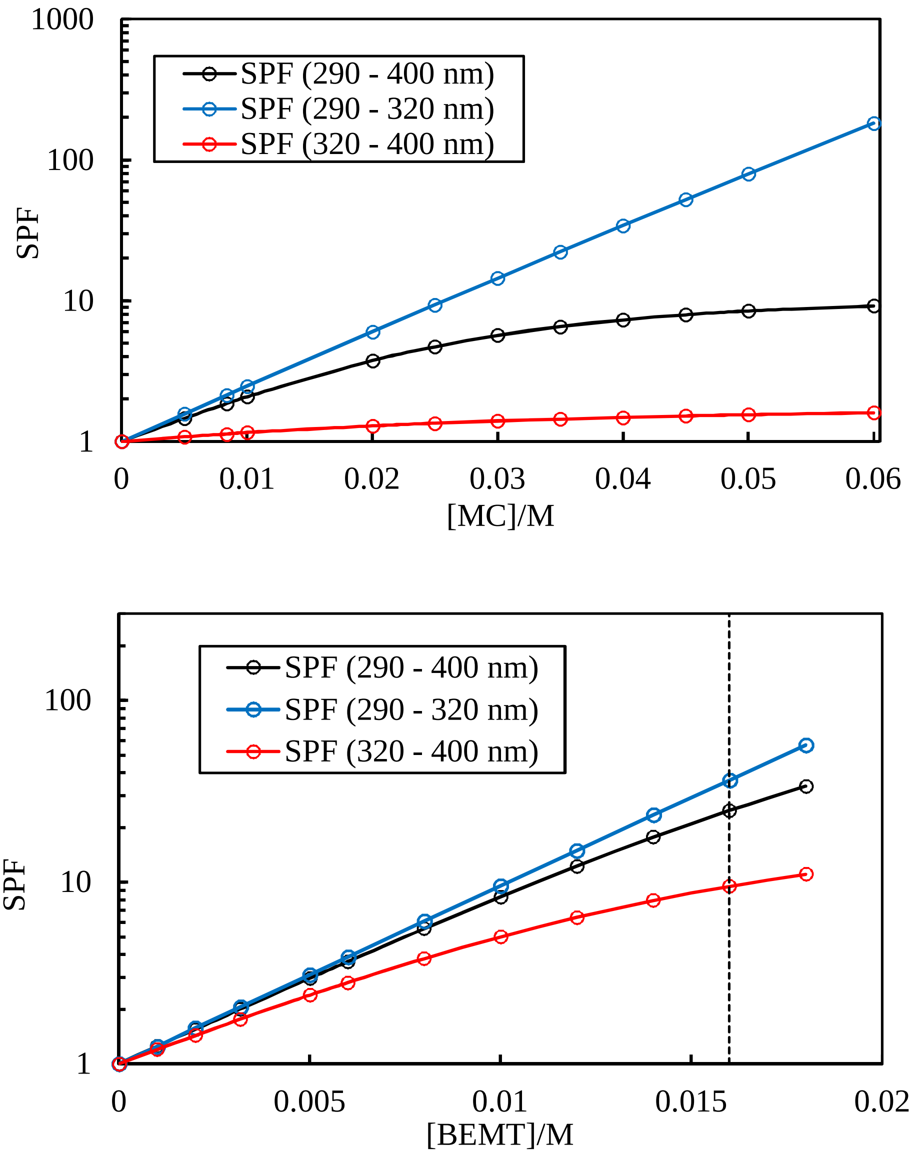

Figure 3.6. Predicted initial *in vitro* SPF values for AVB (upper plot), DHHB (middle plot) and MC (lower plot) in PG. The dashed line corresponds to the solubility of each of UV filters at 32ºC. The solubility limit of MC exceeds the reliable range of the UV/vis spectrophotometer. No data for BEMT in PG due to its very low solubility.

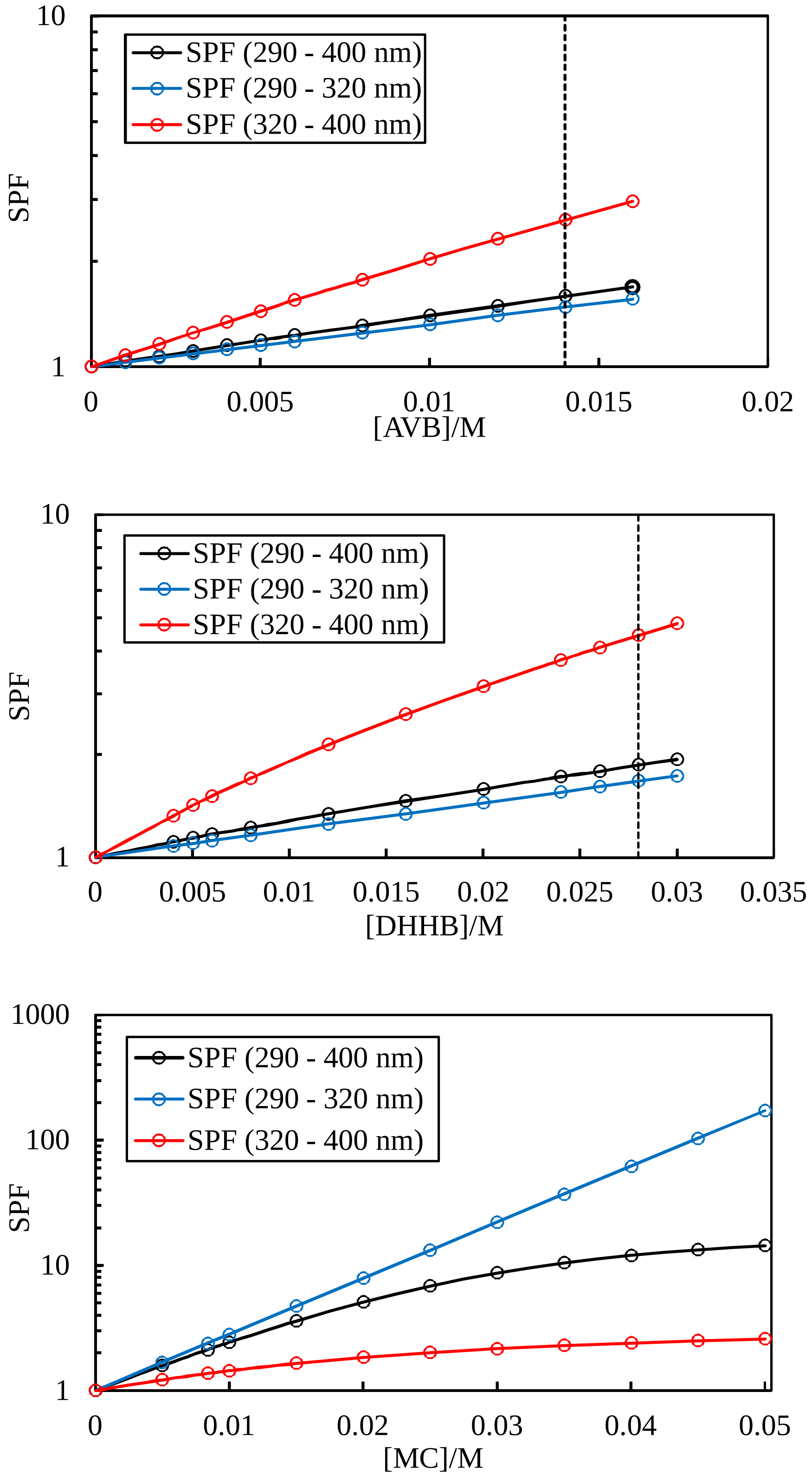

Table 3.2 summarises the values of the predicted initial *in vitro* SPF (290 - 400 nm) of all UV absorbers. The calculated absorbance is derived for concentrations of the UV absorbers at their solubility limit at 32°C. Overall, the efficiency of MC in both solvents and BEMT in SQ is evident.

Table 3.2. Tabulated values of predicted initial *in vitro* SPF for all UV absorbers in both solvents. The SPF values correspond to concentrations of the UV absorbers at their solubility limit at 32°C.

UV absorbers	**Solvent**	**Concentration equal to solubility at 32°C / mM**	**SPF (290 – 400 nm)**
AVB	SQ	38	5.26
AVB	PG	14	1.59
BEMT	SQ	16	24.76
DHHB	SQ	20	2.11
DHHB	PG	28	1.86
MC	SQ	1300	14.64
MC	PG	435	26.71

3.4.2 Predicted initial *in vitro* SPF values of dispersions containing inorganic particles

Having determined the values of the apparent extinction coefficient for all dispersions in both solvents, the next step was to calculate their absorbance and thus, their initial *in vitro* SPF values. Assuming that the dispersions above obey the Beer-Lambert Law, the calculated absorbance can be derived for dispersions containing any particle loading for a uniform film thickness/path length equal to 20 μm.

A comparison of the results presented in Figures 3.7 – 3.10 shows that there are variations in the predicted initial *in vitro* SPF values. From these data sets, it can be seen that there is no specific pattern that can correlate the predicted in *vitro* SPF values with the semiconductor oxide type. It is possible that these variations in the *in vitro* SPF values can be attributed to i) the particle size of the semiconductor type and to ii) the solvent of choice. From the TEM images obtained, which are shown in the experimental section, it can be seen that the CeO_2 and TiO_2 particles are significantly smaller than the WO_3 and ZnO particles. This implies that with the aid of sonication, the CeO_2 and TiO_2 particles were finely dispersed and act more efficiently in absorbing, scattering and reflecting the UV light compared to the WO_3 and ZnO particles. Hence, this behaviour is expressed in higher estimated initial *in vitro* SPF values. It is also of interest to note that based on Figures 3.3, both CeO_2 and TiO_2 particles are expected to show higher extinction coefficient values when dispersed in the polar protic PG as opposed to the apolar SQ.

Figure 3.7. Predicted initial *in vitro* SPF values for CeO_2 (upper plot) and TiO_2 (lower plot) in SQ.

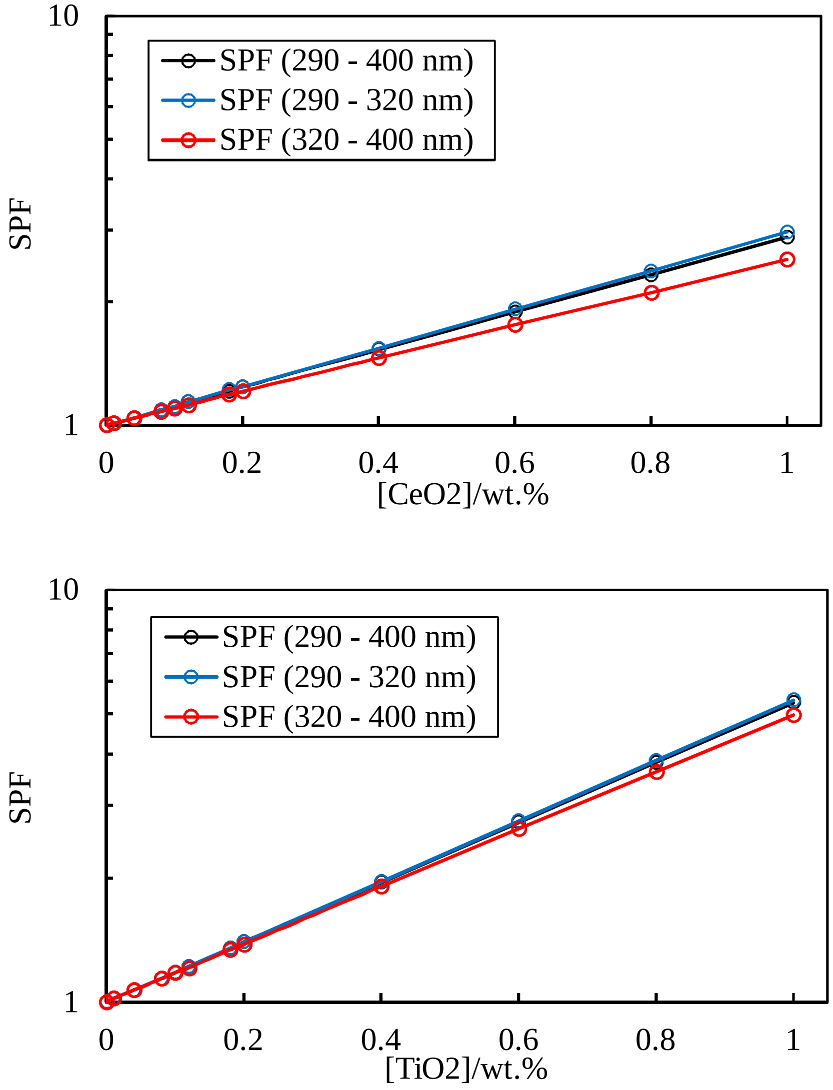

Figure 3.8. Predicted initial *in vitro* SPF values for WO_3 (upper plot) and ZnO (lower plot) in SQ.

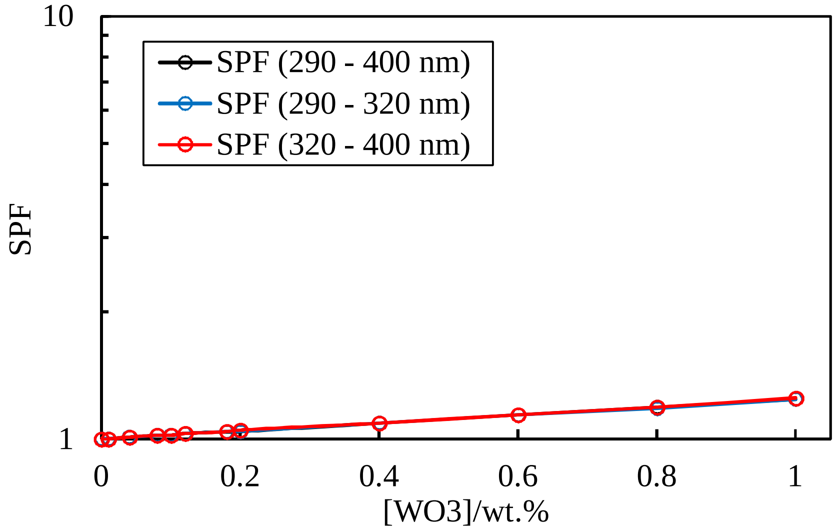

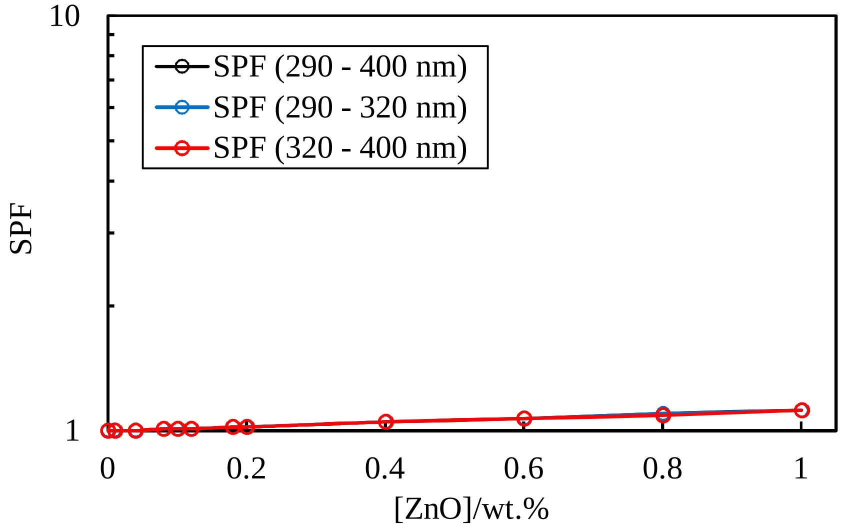

Figure 3.9. Predicted initial *in vitro* SPF values for CeO_2 (upper plot) and TiO_2 (lower plot) in PG.

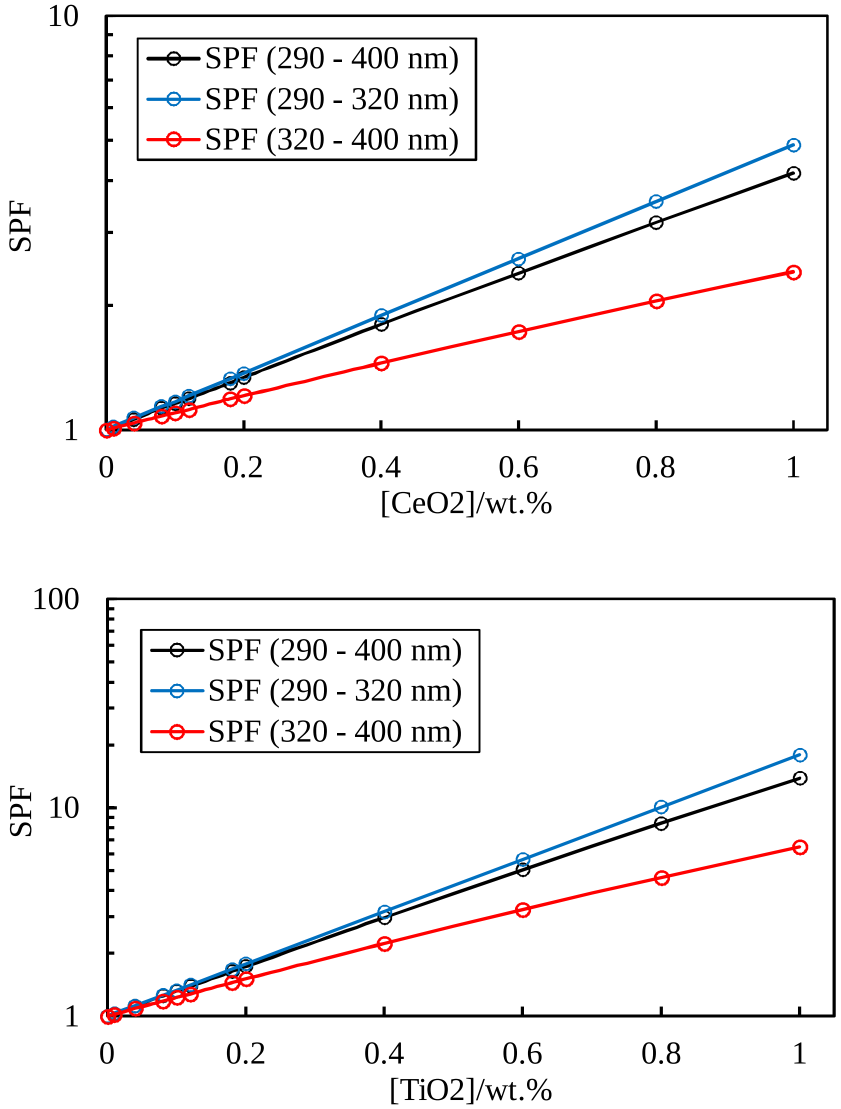

Figure 3.10. Predicted initial *in vitro* SPF values for WO_3 (upper plot) and ZnO (lower plot) in PG.

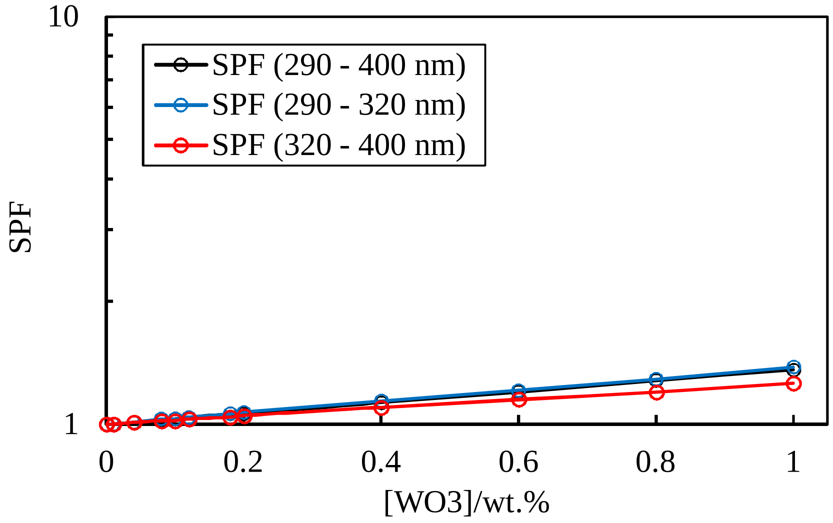

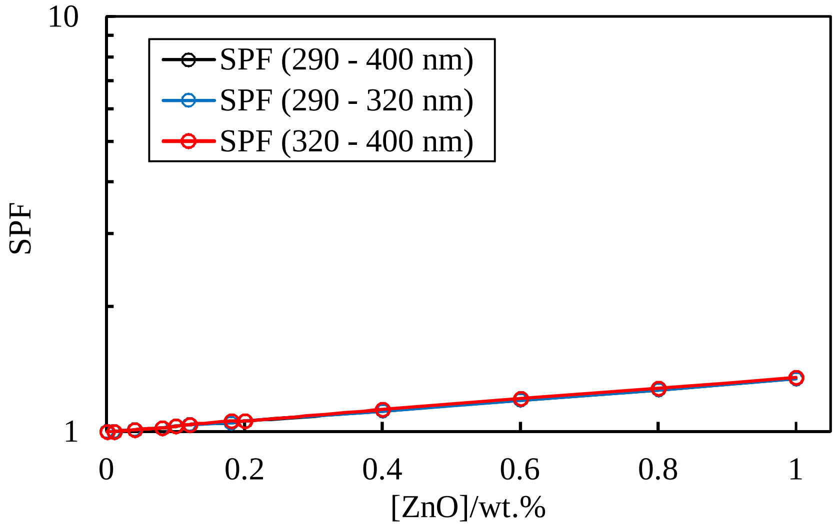

3.4.3 Predicted *in vitro* SPF for a combination of UV absorbers

As already discussed, for a solution containing a concentration of a single UV absorber with a known molar extinction coefficient at a fixed path length of 20 µm, the calculated absorbance and thus the initial *in vitro* SPF values can be predicted. Similarly, it is expected that the initial *in vitro* SPF values can also be predicted for a combination of UV absorbers. This behaviour is a result of the fact that i) all solutions obey the Beer-Lambert Law and that ii) the measured absorbance value due to light absorption is simply additive.

The validity of the model is presented in Figure 3.11, where both measured and calculated absorbance data are compared for a solution containing a mixture of UV absorbers. The measured absorbance data correspond to a solution consisting of 2.50 mM AVB plus 2.23 mM BEMT in SQ for a fixed path length of 100 μm at a temperature of 32°C. The overall calculated absorbance data resulted from the sum of the individual calculated absorbance values of each of the UV absorbers, with the use of Beer-Lambert Law. As expected, the comparison of the measured against the calculated absorbance for this solution indicates that both values are in agreement. This result can be depicted in the initial *in vitro* SPF calculation. As such, for the exact combination of concentrations in SQ and for a film thickness of 20 μm, the value of the initial *in vitro* SPF (290 – 400 nm) is equal to 1.84.

Figure 3.11. Measured and calculated absorbance *versus* wavelength for a combination of 2.50 mM AVB and 2.23 mM BEMT in SQ.

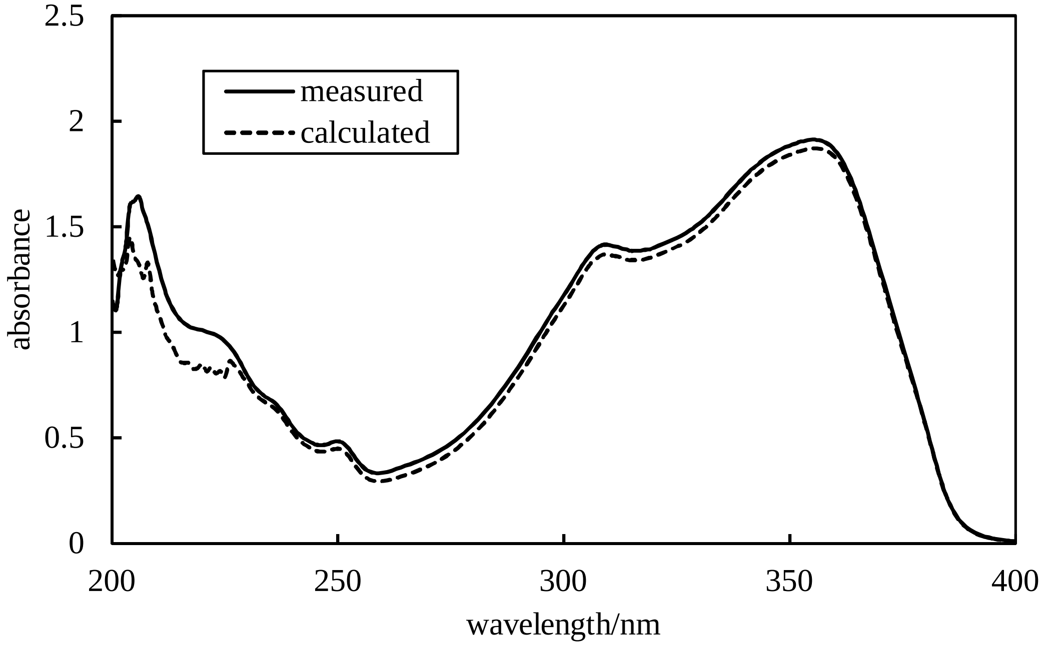

3.4.4 Comparison of predicted initial *in vitro* SPF of all UV filters

Table 3.3 shows a comparison of the predicted initial *in vitro* SPF for all UV filters. The concentration of the UV absorbers was converted to wt.% in order to match the particle loading of the dispersions. Taking into account the solubility limit at 32°C, the most representative value for all UV filters was 0.4 wt.%. As such, the predicted initial *in vitro* SPF indicates that MC in both solvents (SQ and PG) and BEMT are the most efficient UV absorbers. In terms of the commercial nanoparticles that were used in this study, the most efficient is TiO_2 in PG.

Table 3.3. Comparison of predicted initial *in vitro* SPF values of 0.4 wt.% of all UV filters at a fixed temperature of 32°C.

UV filters	Solvent	SPF (290 – 400 nm)
AVB	SQ	1.67
AVB	PG	1.56
MC	SQ	2.54
MC	PG	4.07
DHHB	SQ	1.39
DHHB	PG	1.29
BEMT	SQ	3.06
CeO_2	SQ	1.53
CeO_2	PG	1.80
TiO_2	SQ	1.95
TiO_2	PG	2.97
WO_3	SQ	1.09
WO_3	PG	1.13
ZnO	SQ	1.05
ZnO	PG	1.12

3.5 Conclusions

An initial *in vitro* SPF estimation, is introduced to predict and compare the efficiency of solutions consisting of a single UV absorber in both SQ and PG. For this reason, their molar extinction coefficients of the UV absorbers were determined experimentally from the average of a range of concentrations and path lengths. Using the Beer-Lambert Law, the calculated absorbance for any concentration at the desirable path length of 20 μm can be derived and thus the predicted initial *in vitro* SPF values can be obtained. Three types of SPF have been introduced depending on the wavelength integration limits, but particular attention was given to SPF (290 – 400 nm).

The same approach was applied for the determination of the initial *in vitro* SPF values for dispersions of semiconductor oxide nanoparticles in both SQ and PG of a film thickness equal to 20 μm. Based on the collection of measured absorbance spectra, the apparent extinction coefficient was derived as a result of a combination of absorption, reflection and scattering by the particles. A comparison of 0.4 wt.% of all UV filters in both solvents has confirmed that the most efficient UV sunscreen actives are MC in both solvents, BEMT in SQ and TiO_2 in PG.

In addition, we show that for solutions containing a combination of UV absorbers, both measured and calculated absorbance spectra are in very good agreement. This is shown for a mixture of similar concentrations of AVB and BEMT in SQ. The data confirmed that the absorbance due to the presence of both UV absorbers is simply additive and the calculated absorbance for a film thickness of 20 μm and thus the initial *in vitro* SPF can be effectively described.

3.6 References

1. The European Cosmetic Toiletry and Perfumery Association - COLIPA, *International Sun Protection Factor (SPF) Test Method*, Bruxelles, 2006.
2. J. Stanfield, U. Osterwalder and B. Herzog, *Photochem. Photobiol. Sci.*, 2010, **9**, 489–494.
3. L. Ferrero, M. Pissavini and O. Doucet, *Photochem. Photobiol. Sci.*, 2010, **9**, 540–551.
4. L. E. Agrapidis-Paloympis and R. A. Nash, *J. Soc. Cosmet. Chem*, 1987, **221**, 209–221.
5. D. L. Pavia, G. M. Lampman, G. S. Kriz, and J. R. Vyvyan, *Introduction to Spectroscopy*, BROOKS/COLE, Belmont, 4th edition, 2008.
6. G. J. Mturi and B. S. Martincigh, *J. Photochem. Photobiol. A*, 2008, **200**, 410–420.
7. P. Markov and I. Petkov, *Tetrahedron*, 1977, **33**, 1013–1015.
8. R. A. Morton, A. Hassan, and T. C. Calloway, *J. Chem. Soc.*, 1934, **192**, 883–901.
9. B. L. Diffey and J. Robson, *J. Soc. Cosmet. Chem.*, 1989, **40**, 127–133.
10. A. L. Linsebigler, G. Lu, and J. T. Yates, *Chem. Rev.*, 1995, **95**, 735–758.
11. H. Zhang, Z. Ji, T. Xia, H. Meng, C. Low-Kam, R. Liu, S. Pokhrel, S. Lin, X. Wang, Y. Liao, M. Wang, L. Li, R. Rallo, R. Damoiseaux, D. Telesca, L. Madler, Y. Cohen, J. I. Zink, and A. E. Nel, *ACS Nano*, 2012, **5**, 4349–4368.

CHAPTER 4 EVAPORATION OF SOLUTION AND DISPERSION FILMS CONTAINING UV FILTERS

4.1 Introduction

In this chapter, we discuss the evaporation of films containing solutions of common UV absorber molecules such as avobenzone (AVB), diethylamino hydroxybenzoyl hexyl benzoate (DHHB) and *iso*-pentyl *p*-methoxycinnamate (MC) spread primarily onto a smooth quartz plate substrate. These films of a few μm thickness were left to evaporate in the open lab air. Their mass loss, film area and absorption spectra were monitored at frequent timed intervals. Our findings can successfully describe how the evaporation process affects the decrease in absorbance. As such, during evaporation, the initial film progressively dewets and this area shrinkage results in transient fluctuations in its height. In addition, solvent evaporation causes an increase in the solute concentration until its solubility limit is reached. Beyond that point, solute precipitation is observed. Thus, the measured progressive loss of the absorbance as a function of evaporation time is attributed to both dewetting and solute precipitation as drying proceeds. This behaviour is depicted in the *in vitro* SPF values, which indicate the measure of efficiency of the films. Measured absorbance spectra and calculated absorption values with the use of a simple model are compared and predict the variations of *in vitro* SPF with respect to the evaporation time.

Throughout our experimental procedure, the main solvent of choice was propane-1,2-diol (PG). The reason for the solvent choice was that the evaporation of PG occurred at a slow controlled rate over an extended period of several hours, proving invaluable in terms of understanding and interpreting the collected data. In addition, PG is also an acceptable and common ingredient in sunscreen and in cosmetic formulations in general. However, irrespective of the evaporation rate of the solvent (either fast or slow), the progressive loss of the absorbance as a result of i) film dewetting and ii) solute precipitation, is evident. This was made clear when an alternative solvent with a higher vapour pressure than PG, such as *n*-decane, was used instead.

Current sunscreen formulations can contain both organic UV absorbers and inorganic particulates for photoprotection. Thus, the effect the latter can have on the loss of the absorbance and eventually on the *in vitro* SPF has also been pursued. Films of dispersions containing semiconductor oxide nanoparticles and one UV absorber (AVB) in PG were left to evaporate in the open lab air and their mass loss, film area and absorbance spectra were recorded. The substrate of choice was a smooth quartz plate. For these films, it is expected that the measured absorption spectra are dominated by the presence of the UV absorber (AVB). A minor contribution, however, of absorption, scattering and reflection caused by the nanoparticles, despite their very low loading, cannot be excluded.

In addition, results have indicated that the presence of the nanoparticles aids pinning of the film at its base edge and thus suppressing its dewetting. The loss of the absorbance is primarily a result of solute precipitation as solvent evaporation proceeds. This behaviour was depicted in the film absorption spectra and thus in the *in vitro* SPF calculations. The type of nanoparticles that were used included those that are commercially available to the sunscreen industry such as TiO_2, ZnO and CeO_2. Further investigation included WO_3 and two types of silica particles, one hydrophobic and one hydrophilic. Similarly, the addition of a polymer in a solution containing one UV absorber (AVB) in PG was also investigated. The results have confirmed that film dewetting is inhibited. For our experimental procedure, the polymer of choice was an aqueous solution of poly-DADMAC.

In the last part of this chapter, other substrates with the intention of closely mimicking the properties and the surface of the human skin were investigated. As such, the evaporative behaviour of solutions of a UV absorber (AVB) in PG was examined on two alternative substrates: i) Vitro Skin, which is a commercial polymer sheet and ii) a keratin-lipid film. The results have demonstrated that the rough surface of both substrates aids film pinning. This behaviour is shown in both measured and calculated *in vitro* SPF values, confirming again the loss of the absorbance as a result of solute precipitation with evaporation time.

4.2 Evaporation of solutions of UV absorbers in PG

For the investigation of the evaporation of thin films, solutions consisting of high solute concentrations were prepared in order to closely resemble the behaviour of the "real" concentrations in sunscreen formulations. The choice of the solute concentration was made based on the determination of the molar extinction coefficient per wavelength of all UV absorbers. Thus, the highest possible concentration that will not exceed the reliable range of the spectrophotometer was selected.

4.2.1 Evaporation of AVB in PG

The visual appearance of a deposited film of a solution of 8.0 mM AVB in PG is shown in Figure 4.1. The film, with an initial volume of 11.25 μl, was spread as evenly as possible on top of a smooth quartz plate. This volume represents the required amount of solution which can fully cover a 5.625 cm^2 of the quartz plate area with a thickness of 20 μm. The calculation of the full area of the quartz plate was made based on the manufacturer's dimensions. During the monitored evaporation time, it can be seen that the film area progressively decreases due to the absence of pinning at the three-phase contact line, a process that occurs until its complete solvent evaporation at 690 min. In addition, the solute (AVB) concentration is expected to increase to its solubility limit as solvent evaporation proceeds. Hence, the moment the solubility limit has been reached, AVB is precipitated in the form of crystals and this phenomenon was repeatedly observed after 150 – 180 minutes of evaporation. Upon complete solvent evaporation at 690 min, a film residue of AVB crystals is evident.

In the images of Figure 4.1, the superimposed red rectangular box corresponds to the area (termed illuminated area) where the beam of the spectrophotometer passes through for sample detection. It can be seen that for this particular experiment, the fraction of illuminated area for a period of up to 180 min is equal to 1, implying that the illuminated area is fully covered with the sample solution. However, beyond 240 min, the fraction of the illuminated area becomes less than unity. This indicates that part of the illuminated area was covered with the solution film, whereas part of it remained uncovered as a result of dewetting and/or evaporation.

Figure 4.1. Evolution of film of 8.0 mM AVB in PG deposited on a quartz plate, with evaporation time. Each time step image includes a ruler with a mm scale on the left hand side (for scale) and the quartz slide with the liquid film on the right hand side. The red rectangular box shows the illuminated area depicted in the absorbance measurements.

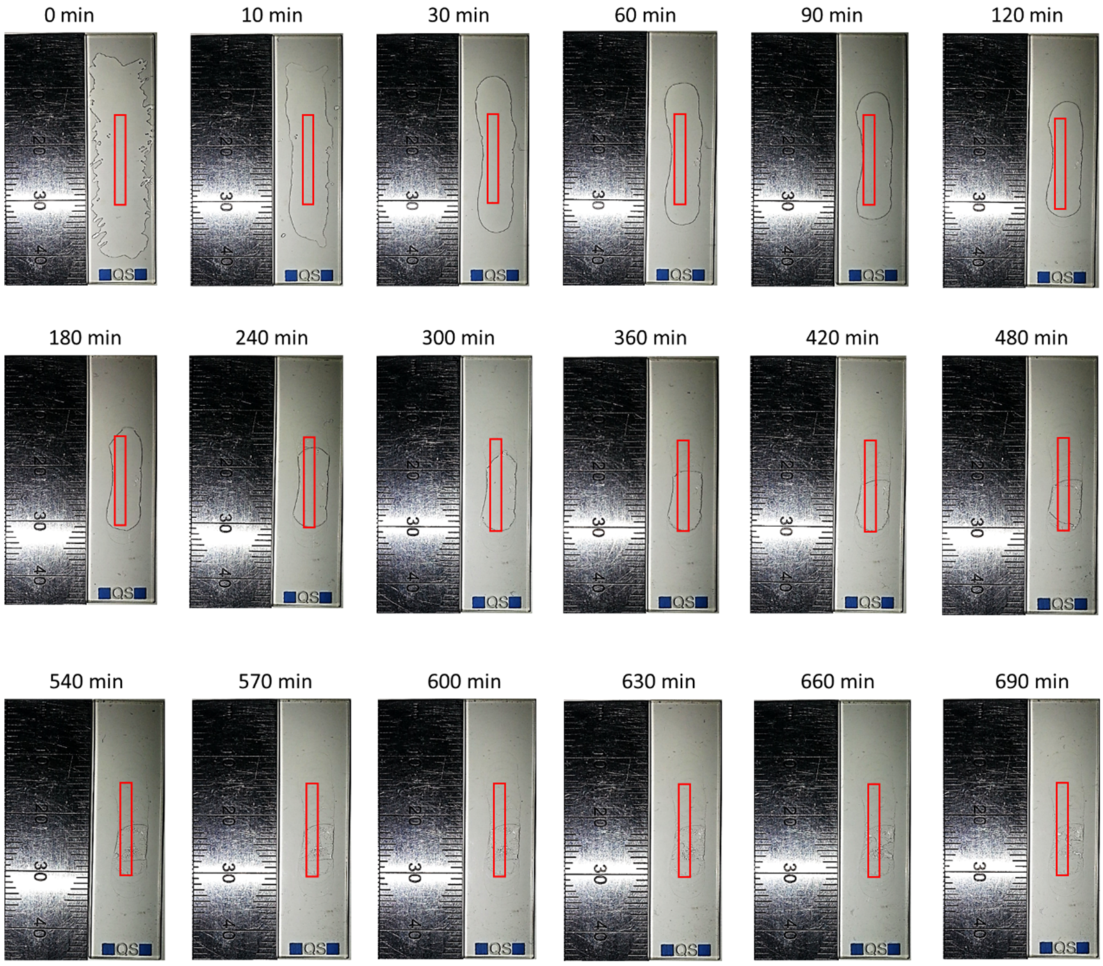

Figure 4.2 corresponds to the data representation derived from the analysis of the images shown in Figure 4.1. It is comprised of a set of three graphs and it is organised as follows. The upper plot of Figure 4.2 shows the measured mass of film remaining deposited on the quartz plate until its complete evaporation. The dashed line shown in the upper plot of Figure 4.2 corresponds to the predicted film mass m* at time t* where the solute concentration of AVB is expected to reach its equilibrium solubility. Beyond that point, AVB precipitation in the form of crystals is expected to occur. The value of m* is estimated according to equation below

$$m^* = \frac{m_o[AVB]_o}{S_{AVB}} \tag{4.1}$$

where m_o is the initial film mass (0.0117 g), $[AVB]_o$ is the initial concentration of AVB equal to 8.0 mM and S_{AVB} is the equilibrium solubility of AVB in PG equal to 14 mM at 32°C. Thus, m* is estimated to be 0.0067 g and t* is 190 minutes, which is a reasonable agreement with the time range (150 – 180 min) at which precipitated crystals of AVB are first observed.

The middle plot of Figure 4.2 presents the film area of the deposited solution. The values of the film area were determined from images of Figure 4.1 with the use of ImageJ software. The initial deposited film area, despite repeat measurements, varied between 3 – 4 cm^2 and did not cover the full area of the quartz plate.

It has been reported[1] that for conditions where the rate limiting step across a "stagnant" gaseous layer is the rate of diffusion, the rate of mass loss by evaporation is described by the following equation

$$-\frac{dm}{dt} = \frac{MADPf}{hRT} \tag{4.2}$$

where m is the mass of the film remaining, t is time, M is the relative molar mass of the evaporating liquid, A is the liquid surface area, D is the diffusion coefficient of the vapour through air, P is the equilibrium vapour pressure of the liquid, h is the thickness of the stagnant vapour layer, R is the gas constant and T is the absolute temperature. The parameter f is a factor, which is dependent primarily on the geometry of the evaporation setup. Under the evaporation conditions used here, h and f are not known but are approximately constant within and between runs. Hence, the evaporation rate expressed as -dm/dt is proportional to the liquid surface area A only, as all other parameters remain constant during our experiment. Since the film area is progressively shrinking, a decrease in the evaporation rate is expected and this behaviour is depicted with the concave shape in the middle plot of Figure 4.2.

The calculated average film thickness with evaporation time is shown in the lower plot of Figure 4.2, since film volume and total film area are recorded values at timed intervals. The relevant equation for the determination of the average film thickness is

$$d = \frac{m}{\rho A} \tag{4.3}$$

where m is the remaining film mass, A is the total film area and ρ is the film density taken to correspond to pure PG and equal to 1.027 g cm^{-3} at 32°C.[2]

From the lower plot of Figure 4.2, it can be seen that for the monitored evaporation time, the calculated average film thickness shows transient fluctuations in its value. These fluctuations are due to changes in the total film area and film volume as progressive film dewetting and solvent evaporation, occur. It is also important to note that these calculated values correspond to average values of the overall film. It is assumed that the same film thickness/path length is present in the illuminated area, which is responsible for the absorbance measurements. It is believed, though, that the film is probably thicker at the edges and thinner in the middle. Ring formation due to solute transport at the film base edge is possible. However, in our experiment, the solute transport does not inhibit film dewetting since the latter is observed until the very last stage prior to complete evaporation. The fraction of the illuminated area with evaporation time is given in Figure 4.3. The illuminated area corresponds to an area of 0.32 cm^2 based on calculations that were made with the aid of ImageJ software.

Figure 4.2. Evolution of film mass (upper plot), total film area (middle plot) and average film thickness (lower plot) with evaporation time for a film of 8.0 mM AVB in PG. The dashed lines indicate film mass and evaporation time at the point at which the AVB concentration equals its solubility.

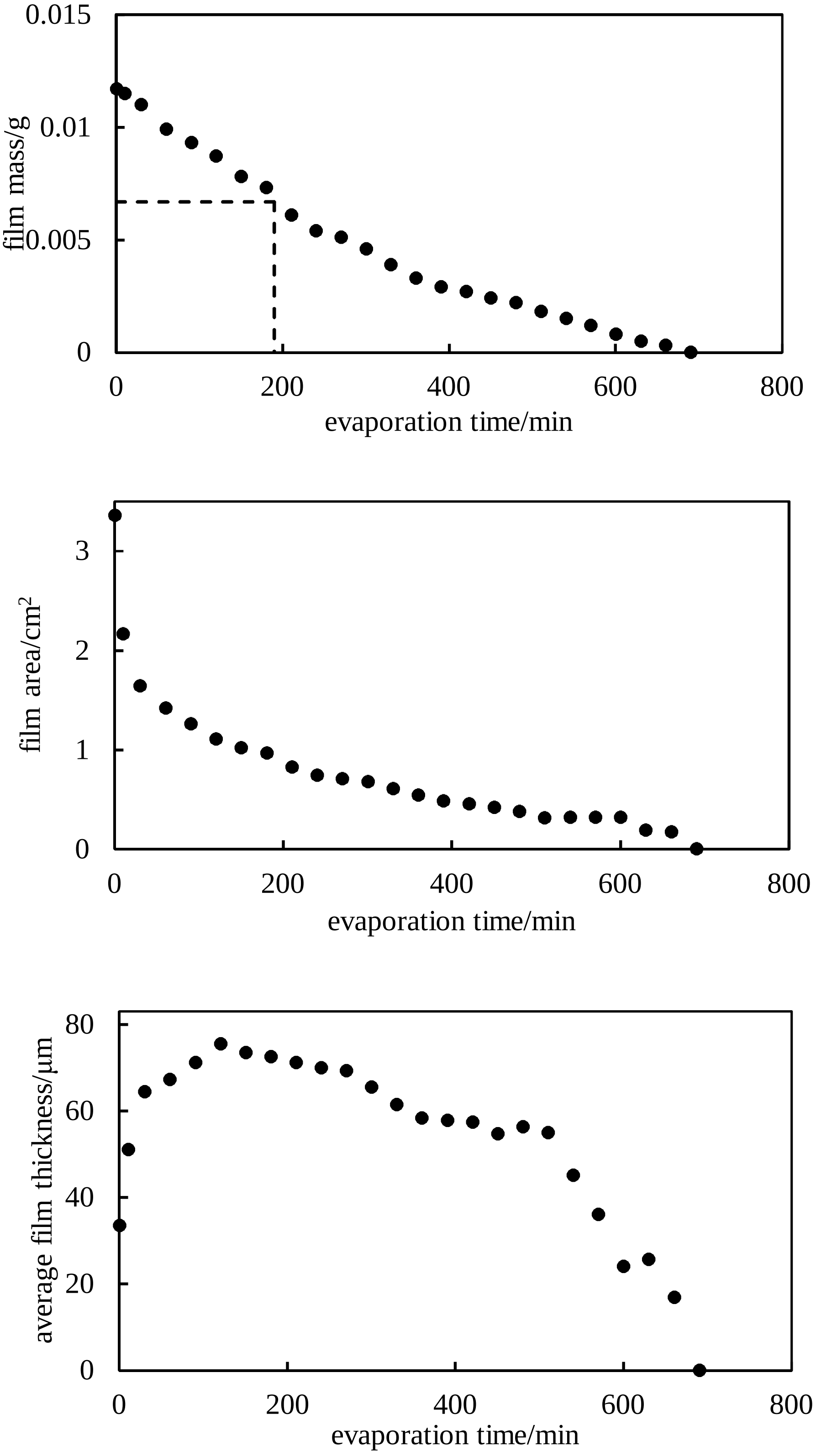

Figure 4.3. Fraction of illuminated area covered by the film with evaporation time for a film of 8.0 mM AVB in PG.

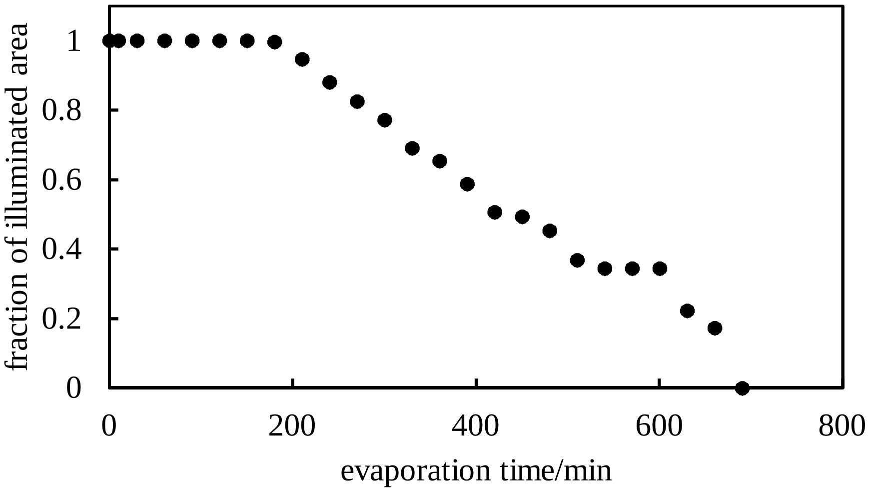

We have assessed the reproducibility of the procedure described above. We have repeated (3 runs) the evaporation process of films of 8.0 mM AVB in PG under the investigated conditions and the mass loss as a function of evaporation time agrees within the estimated errors of ± 10%. The total film area, however, varied in a relatively random fashion since film dewetting on a smooth substrate is uncontrollable and is limited to each run. It is expected that the same conditions will apply to the illuminated area, as part of the total film area and this behaviour will be depicted in the measured absorbance spectra. As will be shown in the following section of this chapter, however, we have successfully modelled the absorbance spectra and we show that their main features are kept constant within the estimated errors.

The evaporative behaviour of a film of 8.0 mM AVB in PG compared to that of a film of pure PG was also studied, since the physical properties between solutions and pure solvents can vary significantly. The results have indicated that the presence of the solute at this concentration did not significantly alter the evaporation behaviour of the solution compared to that of the pure solvent. Evidence for that behaviour is shown later in this chapter (Figure 4.6).

4.2.2 Absorbance measurements of AVB in PG during evaporation

As evaporation proceeds, absorbance measurements at frequent timed intervals were made as shown in the upper plot of Figure 4.4, until complete solvent evaporation at

690 min. In general, for a film containing a concentration of AVB with a uniform thickness/path length d of the illuminated area and with a molar extinction coefficient ε, the absorbance is given by equation 1.4. It is important to note that equation 1.4 is valid for plane parallel light incident normal to the film and non-scattering films, *i.e.* the transmittance is equal to the specular transmittance and contains no significant diffuse contribution. As such, these absorbance data correspond to specular absorbance spectra obtained with the use of a UV/vis spectrophotometer. Unless otherwise stated, it is implied that all absorbance measurements below were in fact specular absorbance measurements.

From the data collected, it is evident that the measured absorbance increased in magnitude compared to the initial absorbance obtained at time t = 0 min. The main reason for this behaviour can be attributed to the transient increase in film height/path length as a result of progressive film dewetting. It is expected that as these solutions obey the Beer-Lambert Law, any increase in their film height/path length will result in the proportional increase of the measured absorbance. A contribution in the absorbance can also result from the increase in solute concentration during evaporation for the investigated period. Overall, this pattern was observed for a period of up to 120 minutes. For this time scale, the solute concentration is below the solubility limit. In addition, a maximum absorbance peak at 361 nm, which corresponds to the UVA-I region of the electromagnetic spectrum, is also evident.

Beyond 150 min however, the measured absorbance values progressively decreased and “flatten” in shape in the maximum absorbance peak. By complete solvent evaporation, the “flattening” of the spectral peaks was observed with values in the range of 0.015 – 0.2 irrespective of the wavelength. The decrease in the absorbance value is in accordance with our estimated time scale for solute precipitation based on equation 4.1, which implies that the solubility limit has been reached. In addition, the “flattening” of the peak can be attributed to the incomplete coverage of the film in the illuminated area.

As discussed, for a deposited solution film on top of a smooth quartz plate, the absence of film pinning can only lead to irregular dewetting patterns during evaporation. For this reason, a simple model is introduced to account for any film variations based on the measured absorbance values. These set of data will correspond to the calculated absorbance values and are shown in lower plot of Figure 4.4. Overall, equations have been developed to tackle the problem of non-uniform thickness and to determine the light absorption properties in sunscreen films.[3-5] Similar approach has been applied to determine the light absorbance of biological sporopollenin particles.[6] Thus, under conditions where the illuminated area due to dewetting is not fully covered, the fraction of the illuminated area is expected to be less than 1. Hence, the calculated absorbance is equal to the negative logarithm of the illuminated area average of the transmittance as shown below

$$Abs = -log_{10}\{A_f 10^{-\frac{\varepsilon c d}{A_f}} + (1 - A_f)\} \tag{4.4}$$

where ε is the molar extinction coefficient, c the concentration, d the average film thickness and A_f the fraction of illuminated area. Equation 4.4 is valid assuming uniform i) film thickness of the illuminated area and ii) light illumination of the spectrophotometer. Variations in the solute concentration are also taken into consideration for the determination of the calculated absorbance above. Thus, for a film containing a solute concentration c, this latter model assumption is implemented in the calculations as follows

$$c = \frac{c_0 m_0}{m} \quad \text{for times less than or equal to } t^* \text{ and} \tag{4.5}$$

$$c = S_{AVB} \quad \text{for times greater than } t^* \tag{4.6}$$

The model presented in equations 4.4 - 4.6 above, does not take into consideration any contribution in the absorbance measurements from the individual crystals of AVB, which resulted from its precipitation during the solvent evaporation. It is expected that the individual crystals of precipitated AVB will absorb strongly because of their localised concentration or at least they will be similar in magnitude to that for AVB in dilute solution.[7] However, the crystals can only cover a very small fraction of the illuminated area and thus it can be assumed that their contribution to the overall specular absorbance will be negligible. The optical micrographs of the precipitated AVB crystals can be of support to this argument and are shown in Figure 4.5. As such, for the film profile model calculations, it is assumed that overall the crystals have negligible contribution and that the calculated absorbance values can be attributed to the dissolved solute molecules alone.

Figure 4.4. Measured (upper plot) and calculated (lower plot) absorbance spectra for a film of 8.0 mM AVB in PG for the investigated period until complete solvent evaporation. Calculated spectra are presented for a period of up to 480 min.

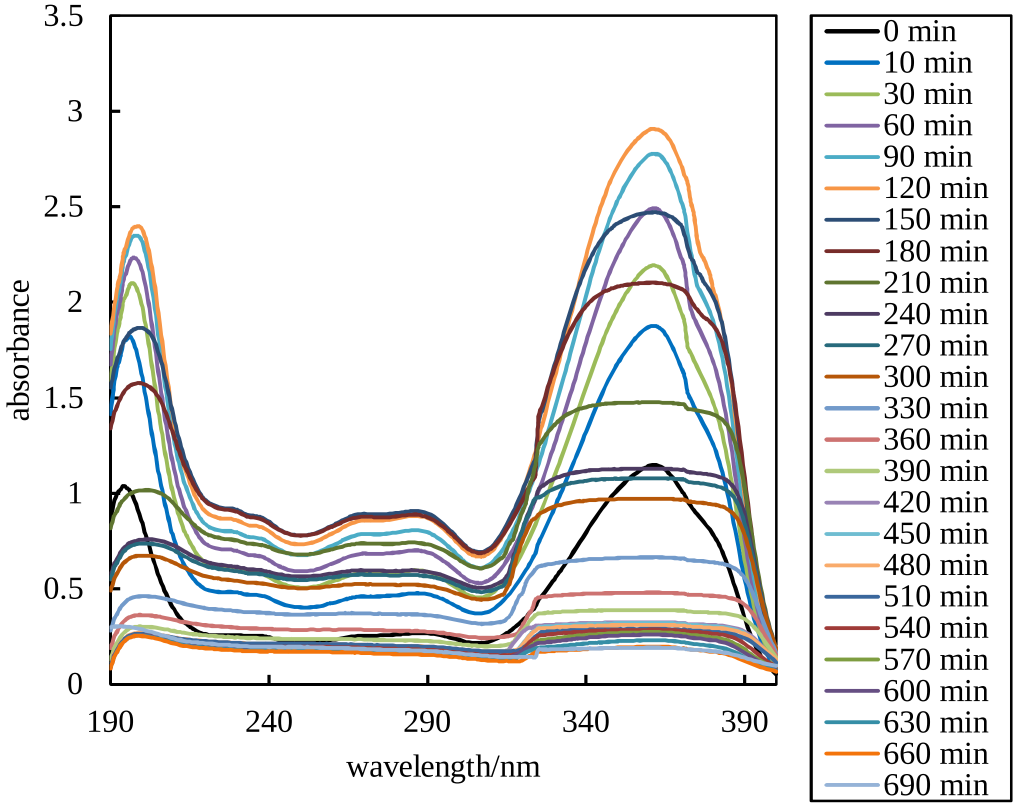

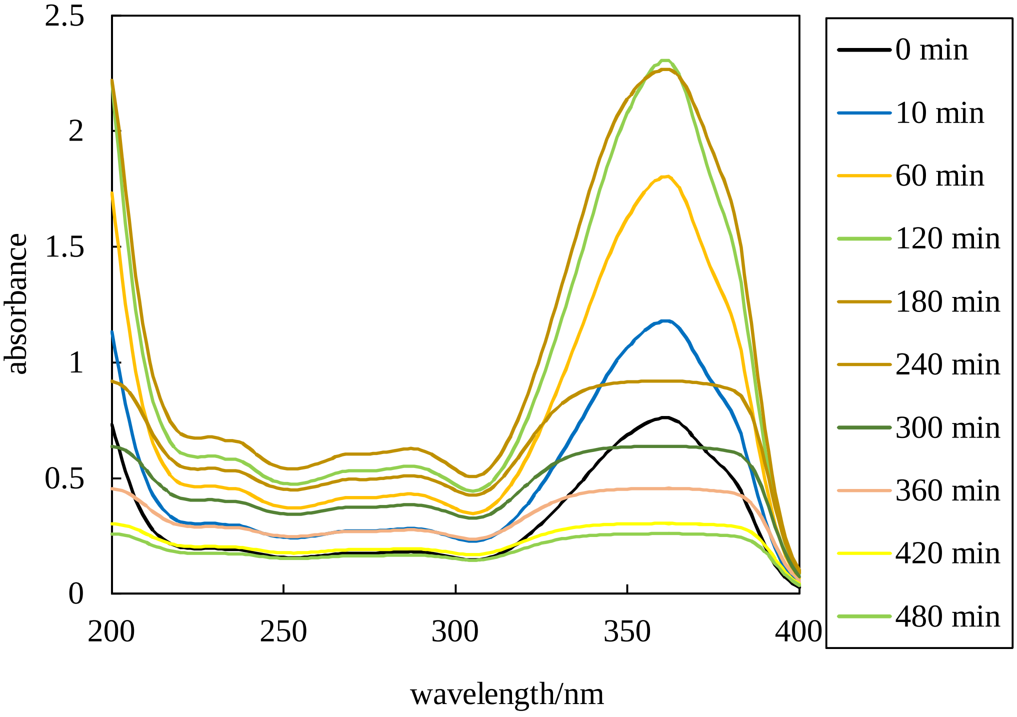

Figure 4.5. Consecutive optical microscopy images of 8.0 mM AVB in PG. These microscopy images were captured from the illuminated area after complete solvent evaporation at 690 min.

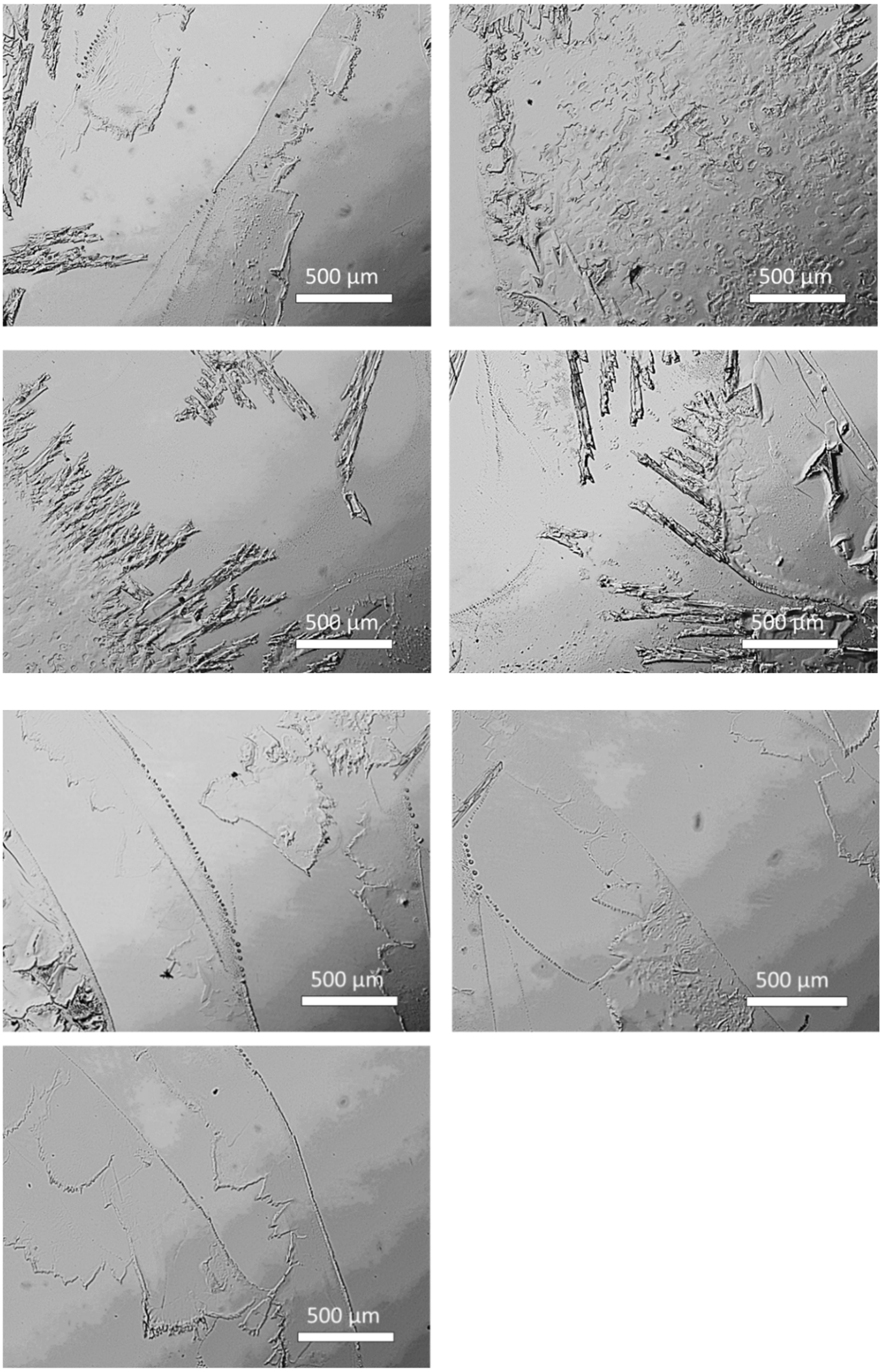

A comparison between the measured and the calculated absorbance spectra shown in Figure 4.4 demonstrates that the model has captured the main features of the evaporative behaviour of AVB in PG solutions in terms of i) the initial increase in the absorbance with retention of the spectral peak shapes and ii) the longer time absorbance decrease and “flattening” of the peaks. However, it is important to note the difference in magnitude between measured and calculated absorbance spectra, especially when the fraction of the illuminated area is below unity. These variations indicate that neither of the assumptions made concerning the uniformity of i) the average film thickness of the illuminated area and of ii) the light illumination of the spectrophotometer, are fully valid. Nevertheless, any further effort to improve the quantitative accuracy with the introduction of further techniques can be at the expense of the simplification of the model. Based on these findings, both measured and calculated absorbance data will be used for the determination of the measured and the calculated *in vitro* SPF values respectively.

4.2.3 Evaporation of DHHB and MC in PG

Similar to the investigation of AVB in PG films, measurements with alternative solutes such as DHHB and MC were also made in PG. The concentrations of UV absorbers were conveniently selected with the intention of measuring the absorbance in the range of 1.5 – 2 and not exceeding the reliability of the UV/vis spectrophotometer. Figure 4.6 presents a comparison between solutions consisting of all UV absorbers of choice and with PG alone. These measurements include the film mass, the film area and the calculated average film thickness of the solutions. It can be seen that the selected method for the investigation of the evaporative behaviour of these thin films is reproducible irrespective of the solute of choice. As already confirmed in this chapter, however, it is the absence of a dewetting pattern in the illuminated area that significantly varies and it is limited for each individual run.

Figure 4.6. Evaporation data of thin films containing solutions of all UV absorbers in PG compared to PG alone. Mass loss (upper plot), total film area (middle plot) and average film thickness (lower plot).

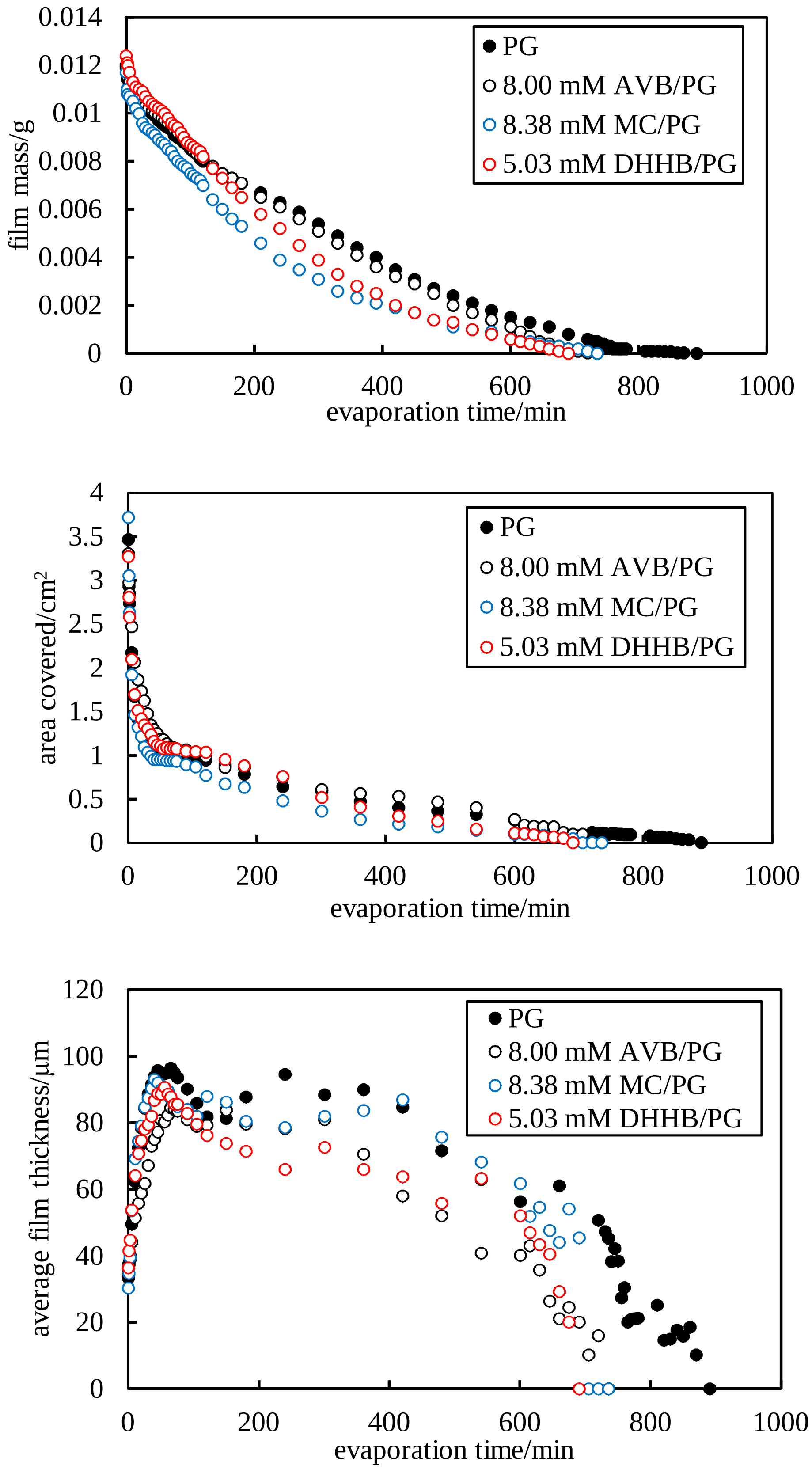

Since AVB and DHHB are solids, it is expected that during evaporation, both solutes will precipitate in the form of crystals. Our results confirm this type of behaviour for both AVB and DHHB which leads to variations in the absorbance measurements and hence in the determination of the *in vitro* SPF values. MC, however, is an involatile liquid, which is miscible with PG. For a deposited initial volume of 11.25 μl of 8.38 mM MC in PG, it is expected as solvent evaporation proceeds, MC will separate as a liquid phase. Hence, after complete evaporation, a small residue spot of liquid MC is present on the smooth quartz plate. Since there is no relevant pattern for the dewetting of the solution, the liquid residue can be observed anywhere confirming the loss in the absorbance, which is also depicted in the *in vitro* SPF values. Had it been the case, however, of the formation of a very thin liquid film of MC, the absorbance and hence the SPF would have been retained.

4.2.4 Absorbance measurements of MC and DHHB in PG during evaporation

Figures 4.7 and 4.8 show the measured and calculated data of DHHB and MC in PG during the evaporation process. The simplified model with the assumptions that already have been made, captures the shape of the maximum absorbance peak for both solutes (*i.e.* for DHHB, the maximum absorbance peak in PG is at 358 nm whereas the maximum absorbance peak of MC in PG is at 312 nm). As expected, however, the calculated spectra show significant variations in their intensity values compared to the measured spectra. In the case of AVB in PG, these variations in the calculated spectra were attributed to i) deviations between the calculated average film thickness and the actual film thickness of the illuminated area and ii) the non-uniformity of the beam of the spectrophotometer. The same explanations seem to apply for these solution films as well.

Figure 4.7. Upper plot: Measured absorbance measurements with evaporation time for 5.03 mM DHHB in PG for a period of up to 780 min. Middle plot: Fraction of illuminated area for the investigated period. Lower plot: Calculated spectra for a period of up to 480 min.

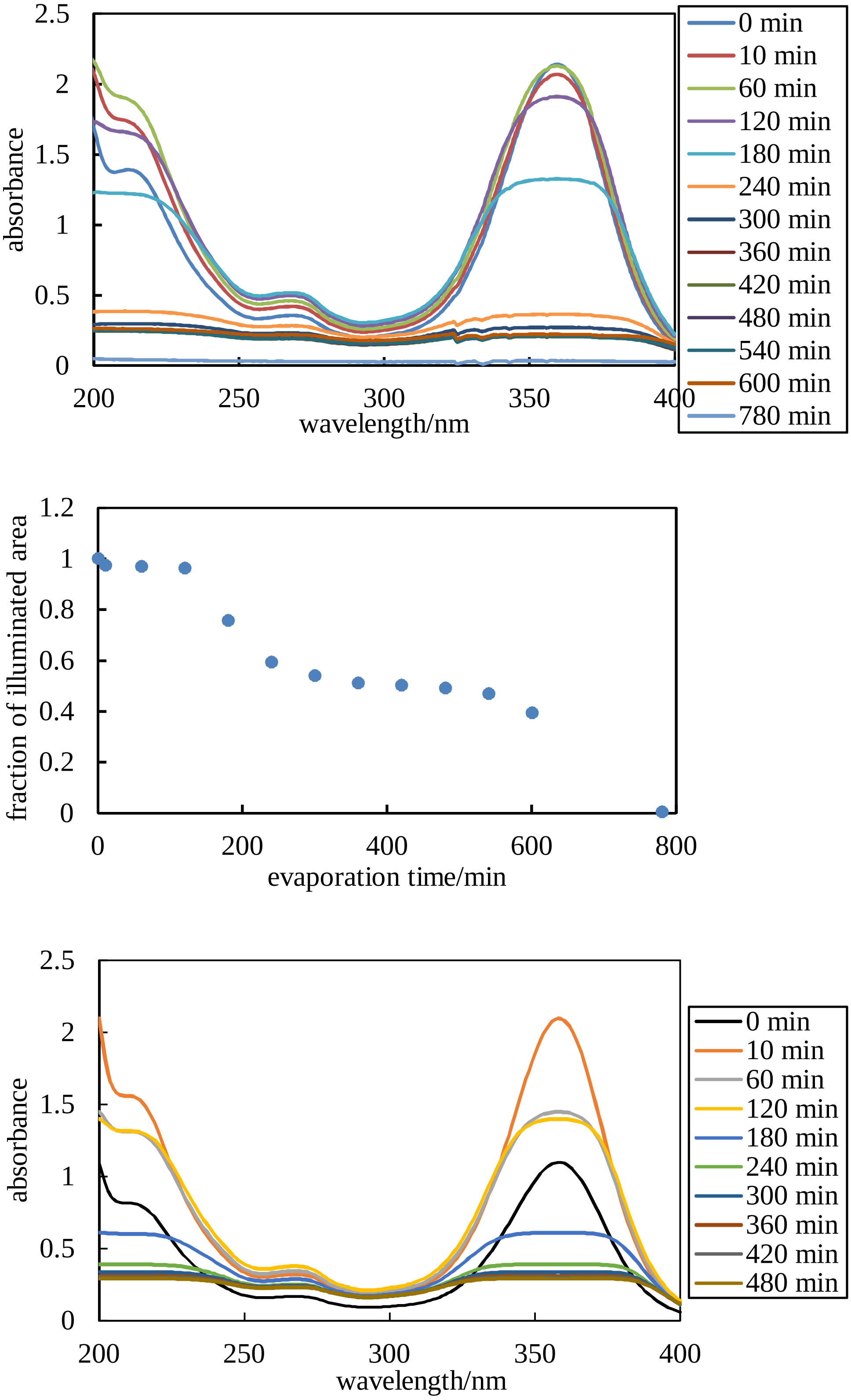

Figure 4.8. Upper plot: Measured absorbance measurements with evaporation time for 8.38 mM MC in PG for a period of up to 420 min. Middle plot: Fraction of illuminated area for the investigated period. Lower plot: Calculated spectra for a period of up to 420 min.

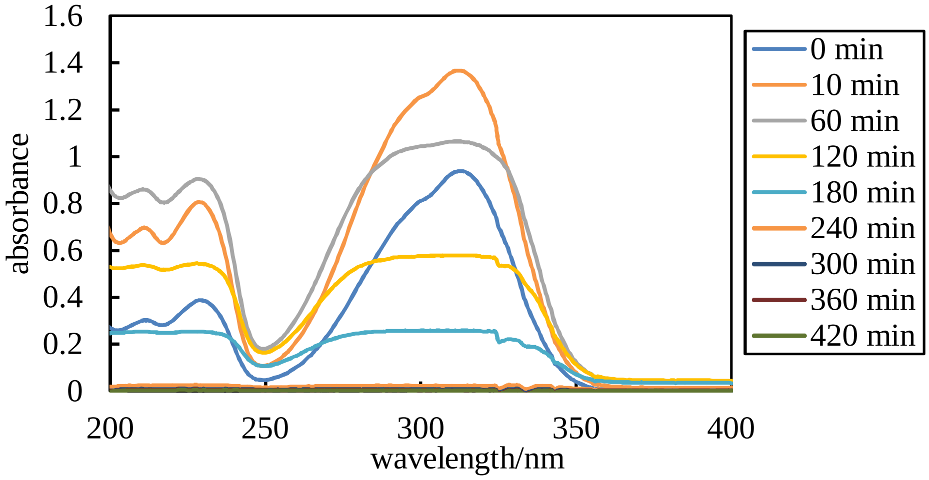

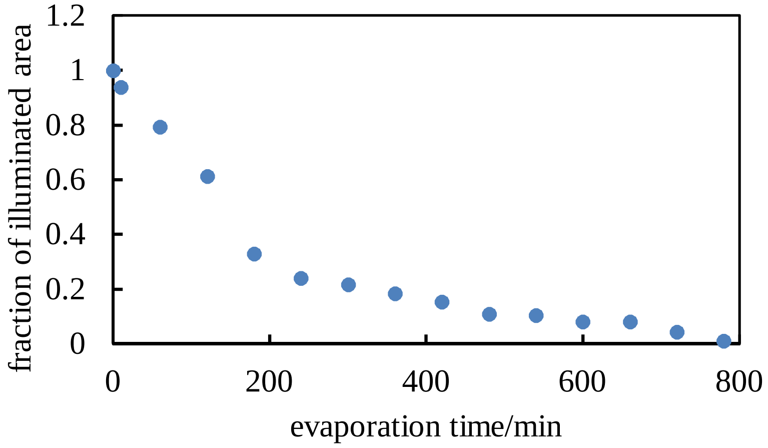

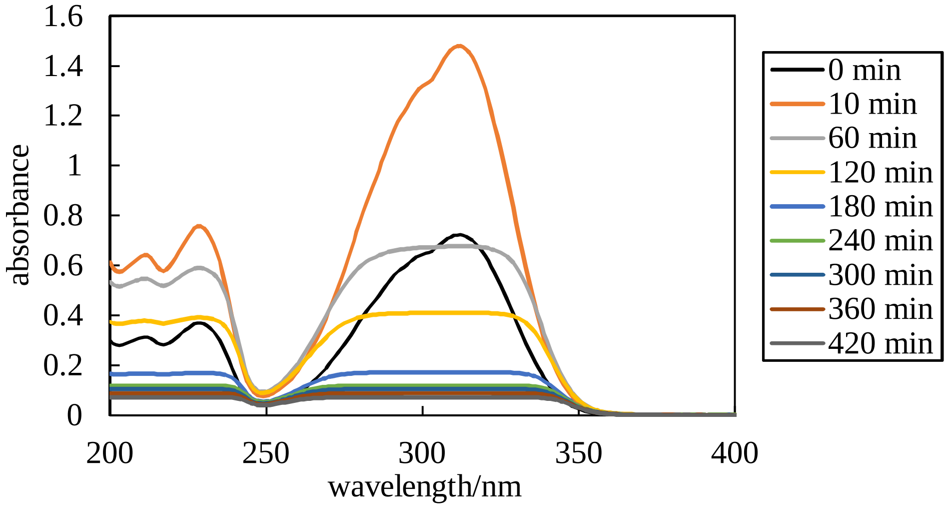

4.2.5 *In vitro* SPF determination of UV absorbers

To further assess the efficiency of the UV filters in terms of their absorbance during the ongoing solvent evaporation, the *in vitro* SPF approach is introduced. Figure 4.9 demonstrates a comparison between measured and calculated time-dependent *in vitro* SPF values for all solution films. These values are derived from both measured and calculated absorbance data respectively using equation 1.2, where $E(\lambda)$ and $S(\lambda)$ are determined values of the erythema action spectrum (erythema inducing effectiveness) and of the spectral irradiance of terrestrial sunlight under defined conditions respectively.[8]

All graphs in Figure 4.9, demonstrate at shorter times a progressive increase in both measured and calculated *in vitro* SPF values. This behaviour is a result of a combined effect i) of an increase in the film thickness/path length of the illuminated area as dewetting occurs and ii) of the solvent evaporation, which leads to an increase in the solute concentration up to its solubility limit. Apparently, the peak in the *in vitro* SPF values corresponds to the maximum solute concentration, which is equal to the solubility limit of each of the UV absorbers in PG. At longer times, however, a decrease and “flattening” in both measured and calculated *in vitro* SPF values is observed. This can be attributed to both solute precipitation during the ongoing solvent evaporation and incomplete coverage over the illuminated area. This is the case for solid AVB and DHHB. For the liquid MC in particular, the decrease in the SPF value is due to the formation of a small liquid residue spot.

The difference, however, between the measured and the calculated *in vitro* SPF values for each solution film, is a result of the assumptions made for the simplification of the model. Despite the lack of quantitative accuracy, however, because of the non-uniformity of the average film thickness and the light illumination intensity of the spectrophotometer, the simplified model still successfully captures the shape and hence, the evaporative behaviour of the solution films containing different UV absorbers. We have also modelled the data collected from repeated measurements of the investigated solution films and we observed that the measured *in vitro* SPF values obeyed the same trend within the estimated errors.

Figure 4.9. Measured and calculated variation of the *in vitro* SPF (290 – 400 nm wavelength range) with evaporation time for films of different UV absorbers in PG spread on quartz. AVB (upper plot), DHHB (middle plot) and MC (lower plot).

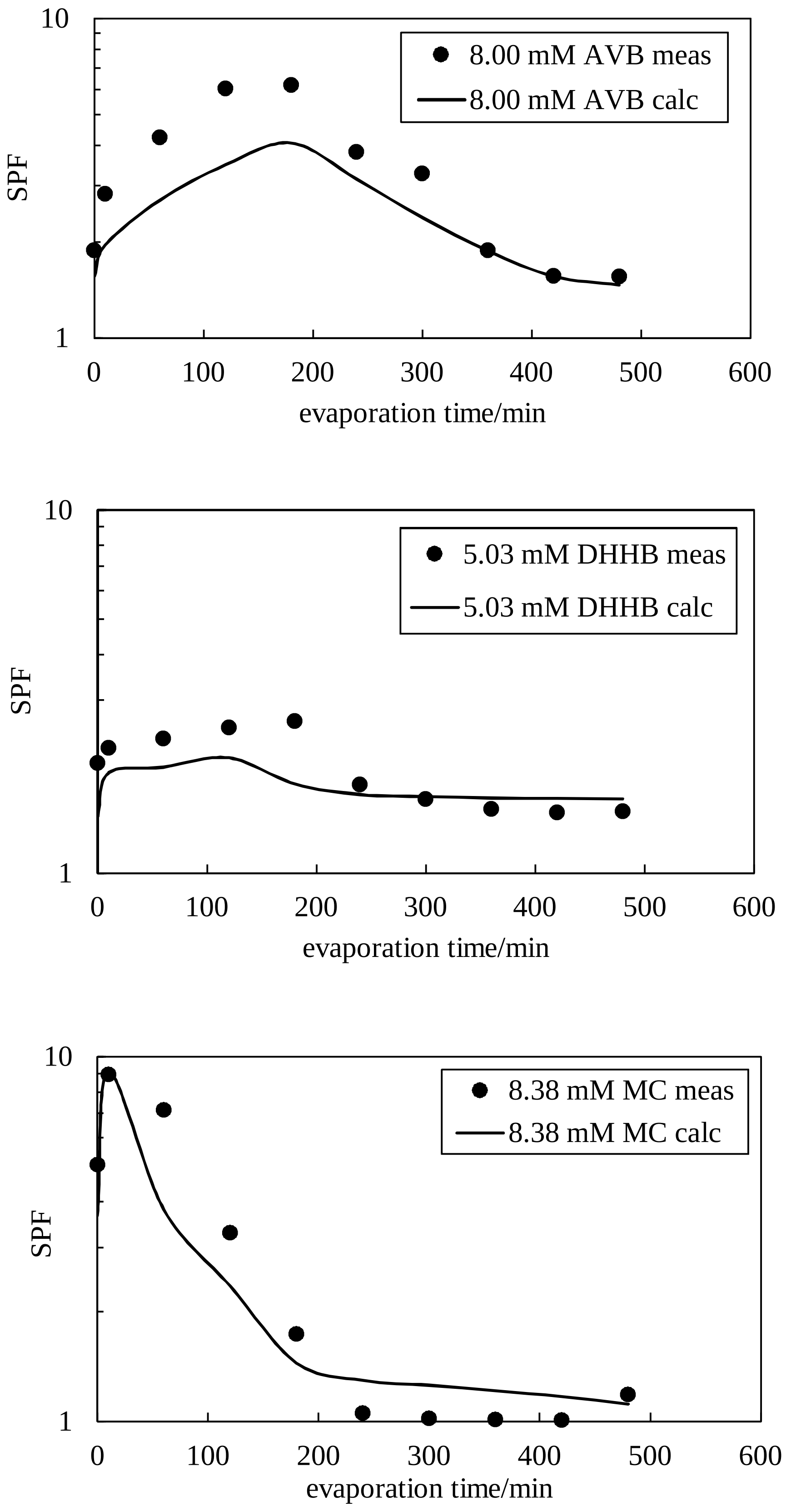

In the previous chapter, the initial *in vitro* SPF calculations were determined assuming a uniform film thickness of 20 μm, which is approximately equal to the standard application of 2.0 mg cm^{-2} of the *in vivo* process. Unfortunately, throughout our experimental procedure, the film deposition never reached the desirable thickness of 20 μm but varied instead for solution films between 30 – 40 μm. Despite this discrepancy, the *in vitro* SPF calculations are still indicative of the efficiency of these thin solution and emulsion films during solvent evaporation.

4.3 Comparison of solutions containing solvents with slow and fast evaporating rate

It can be seen that the *in vitro* SPF values of films of solutions containing one UV absorber in PG are monitored in detail for a period of up to 480 min. The main reason for this long time scale has to do with the solvent choice and the use of the low vapour pressure PG in particular. The evaporative behaviour of a UV absorber (AVB) in an alternative solvent with a higher vapour pressure compared to PG was also pursued. The aim of this experiment was to confirm that the loss of the absorbance and thus of the *in vitro* SPF follows a similar pattern irrespective of the evaporation rate of the solvent of choice.

For films of different liquids, which are monitored under the same conditions and have the same surface area A, the mass loss rate based on equation 4.2 is proportional to the factor MDP. The evaporative behaviour between two solvents with significantly different vapour pressures can be theoretically estimated. If it is assumed that these two solvents are PG and water, the diffusion coefficient D is estimated to be approximately 3 times larger for water than for PG.[1] Thus, it is expected that the theoretical evaporation behaviour of water ($M = 18.015$ g mol^{-1} and $P = 4746$ Pa at 32°C[1]) will be 66 times faster than that of PG ($M = 76.09$ g mol^{-1} and $P = 50.8$ Pa at 32°C[8]) for the same surface area.

Attempts to monitor experimentally the evaporative behaviour of a film of water were made, resulting in its complete evaporation within 10 min. Under the same conditions, an identical PG film was completely evaporated within 690 min. This implies that the water film is evaporating approximately 69 times faster than the PG film of similar surface area. Hence, both theoretical and experimental values are in reasonable agreement. The high evaporation rate of water, however, makes it practically unattractive as a solvent for our experimental procedure. Another limitation has to do with the fact that all UV absorbers are oil-soluble and thus, water-insoluble. Based on data presented[9], it is expected that the evaporative mass loss per unit surface area for an alternative solvent, such as *n*-decane should be approximately 7 times faster than PG. As such, the evaporation evolution of 8.0 mM AVB in *n*-decane was investigated and the film mass, total film area and the average film thickness are illustrated in Figure 4.10. Complete solvent evaporation occurred within 20 minutes, whereas the precipitation of AVB crystals was observed after approximately 13 minutes.

Because of the high evaporation rate of *n*-decane, it was still challenging to monitor the absorbance measurements during the experimental procedure, as it was described for films of solutions containing AVB in PG. Thus, the absorbance measurements at the two extremes (*i.e.* 0 and 20 min) were taken, which correspond to the initial and the complete evaporation of the solution as shown in Figure 4.11. These set of data confirmed the loss of the absorbance as a result of AVB precipitation. It is important to note that the film residue after 20 minutes of evaporation consisted of small particles of precipitated AVB, which formed some type of network in a circular formation. This pattern behaviour of AVB may be due to the presence of highly concentrated drops of AVB in *n*-decane.

Figure 4.10. Variation of film mass (upper plot), total film area (middle plot) and calculated average film thickness (lower plot) during evaporation of a film of 8.0 mM AVB in *n*-decane spread on quartz. The fraction of illuminated area covered by film was equal to 1 throughout the evaporation. The dashed lines indicate the point at which AVB precipitated.

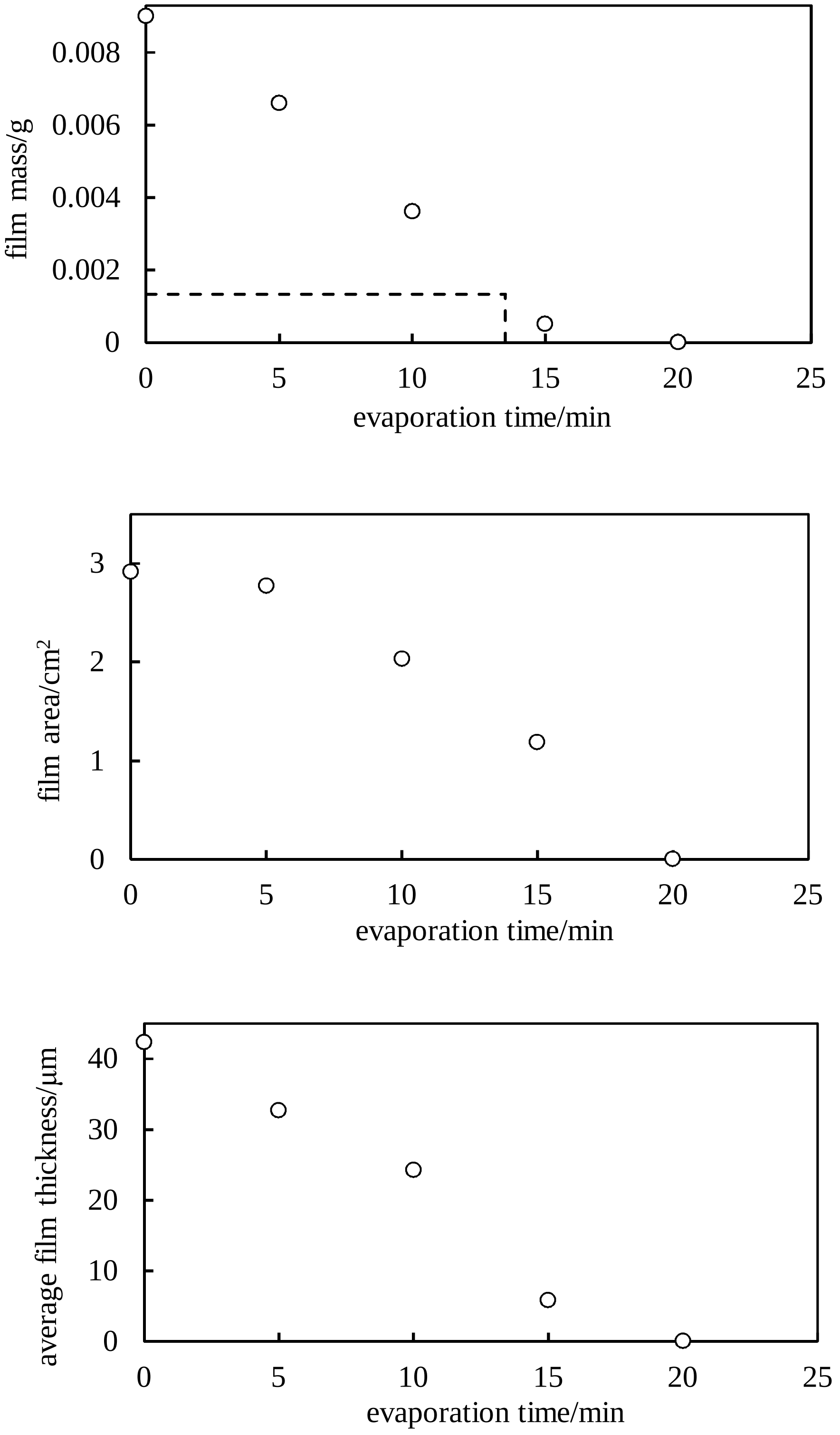

Figure 4.11. Film of solution of 8.0 mM AVB in *n*-decane deposited on top of a quartz plate as a function of evaporation time. Upper plot: Molar extinction coefficient values of AVB in *n*-decane *versus* wavelength. Middle plot: Measured absorbance spectra of film of 8.0 mM AVB in *n*-decane at the start and end of complete evaporation. Lower: Optical micrographs of the film residue within the illuminated area after complete evaporation at 20 min.

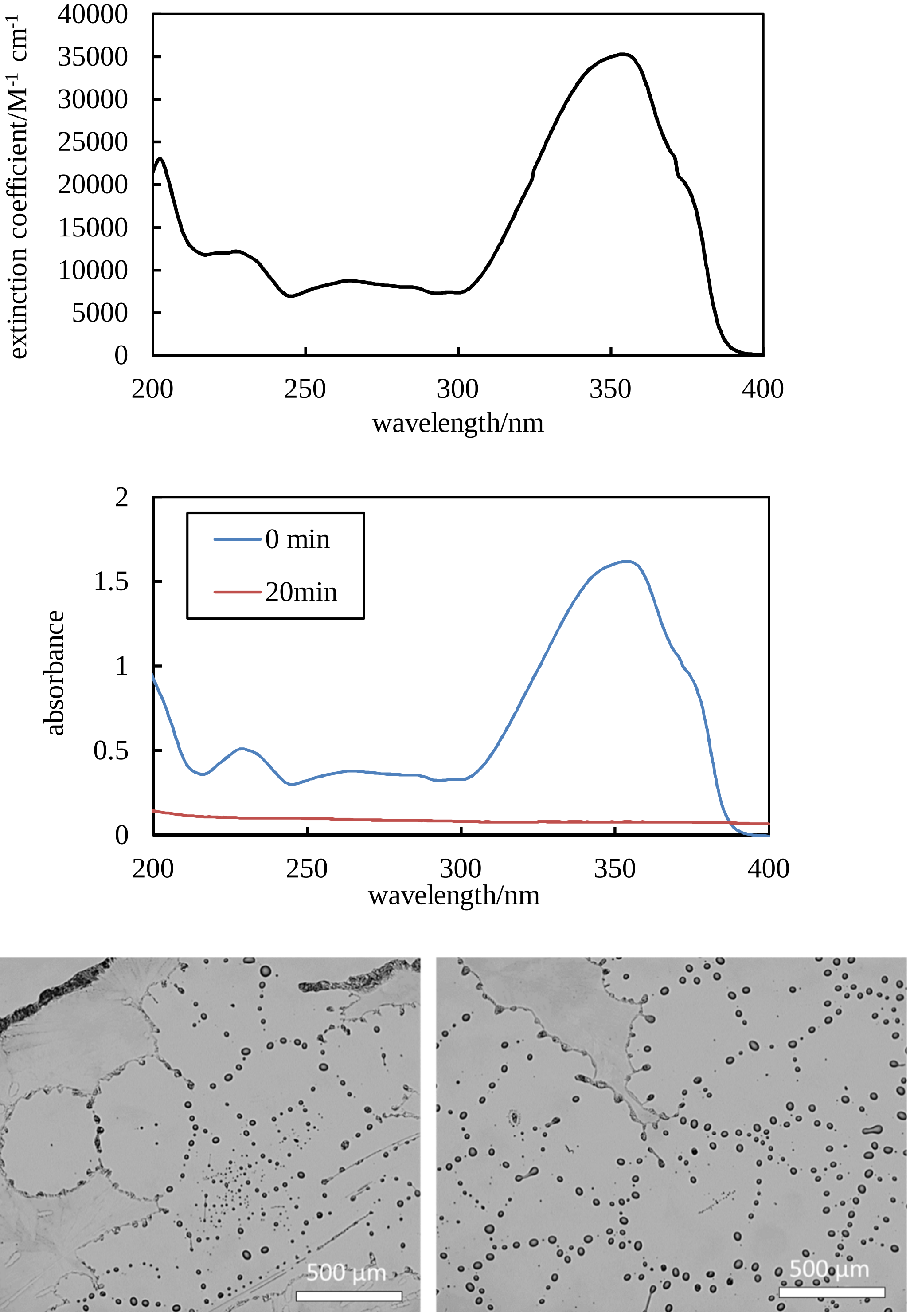

It is important to note that film dewetting on top of a smooth quartz plate is observed for all the investigated liquids despite their contact angles being close to zero. The measured contact angles at 32ºC are: PG: static, advanced = 11º, static, receded = 9º; *n*-decane: static, advanced = 0º, static, receded = 0º and MC: static, advanced = 11º, static, receded = 9º. It is likely that capillary forces resulting from the tendency of the film liquid-air surface to resist localised curvatures higher than the surface capillary length (equal to $(\gamma/\rho g)^{1/2}$ where γ is the liquid-air tension, ρ is the liquid density and g is acceleration due to gravity) also play a role. For the solvents of interest, the capillary lengths are much larger (of the order of a mm or so) than the film thickness and hence are likely to lead to non-uniform film thicknesses in addition to promoting dewetting.

4.4 Evaporation of nanoparticle dispersions containing UV absorber

As already discussed, our investigation was focused on the evaporation evolution of solutions containing UV absorber molecules only. However, current sunscreen formulations contain both molecular UV absorbers and inorganic, semiconductor oxides in the form of small particles. Hence, the next step was to examine how the addition of nanoparticles affects the evaporation behaviour of the film and its impact on the absorbance and thus on the *in vitro* SPF.

For this reason, the following different semiconductor particles were chosen; TiO_2, ZnO, CeO_2 and WO_3 nanoparticles. In addition, two types of silica particles with different degree of hydrophobicity were used; one hydrophilic, unmodified silica with 100% surface SiOH groups and one hydrophobic, 35% surface SiOH groups and 65% modified with DCDMS. Throughout our investigation, the substrate of choice was a smooth quartz plate.

4.4.1 Evaporation of 1.0 wt.% nanoparticle dispersions containing UV absorber

The evaporative behaviour of a solution of 8.0 mM AVB in PG was compared with dispersions of 8.0 mM AVB in PG containing 1.0 wt.% of the above nanoparticles. The upper plot of Figure 4.12 shows the normalised film dispersion mass remaining for each particle type as a function of evaporation time. It can be seen that solvent evaporation in all dispersion films occurred at a faster rate than that of the solution film alone. Since the evaporation rate is proportional to the surface area, it is expected that the high evaporation rate in the case of the dispersions is related to a larger surface area. This is also evident from the middle plot of Figure 4.12 where the film area of all dispersion films is significantly larger compared to the solution film and it is kept constant almost throughout the investigated period. Thus, from Figures 4.12 it can be concluded that the presence of the nanoparticles aids film pinning and suppresses dewetting. The calculated average film thickness as presented in the lower plot of Figure 4.12 does not show fluctuations in its values as monitored in solution films, but it progressively decreases instead.

For our smooth quartz plate of choice, as evaporation proceeds, the deposited solution film is progressively receding due to the absence of pinning at the three-phase contact line.[10] In the case of a particulate film, however, the particles aid pinning maintaining a constant contact area probably at the expense of a smaller contact angle (*i.e.* film thinning).[11] It is believed that this contact line pinning is a result of an increase shear stress between the film and the substrate at the edge of the film, holding the latter at its original position.[10] It has been reported that this behaviour can be attributed to an outward capillary flow, which replenishes the evaporating liquid. In addition, via this mechanism, the flow pushes the particles to the edge of the wetted contact area aiding the pinning.[12]

Attempts to measure the specular absorbance of the dispersion films containing 1.0 wt.% particle loading were problematic since it exceeded the reliable range of the spectrophotometer.

Figure 4.12. Variation of film mass (upper plot), total area (middle plot) and average film thickness (lower plot) for films containing 1.0 wt.% of the selected particles plus 8.0 mM AVB in PG. All values normalised with respect to time zero. The horizontal dashed line shows the normalised film mass at which precipitation of AVB is expected.

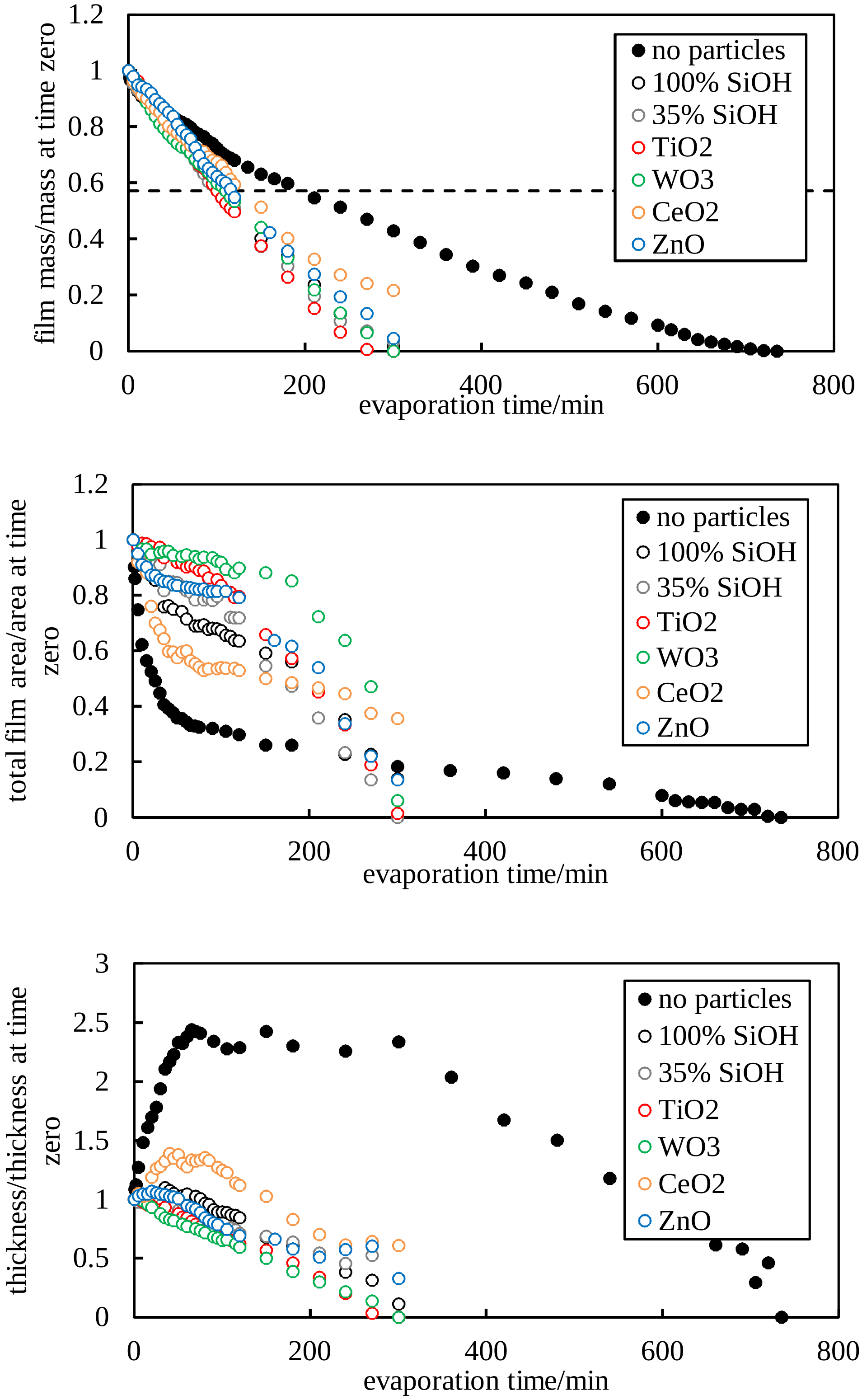

4.4.2 Evaporation of 0.1 wt.% nanoparticle dispersions containing UV absorber

The experimental procedure was repeated this time with the addition of 0.1 wt.% of the nanoparticles instead. The upper and middle plots of Figure 4.13 demonstrate the normalised values concerning film dispersion mass and film area respectively. It can be seen that for a dispersion film with low particle loading, the particles aid pinning as they are progressively deposited at the film base edge. Thus, dewetting is suppressed as evaporation proceeds. For the TiO_2 and hydrophilic (100% SiOH) silica particles, the film dewetting is suppressed from time $t = 0$ min, and the progressive film thinning is only observed. The remaining particles show intermediate behaviour. The lower plot of Figure 4.13 illustrates the calculated average film thickness, which linearly decreases as a function of evaporation time.

We have already investigated the reproducibility of the experimental procedure for solution films of AVB in PG without the presence of nanoparticles. We have confirmed that for repeated measurements (3 runs) the mass loss as a function of evaporation time is approximately the same within the errors (± 10%) but the total film area, due to the absence of pinning, dewets in a relative uncontrollable pattern on top of a smooth substrate such as the quartz plates used in this study. This implies that the illuminated area and as such the measured absorbance spectra are limited to each run. We have managed to tackle the problem of film's non-uniformity by introducing equation 4.4 to account for these variations. A comparison between measured and calculated absorbance spectra confirmed the validity of the model.

From the investigated dispersion films at this low particle loading (0.1 wt.%), we observe that also suppression of film dewetting due to particle deposition at the three phase contact line, occurs in a relative random pattern. It can be seen that this behaviour results in variations in both the mass loss and the total film area with respect to evaporation time as shown in Figure 4.13. The illuminated area, as part of the total film area, remains fully covered throughout the evaporation process for all dispersion films and as such its fraction is unity. Despite the latter being equal to 1, we observe variations in the measured absorbance spectra. This behaviour is illustrated in Figure 4.14 where the specular absorbance values at the major absorbance peak at 361 nm are shown for solutions of AVB in PG (3 runs) and all dispersions containing 0.1 wt.% of nanoparticles containing 8.0 mM AVB in PG.

Figure 4.13. Variation of film mass (upper plot), total area (middle plot) and average film thickness (lower plot) for films containing 8.0 mM AVB in PG with and without added nanoparticles. All values normalised with respect to time zero. The horizontal dashed line shows the normalised film mass at which precipitation of AVB is expected.

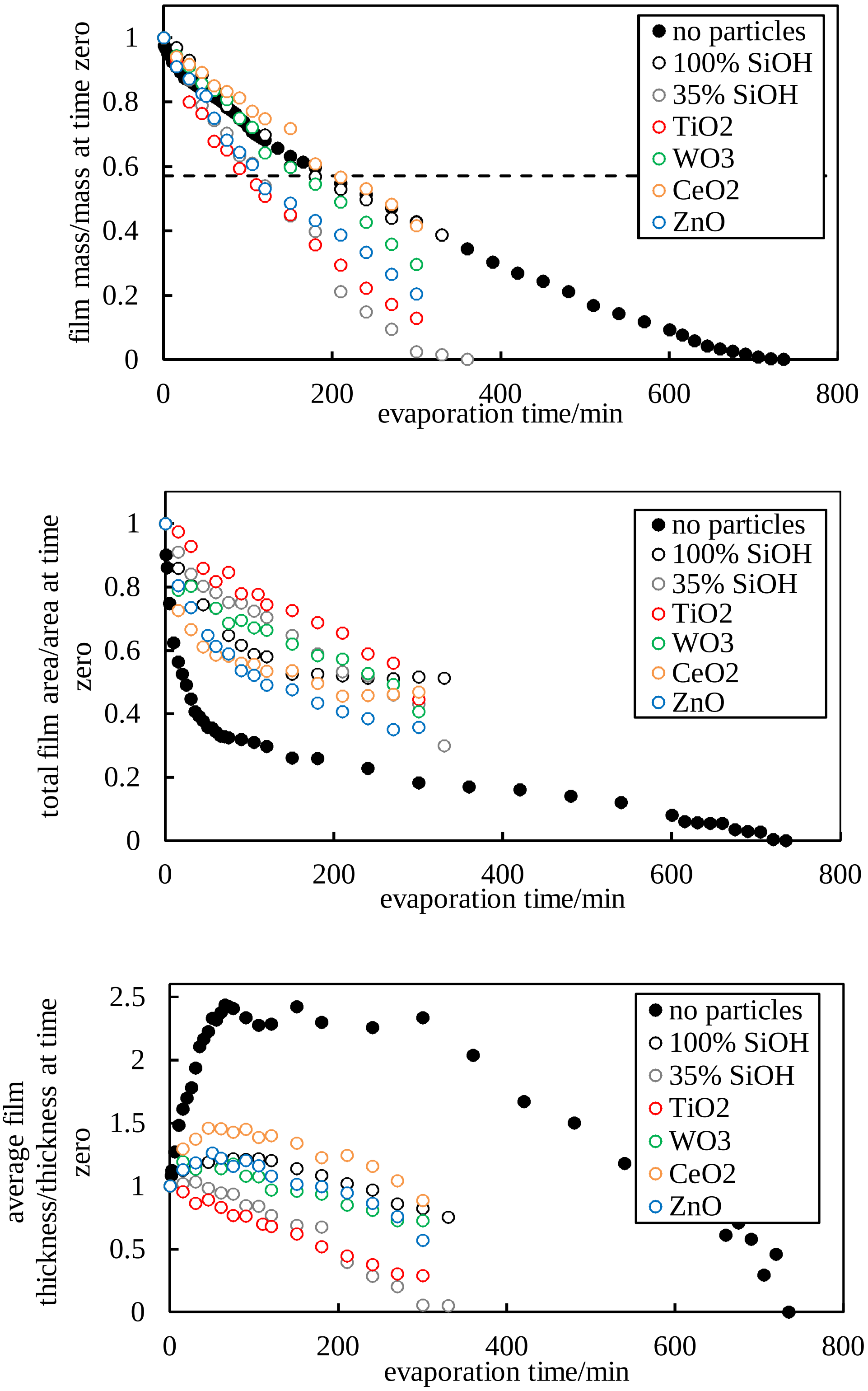

The variations in the measured absorbance values between runs with and without nanoparticles can be attributed to the following uncontrollable factors: i) fluctuations in the film thickness of the illuminated area as part of the total film area during evaporation and ii) to the presence of the nanoparticles. For the latter case, in particular, it is difficult to estimate the contribution of the semiconductor particles to the overall absorbance measurements since absorption, scattering and reflection by the nanoparticles, though minor because of the very low loading, cannot be excluded. Similar to our previously described approach concerning the investigation of solution films, in the following section of this chapter, we will use the simplified model based on equation 4.4 to elucidate the absorbance spectra on one of the dispersion films.

Figure 4.14. Absorbance at 361 nm with evaporation time for all dispersion films containing 0.1 wt.% of nanoparticles in PG.

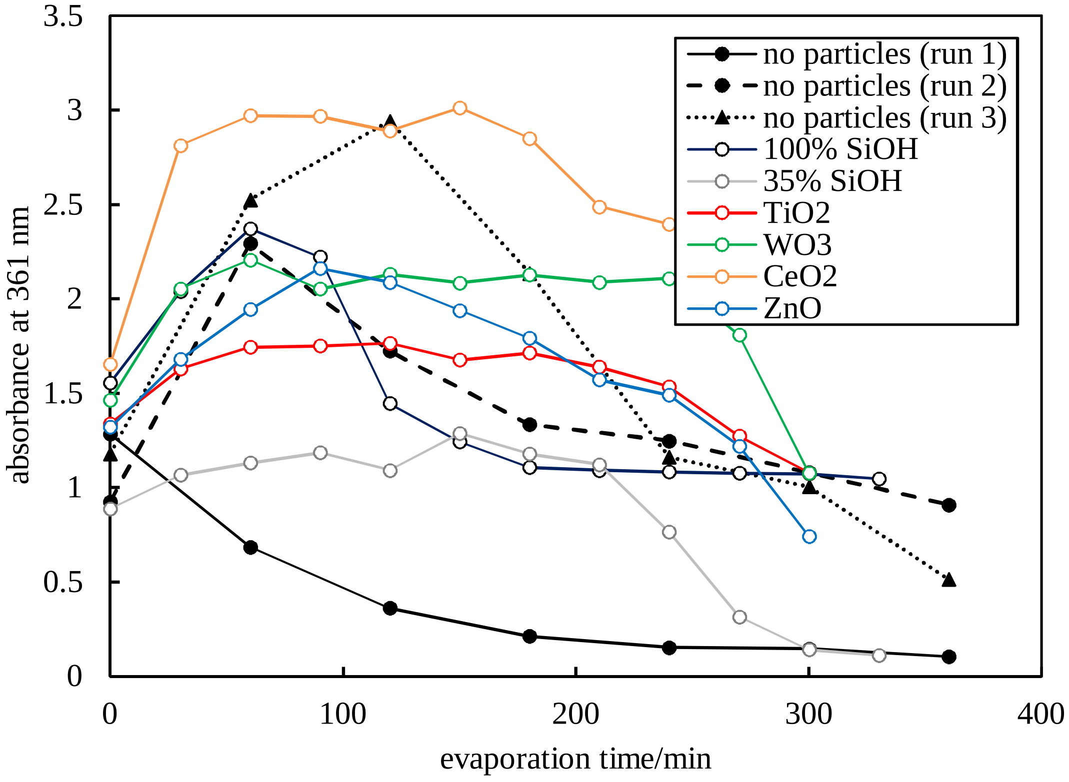

4.4.3 Absorbance measurements of 0.1 wt.% TiO_2 dispersion containing 8.0 mM AVB in PG

For convenience, the measured absorbance spectra of a dispersion containing 8.0 mM AVB plus 0.1 wt.% TiO_2 in PG is only presented below in the upper plot of Figure

4.15. As already described, during the investigated period, the film area is almost kept constant due to film pinning and thus the fraction of the illuminated area remains equal to unity as shown in the middle plot of Figure 4.15. As solvent evaporation occurs and hence the film is progressively thinning, an increase in the solute concentration is expected. It is this increase that it is depicted in the first few measured absorbance spectra, where relatively high values are observed. However, the increase in the absorbance measurements is less than that experienced in the AVB in PG solution only. This is due to the fact that the pinned film area is significantly larger than the illuminated area.

The precipitation of AVB is observed after approximately 100 min. Beyond that point, the absorbance is progressively decreased only in intensity and not in shape. This can be attributed to both the progressive film thinning and the precipitation of AVB since the fraction of the illuminated area is still unity. These data are consistent with our conclusion that the characteristic peak "flattening" can be observed only when the fraction of the illuminated area is below 1. Overall, the absorbance behaviour of the dispersion containing TiO_2 nanoparticles in AVB in PG is similar to that described for the AVB in PG solution but to a lesser extent due to film pinning. This is demonstrated in the lower plot of Figure 4.15, where the calculated absorbance spectra do not show any signs of peak "flattening" but only loss of the intensity due to solute precipitation.

Both measured and calculated absorption spectra of the dispersion film consisting of 8.0 mM AVB in PG plus 0.1 wt.% of TiO_2 are plotted in Figure 4.16 in order to determine the *in vitro* SPF values. Although the calculated spectra are only approximate due to the simplifications that have already been described, the measured and the calculated *in vitro* SPF values indicate some reasonable agreement. The values of the *in vitro* SPF can be attributed primarily to the AVB absorbance. A minor contribution in the overall absorbance due to TiO_2 particles is also present and cannot be excluded. However, it is the presence of the latter that caused the suppression of the film dewetting keeping the film area constant.

Figure 4.15. Upper plot: Measured absorbance spectra (*versus* air reference) of the film containing 8.0 mM AVB plus 0.1 wt.% TiO_2 particles in PG with evaporation time. The dashed line shows the spectrum (*versus* air reference) of a PG film of the same initial thickness containing 0.1 wt.% TiO_2 only. Middle plot: Fraction of the illuminated area. For this evaporating film, the illuminated area remains fully covered by the film during evaporation and precipitation of the AVB occurs after approximately 100 min of evaporation. Lower plot: Calculated absorbance spectra.

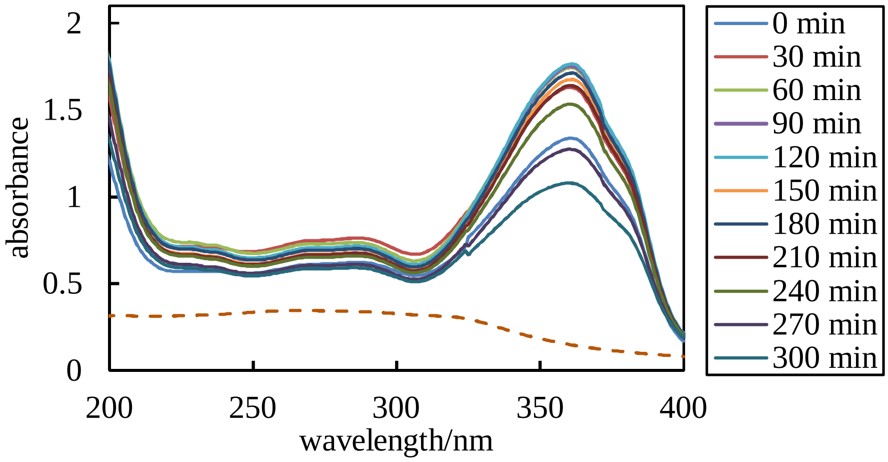

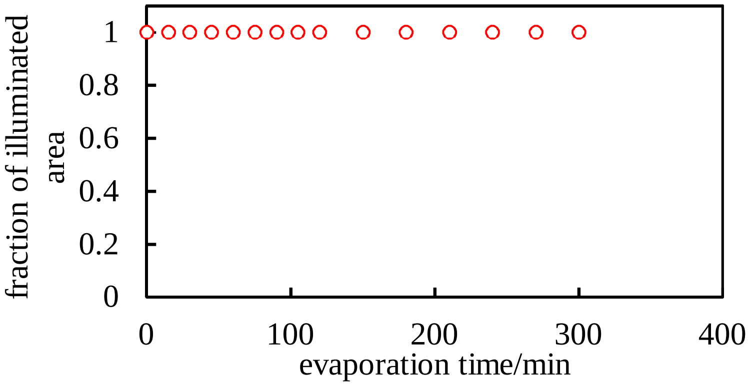

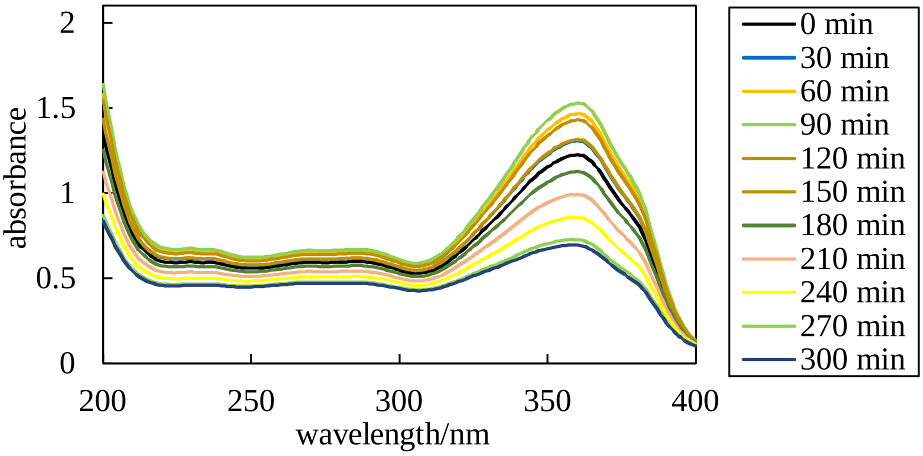

Figure 4.16. Comparison of *in vitro* SPF values derived from both measured and calculated absorbance data.

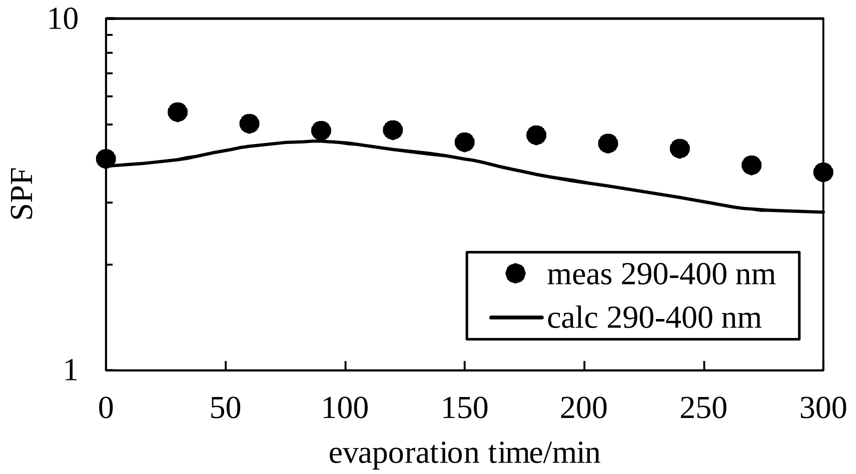

There is an extensive literature on the evaporation of liquid films containing particles[12-16] which discusses how the complex interplay of evaporation-induced liquid flow patterns, particle-particle, particle-substrate and particle-liquid surface interactions control the final pattern of particle deposition in the dried film residue which can include so-called "coffee ring", spot and uniform types of deposition. However, the main topic of interest remains that the presence of semiconductor particles suppresses the dewetting and any effects concerning their UV absorbance properties is not of prime relevance.

4.5 Evaporation of solutions containing UV absorber molecules in the presence of polymer

The evaporation of a solution containing 8.0 mM AVB in PG was also examined with the addition of 1.0 and 5.0 wt.% of poly-DADMAC, a water-soluble polymer. Merits of the choice of poly-DADMAC was its ease of application as well as the fact it does not contribute to the overall absorbance at the wavelength range of interest. The results obtained have indicated that the presence of the polymer is an alternative approach to suppress the dewetting. The upper and middle plots of Figure 4.17 illustrate the progressive mass loss due to solvent evaporation and the film area that was maintained constant for the investigated period respectively. In addition, the calculated average film thickness of the polymer solution decreases linearly as a function of evaporation time as shown in the lower plot of Figure 4.17. For these reasons, hence, the fraction of the illuminated area is expected to be equal to unity as previously investigated.

For the 1 wt.% of poly-DADMAC, the absorbance spectra, as illustrated in the upper and middle plots of Figure 4.18, show a slight increase for the first few minutes followed by a decrease in the absorbance values at longer times. Important to note, however, that the “flattening” of the peak as already described in all solutions containing UV absorbers in PG is not observed in this case. This again demonstrates that the presence of the polymer suppressed the film dewetting.

For the determination of the *in vitro* SPF values, the estimated time for the precipitation of AVB has been calculated based on the assumption that the minor amounts of water present and the polymer itself do not significantly affect the solubility of AVB. The comparison between the measured and the calculated *in vitro* SPF values, presented in the lower plot of Figure 4.18, are in reasonable agreement confirming the validity of the assumptions. As such, polymer addition suppresses the dewetting but does not stop or even delay the AVB precipitation since the loss of the absorbance and consequently that of SPF is monitored.

Figure 4.17. Variation of mass (upper plot), area (middle plot) and average film thickness (lower plot) for films containing 8.0 mM AVB in 100 wt.% PG (denoted as “no polymer”), 7.6 mM AVB in 1 wt.% poly-DADMAC, 4 wt.% water and 95 wt.% PG (denoted “1 wt%.”) and 6.0 mM AVB in 5 wt.% poly-DADMAC, 20 wt.% water and 75 wt.% PG (denoted as “5 wt.%”). The horizontal and vertical lines indicate the estimated points at which AVB will precipitate.

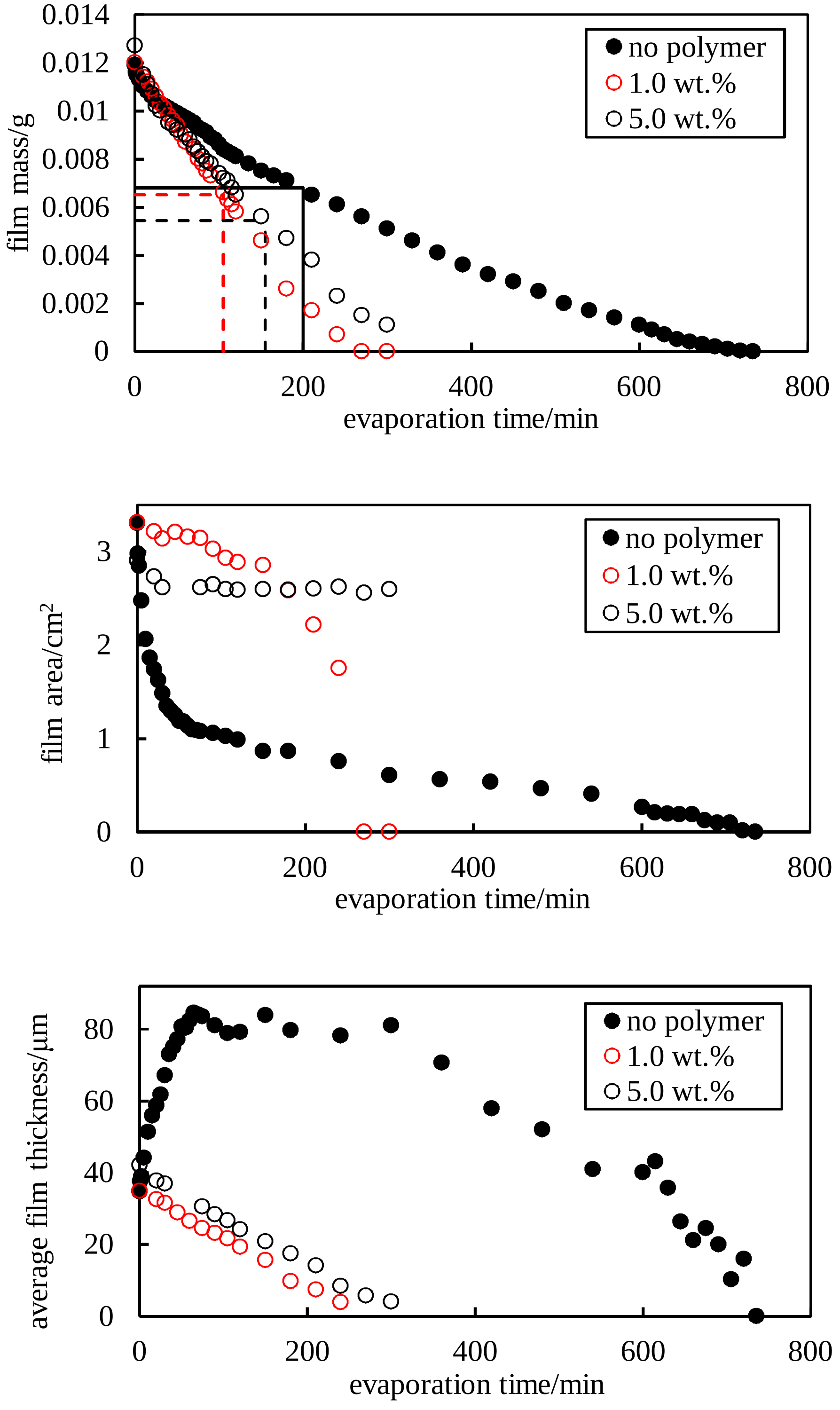

Figure 4.18. Upper plot: Measured absorbance spectra (*versus* air reference) of a film containing 7.6 mM AVB in 1 wt.% poly-DADMAC, 4 wt.% water and 95 wt.% PG. For this film, the fraction of the illuminated area $A_f = 1$ for 200 minutes before decreasing to zero by 300 minutes. The onset of AVB precipitation occurs at approximately 100 minutes. Middle plot: Calculated absorbance spectra. Lower plot: *in vitro* SPF values derived from both measured and calculated absorbance data.

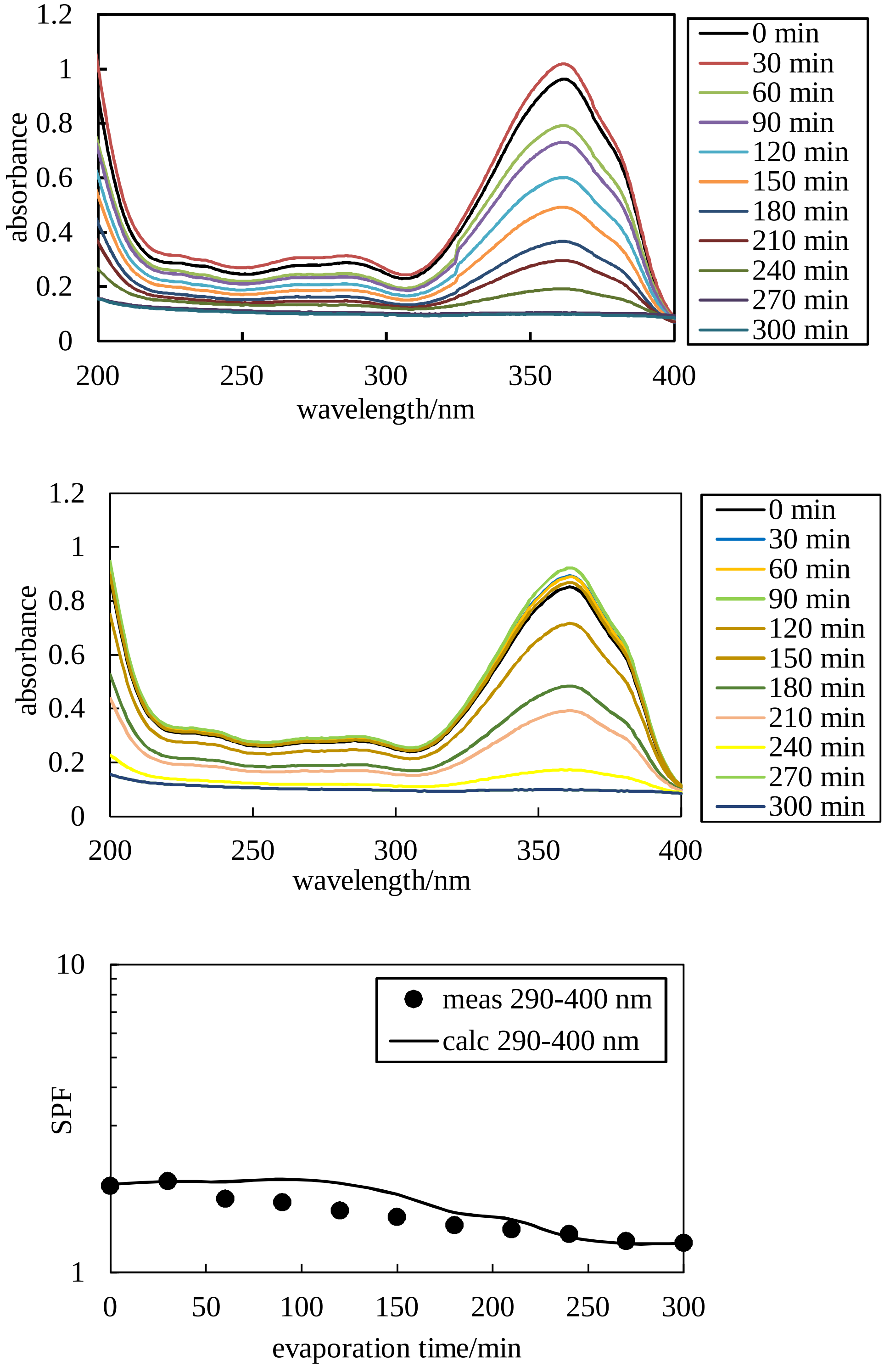

4.6 Evaporation of solutions containing UV absorbers on other substrates

Throughout our experimental procedure, the substrate of choice was a smooth quartz plate, which proved to be rather convenient particularly during the investigation and collection of the specular absorbance data. However, it is evident that the surface energy properties of the smooth quartz plate under no conditions resemble those of the contour and the composition of the human skin. In order to mimic as possible these properties, two alternative substrates were introduced i) Vitro Skin which is a synthetic polymer sheet and ii) a keratin-lipid film.

4.6.1 Vitro Skin as an alternative substrate

Similar to the experimental procedure concerning solution deposition on quartz plate, an initial volume equal to 11.25 μl of 8.0 mM AVB in PG was gently rubbed and spread on the rough side of the Vitro Skin surface. For convenience, Vitro Skin was selotaped by its edges on top of a quartz plate leaving an area of 4.2 cm^2 available for experimental measurements. The upper and middle plots of Figure 4.19 are representative of the film mass, film area and the calculated average film thickness of the evaporated 8.0 mM AVB in PG solution on Vitro Skin respectively. As the drying proceeds, the film area remains constant. This behaviour demonstrates that the rough Vitro Skin surface prevents dewetting at the film base edge. In addition, based on the calculated average film thickness, film thinning is expected until complete solvent evaporation at around 200 min.

Figure 4.20 shows the UV absorbance measurements for a solution of 8.0 mM AVB in PG on Vitro Skin during drying. It can be seen that the rough Vitro Skin film alone reduces light transmittance strongly due to light scattering or reflection. In particular, strong transmittance values are observed in the wavelength range below 290 nm, which corresponds to the UVC region of the electromagnetic spectrum. In addition, significant variations in the light transmittance values have been observed depending on the conditions of the polymer film, *i.e.* whether it is wet or dry. As such, both effects cause additional problems to the determination of the actual absorbance of the AVB in PG solution.

Figure 4.19. Variation of film mass (upper plot), film area (middle plot) and average film thickness (lower plot) for films of 8.0 mM AVB in PG spread by gentle finger "smearing" onto Vitro Skin. The dashed lines indicate the point at which the AVB precipitates.

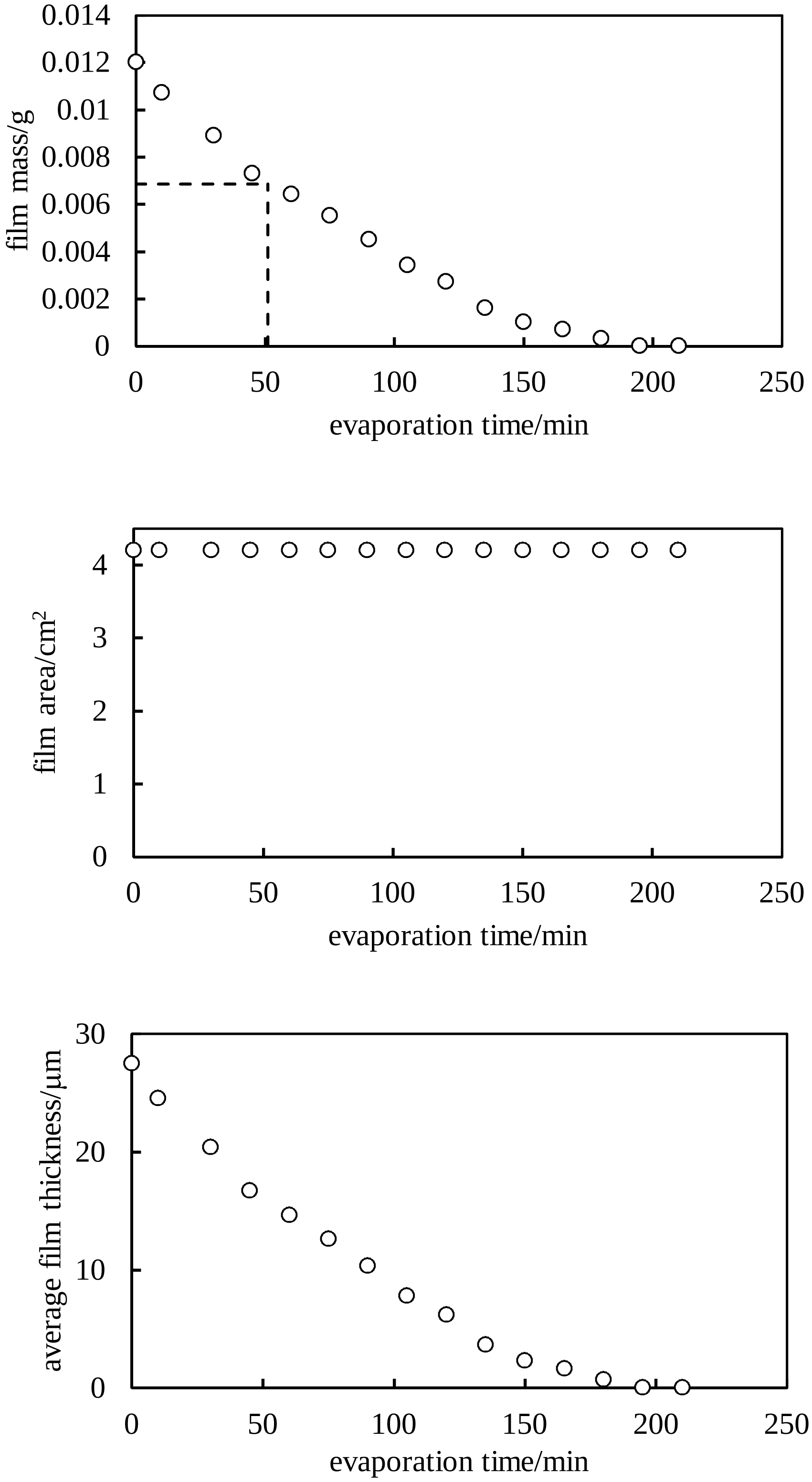

For this reason, the spectral changes shown in Figure 4.20 represent the period up to 120 min. For this investigated period, it is assumed that the Vitro Skin corresponds to that of the wet substrate. For the investigated period, the absorbance values of the latter remain approximately constant. It has been reported that the texture of the wet Vitro Skin resembles that of the human epidermis.[17] Since the wet Vitro Skin substrate is the choice of the reference, the actual spectrum of the film represented in the upper and middle plots of Figure 4.20 resulted from the subtraction of the film solution deposited on the wet Vitro Skin minus the wet Vitro Skin as a reference.

Thus, as shown in the upper plot of Figure 4.20, for the investigated period of up to approximately 45 min, it can be seen that there is a progressive decrease in the measured absorbance values during the ongoing solvent evaporation and the efficient suppression of the film dewetting. Beyond 60 min, however, the measured absorbance remains approximately constant. The absence of peak “flattening” implies that the fraction of the illuminated area remains unity. However, solute precipitation already occurred around 50 min as shown in the dashed line of the upper plot of Figure 4.19.

The calculated absorbance values for the same investigated period of up to 120 min confirm this type of evaporative behaviour of the solution on the rough Vitro Skin as presented in the lower plot of Figure 4.20. As such, for the first 60 min, the calculated absorbance is kept constant as i) film thinning and ii) increase of the solute concentration up to its solubility limit is expected. Beyond 60 min, the loss of the absorbance is due to solute precipitation of AVB in the form of crystals.

Further evidence of this type of behaviour is shown in Figure 4.21, where the measured and the calculated *in vitro* SPF values are plotted as a function of evaporation time. As already discussed, for the determination of the measured *in vitro* SPF values, the relevant absorbance data were derived from the measured solution film deposited on the wet Vitro Skin substrate minus the wet Vitro Skin substrate spectrum alone as a reference. Hence, for the investigated period of 120 min, it can be seen that both measured and calculated *in vitro* SPF values are in agreement showing a progressive decrease as a result of solute precipitation.

Figure 4.20. Upper plot: Measured absorbance spectra (*versus* air reference) of a solution film containing 8.0 mM AVB in PG deposited on Vitro Skin. The dashed and dotted lines show the separately measured spectra (*versus* air reference) of wet and dry Vitro Skin. For this film, the fraction of the illuminated area A_f = 1 and the onset of AVB precipitation occurs at 51 minutes. Lower plot: Calculated absorbance spectra.

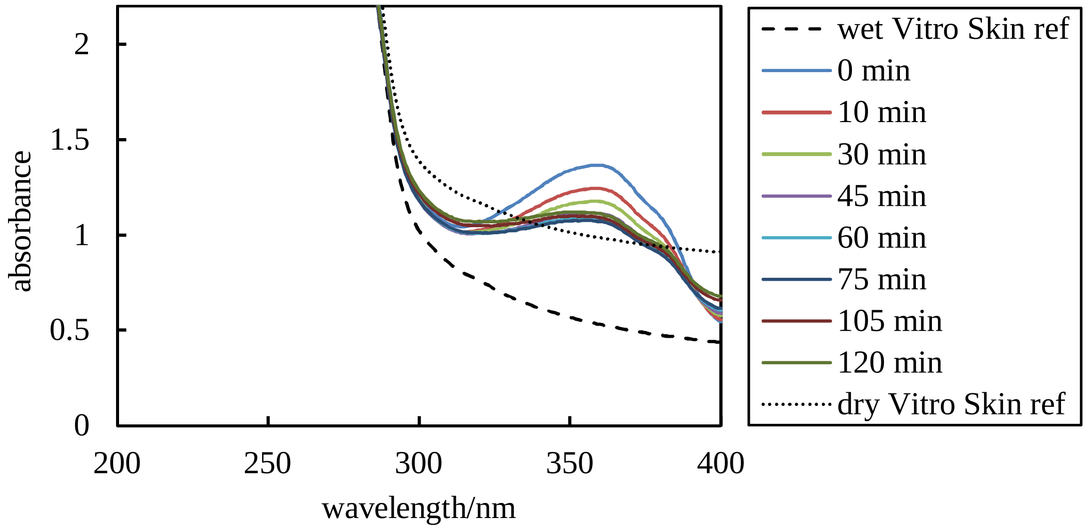

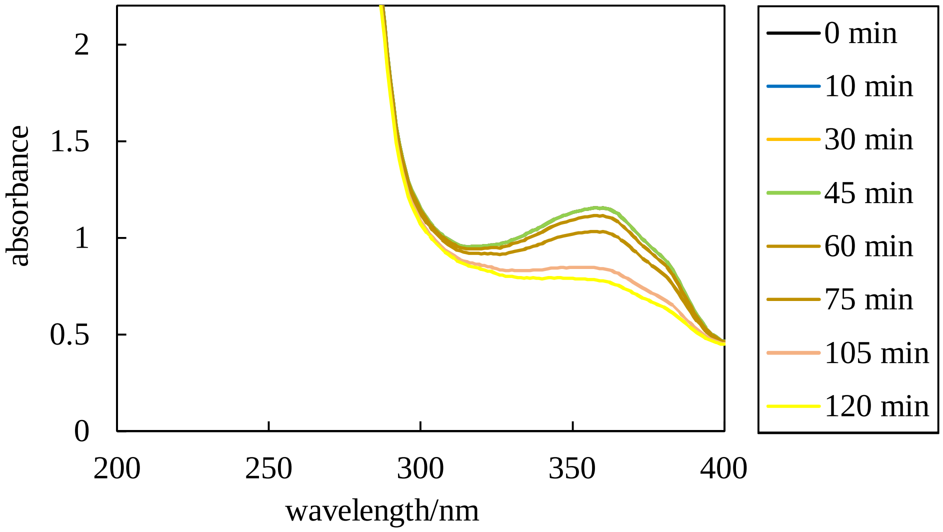

Figure 4.21. Comparison of *in vitro* SPF values derived from both measured and calculated absorbance data.

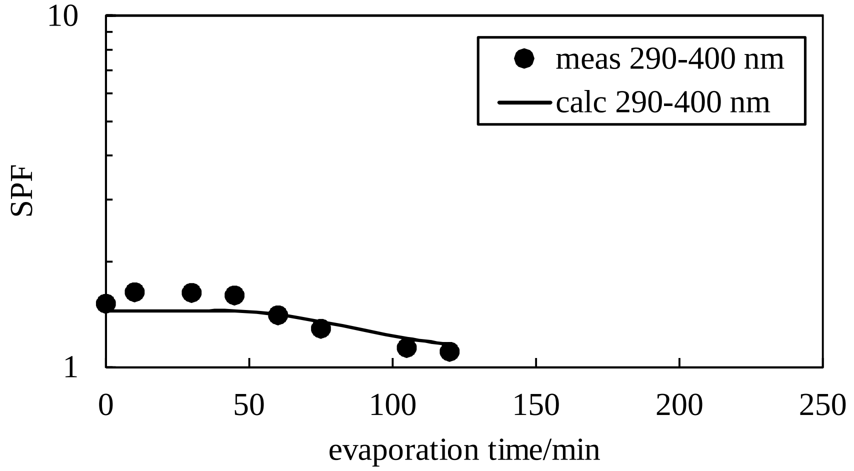

4.6.2 Keratin – lipid film as an alternative substrate

The keratin – lipid film was designed in order to approximately mimic the chemical composition of the outermost, stratum corneum layer of the skin.[18-21] It consists of 80 wt.% keratin particles mixed with 20 wt.% of three types of lipids (cholesterol, ceramide III and lignoceric acid). Its preparation and deposition on top of a smooth quartz plate is described in the experimental section. Upon deposition and drying, the substrate has a matt white appearance and strongly scatters and/or reflects light.

Drops of 8.0 mM AVB in PG with a total equal volume of 11.25 μl were placed on top of the keratin – lipid film. The progressive mass loss, film area, average film thickness and fraction of the illuminated area with evaporation time are presented in Figures 4.22 – 4.23 respectively. During the monitored evaporation time, an initial temporary increase in the film area is observed for the first 30 min with an expected decrease of the average film thickness. For the period, however, between 30 – 120 min, the film area remains approximately constant followed by a further decrease until complete solvent evaporation. The main reason for this type of behaviour is believed to be due to the porosity of the keratin – lipid substrate film, which allows part of the deposited AVB in PG solution to penetrate it initially. The average film thickness is also affected showing a high value at time t = 0 upon deposition, which progressively decreases until the whole keratin – lipid film is fully wetted by the solution. The solution is evaporated at 300 min.

Figure 4.22. Variation of film mass (upper plot), film area (middle plot) and average film thickness (lower plot) for films of 8.0 mM AVB in PG spread onto the keratin – lipid film supported on quartz plate. The dashed lines indicate the point at which the AVB precipitates.

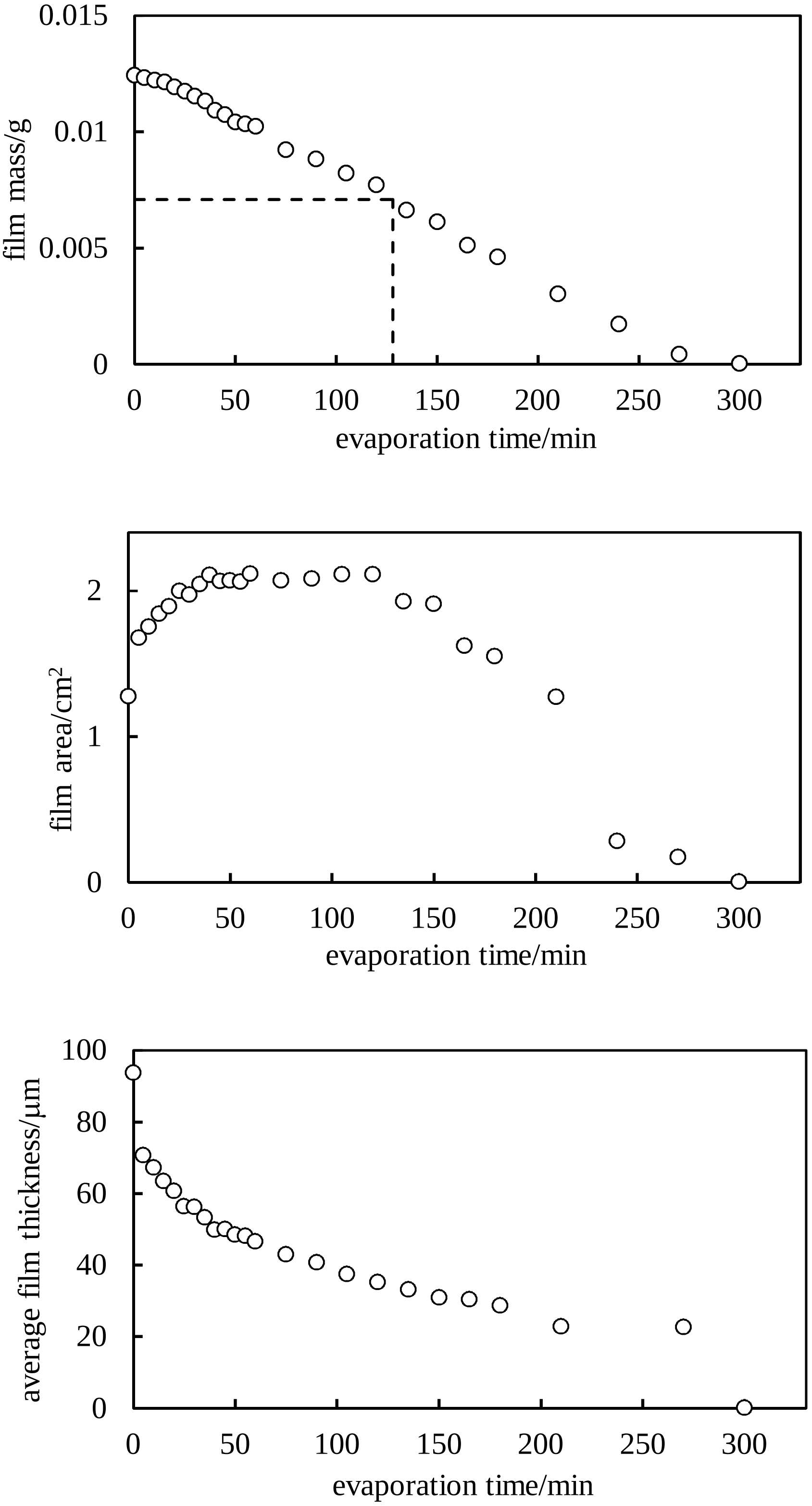

Figure 4.23. Fraction of illuminated area for films of 8.0 mM AVB in PG spread onto the keratin – lipid film supported on quartz plate

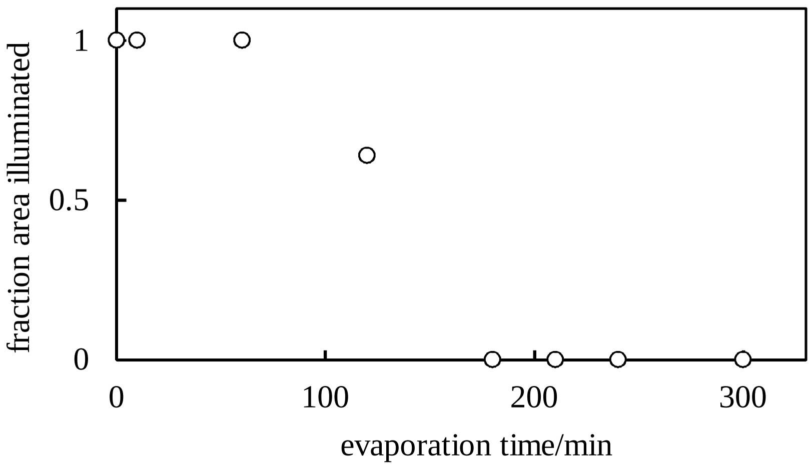

The measured and the calculated absorbance measurements of the deposited solution film on the keratin – lipid substrate is shown in Figure 4.24. The fraction of the illuminated area becomes less than unity after approximately 80 min and the AVB precipitation is expected to occur at 130 min. Thus, the absorbance due to AVB is decreasing at shorter times as a result of film thinning. After 100 – 120 min, the absorbance decreases rapidly and is practically lost. The reason has to do with the combined effect of i) AVB precipitation and ii) incomplete coverage of the illuminated area.

As previously described for Vitro Skin, the optical extinction of the keratin – lipid substrate alone is significantly high due to light scattering and reflection. With the addition of an AVB in PG solution film on the keratin-lipid substrate it can be seen that the absorbance value measured by the spectrophotometer exceeds its reliable range compromising the data interpretation. As a reminder, specular transmittance measurements are monitored by the UV/vis spectrophotometer. Thus, the measured (specular) absorbance values are likely to overestimate the true optical extinction of the film. Despite these problems, it is evident that a comparison between measured and calculated *in vitro* SPF values shown in Figure 4.25, are in good agreement providing a good estimate for the evaporative behaviour of an AVB in PG solution deposited on top of the keratin – lipid film. Again, the measured *in vitro* SPF values were derived from the absorbance values of the solution film plus substrate minus the substrate alone.

Figure 4.24. Upper plot: Measured absorbance spectra (*versus* air reference) of a solution film containing 8.00 mM AVB in PG on a keratin – lipid substrate. The dashed line shows the separately measured spectra (*versus* air reference) of the keratin – lipid substrate. The absorbance scale is limited to 3.3 as measured values greater than this are unreliable due to the detector sensitivity. For this film, the onset of AVB precipitation occurs at 121 minutes. Lower plot: Calculated absorbance spectra.

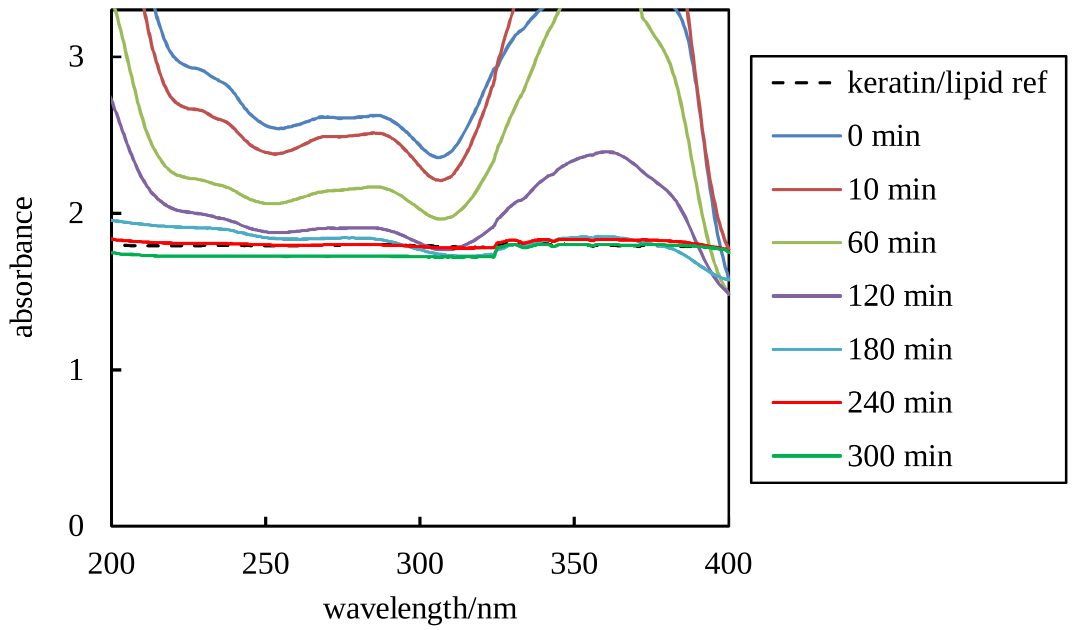

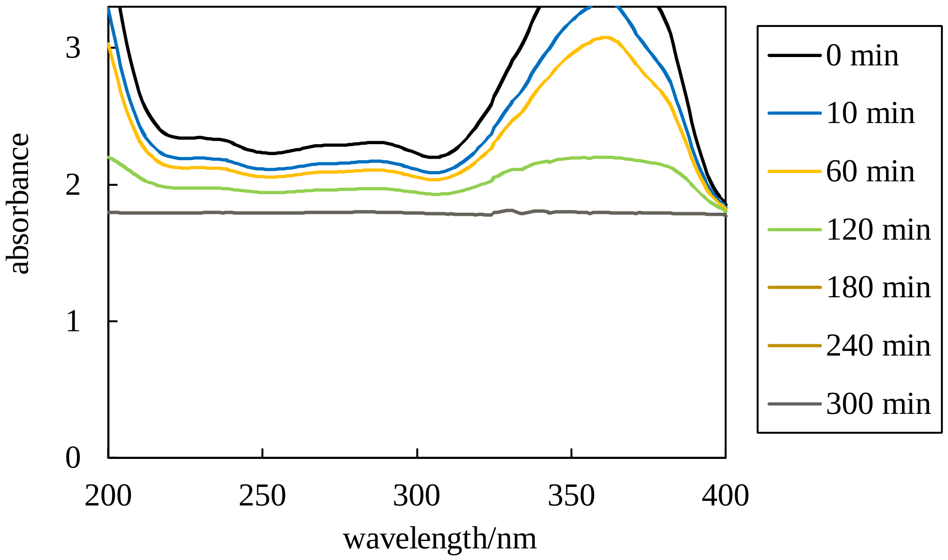

Figure 4.25. Comparison of *in vitro* SPF values derived from both measured and calculated absorbance data.

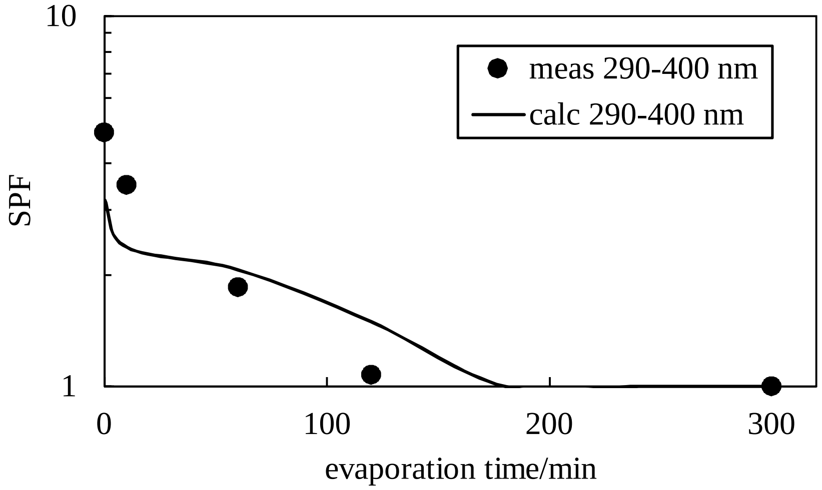

4.7 Conclusions

The evaporative behaviour of thin solution films consisting of UV absorber molecules such as AVB, DHHB and MC in PG was investigated. Results have shown that these thin solution films deposited on top of a smooth quartz plate progressively dewet as evaporation proceeds with an increase in their solute concentration until its solubility limit. The loss of the absorbance is a result of a combined effect of i) dewetting and ii) solute precipitation. A simple model in order to account for the variations in the *in vitro* SPF calculations has been introduced. This model aids to capture the *in vitro* SPF behaviour as a function of evaporation time.

An alternative solvent with a higher vapour pressure than PG, such as *n*-decane was also examined. The data confirmed that the evaporation pattern is similar for both fast and slow evaporating solvents and thus the loss of the absorbance can only be attributed to dewetting and solute precipitation.

A selection of nanoparticles was used to determine how their presence affect the evaporation behaviour of the dispersions containing a UV absorber (AVB) in PG. Results have indicated that the presence of nanoparticles, which are deposited on top of a smooth quartz plate, suppresses the dewetting by forming a contact line pinning at the base edge. Similar behaviour is observed with the addition of a polymer, such as poly-DADMAC. In both cases, the loss of the absorbance resulted from the solute precipitation as the drying proceeds.

Alternative substrates with the aim of closely resembling the human skin were also used, such as Vitro Skin and a keratin-lipid film. The data have shown that both substrates due to their rough surface can suppress dewetting of deposited solutions of AVB in PG. However, both do not inhibit solute precipitation, which is depicted progressively in the loss of the absorbance and eventually in the time dependent *in vitro* SPF values. It is important to note that despite the high optical extinction of both Vitro Skin and keratin – lipid films, the main features of the evaporative behaviour of solutions deposited on top of these alternative substrates are still captured.

4.8 References

1. K. J. Beverley, J. H. Clint and P. D. I. Fletcher, *Phys. Chem. Chem. Phys.*, 1999, **1**, 149–153.
2. J. George and N. V Sastry, *J. Chem. Eng. Data*, 2003, **48**, 1529–1539.
3. L. Ferrero, M. Pissavini and O. Doucet, *Photochem. Photobiol. Sci.*, 2010, **9**, 540–551.
4. B. Herzog and U. Osterwalder, *Pure Appl. Chem.*, 2015, **87**, 1–15.
5. J. J. O'Neill, *J. Pharm. Sci.*, 1984, **73**, 888-891.
6. S. L. Atkin, S. Barrier, Z. Cui, P. D. I. Fletcher, G. Mackenzie, V. Panel, V. Sol and X. Zhang, *J. Photochem. Photobiol. B.*, 2011, **102**, 209–217.
7. H. Hoppe and N. Sariciftci, *J. Mater. Res.*, 2004, **19**, 1924–1945.
8. B. L. Diffey and J. Robson, *J. Soc. Cosmet. Chem.*, 1989, **40**, 127–133.
9. D. R. Stull, *Ind. Eng. Chem.*, 1947, **39**, 517–540.
10. A. F. Routh, *Reports Prog. Phys.*, 2013, **76**, 1-30.
11. K. Sefiane, *Adv. Colloid Interface Sci.*, 2014, **206**, 372–381.
12. R. D. Deegan, O. Bakajin and T. F. Dupont, *Nature*, 1997, **389**, 827–829.
13. P. J. Yunker, T. Still, M. A. Lohr and A. G. Yodh, *Nature*, 2011, **476**, 308–311.
14. R. Bhardwaj, X. Fang, P. Somasundaran and D. Attinger, *Langmuir*, 2010, **26**, 7833–7842.
15. M. Anyfantakis and D. Baigl, *ChemPhysChem*, 2015, **16**, 2726–2734.
16. M. Anyfantakis, Z. Geng, M. Morel, S. Rudiuk and D. Baigl, *Langmuir*, 2015, **31**, 4113–4120.
17. A. Springsteen, R. Yurek, M. Frazier, and K. F. Carr, *Anal. Chim. Acta*, 1999, **380**, 155–164.
18. P. W. Wertz, *Adv. Drug Deliv. Rev.*, 1996, **18**, 283–294.
19. P. W. Wertz and B. Van Den Bergh, *Chem. Phys. Lipids*, 1998, **91**, 85–96.
20. K. C. Madison, *J. Invest. Dermatol.*, 2003, **121**, 231–241.
21. M. Boncheva, *Int. J. Cosmet. Sci.*, 2014, **36**, 505–515.

CHAPTER 5 EVAPORATION OF PARTICLE-STABILISED EMULSION FILMS

5.1 Introduction

In the previous chapter, we discussed the evaporation of films containing solutions of a UV absorber (either AVB, DHHB or MC). These thin films of a few μm thickness were deposited on a smooth quartz plate and they were left to evaporate in the open lab air. Our results have confirmed that as solvent evaporation proceeds, the films dewet. In addition, the solute concentration increases until its solubility limit is reached. Beyond that time scale, solute precipitation is observed. The effect the evaporation process has on the absorbance of these solution films was also pursued. It was shown that the progressive loss in the absorbance is attributed to both dewetting and solute precipitation. This behaviour was also depicted in time dependent *in vitro* SPF calculations.

Moving to more complex systems, in this chapter, we discuss the evaporation of thin films of particle-stabilised emulsions, which are also deposited on top of a smooth quartz plate. Their mass loss, film area, optical micrographs and film absorption spectra were monitored at timed intervals in the open lab air. These particle-stabilised emulsions were prepared from equal volumes of a polar phase such as PG and of the non-polar involatile SQ. Modified silica particles of different degrees of hydrophobicity (23% and 35% SiOH surface groups) were the choice of the emulsifier resulting in the preparation of PG-in-SQ and SQ-in-PG emulsions respectively.

Our investigation was particularly focused on particle-stabilised emulsions containing a dissolved UV absorber (either AVB or MC), which was initially introduced in the polar PG phase. Our findings have demonstrated that the loss in the overall specular absorbance is due to the loss of light scattering. The latter is directly related to the collapse of the emulsion structure upon complete evaporation of the PG phase. In particular, it was shown that for these emulsion films with a much larger droplet size than the wavelength of light, the light is scattered at a small forward angle and it does not contribute to the diffuse absorbance.

Throughout our experimental procedure, the UV absorber of choice (either AVB or MC) remained soluble. Unlike the investigated solutions, no peak absorbance "flattening" is observed for these emulsions. This implies that the illuminated area remains fully covered due to the absence of dewetting of the involatile SQ. Measured and calculated absorbance data are compared and their behaviour is depicted in the *in vitro* SPF values. As previously, the use of a simple model is introduced for the determination of the calculated absorbance data.

The last part of this chapter includes the evaporation evolution of particle-stabilised emulsions consisting of equal volumes of two evaporating solvents such as the polar PG and *n*-decane. For the investigated *n*-decane-in-PG emulsion film, it is expected that *n*-decane will rapidly evaporate followed by the slower PG. Results have confirmed the progressive film area shrinkage and the solute precipitation, both of which are the cause for the loss in the absorbance.

5.2 Evaporation evolution of AVB in solvents of different polarity

Prior to introducing our findings concerning the investigated emulsion films, a comparison of the evaporative behaviour of 8.0 mM AVB in both SQ and PG is presented. All measurements were made in the open lab air at a fixed temperature of 32°C, which corresponds to skin's surface temperature.

5.2.1 Evaporation evolution of AVB in SQ and PG

Figure 5.1 is a comprised of a set of three graphs and it is organised as follows. The upper plot of Figure 5.1 illustrates the measured film masses remaining deposited on top of a smooth quartz plate for both solution films. It can be seen that the deposited mass of the SQ solution film remains constant with evaporation time, confirming that SQ is practically involatile under the investigated conditions. The vertical dashed line corresponds to the predicted film mass m* at time t* for solute precipitation based on equation 4.1. The middle plot of Figure 5.1 illustrates the film area of the deposited solutions as a function of evaporation time. For the SQ solution film, its area remains initially constant for the first 30 min. For the investigated period between 30 to 240 min, a minor decrease in its film area is observed as a result of transient dewetting. Beyond 240 min, however, the film area remains constant throughout. As thoroughly discussed in Chapter 4, these findings regarding the SQ solution film are in contrast with the investigated PG solution film where a progressive mass loss and area shrinkage are observed as evaporation proceeds.

The lower plot of Figure 5.1 shows the calculated average film thickness of AVB in SQ and AVB in PG solution based on equation 4.3. For an involatile deposited mass and an approximately constant film area, it is expected that the calculated average film thickness of the SQ solution will reach a plateau value. This behaviour of the SQ solution film is again in contrast with the investigated PG solution film, where the latter shows significant variations as a result of dewetting and precipitation during the ongoing solvent evaporation.

The transient dewetting of the involatile SQ solution film will cause no change in the illuminated area. Thus, for our absorbance measurements, the fraction of the illuminated area will remain constant and equal to unity throughout. A comparison between the fraction of the illuminated area of SQ and PG solution films is shown in Figure 5.2.

Figure 5.1. Variation of film mass (upper plot), total film area (middle plot) and calculated average film thickness (lower plot) for films containing 8.0 mM AVB in PG (open circles) and in SQ (black circles). The horizontal dashed lines indicate the long-time behaviour of the SQ films (measured for a period of up to 1440 min). The vertical dashed line indicates the time at which AVB precipitates in the PG film.

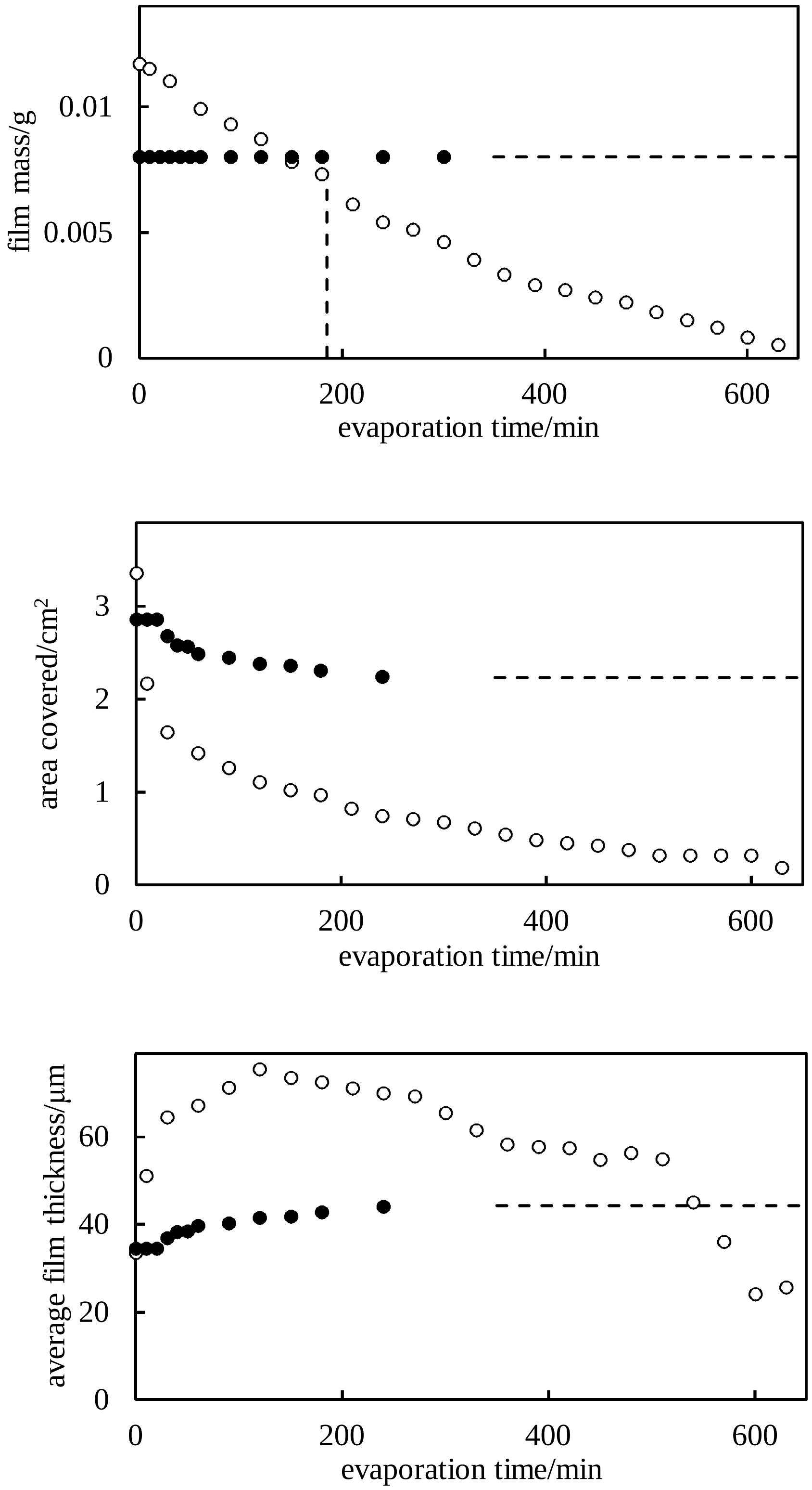

Figure 5.2. Fraction of illuminated area covered with evaporation time for films containing 8.0 mM AVB in PG (open circles) and in SQ (black circles). The horizontal dashed lines indicate the long-time behaviour of the SQ films (measured for a period of up to 1440 min).

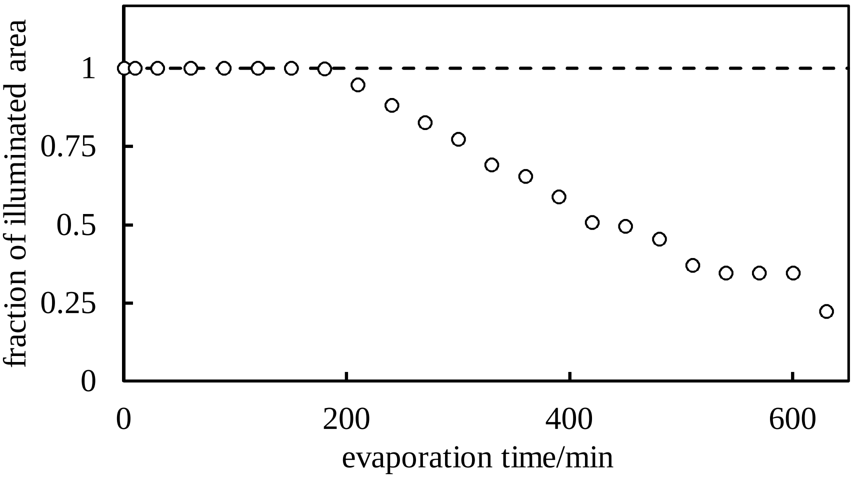

5.2.2 Absorbance measurements of AVB in SQ and PG

Figure 5.3 shows the peak absorbance values of SQ and PG solution films containing 8.0 mM AVB with evaporation time. As a reminder, the bathochromic shift of the peak absorbance of AVB in the UVA region from 354 nm (in SQ) to 361 nm (in PG) is solvent dependent.[1–4]

For the PG solution film in particular, it is confirmed that the initial transient increase in the peak absorbance value was due to a combined effect of dewetting and increase in solute concentration for the first 120 min during solvent evaporation. For this period, the fraction of the illuminated area is equal to unity. Beyond that time scale, a decrease in the peak absorbance values is attributed to both the incomplete coverage of the illuminated area and the solute precipitation since the solubility limit has been reached. In the case of the SQ solution film, however, the peak absorbance values do not show significant variations but they are retained instead, even for a period of 24 h. This behaviour is due to i) lack of dewetting and to ii) the involatility of SQ under the investigated conditions.

Figure 5.3. Variation of peak absorbance values (at 354 nm for SQ and 361 nm for PG *versus* air reference) with evaporation time for films containing 8.0 mM AVB in SQ and in PG. The absorbance values of the quartz plate plus PG or SQ film without AVB are both 0.033. The horizontal dashed line indicates the long-time behaviour of the SQ film (measured at 1440 min).

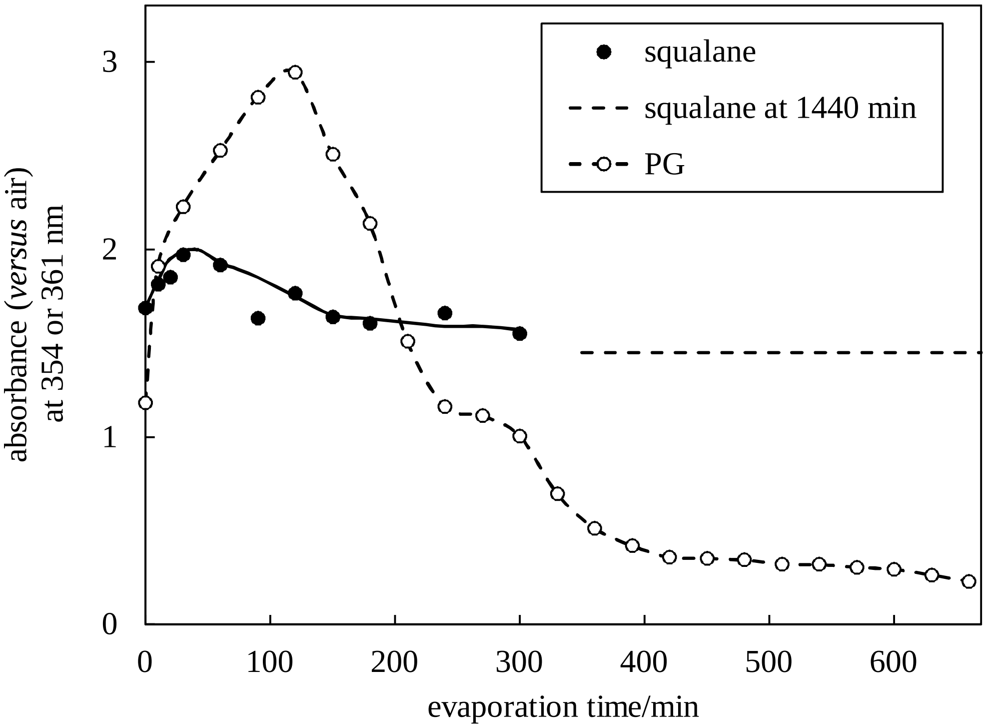

5.3 *Evaporation evolution of SQ-in-PG and PG-in-SQ emulsion films*

In the experimental section, the preparation of particle-stabilised emulsions consisting of equal volumes of PG and SQ was described. Small volumes of the emulsions, with an initial total mass approximately in the range of 13 – 20 mg, were deposited on top of a smooth quartz plate and they were carefully spread in order to achieve even distribution and to avoid droplet breakage.

The evaporation behaviour of both emulsion types was monitored at frequent timed intervals in terms of their mass loss, film area, optical micrographs and film absorbance measurements. A solute concentration of one UV absorber (AVB) equal to 8.0 mM was initially added in the PG phase alone. As such, after emulsification the overall concentration of AVB was equal to 4.0 mM. The same experimental procedure was repeated, with the addition of an alternative UV absorber (MC). 8.38 mM MC were also introduced initially in the PG phase and after emulsification, the overall concentration of MC in the emulsions was 4.19 mM.

Figure 5.4 shows the visual appearance of one of the investigated emulsion films, which corresponds to the SQ-in-PG emulsion with 4.0 mM AVB with respect to the overall emulsion volume. During the ongoing evaporation of the PG-continuous phase, it is observed that the total film area of the deposited emulsion remains unaltered, implying that no dewetting occurred. In addition, the initial grey opaque colour of the emulsion is progressively lost as a result of the evaporation of the PG-continuous phase, leaving behind a transparent dispersion film of SQ with AVB plus silica particles. Similar observations concerning their appearance, though not shown here, have been recorded for the SQ-in-PG emulsion containing MC as well as for the PG-in-SQ emulsions in the presence of both solutes. In addition, as previously described in Chapter 4, the superimposed red rectangular box corresponds to the illuminated area where the beam passes through for sample detection. With the aid of ImageJ software, this area has been determined to be equal to 0.32 cm^2.

It is expected that within the emulsion, the AVB will be distributed between the two phases (SQ and PG). The partition coefficient $P_{SQ/PG}$ is given by the ratio of the AVB solubilities in the two solvents and is presented by the following equation

$$P_{SQ/PG} = \frac{[AVB]_{SQ}}{[AVB]_{PG}} = \frac{S_{SQ}}{S_{PG}} \qquad (5.1)$$

where [AVB] and S are the equilibrium AVB concentration and solubility respectively in the phase indicated by the subscript.

Figure 5.4. Evaporation evolution of a SQ-in-PG emulsion film initially with 17.5 mg mass and containing 4.0 mM AVB in the total emulsion. Each time step image includes a ruler with a mm scale on the left hand side (for scale) and the quartz slide with the liquid film on the right hand side. The red rectangular box shows the illuminated area depicted in the absorbance measurements.

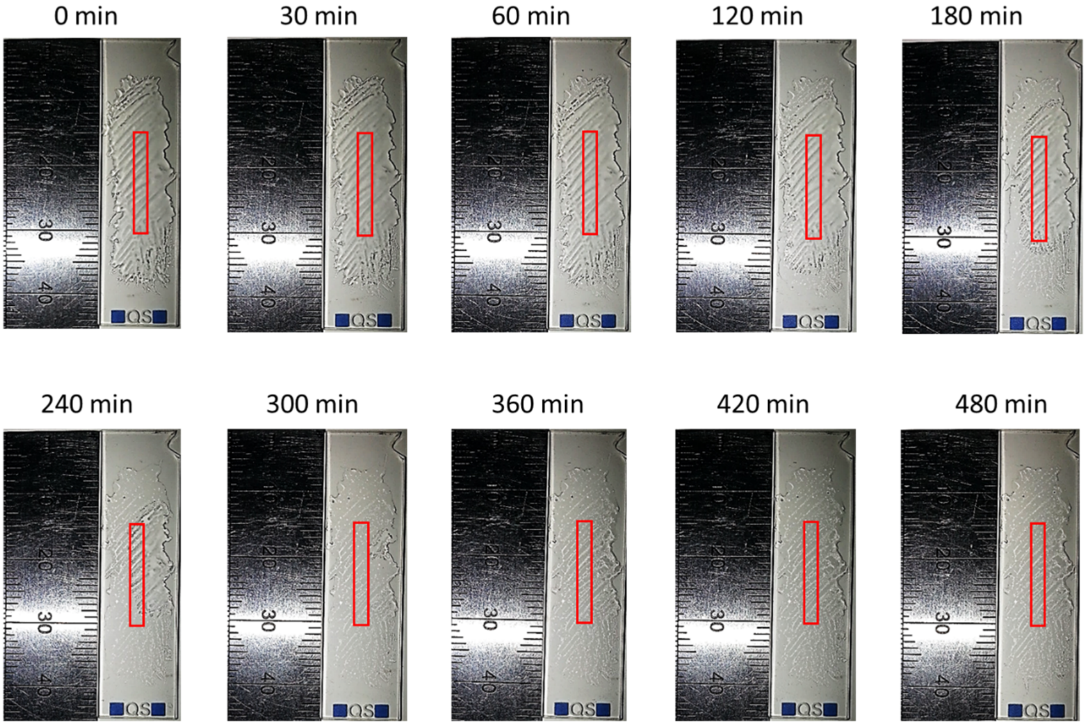

Based on the derived solubility values, AVB partitions in favour of the SQ phase with $P_{SQ/PG} = 38/14 = 2.7$. Using mass balance equation in combination with equation 5.1, the overall and individual phase concentrations of AVB can be determined accordingly

$$[AVB]_{ov} = \phi_{SQ}[AVB]_{SQ} + \phi_{PG}[AVB]_{PG} = \left(\phi_{SQ}P_{SQ/PG} + \phi_{PG}\right)[AVB]_{PG} \qquad (5.2)$$

where ϕ is the volume fraction of the phase indicated by the subscript. For the calculation of the individual [AVB] in equation 5.2, the volume fraction of the stabilising particles is not included, since this is < 0.01. It can be seen that since the volume fraction of PG, expressed as ϕ_{PG}, decreases during evaporation, the individual phase concentrations of AVB will also change with respect to time. These concentrations can be determined by the use of equation 5.2 assuming that the solute AVB can rapidly equilibrate relative to the evaporation. It is likely that AVB achieves its equilibrium distribution during the high shear emulsification process. For the emulsions of interest, the initial AVB concentrations in the two phases are calculated to be $[AVB]_{PG}$ = 2.16 mM and $[AVB]_{SQ}$ = 5.84 mM. Upon complete evaporation of the PG phase, it is expected that the maximum concentration of AVB present in the SQ phase will be equal to 8.0 mM. This concentration is below the solubility limit of AVB in SQ, which is equal to 38 mM. Since SQ is involatile, no solute precipitation is expected to occur.

Figure 5.5 contains the relevant data for the evaporation of both SQ-in-PG and PG-in-SQ emulsion films. As previously in the case of solution films, these set of data were derived from the analysis of the relevant digital photographs. The upper plot of Figure 5.5 shows the measured film masses of the emulsion films remaining deposited. Again, the film mass loss is due to PG evaporation alone. This behaviour will practically stop when the total emulsion mass is approximately halved due to solvent density differences. In our experiments, this is commonly observed at around 240 min. Beyond that time scale, the remaining deposited mass will correspond to a dispersion film of SQ with AVB plus silica particles, which will remain constant in terms of its total film area and its calculated average film thickness as shown in the middle and lower plot of Figures 5.5 respectively.

From the upper plot of Figure 5.5, it can also be seen that the evaporation rate for the PG-in-SQ film is slightly faster compared to that of SQ-in-PG film. A plausible explanation for this type of behaviour could be related to the larger area occupied by the PG-in-SQ film as opposed to that of the SQ-in-PG film, as shown in the middle plot of Figure 5.5. Thus, it can be inferred that the mass loss rate per unit area for both emulsion types is similar and does not significantly differ.

This is an interesting observation which requires further explanation. It is true that for emulsions consisting of two liquid phases, the equilibrium vapour pressures of both liquid phases (assuming complete mutual immiscibility) are identical to the equilibrium vapour pressures of the individual pure liquids. It has been discussed that the evaporation rate is proportional to the equilibrium vapour pressure assuming that the rate limiting step is the rate of diffusion of vapour molecules across a “stagnant” gaseous layer at the liquid surface. This behaviour is successfully described by equation 4.2.[5] As such, it is expected that both the dispersed and the continuous phase of an emulsion will evaporate at the same rate as the pure solvents under the same conditions.

For the continuous phase of an emulsion in particular, it has been reported that the presence of emulsifiers at the emulsion-vapour interface do not inhibit the evaporation.[5] Hence, the evaporation rate of the continuous phase is almost identical to that of the pure solvent.[5] For the dispersed (droplet) phase of the emulsion, however, two suggested mechanisms of oil transport are expected to occur. The first mechanism considers the oil droplet entry and/or spreading at the emulsion-vapour interface as the rate limiting step for evaporation. If entry does not occur, the second mechanism considers the droplet to remain separated from the vapour phase by the presence of a thin film of the continuous phase. The rate limiting step in the latter case is the droplet phase dissolution across the thin film of the continuous phase to the vapour phase. Under these conditions, the oil evaporation rate is dependent primarily on its solubility in the second liquid.[5]

This behaviour has been shown for surfactant-stabilised oil-in-water emulsions where the oil droplets have very low solubility in the water-continuous phase.[5] For a dispersed oil with high solubility in the continuous phase, mass transport to the emulsion-vapour surface is fast and the rate limiting step reverts to diffusion across the stagnant vapour layer. As such, the droplet phase which is relatively soluble in the continuous phase, evaporates with the same rate as the pure droplet liquid. For the emulsions of interest, it is observed that the PG phase, either as a dispersed or a continuous phase, is evaporating at approximately the same rate as that of pure PG. Although we have not measured the solubility of PG in squalane at 32^{o}C, we note that the solubility of PG in mineral oil at 20^{o}C is relatively high (0.31 $\underline{+}$ 0.06 wt.%).[6] Hence, if PG droplet entry does not occur, PG droplets are expected to evaporate at a rate similar to PG as continuous phase and pure PG, as observed here. The absence of any type of dewetting confirms that the illuminated area remains fully covered and thus its fraction is equal to 1 throughout.

Figure 5.5. Variation of film mass (upper plot), film area (middle plot) and average film thickness (lower plot) for particle-stabilised emulsion films initially containing equal volumes of SQ and PG and 4.0 mM AVB in the total emulsion (initially dissolved in the PG phase). PG-in-SQ emulsions were stabilised using 1 wt.% of 23% SiOH particles whereas SQ-in-PG emulsions were stabilised using 1 wt.% of 35% SiOH silica particles.

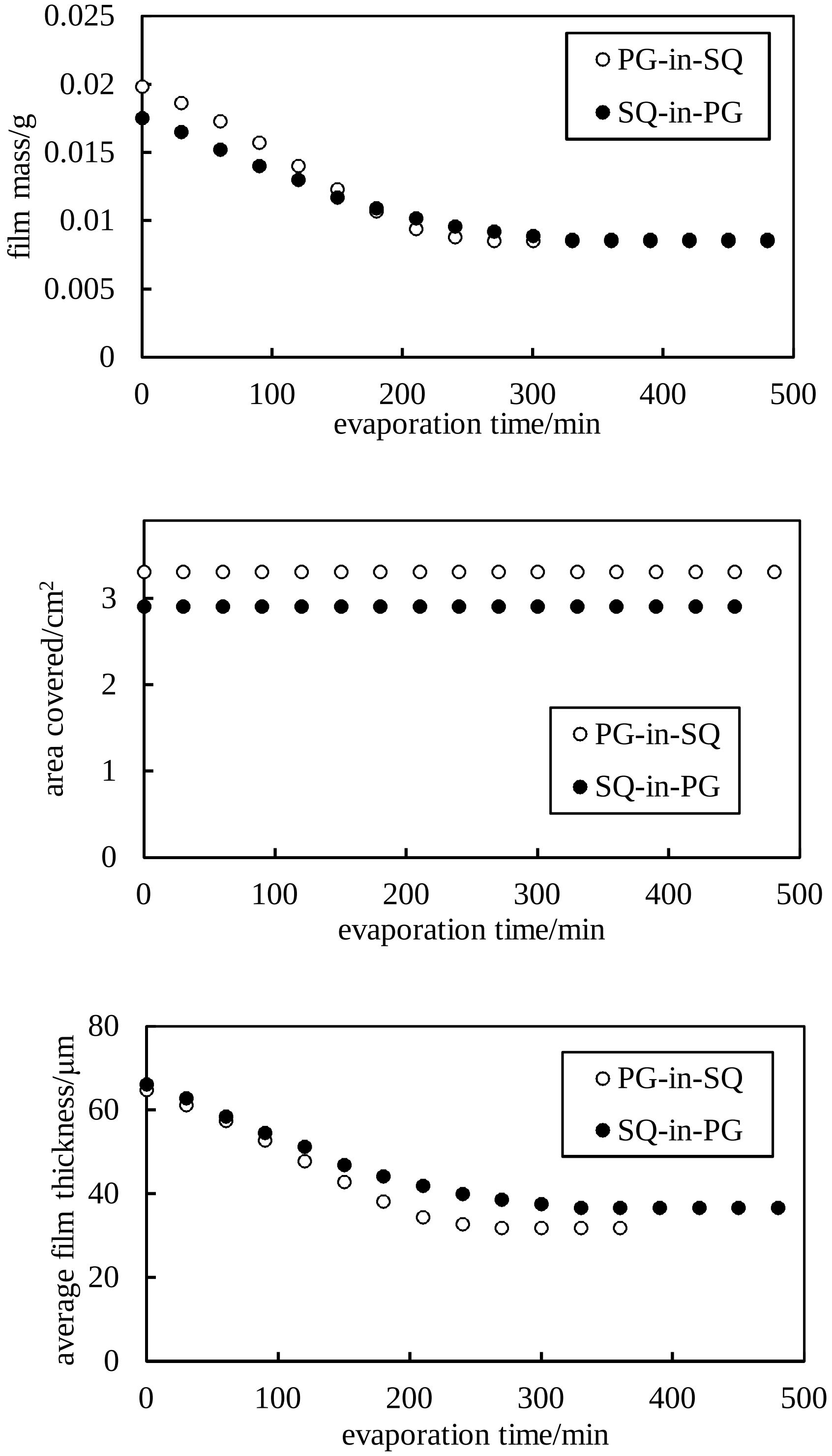

5.4 Optical microscopy measurements of SQ-in-PG and PG-in-SQ emulsion films

5.4.1 Optical microscopy measurements of PG-in-SQ emulsion film

The evaporation of thin emulsion films was repeated for both emulsion types and their behaviour was captured with the use of optical microscopy. Figure 5.6 shows the optical micrographs of a PG-in-SQ emulsion film with an initial mean droplet diameter of 20 μm. The initial calculated average film thickness is approximately equal to 65 μm. This implies that at time t = 0 min, the emulsion film is comprised of a multilayer of PG droplets in the SQ-continuous phase. As evaporation proceeds, it can be seen that the PG droplets decrease in concentration but their apparent mean drop diameter increases. After 100 min, a monolayer of polydispersed PG droplets is observed.

For the investigated period between 120 – 140 min, the denser PG droplets will sediment on top of the quartz plate and may partially wet it to form a layer of adhering PG lenses under a covering layer of SQ. It is expected that the PG droplets will progressively deform during evaporation, leading to the formation of a filigree pattern of silica and PG residue at 160 min. At 180 min, this filigree pattern is lost. A dispersion film is expected to be present containing silica particles and AVB in SQ. For the investigated period shown here, a PG residue might also be present based on the volume fraction calculations. Although other interpretations of the images (*e.g.* catastrophic phase inversion from PG-in-SQ to SQ-in-PG) cannot be rigorously excluded, the scenario described above provides a plausible interpretation.

Figure 5.6. Optical micrographs of PG-in-SQ emulsion films during their evaporation. The emulsion films initially contained equal volumes of SQ and PG and 4.0 mM AVB in the total emulsion (initially dissolved in the PG phase) and were stabilised using 1 wt.% of 23% SiOH silica particles.

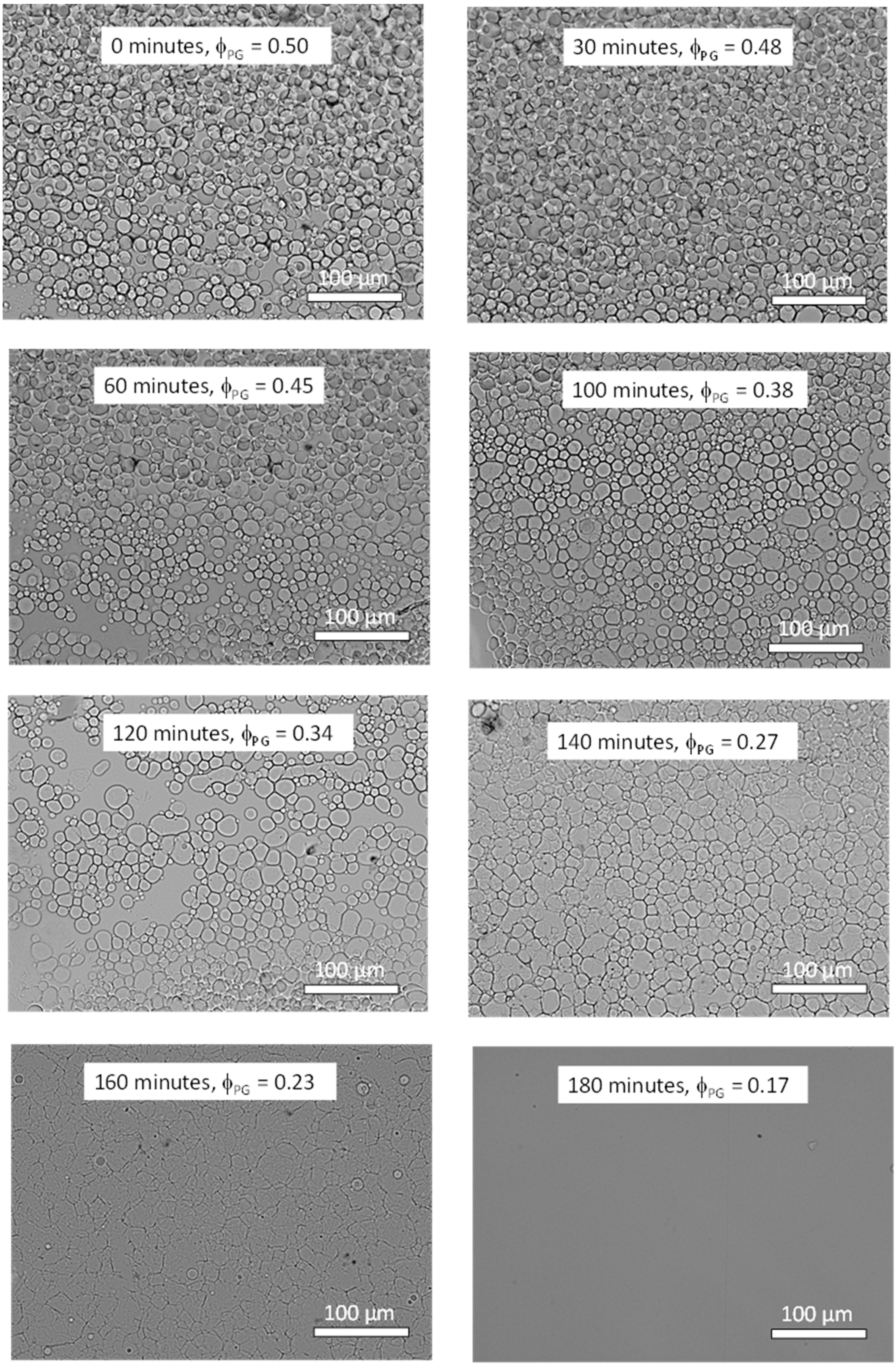

5.4.2 Optical microscopy measurements of SQ-in-PG emulsion film

Figure 5.7 shows the optical micrographs of a SQ-in-PG emulsion film with an initial mean droplet diameter equal to 20 μm. For this particular emulsion, the initial calculated average film thickness was found to be approximately 65 μm. As the evaporation of the PG-continuous phase occurs, it can be seen that the SQ droplets increase in concentration but their mean droplet diameter remains approximately the same. This behaviour is observed for the investigated period of up to 80 min. Beyond that time scale, the SQ droplets start deforming until a high internal phase emulsion (HIPE) is observed at 100 min. Again, a filigree pattern of silica particles, SQ and PG residue is present at 120 min as PG evaporation continues. As previously, at 140 -160 min, the filigree pattern is lost. The remaining film contains silica particles and AVB in SQ. For the investigated period of time shown here, a PG residue might also present based on the volume fraction calculations.

Figure 5.7. Optical micrographs of SQ-in-PG emulsion films during their evaporation. The emulsion films initially contained equal volumes of SQ and PG and 4.0 mM AVB in the total emulsion (initially dissolved in the PG phase) and were stabilised using 1 wt.% of 35% SiOH silica particles.

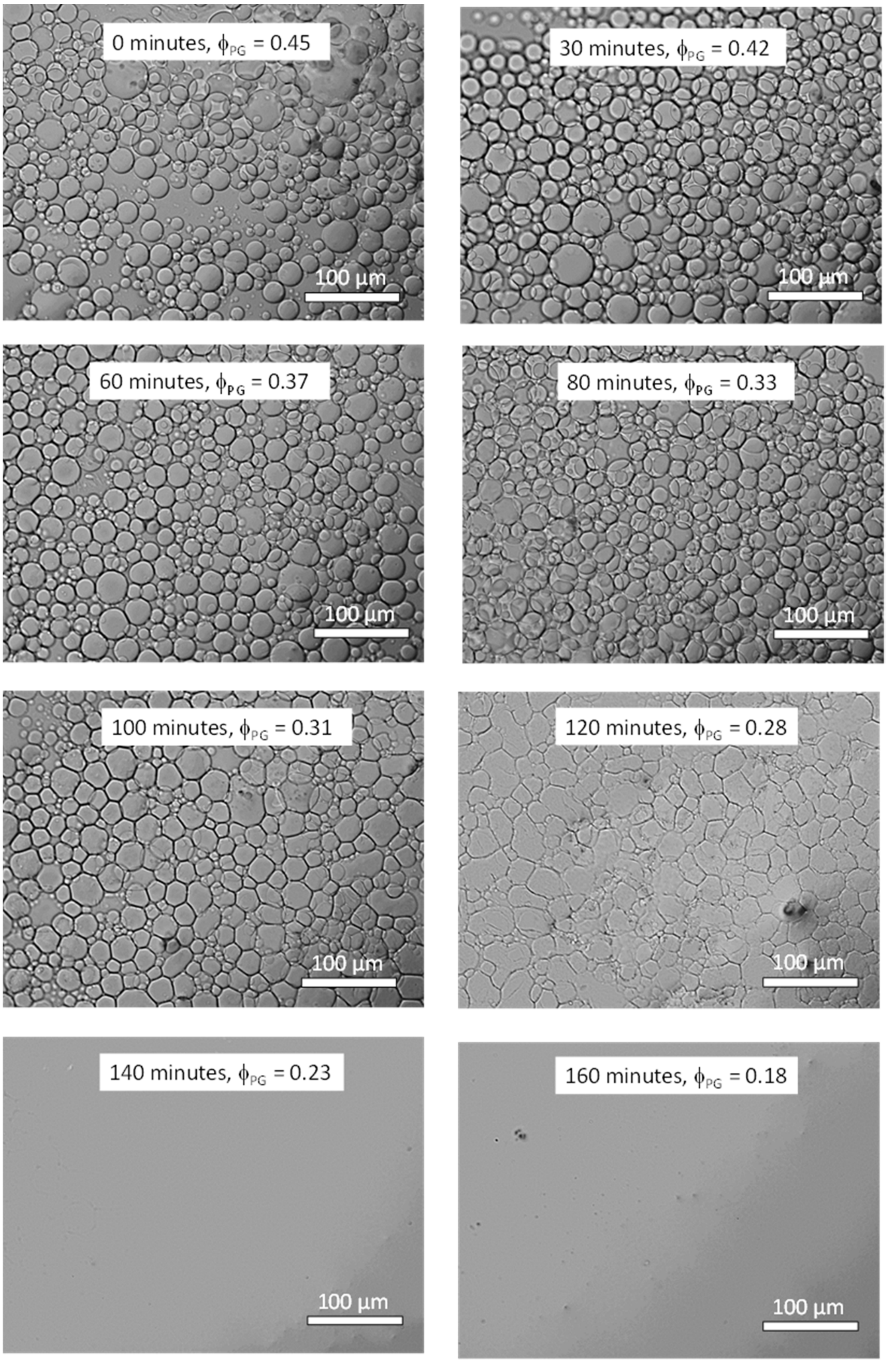

5.5 *Absorbance measurements of SQ-in-PG and PG-in-SQ emulsions during evaporation*

5.5.1 Theoretical considerations

For the investigated solution films, the measured absorption spectra resulted from the absorption of the UV filter alone. Unlike these solution films, the measured absorption spectra for emulsion films, which contain a single UV absorber, are expected to contain contributions from i) reflection from the interfaces of the emulsion and the quartz plate, ii) absorption of the UV absorber and iii) scattering from the emulsion structure and the particles.

The measured specular absorbance A (also expressed as $-\log_{10}T$ where T is the fraction of incident light transmitted) is taken to be the sum of the following three contributions

$$A = A_{reflect} + A_{abs} + A_{scat} \qquad (5.3)$$

where $A_{reflect}$ is the absorbance due to reflection losses from the emulsion and quartz plate surfaces, A_{abs} is the absorbance due to absorption (by AVB in this case) and A_{scat} is the absorbance resulting from light scattering by the emulsion.

It is important to note that equation 5.3 is an approximation. Within an emulsion, it is expected that the presence of the droplets can affect their scattering properties and thus influencing the overall absorption properties of the emulsion film. The continuous phase can also cause an increase in the overall absorbance since it allows multiple light scattering to occur. However, the effect due to light scattering is only significant when its absorbance contribution is more than approximately three times larger than the contribution because of absorption.[7]

The absorbance values $A_{reflect}$ due to reflection of the quartz plate alone or in the presence of either of the pure solvents (PG or SQ) deposited as thin films are significantly low. These values have been determined in the range of 0.035 and are wavelength independent. As such, their contribution to the overall absorbance is minimal.

For solution films that obey the Beer-Lambert Law, the absorbance can be calculated based on equation 1.4 as long as the solute concentration, the path length and the molar extinction coefficient of the solute in that particular wavelength, are determined. For our investigated emulsion films, equation 1.4 can also be applied. The values of the molar extinction coefficients of the UV absorber in each solvent are known. The solute concentration in each solvent, however, varies with changes in the volume fraction and has to be defined accordingly until its solubility limit is reached. Finally, the path length is also dependent on the values of the calculated average film thickness, as those shown in the lower plot of Figure 5.5.

Thus, the absorbance A_{abs} can be calculated by introducing equation 5.4 below. This equation shows that the absorbance A_{abs} contains contributions from the individual solute concentration in each phase for a path length equal to its film thickness

$$A_{abs} = d\left(\phi_{SQ}[AVB]_{SQ}\varepsilon_{SQ} + \phi_{PG}[AVB]_{PG}\,\varepsilon_{PG}\right) \tag{5.4}$$

where the subscripts indicate the solvent phase, d corresponds to the path length/film thickness and ε the molar extinction coefficient.

For equation 5.4 to be valid, it is assumed that the spatial distribution of the UV absorber is uniform throughout the illuminated area. In addition, the illuminated area is expected to be fully covered with the emulsion film and as such its fraction should be equal to 1. This is because the measured optical absorbance (or measured transmittance) will correspond to an average value instead, if the illuminated area is neither uniform nor fully covered with the sample of interest.

Within the emulsion films, the solute concentration is inhomogeneously distributed between the droplet and the continuous phase with a ratio based on the partition coefficient. However, the amount of solute per unit film area is expected to be reasonably uniform, assuming that the emulsion droplet size is small relative to the calculated average film thickness and that they will form a multilayer. This is the case for the emulsion films in the initial stages of the evaporation. When all the PG phase has evaporated, the solute concentration is uniformly distributed within the SQ phase over the total film area. At intermediate evaporation times, the solute distribution is not expected to vary significantly and thus it is assumed to be uniform from point to point across the total depth of the film.

Figure 5.8 shows a comparison between specular absorbance spectra and diffuse spectra of the same emulsion film. As a reminder, the specular absorbance data were derived with the use of UV/vis spectrophotometry whereas the diffuse spectra were determined by introducing diffuse transmittance spectroscopy.

For the specular absorbance data, it can be seen that a PG-in-SQ emulsion film without any UV absorber and with a film thickness of 100 μm, has values in the range of 0.7 – 1.0, which are only weakly wavelength dependent. Similarly, for a PG-in-SQ emulsion film, which contains a single UV absorber (either AVB or MC), it can be seen that the absorbance due to UV absorber is simply additive and wavelength independent. It is important to note that for the wavelength of 400 nm, the absorbance of all emulsion films with and without the UV absorbers present is similar in magnitude. The reason has to do with the fact that at this wavelength the extinction coefficient of both AVB and MC is close to zero. Thus, it can be inferred that the absorbance at 400 nm is due to scattering alone. These values were measured *versus* air as reference.

Similarly, for the diffuse spectra, it can be seen that a PG-in-SQ emulsion film without any UV absorber and with a film thickness of 100 μm has values in the range of 0.03, which agree with our measurements due to reflection alone. This implies that the diffuse absorbance due to scattering is virtually zero. For a PG-in-SQ emulsion film, which contains a single UV absorber (either AVB or MC), it can also be seen that the diffuse spectra due to UV absorber is again simply additive and wavelength independent. Thus, the scattered light is fully transmitted through the emulsion film and detected by the diffuse spectrophotometer with an acceptance angular range of ± 60°, though in reality it is expected that the angular range with respect to normal incident light to be ± 90°. Again, these values were measured *versus* air as reference.

Figure 5.8. Comparison of the specular and the diffuse spectra (all *versus* air reference) of 100 μm path length PG-in-SQ emulsion films containing equal volumes of SQ and PG with and without AVB or MC. The films were stabilised using 1 wt.% of 23% SiOH silica particles and the spectra were measured in closed cuvettes without evaporation. For the diffuse measurements, the instrument sensitivity limits the wavelength range to wavelengths greater than approximately 250 nm.

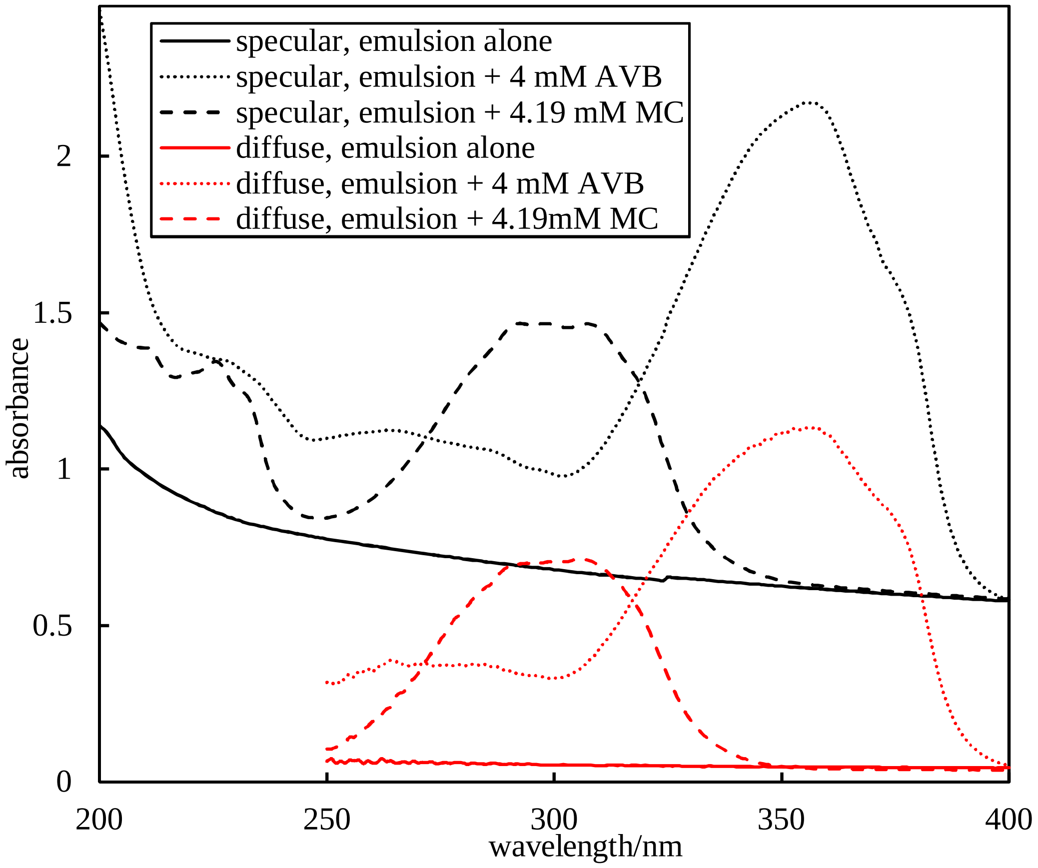

Theoretical calculations can be of support to the argument concerning the scattering behaviour of the emulsion films. Using relevant software[8], the scattering efficiency Q_{scat} can be calculated, which corresponds to non-interacting, non-multiply scattering emulsion droplets of 10 μm mean radius and 30% polydispersity as a function of wavelength. For our simulations, the scattering efficiency is found to be equal to two.

For these calculations, the refractive index values of the solvents, shown in Table 5.1, were taken to be wavelength independent since the wavelength dependence was not available. Scattering efficiency values were converted to A_{scat} values using the equation below,[9]

$$A_{scat} = \frac{3\phi_{drops} Q_{scat} d}{4ln(10)\langle r \rangle} \tag{5.5}$$

where ϕ_{drops} is the volume fraction of emulsion droplets and <r> is the mean droplet radius and d is the path length.

Table 5.1. Physical properties of PG, SQ and *n*-decane at 32°C.[10-16]

Solvent	Density/g cm^{-3}	Vapour pressure/Pa	Refractive index (at 589.3 nm)
PG	1.0276	50.8	1.429
SQ	0.8009	0.007	1.4425
n-decane	0.72106	280	1.4066

From equation 5.5, the value of A_{scat} can be estimated, assuming that all scattering intensity is contributing to the overall loss in transmittance. With this approach, any droplet interactions, multiple scattering and wavelength dependences of the refractive index values of the solvents are excluded and not taken into consideration. As an example, the calculated scattering angle dependence of the scattering intensity at fixed wavelength of 300 nm is presented in Figure 5.9. Our calculations have shown that the light is strongly forward scattered within an angular range of ± 2° with respect to the incident light direction. Similar calculations in order to determine the angular dependence were made for all wavelengths in the range of 200 – 400 nm.

These theoretical calculations confirm that i) these emulsion films scatter light only at small scattering angles, ii) A_{scat} is weakly dependent on the wavelength and that iii) the calculated values of A_{scat} are much larger than the apparent values measured using either specular absorbance or diffuse transmittance measurements.

Hence, the specular instrument used with a detector angular range of $\pm < 5^{o}$ detects most of the forward scattered light and thus only a small fraction of the total absorbance due to scattering is collected. For the diffuse spectrophotometer, however, with a detector angular of $\pm$ 60° virtually all the scattered light intensity is detected. Thus, the absorbance contribution due to scattering is recorded to be zero. The calculations are consistent with the experimental observations. This implies that the light scattering from these emulsion films is strongly forward scattering and hence the scattering does not contribute to the overall absorbance of these films.

Figure 5.10 shows the variation of the volume fraction of PG with evaporation time for both emulsion types. This set of data in combination with Figure 5.11, concerning the change in the specular absorbance at 400 nm as a function of evaporation time, demonstrate how the PG evaporation affects the emulsion film. In particular, for the investigated period between 210 – 300 min, the collapse of the emulsion structure due to very low volume fraction of PG is accompanied with a significant decrease in the specular absorbance. The optical micrographs shown in Figures 5.6 – 5.7 confirm the relevant timescale.

Figure 5.9. Upper plot: Calculated film absorbance due to scattering of PG-in-SQ and SQ-in-PG emulsion films of 65 μm thickness containing equal volumes of SQ and PG without AVB. The calculations are for non-interacting droplets of mean radius 10 μm with a polydispersity (standard deviation/mean) of 30% with no multiple scattering. Lower plot: Scattering intensity (arbitrary units) versus scattering angle for the PG-in-SQ emulsion film at wavelength of 300 nm.

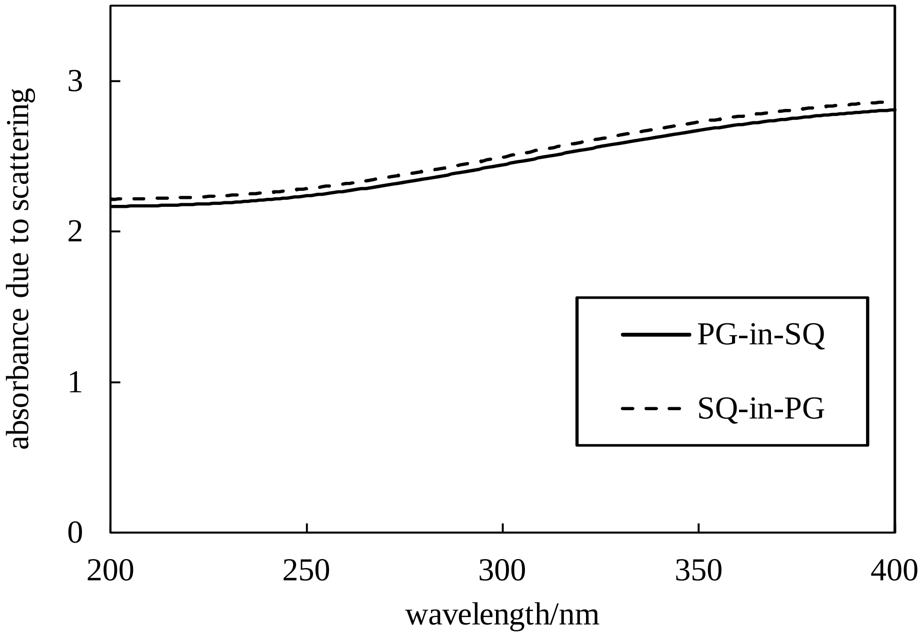

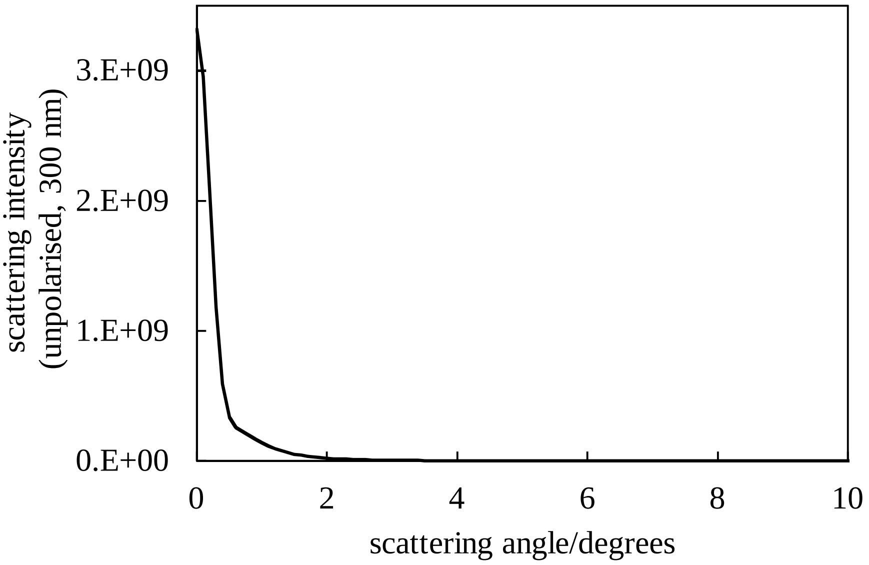

Figure 5.10. Variation of the volume fraction of PG with evaporation time for PG-in-SQ and SQ-in-PG emulsion films initially containing equal volumes of SQ and PG and 4.0 mM AVB in the total emulsion.

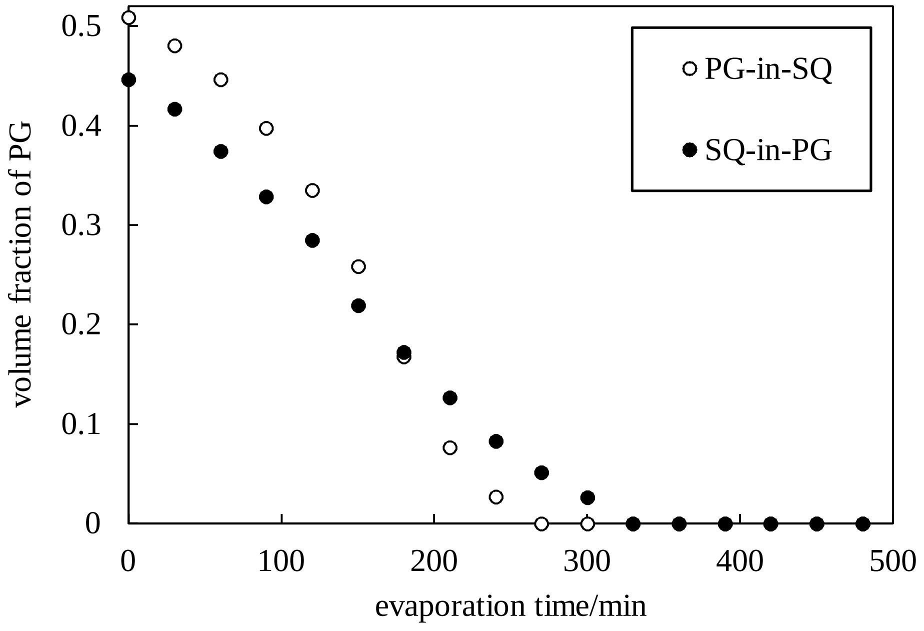

Figure 5.11. Variation of the specular absorbance at 400 nm wavelength with evaporation time for PG-in-SQ and SQ-in-PG emulsion films initially containing equal volumes of SQ and PG and 4.0 mM AVB in the total emulsion.

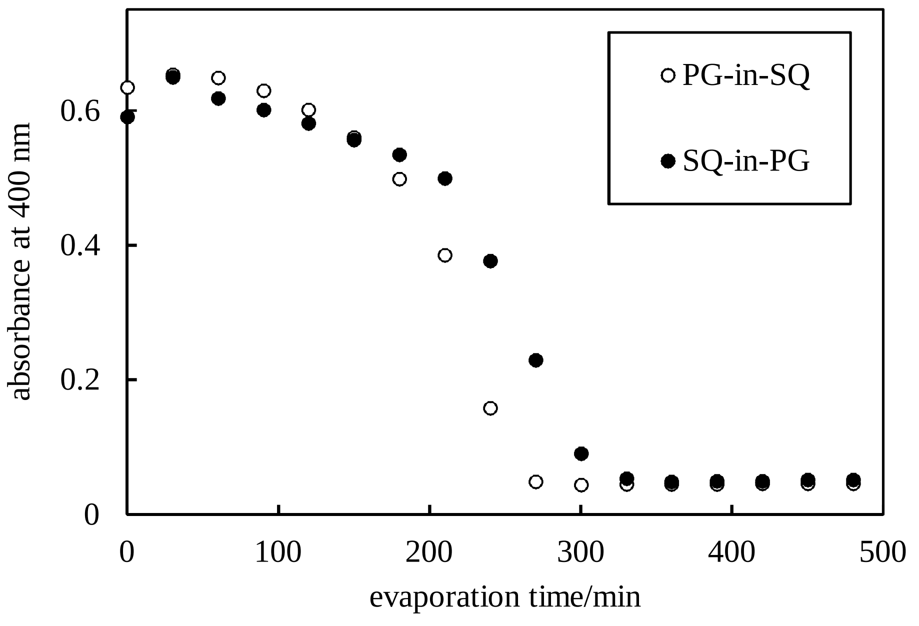

5.5.2 Determination of measured and calculated absorbance values of PG-in-SQ and SQ-in-PG emulsion films containing 4.0 mM AVB overall

The measured absorbance spectra of the emulsion films in the presence of a single UV absorber were investigated. All measurements are plotted *versus* air alone as a reference. As in the case of the solutions, the absorbance data of the emulsion films are also limited to individual runs and thus possible variations in the reflection and/or scattering cannot be controlled. The smooth quartz plate could also be used as a reference. However, the wavelength independent absorbance values around 0.035 as a result of reflection alone would have introduced only a relatively small correction.

The upper plot of Figure 5.12 shows the measured absorbance data of a PG-in-SQ emulsion film containing 4.0 mM AVB with respect to the overall emulsion volume, as a function of evaporation time. For the first 120 min, it can be seen that the measured absorbance values remained approximately constant. A decrease in the absorbance values, however, is observed for the investigated period between 120 – 240 min. From 240 min onwards, it can be argued that all the PG has evaporated, leaving behind a dispersion of SQ film with 8.0 mM AVB plus the silica particles. This implies that the collapse of the emulsion structure occurred at 240 min and the measured absorbance values taken from 240 min onwards, correspond to the SQ dispersion film alone. Thus, at 240 min, the measured peak absorbance of the SQ film at 354 nm is equal to 1.06. It is assumed that the silica particles present have negligible contribution in the overall absorbance. In addition, the calculated average film thickness is approximately 32 μm.

A quick calculation with the use of the Beer-Lambert Law confirms that the calculated absorbance at 354 nm, for the investigated period of 240 min, is 0.90. This corresponds to a SQ solution film assuming the same film thickness (32 μm), the solute concentration of 8.0 mM AVB and the molar extinction coefficient of AVB in SQ at the peak absorbance (354 nm) to be 35,000 M^{-1} cm^{-1}. Thus, both experimental and calculated absorbance at 354 nm are in agreement within the estimated errors assuming that the latter are in the range of ± 10%.

It is important to note that during the investigating period, no peak "flattening" is observed. This result demonstrates that the illuminated area is fully covered and thus the fraction of the illuminated area remained equal to unity. The calculated absorbance spectra have been determined with the use of equations 4.4, 5.3 and 5.4 assuming that the A_{scat} is equal to the measured absorbance at 400 nm during evaporation and are shown in the lower plot of Figure 5.12. For our calculations, it is expected that the fraction of the illuminated area remains constant and equal to 1.

A comparison of measured and calculated absorbance spectra for both emulsion types indicate that they are in reasonable agreement. The largest film absorption spectra changes result from the decrease in A_{scat} due to the collapse of the emulsion droplet structure. The changes in the absorbance contribution by the solute AVB are minor. This is because the molar extinction coefficients of AVB in both solvents are quite similar.

The same approach was investigated for a SQ-in-PG emulsion film containing 4.0 mM AVB with respect to the overall emulsion volume and is presented in the upper plot of Figure 5.13. As in the case of the PG-in-SQ emulsion film, a slight decrease in the absorbance values over the investigated period is observed for the first 210 min. Beyond that time scale, there are two distinct absorbance peaks at 240 and 270 min indicating the time where the emulsion film is expected to collapse resulting again in the dispersion of SQ film with 8.0 mM AVB and the silica particles. Similarly, there is no observed peak “flattening”. Since the fraction of the illuminated area remains unity, both measured and calculated data capture the peak shape but with a difference in their values.

Figure 5.12. Measured (upper plot) and calculated (lower plot) absorbance spectra *versus* air as reference during evaporation of a PG-in-SQ emulsion film initially with 19.8 mg mass and containing equal volumes of SQ and PG and 4.0 mM AVB in the total emulsion (initially dissolved in the PG phase). The film was stabilised using 1 wt.% of 23% SiOH silica particles.

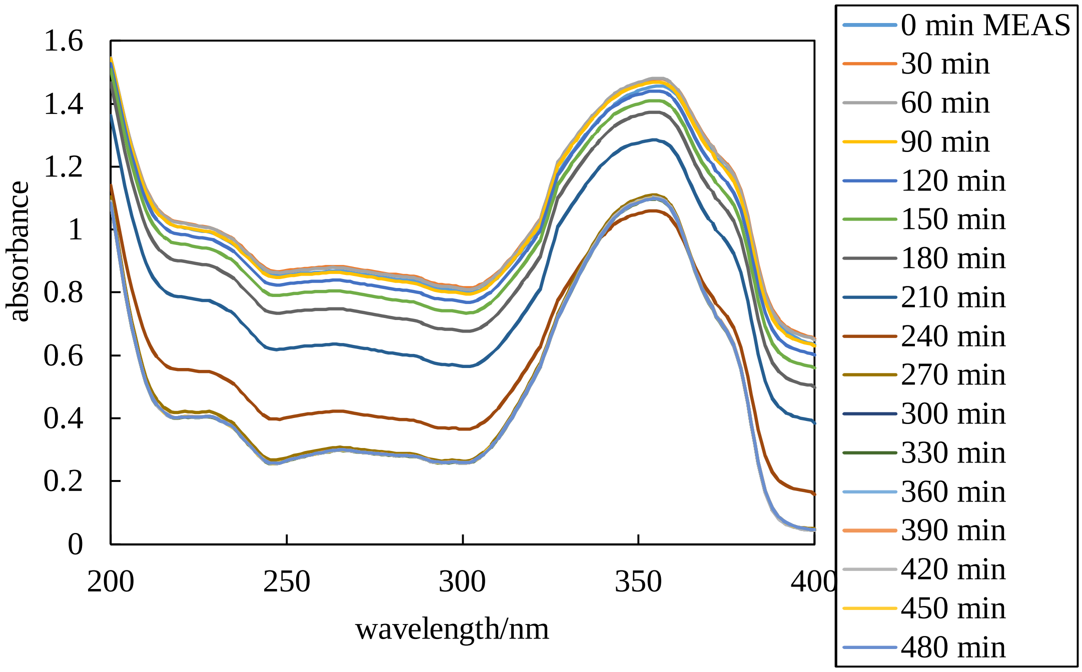

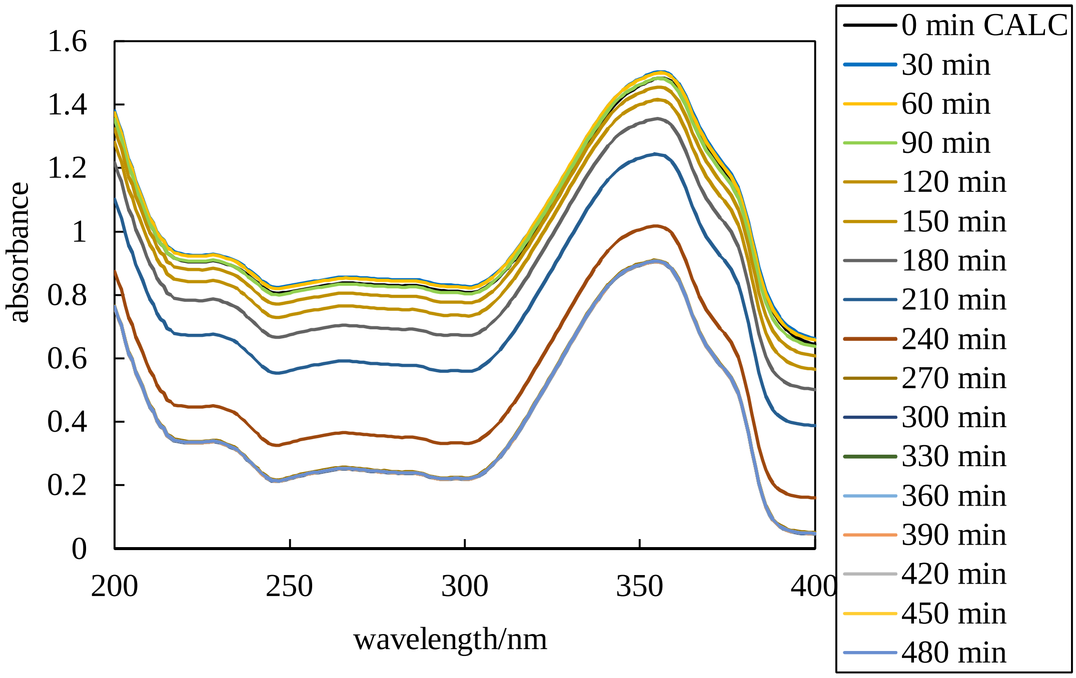

Figure 5.13. Measured (upper plot) and calculated (lower plot) absorbance spectra *versus* air as reference during evaporation of a SQ-in-PG emulsion film initially with 17.5 mg mass and containing equal volumes of SQ and PG and 4.0 mM AVB in the total emulsion (initially dissolved in the PG phase). The film was stabilised using 1 wt.% of 35% SiOH silica particles. The peak at 325 nm corresponds to the lamp change of the UV/vis spectrophotometer.

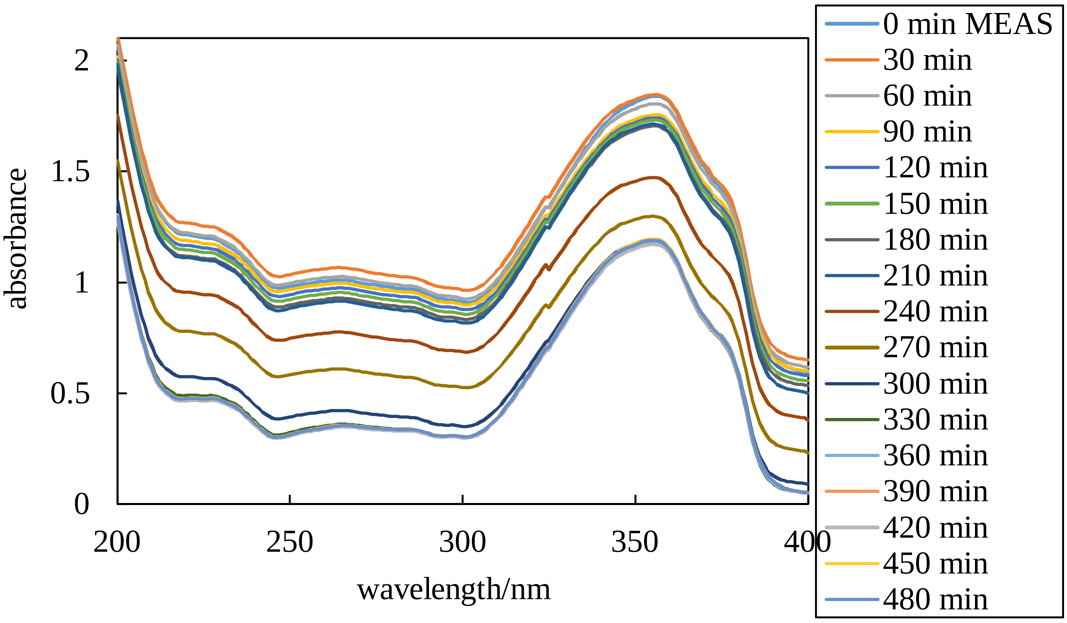

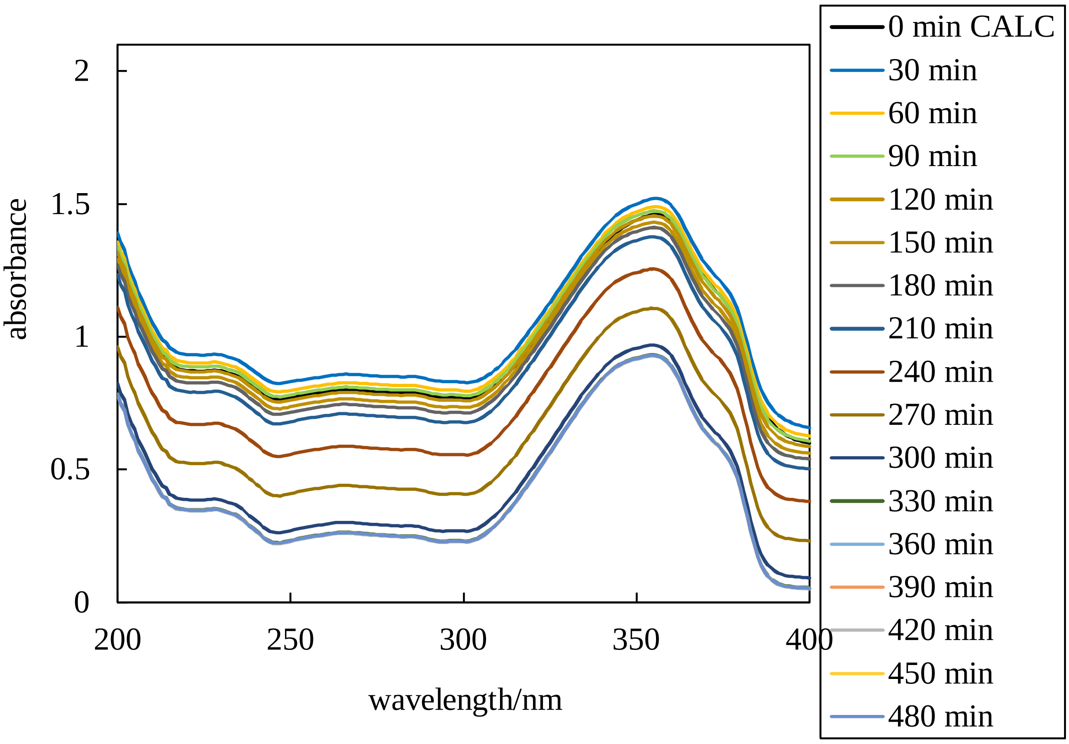

5.5.3 Determination of measured and calculated absorbance values of PG-in-SQ and SQ-in-PG emulsion films containing 4.19 mM MC overall

Our investigation was also extended to liquid sunscreen actives such as MC. Results have shown similar behaviour of SQ-in-PG and PG-in-SQ emulsion films containing MC with that of films containing AVB, which were described earlier. From Figures 5.14 and 5.15 it can be seen that the loss in the overall absorbance agrees with the observed collapse of the emulsion structure at around 240 min. Upon complete PG evaporation, the liquid MC remained soluble in the involatile SQ phase and this behaviour is depicted in the measured absorbance spectra. This is another confirmation that for emulsions films, with an involatile liquid phase, the changes in the film absorption spectra can be attributed to the loss of light scattering as a result of the collapse of the structure.

Figure 5.14. Measured (upper plot) and calculated (lower plot) absorbance spectra *versus* air as reference during evaporation of a PG-in-SQ emulsion film initially with 13.7 mg mass and containing equal volumes of SQ and PG and 4.19 mM MC in the total emulsion (initially dissolved in the PG phase). The film was stabilised using 1 wt.% of 23% SiOH silica particles. The peak at 325 nm corresponds to the lamp change of the UV/vis spectrophotometer.

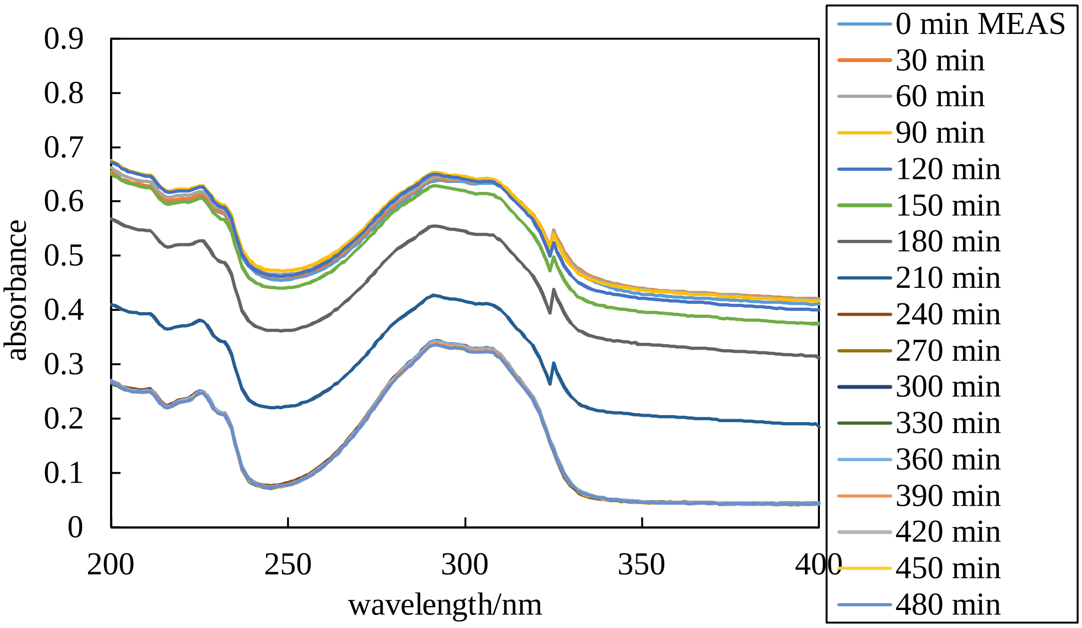

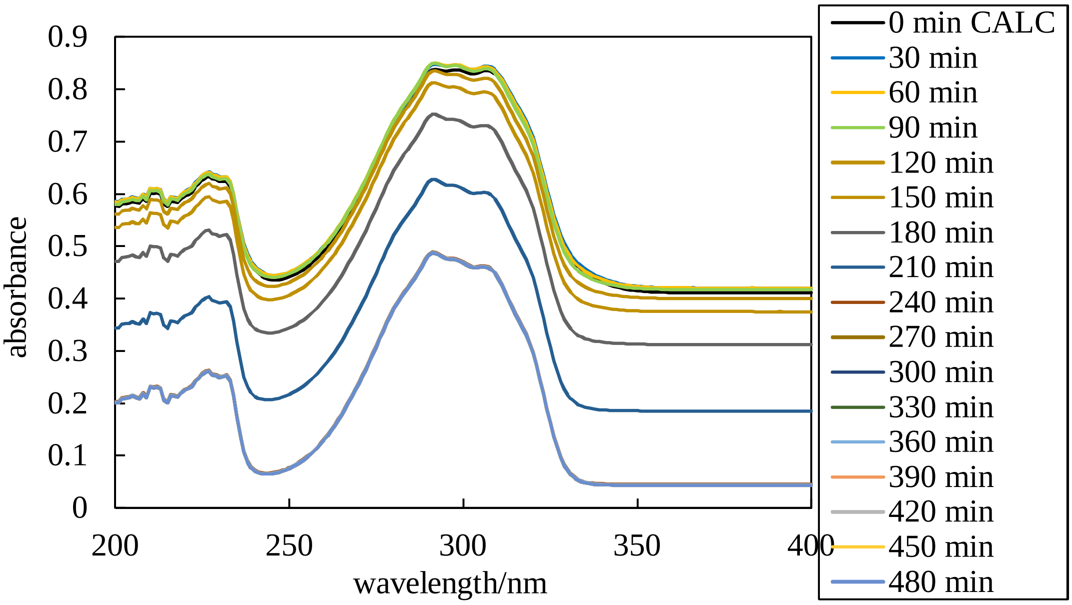

Figure 5.15. Measured (upper plot) and calculated (lower plot) absorbance spectra *versus* air as reference during evaporation of a SQ-in-PG emulsion film initially with 15.7 mg mass and containing equal volumes of SQ and PG and 4.19 mM MC in the total emulsion (initially dissolved in the PG phase). The film was stabilised using 1 wt.% of 35% SiOH silica particles.

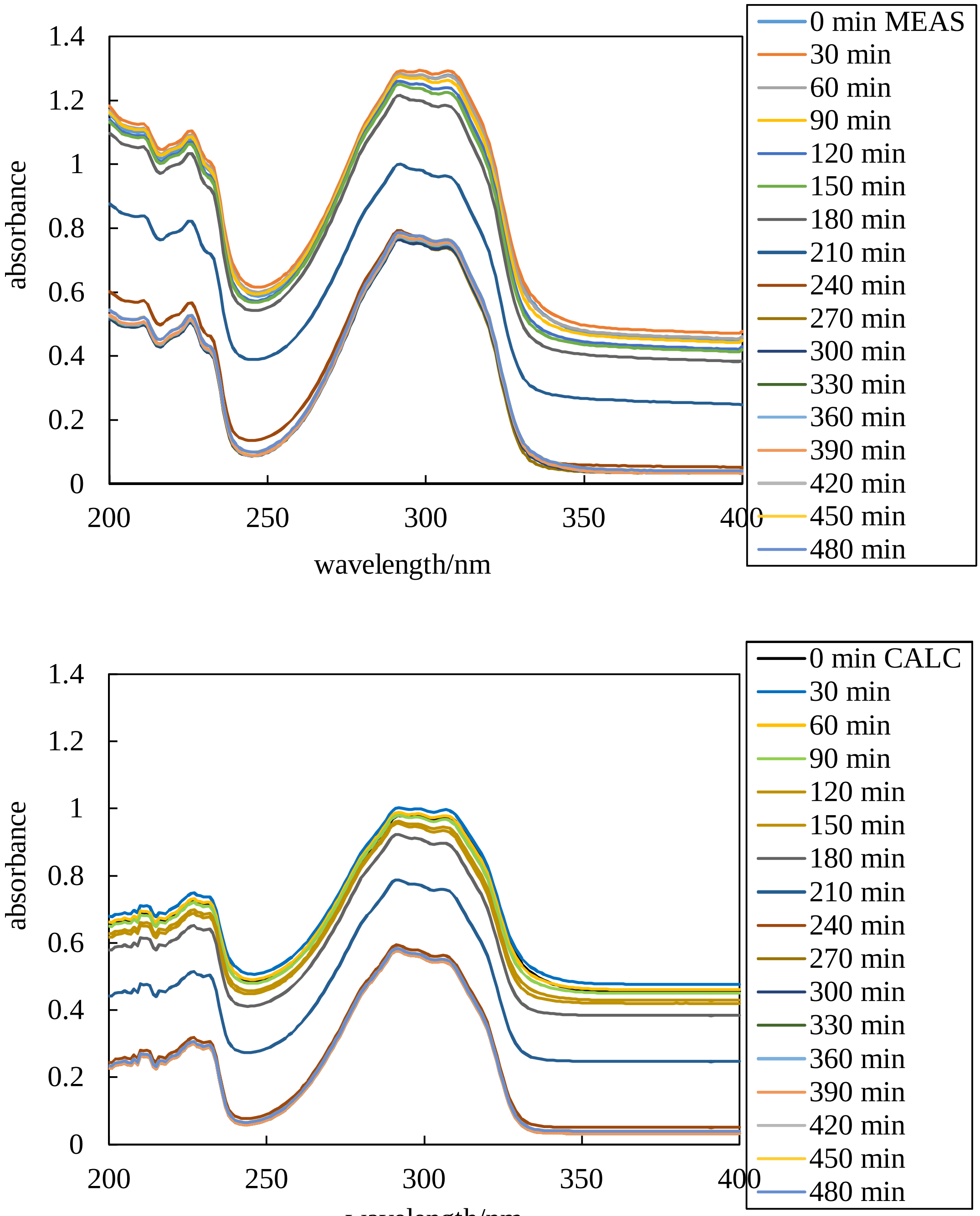

5.6 In vitro SPF determination of UV absorbers

Measured and calculated specular absorbance spectra of both emulsion types during PG evaporation are presented in terms of their time dependent *in vitro* SPF values in Figures 5.16 – 5.17. As discussed in Chapter 4, all calculations were made under defined conditions, with the use of equation 1.2.[17] Overall, it can be seen that for the emulsion films containing a single UV absorber, the shape and the main features of the *in vitro* SPF, based on specular absorbance measurements, are captured. The loss of the *in vitro* SPF at intermediate times can be attributed to light scattering at the period of time where the collapse of the emulsion structure occurs. The *in vitro* SPF calculations based on diffuse transmittance measurements of both emulsion films are also presented in Figures 5.16 – 5.17. It is evident that for these emulsions, the SPF does not change significantly as a result of evaporation.

Hence, for emulsion films containing an involatile liquid component and where the UV filter remains soluble during evaporation, it can be inferred that the changes in the film spectra and the corresponding SPF due to film evaporation result mainly from the loss of light scattering due to the collapse of the emulsion structure. As in the case of solutions, it can be seen that throughout our experimental procedure, the film deposition never reached the desirable thickness of 20 μm but varied for emulsions in the range of 60 - 70 μm. The *in vitro* SPF values obtained, however, allow us to have a good understanding of the evaporation behaviour of “real” sunscreen formulations.

Figure 5.16. Measured and calculated variation of the SPF (290 – 400 nm wavelength range) with evaporation time for emulsion films containing equal volumes of SQ and PG spread on quartz. Upper plot: 19.8 mg mass of PG-in-SQ emulsion and 4.0 mM AVB in the total emulsion. Lower plot: 17.5 mg mass of SQ-in-PG emulsion and 4.0 mM AVB in the total emulsion. For all graphs, the dashed line shows the time dependent SPF based on diffuse absorbance.

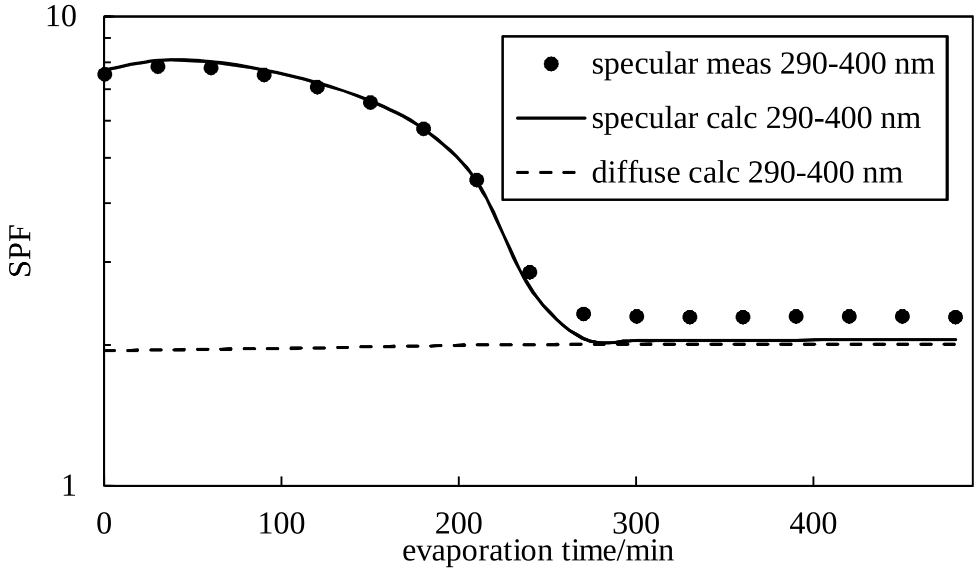

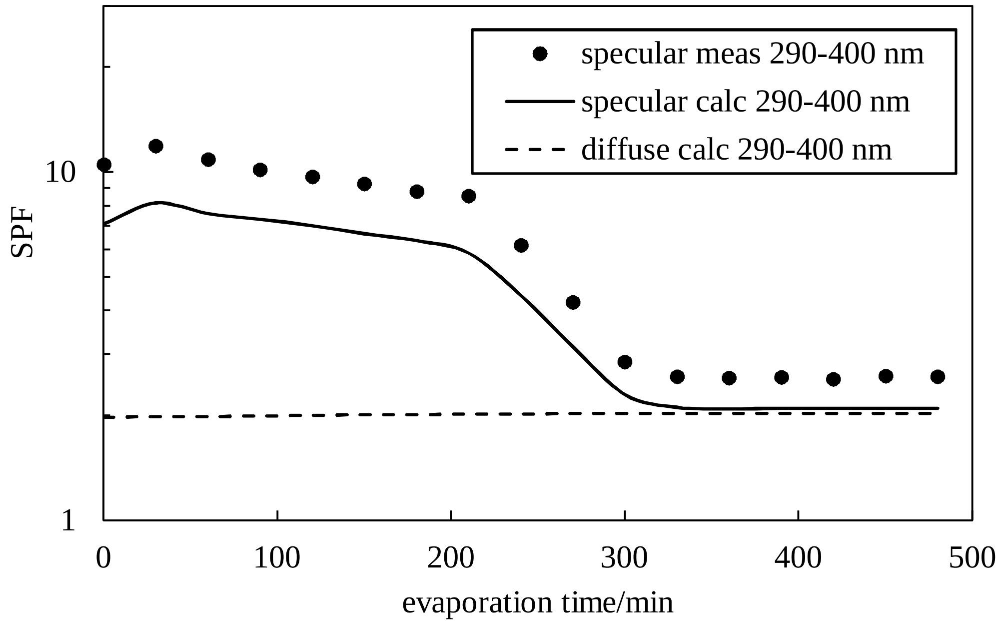

Figure 5.17. Measured and calculated variation of the SPF (290 – 400 nm wavelength range) with evaporation time for emulsion films containing equal volumes of SQ and PG spread on quartz. Upper plot: 13.7 mg mass of PG-in-SQ emulsion and 4.19 mM MC in the total emulsion. Lower plot: 15.7 mg mass of SQ-in-PG emulsion and 4.19 mM MC in the total emulsion. For all graphs, the dashed line shows the time dependent SPF based on diffuse absorbance.

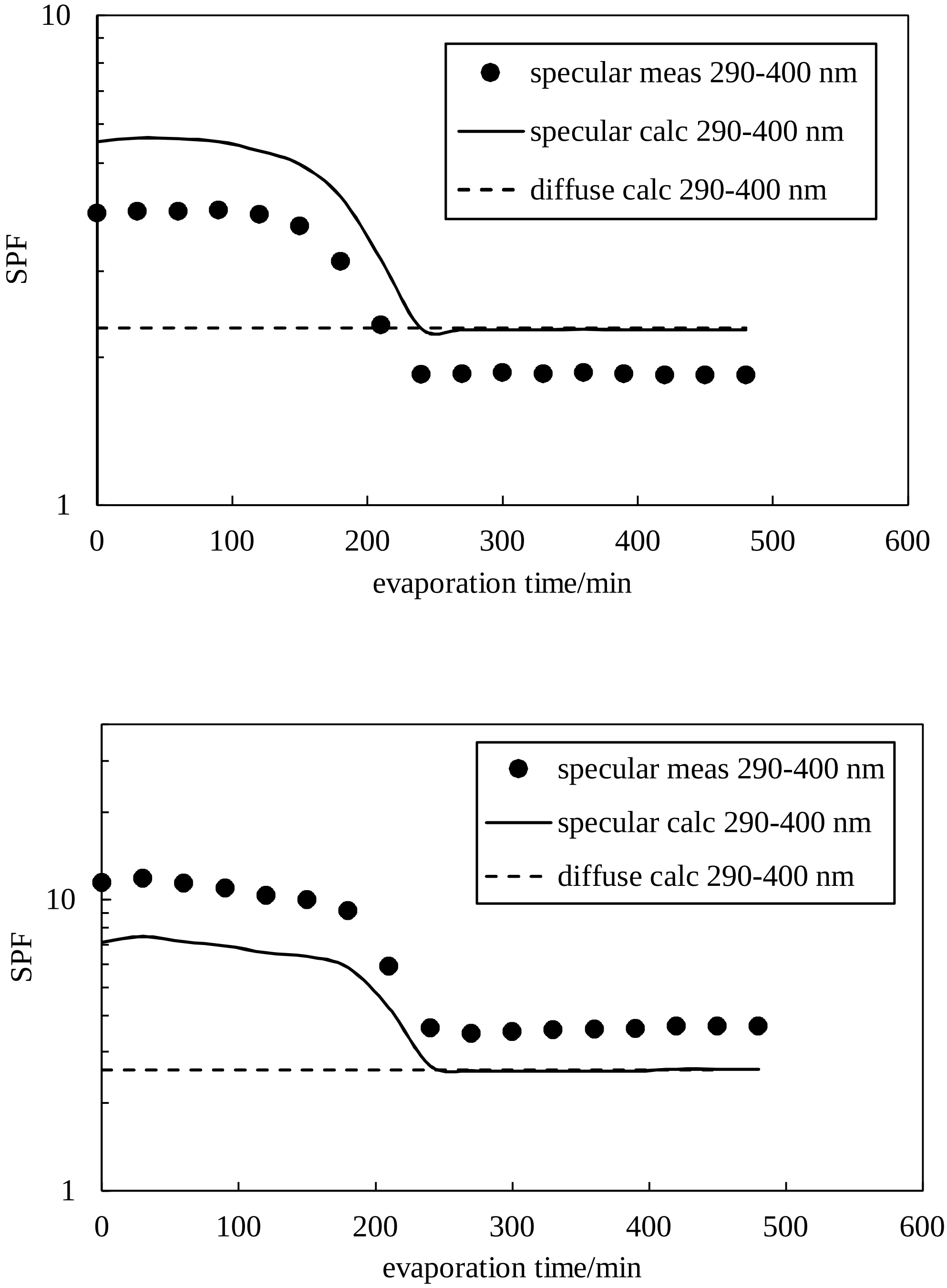

5.7 *Comparison of emulsions containing solvents with slow and fast evaporating rate*

As already discussed, the evaporative behaviour of emulsions consisting of an evaporating PG and an involatile SQ phase was investigated. It was shown that the UV absorber will initially be distributed between the two phases and after complete PG evaporation, it will be present in the involatile SQ phase. Since the solubility limit of AVB is higher in SQ as opposed to PG, no precipitation will be observed.

It is interesting, though, to investigate the evaporative behaviour of an emulsion where both phases (either slowly or fast) evaporate. For this reason, equal volumes of *n*-decane and PG containing initially 6.35 mM AVB and 1.65 mM AVB respectively were used. After emulsification and assuming that AVB equilibrates rapidly between the two phases, an overall concentration of 4.0 mM AVB in the emulsion film is expected.

The visual appearance of the *n*-decane-in-PG emulsion film containing 4.0 mM AVB with respect to the overall emulsion volume, is shown in Figure 5.18. Again, the superimposed red rectangular box corresponds to the illuminated area of where the beam of the spectrophotometer passes through for sample detection. The initial grey opaque deposited film formed three distinct areas ("patches") and became transparent within the first 15 – 20 min. This time scale agrees with the observed *n*-decane evaporation which leaves behind a dispersion of PG with AVB plus silica particles.

Figure 5.18. Images of an evaporating film of a *n*-decane-in-PG emulsion initially containing equal volumes of *n*-decane and PG with 4.0 mM AVB. The emulsion was stabilised by 1 wt.% of 23% SiOH particles.

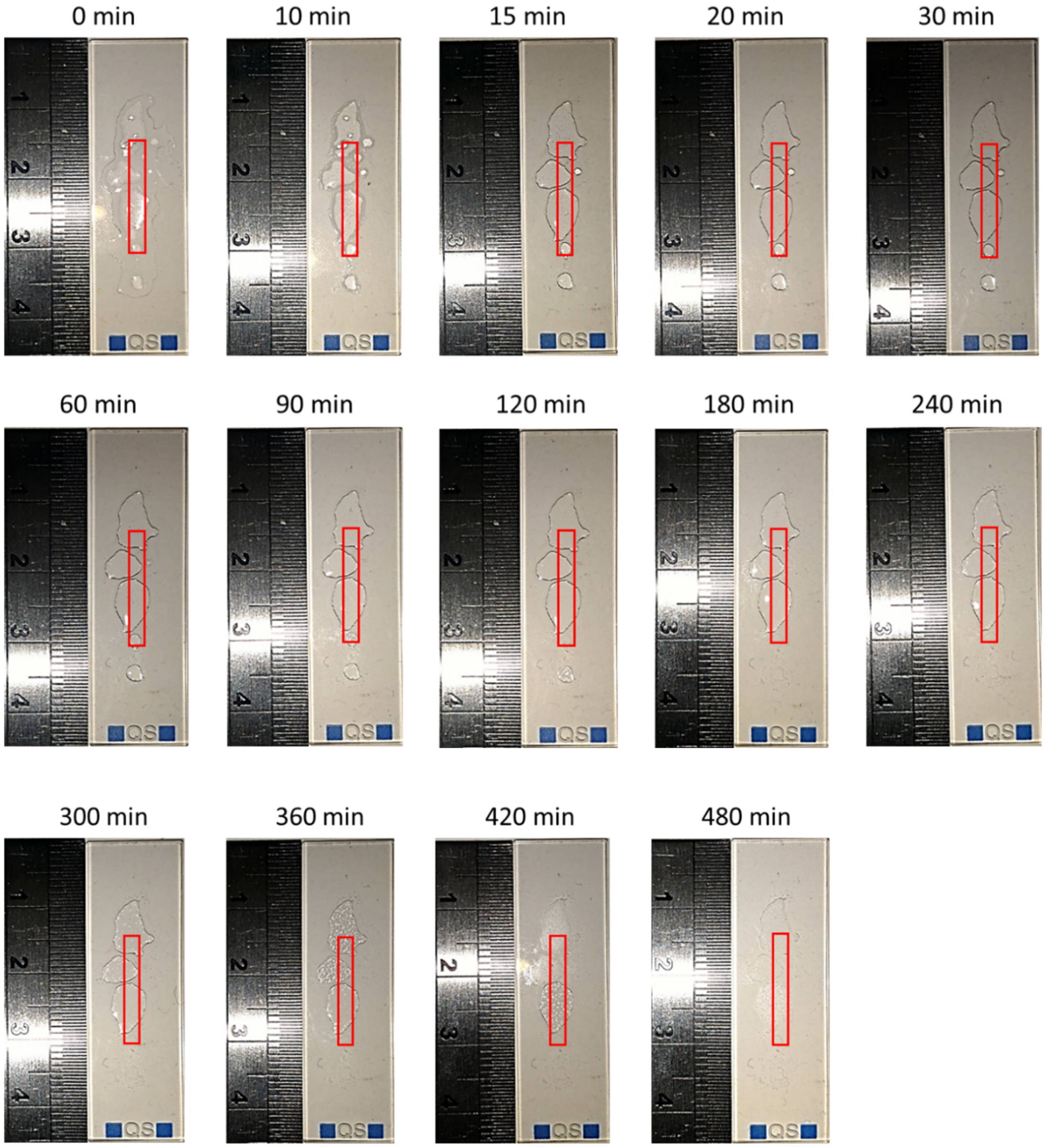

Figures 5.19 – 5.20 shows the mass loss, film area, average film thickness and the fraction of illuminated area with evaporation time for the *n*-decane-in-PG emulsion film. From the upper plot of Figure 5.19, it can be seen that there is a significant initial mass loss for the first 20 min. Based on the solubility values, the equilibrium partition coefficient of AVB between *n*-decane and PG is equal to $P_{decane/PG} = 3.9$.

Assuming that the equilibrium partitioning is maintained, it is expected that the overall initial concentration of 4.0 mM AVB will be fully transferred to the PG phase upon complete *n*-decane evaporation. As such, the overall concentration of AVB will be equal to 8.0 mM and will progressively increase until its solubility limit (14 mM) is reached. If the equilibrium partitioning is maintained, AVB precipitation is expected to occur at a time approximately equal to 180 min, based on equation 4.1. However, the first sign of AVB precipitation in the form of crystals is observed within 20 min, which corresponds to complete evaporation of *n*-decane. Thus, it can be inferred that the evaporation of *n*-decane is sufficiently rapid such that the AVB in *n*-decane precipitates rather than transferring to the PG phase.

The middle plot of Figure 5.19 presents the total emulsion film area as a function of evaporation time. It can be seen that there is an initial rapid decrease due to dewetting of the emulsion film. Beyond that point, however, the area of the emulsion film remains practically constant until the complete PG evaporation. This can be attributed to the film pinning that was formed as a result of silica deposition that occurred at the film base edge. Fluctuations in the calculated average film thickness are also expected to occur based on equation 4.3 and these are depicted in the lower plot of Figure 5.19. In Figure 5.20, the fraction of the illuminated area with evaporation time is shown.

Figure 5.19. Variation of film mass (upper plot), film area (middle plot) and average film thickness (lower plot) with evaporation time for a *n*-decane-in-PG film initially containing equal volumes of *n*-decane and PG and 4.0 mM AVB. The film was stabilised by 1 wt.% of 23% SiOH silica particles.

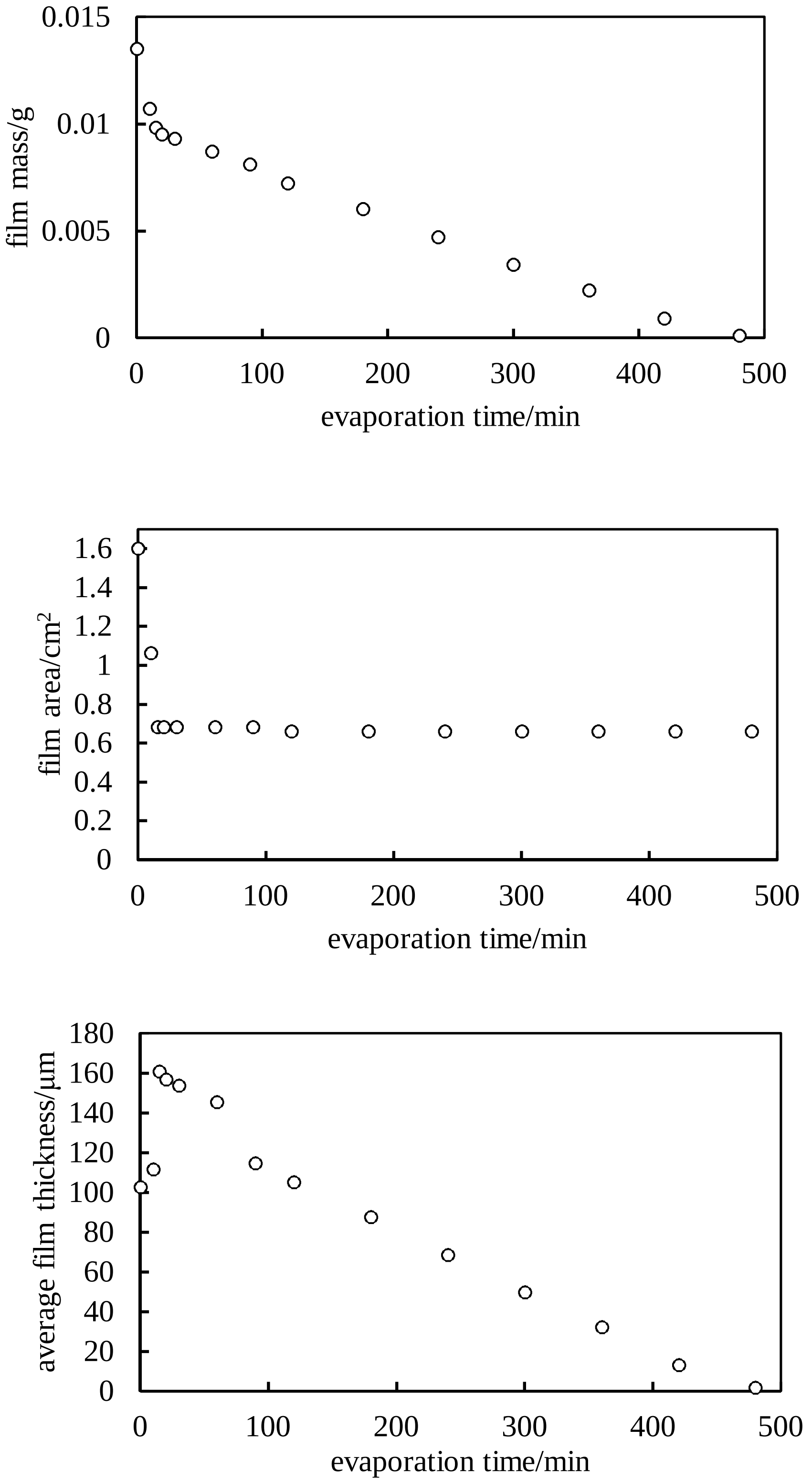

Figure 5.20. Fraction of illuminated area covered with evaporation time for a *n*-decane-in-PG film initially containing equal volumes of *n*-decane and PG and 4.0 mM AVB. The film was stabilised by 1 wt.% of 23% SiOH silica particles.

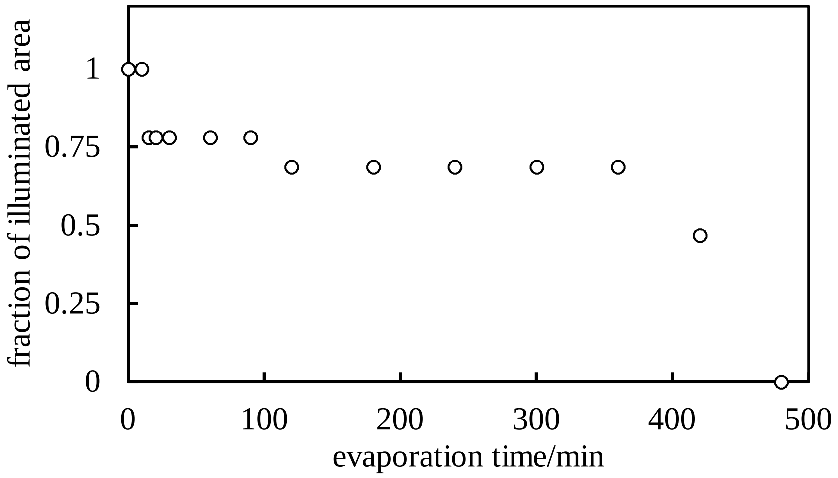

5.7.1 Optical microscopy measurements of *n*-decane-in-PG emulsion film

Figure 5.21 shows the optical micrographs of the evaporation of a *n*-decane-in-PG emulsion film. Further investigation concerning the stability of these emulsions revealed that their droplet size remained constant over 240 min. During the evaporation process, the *n*-decane droplets decrease in size rapidly until their complete evaporation within 20 min. Overall, the emulsion film is progressively dewetting on the smooth quartz plate, leaving behind small amounts of precipitated AVB crystals. It is interesting to note that the emulsion did not dewet as a single film but formed “patches” of bare quartz plate and areas covered with the PG-continuous phase. Upon complete PG evaporation, however, a residue of precipitated AVB crystals is evident.

Figure 5.21. Representative images of an evaporating film of a *n*-decane-in-PG emulsion initially containing equal volumes of *n*-decane and PG with 4.0 mM AVB overall (initially 1.65 mM in PG and 6.35 mM in *n*-decane). The emulsion was stabilised by 1.0 wt.% of 23% SiOH silica particles.

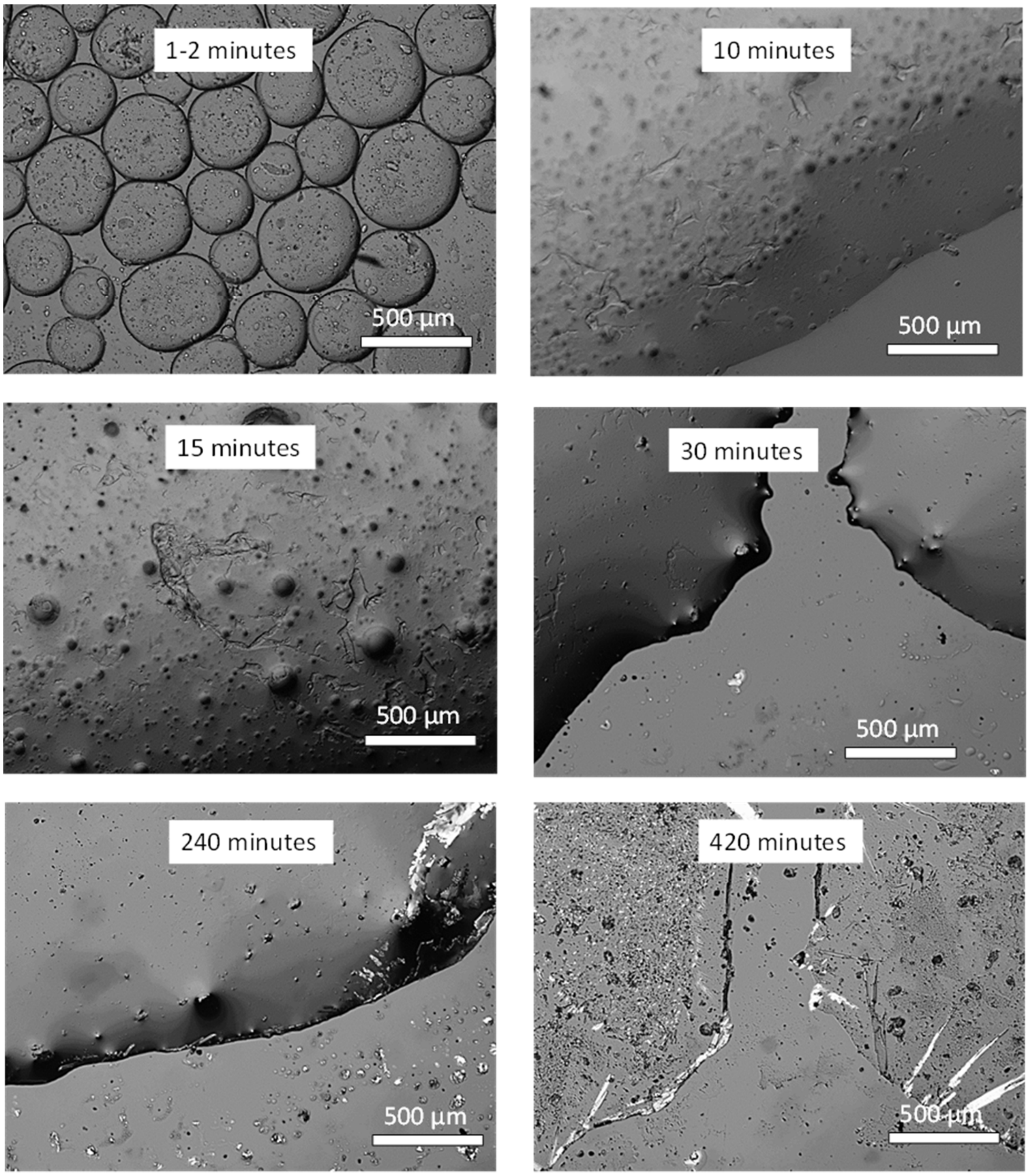

5.7.2 Absorbance measurements of *n*-decane-in-PG emulsion film

Figure 5.22 shows the measured and calculated absorbance spectra of a *n*-decane-in-PG emulsion film with evaporation time. For the measured absorbance data, it can be seen that there is an initial decrease in the peak absorbance of AVB within the first 10 min. A slower decrease in the peak absorbance is observed until complete evaporation of the emulsion film at 480 min. As previously, the absorbance at 400 nm corresponds to the specular absorbance. It is expected that these values vary with evaporation due to film scattering as shown in Figure 5.23. The changes in the absorbance can be attributed to the progressive collapse of the emulsion structure, the formation of a "patchy" film of PG and the formation of the residue of the precipitated AVB crystals. The calculated absorbance values were derived with the use of equations 4.4, 5.3 and 5.4. For equation 4.4, in particular, it is expected that the fraction of the illuminated area is below 1 as a function of evaporation time. These equations are valid, assuming that i) the AVB does not partition significantly during the rapid evaporation of the *n*-decane and that ii) the precipitated AVB in the form of crystals does not contribute to the overall absorbance.

As such, the film profile model calculations capture the observed decrease in the absorbance until complete evaporation. However, the calculated short time increase in the absorbance does not agree with the measured spectra. This may be a result of inaccuracy in the exact extent of *n*-decane evaporation corresponding to the time at which the first spectrum was measured. It is also likely that the measured specular absorbance of the final film residue due to light scattering by the large particles remaining after evaporation corresponds to strongly forward scattering. Hence, evaporation of emulsion films without an involatile component is expected to result in complete loss of film SPF.

Figure 5.22. Measured (upper plot) and calculated (lower plot) absorbance spectra *versus* air as reference during evaporation of a *n*-decane-in-PG emulsion film initially containing equal volumes of *n*-decane and PG and 4.0 mM AVB in the total emulsion. The solute AVB was initially dissolved in both phases at their equilibrium concentrations. The film was stabilised using 1 wt.% of 23% SiOH particles.

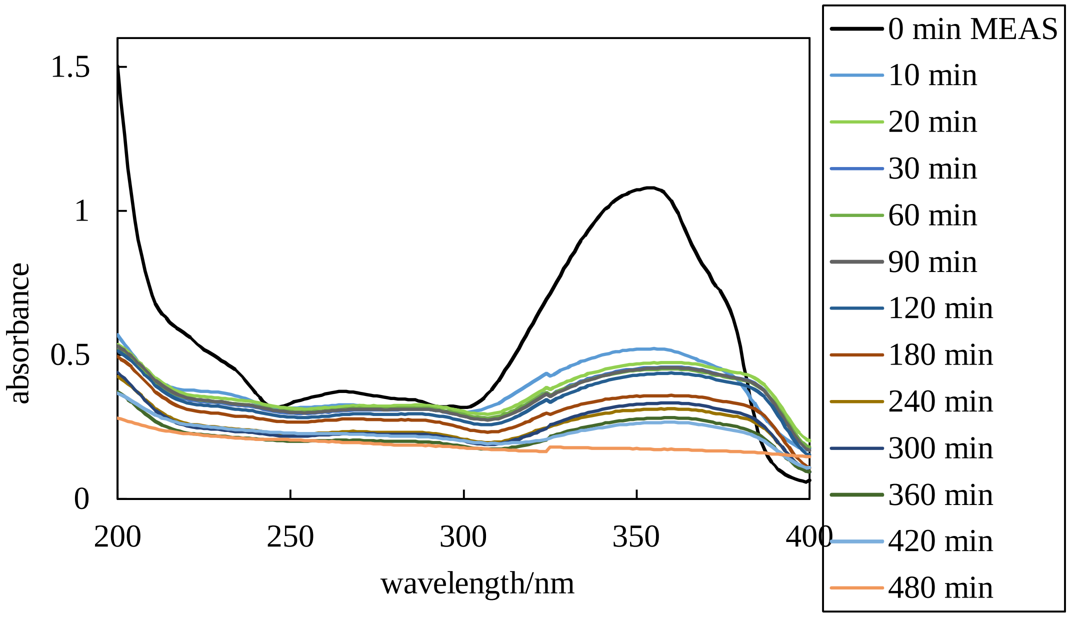

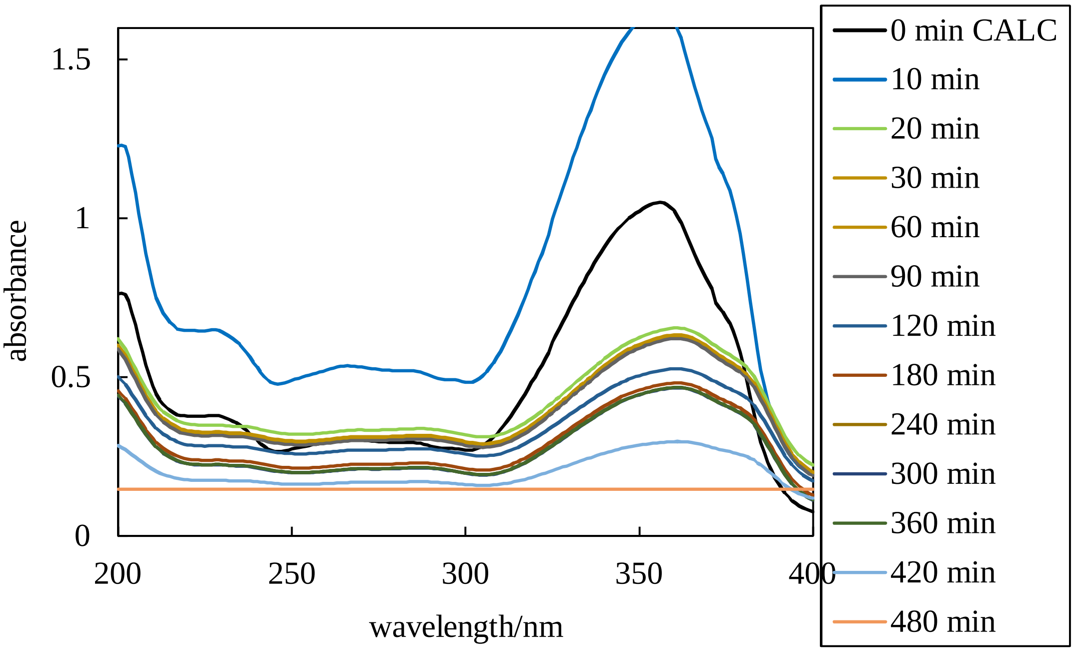

Figure 5.23. Variation of the specular absorbance at 400 nm with evaporation time.

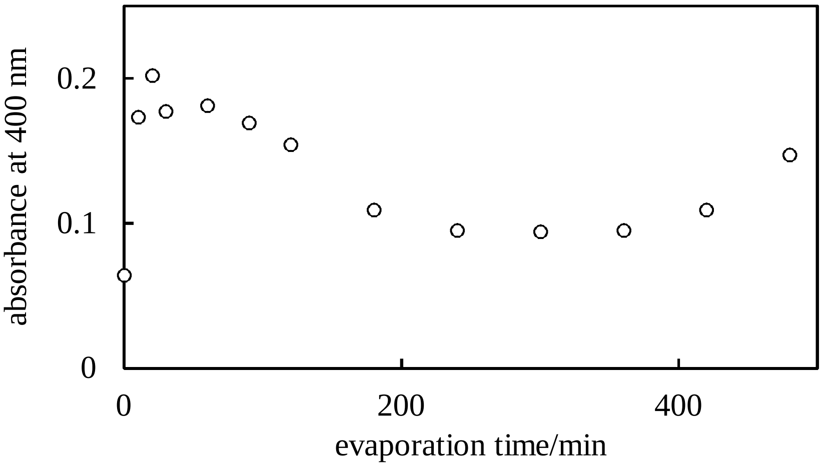

5.8 Conclusions

The evaporation behaviour of more complex systems such as emulsions was investigated. Particle-stabilised emulsions consisting of a polar PG and an apolar SQ phase of both types, SQ-in-PG and PG-in-SQ, with and without UV absorbers were deposited on top of a quartz plate and they were left to evaporate in the open lab air. Since SQ is practically involatile, results have shown that PG evaporation is only observed leaving behind a SQ dispersion film with AVB and silica particles deposited on the quartz plate with minor changes in its initial total film area. In addition, it was shown that the UV absorber remained soluble throughout since it partitioned between the two phases.

The intermediate loss in the absorbance is a result of the loss of the light scattering due to the collapse of the emulsion structure. Measured and calculated absorbance spectra are compared and their behaviour is also depicted in the *in vitro* SPF calculations. For the latter case, the calculated absorbance data were derived with the use of a simplified model that has already been described for the evaporation of solution films. As such, the use of complex systems such as emulsions and in particular this type of waterless emulsion is an effective approach to tackle the problem of dewetting and solute precipitation.

5.9 References

1. L. E. Agrapidis-Paloympis and R. A. Nash, *J. Soc. Cosmet. Chem*, 1987, **221**, 209–221.
2. G. J. Mturi and B. S. Martincigh, *J. Photochem. Photobiol. A*, 2008, **200**, 410–420.
3. P. Markov and I. Petkov, *Tetrahedron*, 1977, **33**, 1013–1015.
4. R. A. Morton, A. Hassan and T. C. Calloway, *J. Chem. Soc.*, 1934, **192**, 883–901.
5. I. Aranberri, K. J. Beverley, B. P. Binks, J. H. Clint and P. D. I. Fletcher, *Langmuir*, 2002, **18**, 3471–3475.
6. B. P. Binks, P. D. I. Fletcher, M. A. Thompson and R. P. Elliott, *Colloids Surf. A*, 2011, **390**, 67–73.
7. B. Herzog and F. Sengün, *Photochem. Photobiol. Sci.*, 2015, **14**, 2054-2063.
8. MiePlot v. 4.5.01 downloaded from http://www.philiplaven.com/mieplot.htm
9. D. J. McClements, *Adv. Colloid Interface Sci.*, 2002, **97**, 63–89.
10. J. George and N. V. Sastry, *J. Chem. Eng. Data*, 2003, **48**, 1529-1539.
11. D. R. Stull, *Ind. Eng. Chem.*, 1947, **39**, 517-540.
12. M. J. Fontao and M. Iglesias, *Int. J. Thermophys.*, 2002, **23**, 513-527.
13. K. A. G. Schmidt, D. Pagnutti, M. D. Curran, A. Singh, J. P. M. Trusler, G. C. Maitland, and M. McBride-Wright, *J. Chem. Eng. Data*, 2015, **60**, 137-150.
14. D. M. VonNiederhausern, G. M. Wilson and N. F. Giles, *J. Chem. Eng. Data*, 2000, **45**, 157-160.
15. G. P. Dubey, N. Tripathi and S. C. Bhatia, *Ind. J. Pure & Appl. Phys.*, 2005, **43**, 175-179.
16. C. W. Haas, Selected values of properties of hydrocarbons and related compounds, Thermodynamic Research Center, Texas A&M University, College Station, Texas, 1978.
17. B. L. Diffey and J. Robson, *J. Soc. Cosmet. Chem.*, 1989, **40**, 127–133.

CHAPTER 6 IRRADIATION OF SOLUTIONS, DISPERSIONS AND EMULSIONS CONTAINING UV FILTERS

6.1 Introduction

In the previous chapters, we discussed the evaporation of solutions, dispersions and emulsions containing UV absorbers. For each system, we showed how the solvent evaporation affects the loss in the absorbance of the UV filters present. In addition, we have developed a validated model in order to account for the film variations during evaporation. Based on these findings, we can predict the *in vitro* SPF changes as a function of evaporation time.

In this chapter, we investigate the photochemical behaviour of these systems. Solutions of a single UV absorber such as AVB, MC, DHHB and BEMT, were irradiated for a range of concentrations and path lengths. The solvents of choice were the polar protic PG and the apolar SQ. For the DHHB and BEMT solutions, we show that both are photostable irrespective of the solvent type. For the photolabile AVB and MC solutions, our results can describe how irradiation affects the change in the absorbance. The complex photochemical processes of AVB and MC in both solvents are further depicted in the *in vitro* SPF values as a function of irradiation time.

Our investigation was extended to solutions containing a mixture of UV absorbers (AVB and BEMT). Irradiation of these solutions has shown that the degradation of AVB occurs at a slower rate with the addition of a second UV absorber (BEMT), which acts as a photostable “spectator” species. For mixtures containing AVB and metal oxide nanoparticles, AVB degradation occurs at a slightly slower rate compared to solutions of AVB alone.

Similarly, we have examined the photochemical behaviour of a single UV absorber (either AVB or MC) when dissolved within emulsions of PG and SQ that are stabilised by partially hydrophobised silica particles. For these systems, it was shown that the photochemical rates of the UV absorbers were independent of the emulsion type but dependent on the volume fraction of PG present in the formulation. Throughout our investigation, two types of light sources were used: i) a UV lamp set at three fixed distances from the samples (3.6, 7.2 and 14.4 cm) and ii) a solar simulator. With the use of a known chemical actinometer, we determined their absolute spectral irradiances. In the last part of this chapter, we show how the SPF varies when irradiated with sunlight. Hence, for any data set with any concentration and path length, we can predict the variation of sunscreen film absorbance spectra and the derived SPF as a function of irradiation time with “standard” sunlight.

6.2 Theoretical considerations

For a simple photochemical reaction where a single reactant (placed in a cell with an optical path length d) is converted to a product upon irradiation, we investigate the rate of the reaction per unit illuminated cell area per unit time (units: mol m^{-2} s^{-1}) as opposed to the rate of change of concentration per unit time that is used for non-photochemical reaction kinetics.[1,2]

For polychromatic irradiation, the reaction rate is described as follows

$$rate = \int \phi(\lambda)\, I_a(\lambda) d\lambda \tag{6.1}$$

where $\phi(\lambda)$ is the wavelength-dependent quantum yield for the reaction and $I_a(\lambda)$ is the number of moles of irradiating photons of wavelength λ absorbed by reactant per unit illuminated area per unit time per unit wavelength (units: mol m^{-2} s^{-1} nm^{-1}). Integration over the wavelength range of the light source (250 – 400 nm) results in the determination of the overall reaction rate. The number of moles of photons incident on the sample per unit illuminated area per unit time per unit wavelength $I_o(\lambda)$ is expressed by the following equation

$$I_a(\lambda) = 0.96 I_o(\lambda)\left(1 - 10^{-A_{reac}(\lambda)}\right) \tag{6.2}$$

where $A_{reac}(\lambda)$ is the optical absorbance due to the reactant species and 0.96 is a correction factor to account for light transmittance losses due to reflection at the front face of the irradiation cell. Equation 6.2 is valid for systems where only the reactant species absorb in the wavelength range of interest (250 – 400 nm). For systems, however, where additional species (termed “spectators”) also absorb in the same wavelength range, equation 6.2 has to be modified in order to account for the light transmittance losses due to absorption by the “spectator” species

$$I_a(\lambda) = 0.96 I_o(\lambda)\left(1 - 10^{-A_{reac}(\lambda)}\right)\frac{\left(1-10^{-A_{spec}(\lambda)}\right)}{A_{spec}(\lambda)\ln(10)} \tag{6.3}$$

where $A_{spec}(\lambda)$ corresponds to the absorbance of all “spectator” species present. The incident photon flux $I_o(\lambda)$ is related to the spectral irradiance of the light source $S(\lambda)$ by

$$I_o(\lambda) = \frac{S(\lambda)\lambda}{hcN} \tag{6.4}$$

where h is Planck’s constant, c is the speed of light and N is the Avogadro’s number. We briefly describe how equations 6.2 and 6.3 are derived in Appendix B. In general, the overall calculated photochemical reaction rate can be determined from equations 6.1 – 6.4 for known values of absolute spectral irradiance $S(\lambda)$, quantum yield and absorbance spectra of all reactant and “spectator” species.

6.3 Determination of the absolute spectral irradiances of the light sources

For the selected light sources (UV lamp and solar simulator), it is expected that their absolute spectral irradiances $S(\lambda)$ are proportional to their measured relative light emission intensities (expressed in arbitrary units) as a function of wavelength $I(\lambda)$. We use chemical actinometry in order to determine the constant of proportionality. The latter is obtained by comparison of the measured and calculated photochemical reaction rates of an actinometric reaction with a known quantum yield.

The selected actinometric reaction for the determination of the measured photochemical reaction rates was the self-sensitised photo-oxygenation reaction of 9,10-dimethylanthracence (DMA) in air-saturated Freon 113 solvent.[3] For this reaction, the quantum yield is independent of the wavelength over the range 334 – 395 nm and equal to 0.58 ± 0.02.[4]

The absorbance spectra of irradiated solutions of DMA in Freon 113 were recorded at frequent timed intervals. The upper plot of Figure 6.1 presents the measured absorbance spectra of an irradiated solution of 0.47 mM DMA in Freon 113 with a path length 1 cm. For this example, the light source used was a UV lamp placed at a fixed distance of 7.2 cm from the sample. The middle plot of Figure 6.1 shows the measured absorbance at a particular wavelength (365 nm) as a function of irradiation time. From both graphs it can be seen that complete conversion of DMA to its product, is observed within 8 min.

The initial reaction rate is determined according to the following equation

$$rate = -\left(\frac{dA}{dt}\right) / \left(\varepsilon_{reactant} - \varepsilon_{product}\right) \qquad (6.5)$$

where –(dA/dt) is the slope of the best-fit straight line of the middle plot of Figure 6.1 to the initial time data (4 min) for which the rate is constant and ε is the molar extinction coefficient of the subscripted species. The values of $\varepsilon_{reactant}$ were obtained from the initial absorbance spectrum prior to irradiation. The $\varepsilon_{product}$, however, is negligible because the products do not absorb over the wavelength range of interest.

Using equation 6.5 we determine the initial reaction rate for each wavelength ranging between 250 – 400 nm. From the lower plot of Figure 6.1 it can be seen that the initial reaction rates are virtually identical within the wavelength range of 320 – 400 nm. Deviations in the initial rates are observed, however, in the wavelengths i) below 300 nm and ii) around 375 and 395 nm. These can be attributed to the fact that the measured absorbance exceeded the reliable range of the UV/vis spectrophotometer. The initial overall reaction rate was averaged over the wavelength range (300 – 400 nm).

The overall calculated photochemical reaction rate of DMA in Freon 113 solutions are determined from equations 6.1 – 6.4 for the known values of quantum yield and the absorbance spectra. From the measured and calculated photochemical rates, the constant of proportionality is derived and adjusted accordingly until both values of initial rates agree. This process was repeated for all light sources used. Figure 6.2 summarises the derived values of S(λ) for different light sources used and compares them with the values of S(λ) for terrestrial sunlight. The latter are used in the derivation of the *in vitro* SPF according to equation 1.2.

Figure 6.1. Upper plot: Absorbance spectra (*versus* air reference) of 0.47 mM DMA in Freon 113 in a 1 cm path length cuvette during irradiation with the portable UV lamp at 7.2 cm. Middle plot: Absorbance at 365 nm as a function of irradiation time. The solid black line indicates the slope –(dA/dt). Lower plot: Measured initial rates for each wavelength. The red dashed line corresponds to their average value.

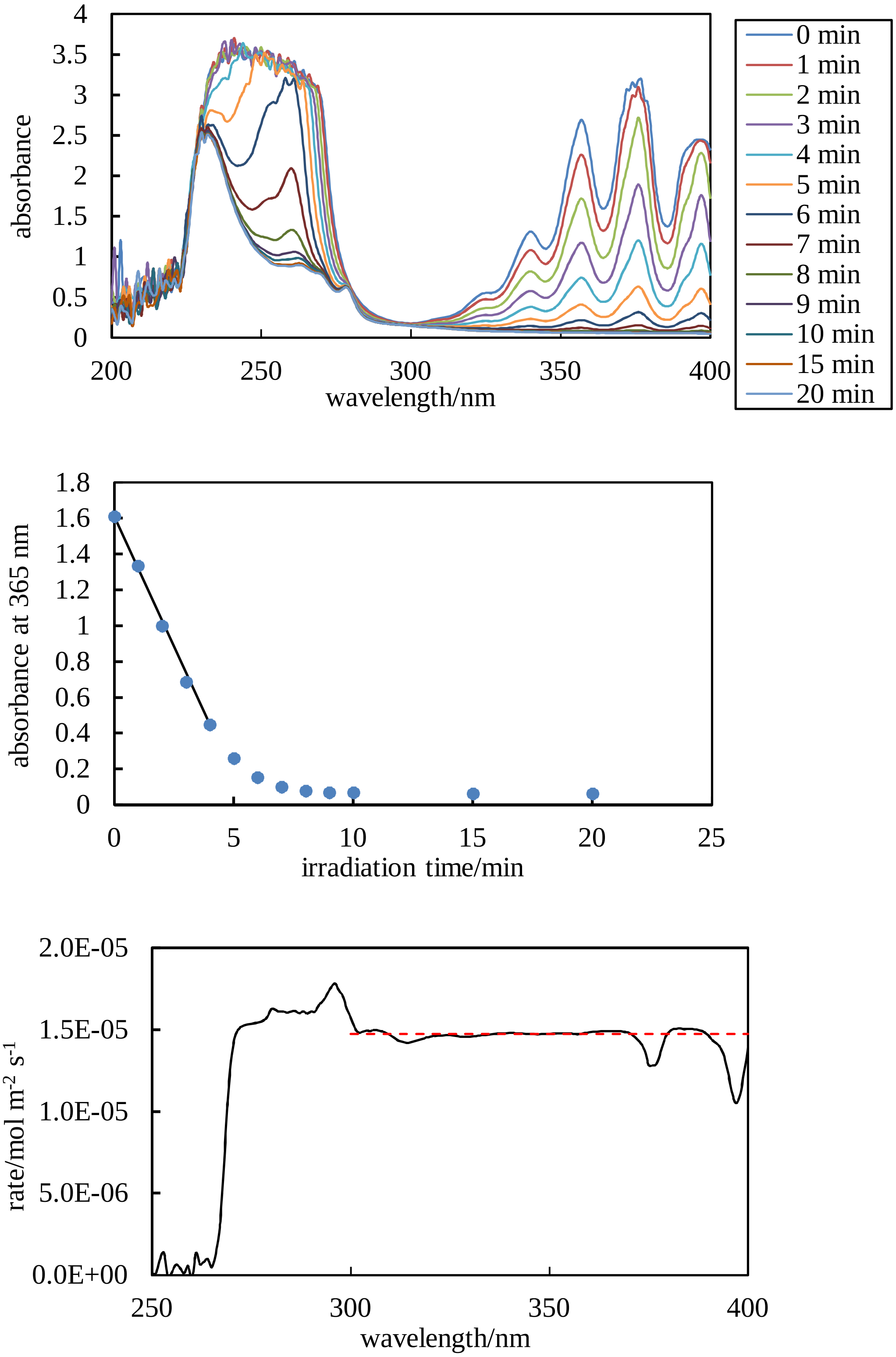

Figure 6.2. Derived spectral irradiances of the light sources used and standard light.

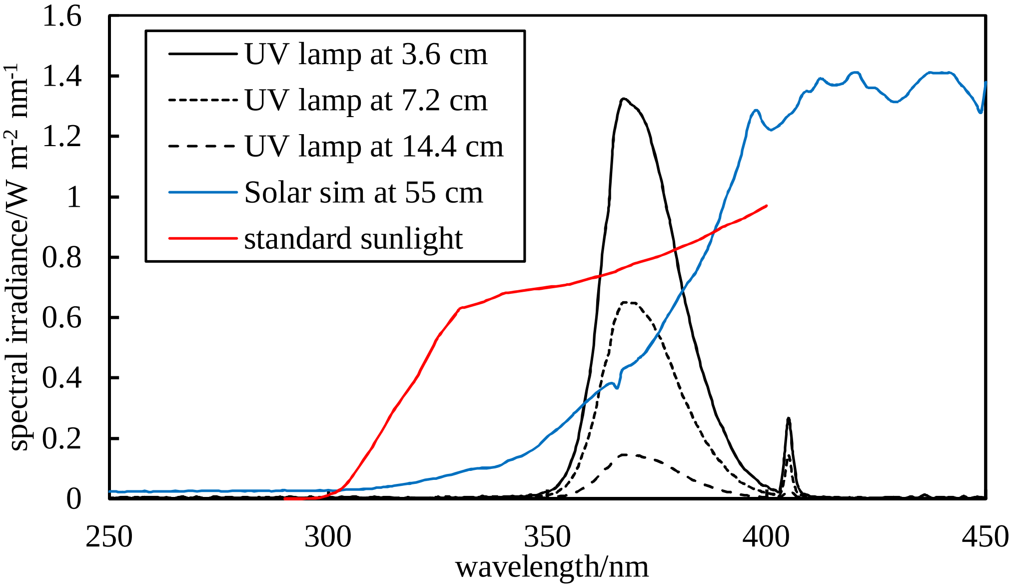

6.4 Photochemical kinetics of solutions of a single UV absorber

Having determined the absolute spectral irradiances of all light sources, the next step was to investigate the photochemical behaviour for a range of concentrations and path lengths of solutions containing a single UV absorber such as AVB, MC, DHHB and BEMT in either SQ or PG.

Irradiation of solutions consisting of AVB or MC in both solvents, resulted in significant changes in their measured absorbance spectra and these are thoroughly discussed in the following sections of this chapter. Extensive irradiation of solutions containing DHHB and BEMT, however, has indicated no changes in their measured absorbance values and these are shown in Figure 6.3. This implies that both DHHB and BEMT are photostable. Due to the very low solubility of BEMT in PG, no data are presented. We have already discussed in Chapter 2 (Experimental) that the actual absorbance plotted in the graphs of this section were obtained by subtraction of the reference spectrum from the sample spectrum. As such, unless otherwise stated, it is implied that all absorbance spectra are *versus* the relevant solvent as reference.

Figure 6.3. Absorbance spectra for 5.03 mM DHHB with path length 0.01 cm in SQ (upper plot) and in PG (middle plot). Lower plot: Absorbance spectra for 3.18 mM BEMT in SQ with path length 0.01 cm. In all cases, the light source was the UV lamp set at 7.2 cm.

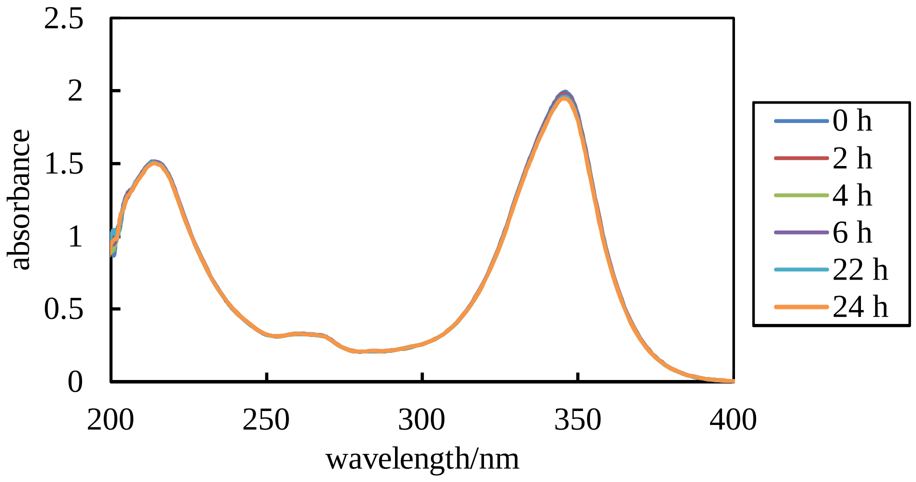

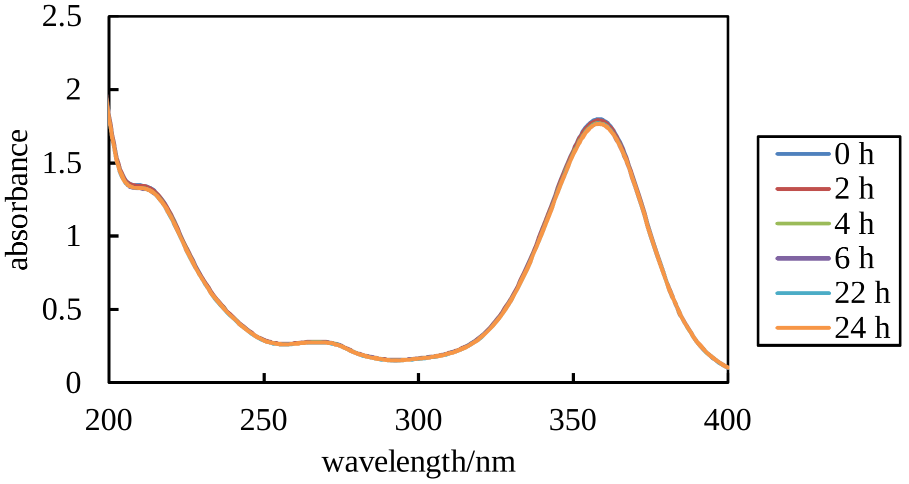

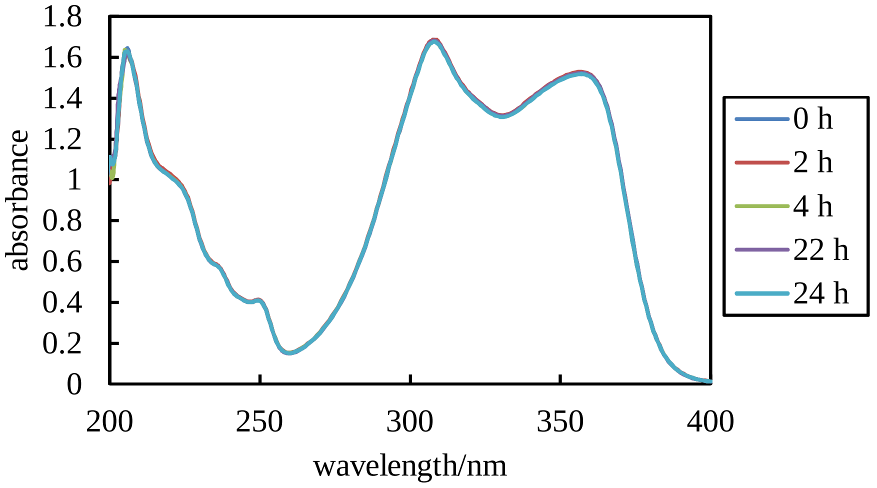

6.4.1 Photochemical kinetics of solutions containing AVB

The photochemistry of AVB in polar and apolar solvents has been extensively investigated.[5-15] Prior to UV irradiation, in the ground state, AVB exists in a mixture of the following two forms: i) the enol (with a strong absorption band around 360 nm) and ii) the keto (with a peak absorbance around 260 nm) in an approximate 9:1 ratio respectively.[14,16] In this study, though in a different solvent such as $CDCl_3$, we have confirmed the initial (*i.e.* pre-irradiated) enol/keto ratio with the use of ^{1}H-NMR. It is the enol form of AVB that it photoisomerises to the keto form upon irradiation. As discussed in Chapter 1 (Introduction), further irradiation of the keto form leads to the formation of photodegradation products (radicals) via a Norrish type I mechanism. The final photoproducts mostly absorb at the UVC region of the electromagnetic spectrum below 280 nm.[10]

It has been reported, however, that the keto can revert to the enol form in a dark reaction.[17] Figure 6.4 illustrates the two peak absorbance values of solutions of 8.0 mM AVB in both solvents with a path length of 0.01 cm. These solutions were initially irradiated for 6 h followed by a consecutive period of 24 h during which they were left in the dark to allow for recovery. The temperature was set at 32^{o}C, which corresponds to skin's outer surface temperature. The peak absorbance changes of AVB during irradiation will be discussed in the following Figure 6.5. From Figure 6.4, we show that for the investigated period of 24 h after sample irradiation there are no signs of recovery of the enol form. However, it is also possible that the reverse reaction might occur at a longer timescale than that examined. This behaviour is observed for solutions of AVB in SQ and PG solvents.

Figure 6.4. Peak absorbance values as a function of time for 8.0 mM AVB in both SQ and PG with path length 0.01 cm. All samples were irradiated (UV lamp at 7.2 cm) for a period up to 6 h as indicated by the dashed line. Beyond that point, no further irradiation occurred. For all measurements, the temperature was set at 32°C.

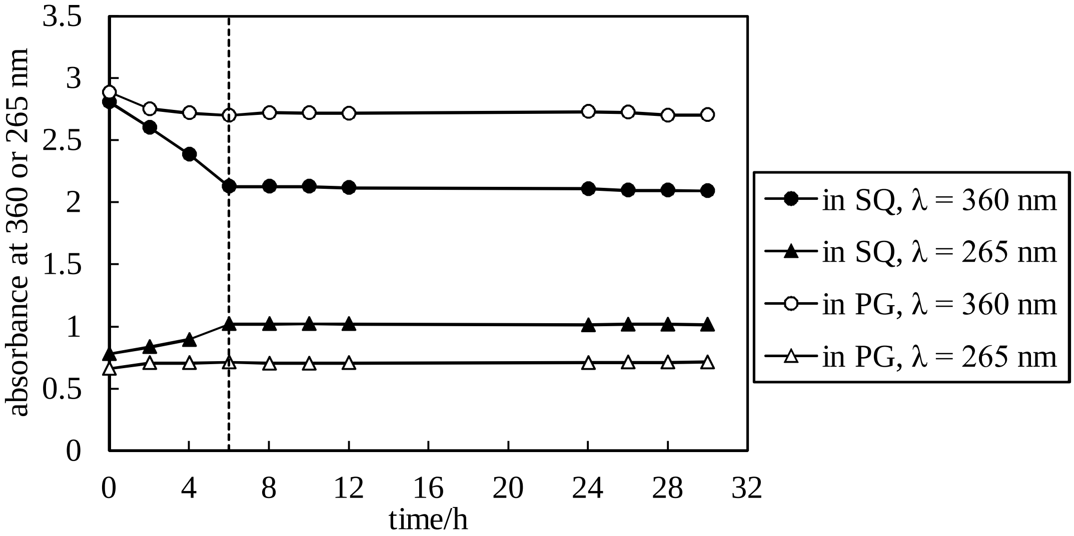

The upper plot of Figure 6.5 shows the measured absorbance spectra of a solution of 8.0 mM AVB in SQ with path length 0.01 cm for an extensive irradiated period of 48 h. The peak absorbance around 360 nm, which is attributed to the enol form, progressively decreases with irradiation time. A second peak, however, which is observed around 262 nm, increases for the same irradiated period. The latter peak absorbance is attributed to the keto species present. It is important to note that the absorbance spectra cross over at several wavelengths (around 230, 240 and 290 nm) within the investigated wavelength range (200 – 400 nm). However, these cross over points are not true isosbestic points, which would be observed if the only process occurring was the conversion from enol to keto form and the solutions contained only mixtures of these two species. The absence of clear isosbestic points confirms the presence of more than two species, which contribute to the overall absorbance.

For AVB, two photochemical processes occur sequentially: i) the enol is converted to the keto form and ii) the keto is converted to a mixture of photo-products. For convenience, we treat the mixture of photo-products as a single species (termed "prod"). For each process, we have to determine its quantum yield. In order to obtain the two quantum yields, we have to estimate the individual molar extinction coefficients of the enol, keto and the photo-product species. For each wavelength, the total absorbance A is the sum of the contributions from the enol, keto and the photo-products according to

$$A = \left(\varepsilon_{enol}[enol] + \varepsilon_{keto}[keto] + \varepsilon_{prod}[prod]\right)d \qquad (6.6)$$

where [enol], [keto] and [prod] correspond to enol, keto and prod concentrations respectively, ε is the wavelength-dependent extinction coefficient of the subscripted species and d is the path length. The sum of the concentrations of the enol, keto and prod species is equal to the initial overall concentration of AVB. Equation 6.6 was used to determine the calculated absorbance spectra as a function of irradiation time for guessed values of the concentrations of all species (enol, keto and the prod) and their molar extinction coefficients for the wavelength range 235 – 400 nm.

The calculated absorbance spectra were compared with the measured absorbance spectra and the sum of the absolute differences computed. The residual sum between the global set of measured and calculated spectra was minimised by adjustment of all the unknown parameters with the use of Solver function in MS Excel. This procedure involves fitting a total of over 500 unknown parameters; it is important to note here that Solver allows only fitting of a maximum of 200 unknown parameters and so the fitting was performed in several stages. Despite this large number of fitting parameters, it was found that the fitting procedure successfully converged to a solution for which the average deviation between measured and calculated values of the overall absorbance was approximately equal to the experimental uncertainty in the measured absorbance (approx. 0.003 absorbance units). It was checked that consistent fits were obtained when starting the fitting procedure from widely different initial parameter values.

The middle plot of Figure 6.5 shows the fitted values of the species' concentrations as a function of irradiation time. The initial estimated concentrations of enol and keto in the SQ solution are approximately 95% and 5% respectively, which are in very good agreement with the enol/keto ratio.[14,16] The initial prod concentration is zero. It can be seen that the [enol] progressively decreases for the investigated irradiation time, as opposed to the [keto], which increases instead. In this particular example, the [keto] has reached its highest value after 24 h during which the [prod] is negligible. Beyond 26 h, however, the [keto] starts decreasing whereas the [prod] increases steadily.

The lower plot of Figure 6.5 shows the final derived molar extinction coefficient spectra from the fitting procedure described above. It is important to note that the values of the molar extinction coefficients of both enol and keto forms are accurate. This is not the case, however, for the values of the molar extinction coefficient of the products. A relatively large uncertainty is introduced as a result of the very low product formation. The product absorbance is approximately zero within the uncertainty for all wavelengths greater than 250 nm.

Figure 6.5. Upper plot: Measured absorbance spectra (*versus* SQ reference) for 8.0 mM AVB in SQ with path length 0.01 cm. Middle plot: Species concentrations as a function of irradiation time (UV lamp at 7.2 cm) obtained by fitting the measured absorbance spectra shown above. Lower plot: Derived molar extinction coefficient spectra of the enol, keto and product species.

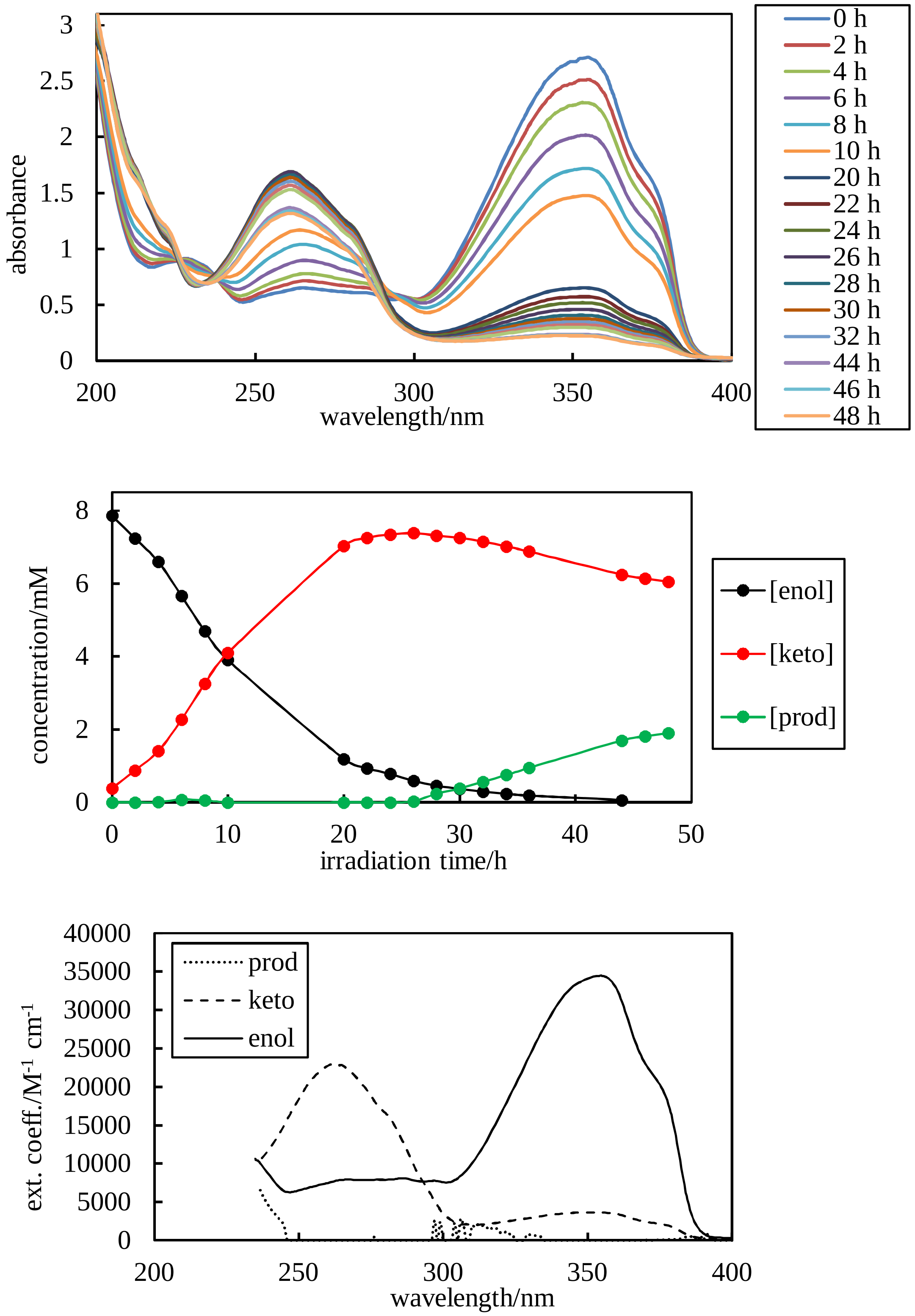

The estimated quantum yields of the two photochemical processes of AVB, the calculated absorbance spectra and the calculated *in vitro* SPF values during irradiation were determined using the following procedure.

1. For time zero, the initial absorbances due to each species are calculated using the relevant extinction coefficient spectra (equation 6.6). Using guessed initial values of the two quantum yields (assumed to be wavelength independent) and the known spectral irradiance spectra of the light source, the rates of the enol to keto and keto to product processes are calculated (using equations 6.1 – 6.4) for each wavelength and summed over the emission wavelength range of the lamp to obtain the overall rates.
2. The irradiation time is incremented by a suitable time step, the overall rates from the previous time step are used to calculate the new concentrations of the enol, keto and prod species. Absorbances due to the individual species and total absorbance are calculated and used to derive the new values of the rates. In addition to obtaining the absorbance spectra at each time step, the *in vitro* SPF is also derived according to equation 1.2.
3. Step 2 is repeated over sufficient time steps until calculated spectra and *in vitro* SPF values are obtained, which cover the same irradiation times as the measured spectra (and their derived *in vitro* SPF). For time steps at which measured and calculated spectra are available, the absolute differences between the measured and calculated spectra are summed. Using Solver, the two quantum yields are floated to minimise the residual sum between measured and calculated spectra as a function of irradiation time for the entire data set.

The upper and middle plots of Figure 6.6 show the measured and the calculated absorbance spectra respectively of 12.0 mM AVB in SQ for the irradiation period of up to 360 min. The latter were derived from the simulation procedure described above. It can be seen that both data sets are in excellent agreement. The lower plot of Figure 6.6 also compares both measured and calculated time-dependent *in vitro* SPF values, which resulted from measured and calculated absorbance data respectively using equation 1.2. Based on the wavelength integration limit, all three types of *in vitro* SPF are shown. The SPF (320 – 400 nm) is progressively decreasing due to the conversion of the enol, which is the only species that absorbs in the UVA region, to the keto form and eventually to photo-products. The absorbance of the keto form does not contribute to the overall *in vitro* SPF values.

Figure 6.6. Comparison of measured (upper plot) and calculated (middle plot) absorbance spectra for 12.0 mM AVB in SQ with 18 μm path length and with the UV lamp set at 7.2 cm. Lower plot: *in vitro* SPF values derived from both measured and calculated absorbance data as a function of irradiation time.

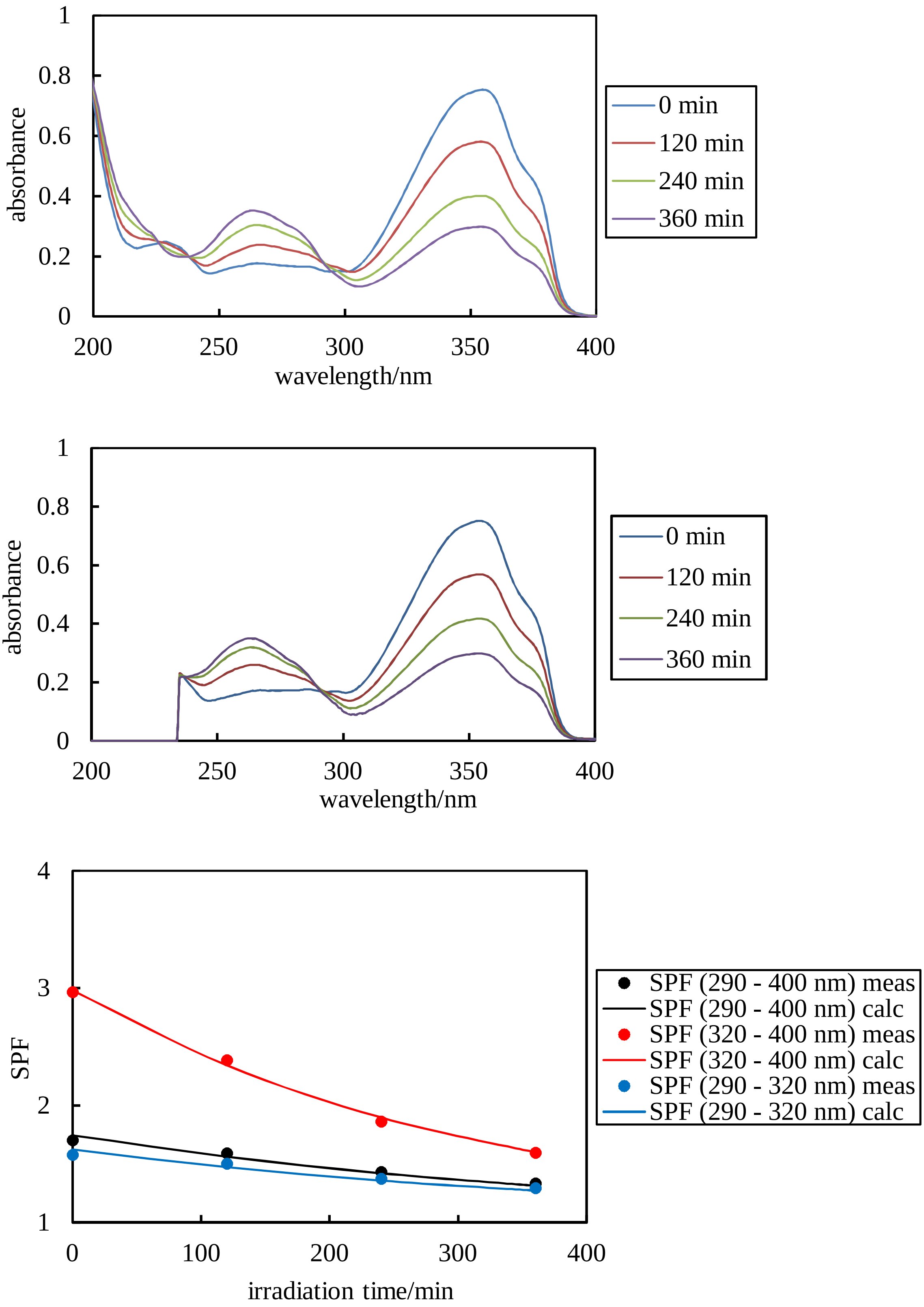

To further assess the validity of the fitting procedure, all steps were repeated for another data set with significantly different concentration and path length. The upper plot of Figure 6.7 shows the measured absorbance spectra of 0.045 mM AVB in SQ solution with a path length 1 cm. The lower plot of Figure 6.7 presents the relevant calculated absorbance spectra, which are derived from the simulation procedure. A comparison between measured and calculated values show that they are in reasonable agreement.

The upper plot of Figure 6.8 shows the calculated values of species' concentrations as a function of irradiation time. As expected, the fitted values demonstrate the decrease of the [enol] and the increase of the [keto] for the investigated period. In this particular example, the [keto] reaches a plateau value after around 40 h of irradiation. For the same investigated period, the initially negligible [prod] starts increasing. It is also important to note that the molar extinction coefficient values, though not shown here, were consistent with our previous example.

This behaviour is also depicted in the lower plot of Figure 6.8 for both measured and calculated *in vitro* SPF values. Similar to our previous findings, the initial SPF (320 – 400 nm) performance is progressively lost as a result of the enol conversion to the keto form and finally to photoproducts. Overall, a comparison between widely different concentrations and path lengths of AVB in SQ solutions presented above, confirms the quality of the fitting procedure.

Figure 6.7. Measured (upper plot) and calculated (lower plot) absorbance spectra for 0.045 mM AVB in SQ with path length 1 cm. UV lamp at 7.2 cm. All samples *versus* SQ reference.

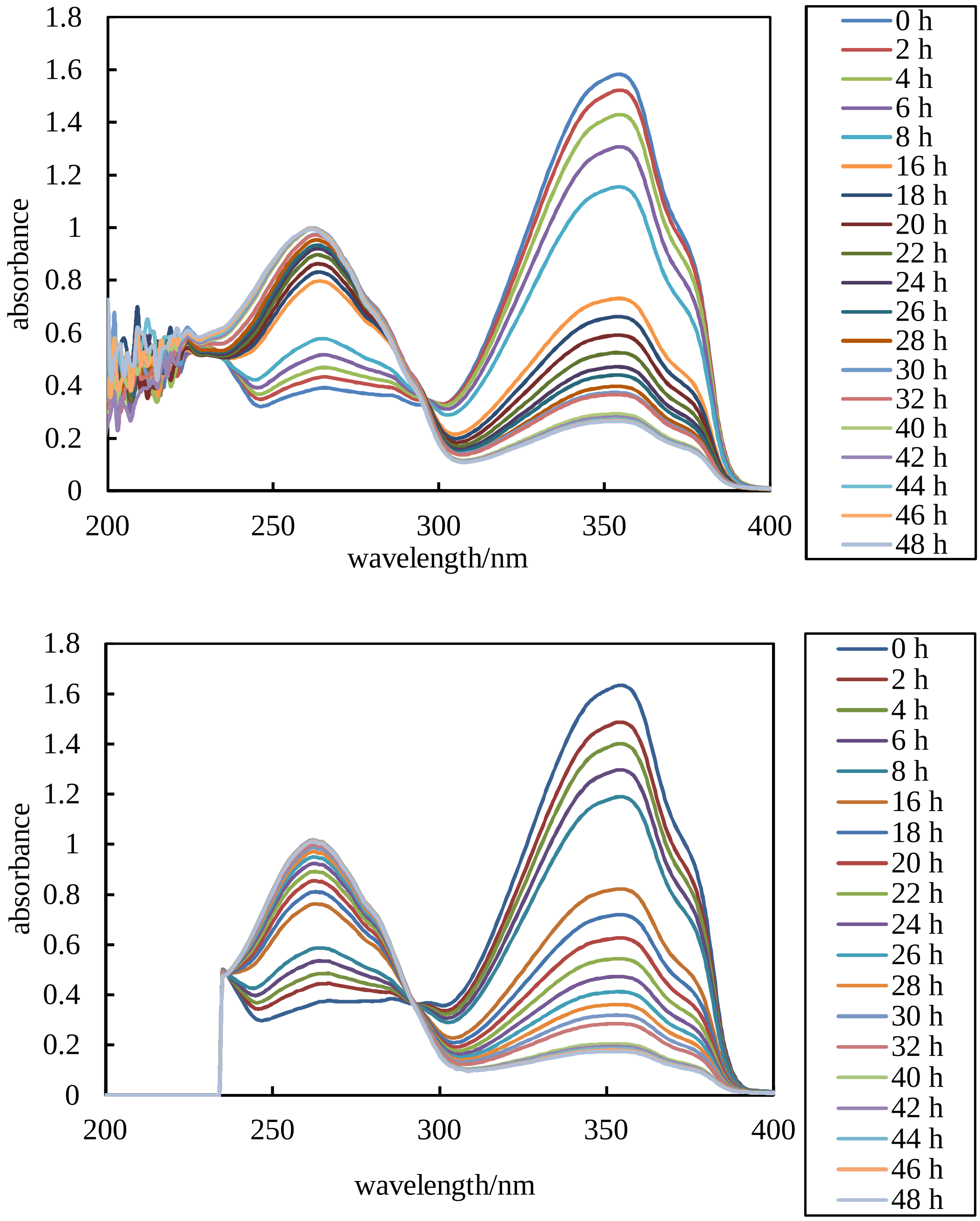

Figure 6.8. Upper plot: Species concentrations as a function of irradiation time (UV lamp at 7.2 cm) obtained by fitting the measured absorbance spectra shown above. Lower plot: *in vitro* SPF values as a function of irradiation time.

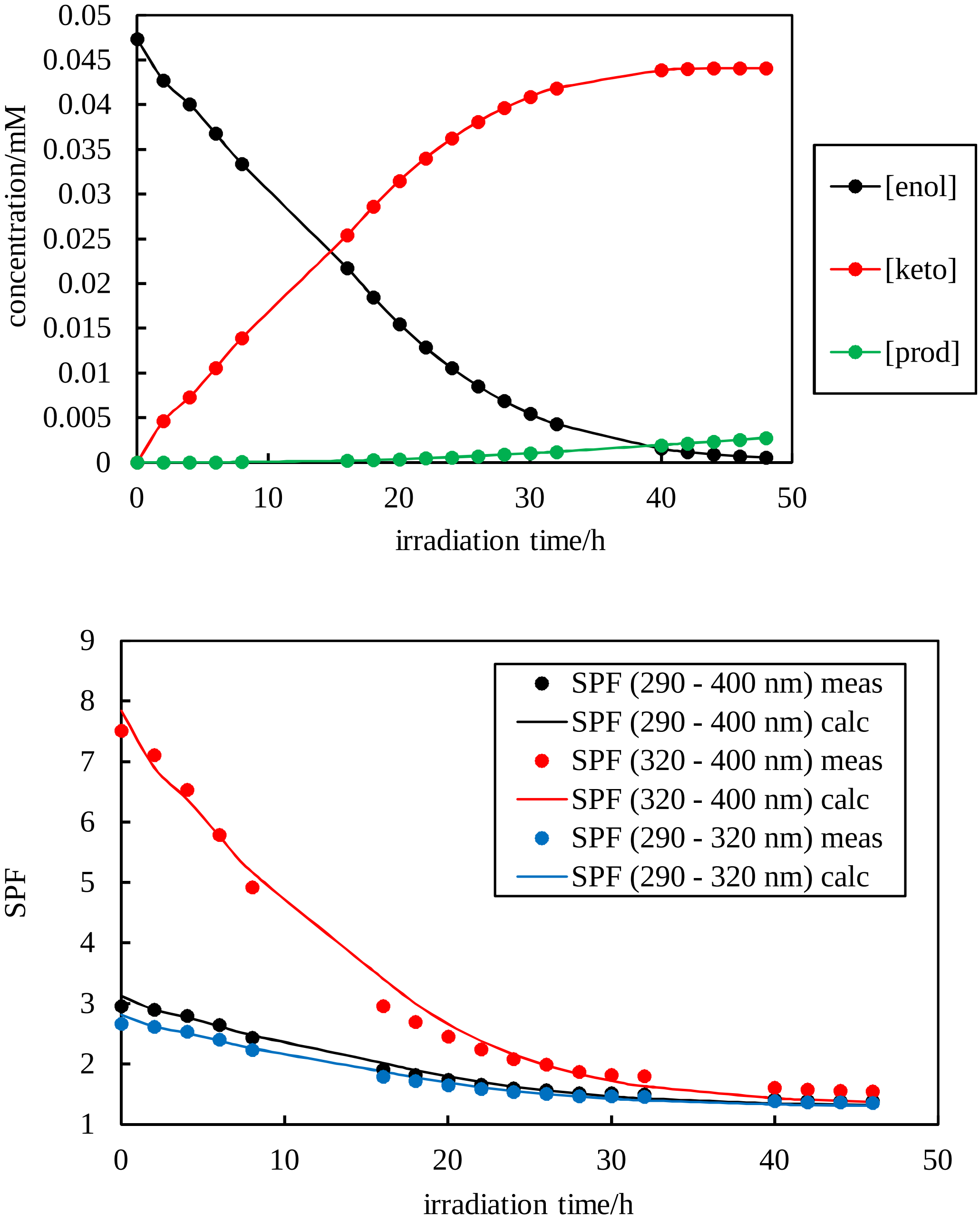

The fitting procedure for the determination of the quantum yields was repeated for a total of six different data sets of AVB in SQ solutions. The data sets included the following combinations: i) the use of different light sources and ii) a wide range of concentrations from 0.045 to 12 mM with path lengths from 1 to 0.0018 cm respectively.

The photochemical behaviour of AVB was also examined in a polar protic solvent such as PG. The upper plot of Figure 6.9 shows the measured absorbance spectra of a solution containing 8.0 mM AVB in PG with a path length 0.01 cm. Again, two peaks in the absorbance spectrum are present, which are attributed to the enol (around 360 nm) and keto form (around 260 nm). For the wavelength range of interest, three cross over wavelengths around (240, 250 and 300 nm) are observed, which are not however clear isosbestic points. The middle plot of Figure 6.9 shows the fitted values of species' concentrations as a function of irradiation time. The initial estimated concentrations of enol and keto in the PG solution are approximately 97% and 3% respectively. Similar to our previous estimation, the [enol] decrease and the [keto] increase is predicted but at a slower rate than that described in SQ. The [prod] progressively increases. The lower plot of Figure 6.9 shows the final derived molar extinction coefficient spectra of all species involved.

The upper and middle plots of Figure 6.10 show measured and calculated absorbance values for 8.0 mM AVB in PG solution with path length 0.01 cm. The latter values were obtained from the fitting procedure that was earlier described. The agreement for both data sets is evident. This behaviour is depicted in the lower plot of Figure 6.10, where the *in vitro* SPF values are presented as a function of irradiation time. SPF (320 – 400 nm) values decrease linearly as a result of enol conversion, whereas the other two types of SPF remain constant throughout.

Figure 6.9. Upper plot: Absorbance spectra (*versus* PG reference) for 8.0 mM AVB in PG with path length 0.01 cm. Middle plot: Species concentrations as a function of irradiation time (UV lamp at 7.2 cm) obtained by fitting the measured absorbance spectra shown above. Lower plot: Derived molar extinction coefficient spectra of the enol, keto and the prod species.

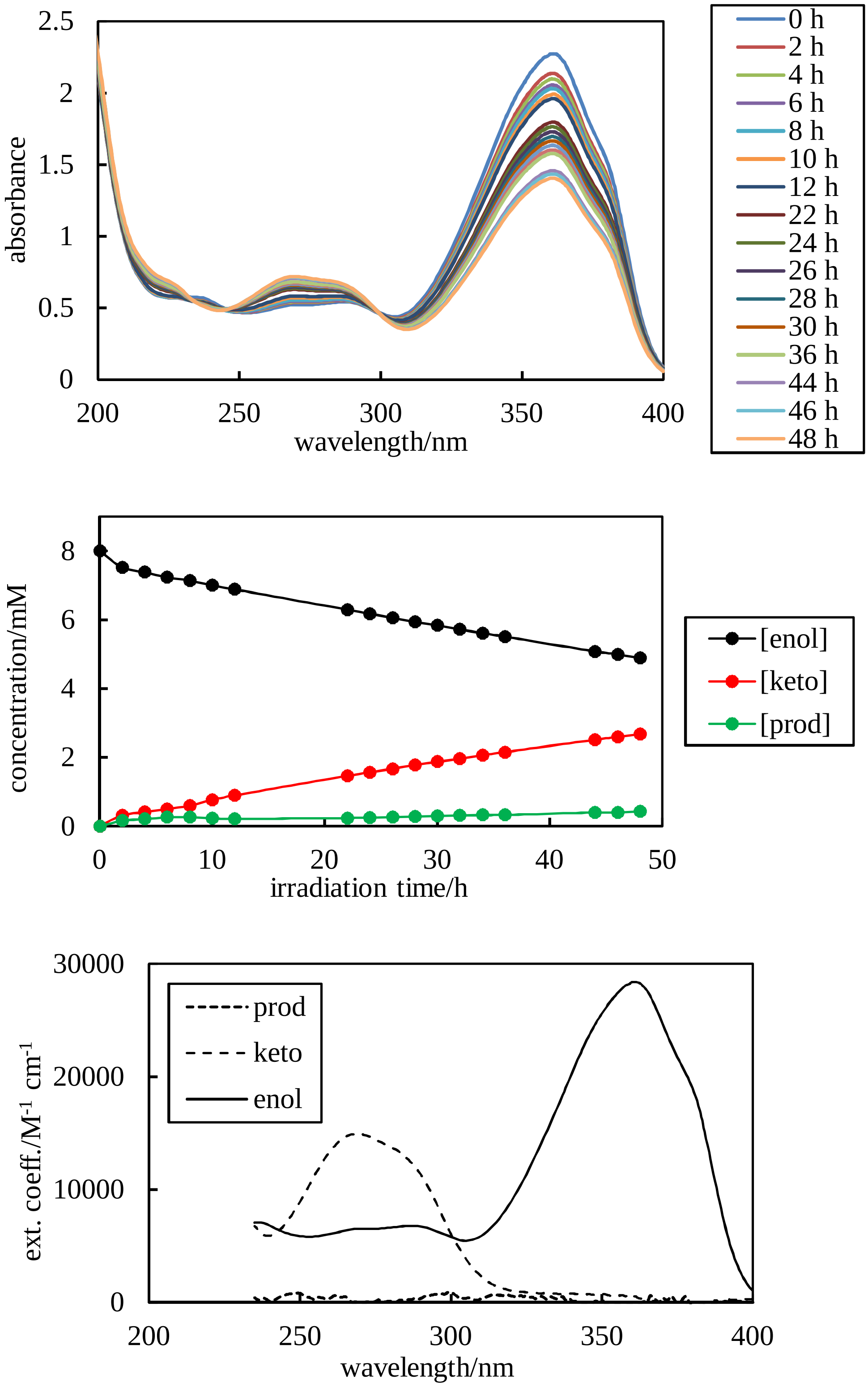

Figure 6.10. Comparison of measured (upper plot) and calculated (middle plot) absorbance spectra for 8.0 mM AVB in PG with 0.01 cm path length with the solar simulator. Lower plot: *in vitro* SPF values derived from both measured and calculated absorbance data as a function of irradiation time.

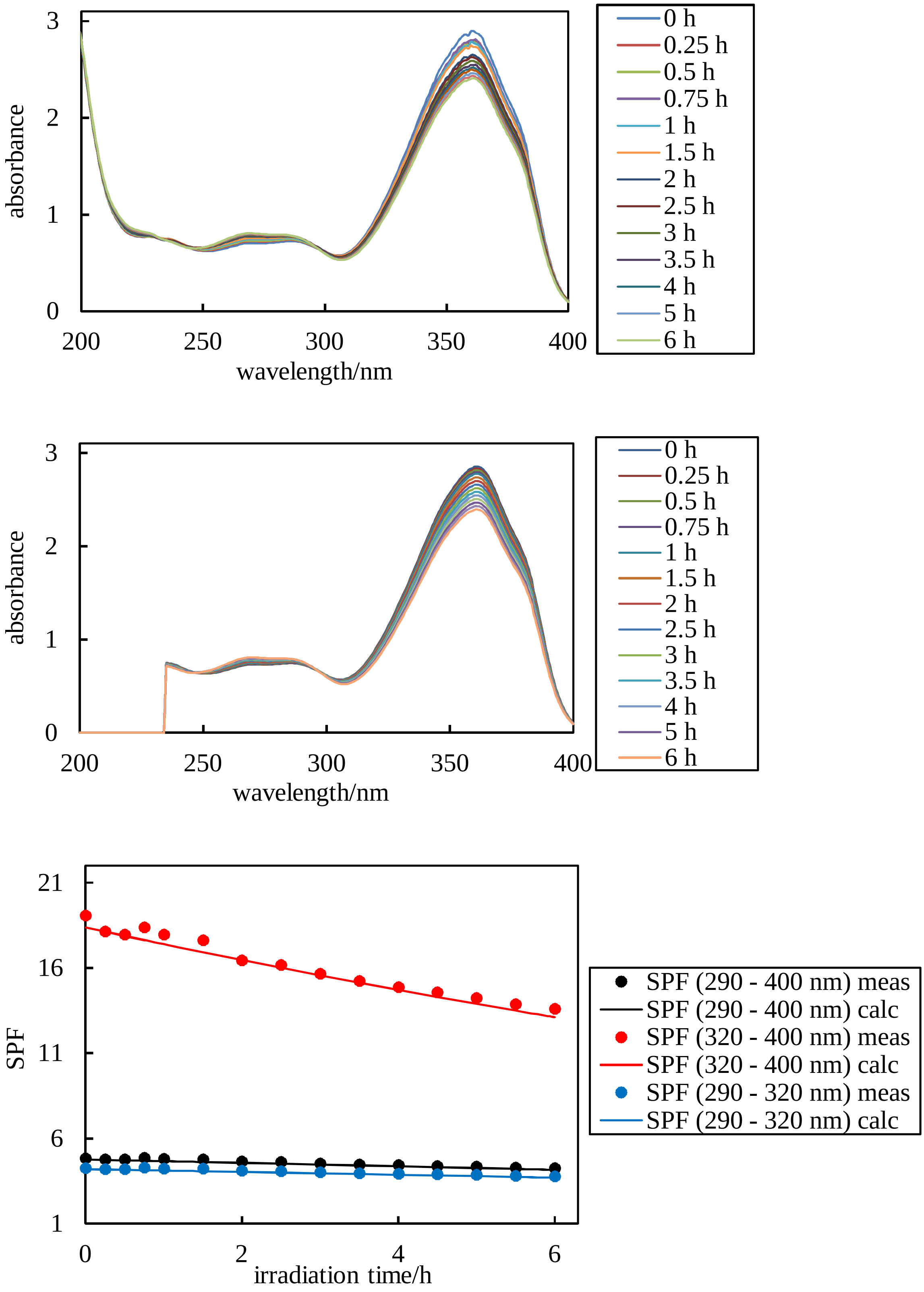

6.4.2 Photochemical kinetics of solutions containing MC

In general, cinnamates undergo both *trans* to *cis* and *cis* to *trans* isomerisations upon irradiation.[6,12,13,18-23] For the received MC, though $CDCl_3$ was the solvent of choice, we have confirmed by ^{1}H-NMR that it consisted entirely of the *trans* isomer. As such, irradiation of the *trans* form of MC results in its conversion to the *cis* isomer. However, the reversible reaction with the conversion of the *cis* isomer back to the *trans* form upon irradiation is also present. Hence, the *trans*/*cis* ratio initially changes, but eventually reaches a steady-state where the photochemical rates for both reactions do not change with further irradiation. This behaviour is observed irrespective of the nature of the solvent.

Figure 6.11 illustrates the behaviour of solutions of MC in both solvents with a path length 0.01 cm that were initially irradiated for 1 h followed by a consecutive period of 24 h during which they were left in the dark to allow for recovery. For the irradiated period, the decrease in the peak absorbance is a result of the isomerisation process of the *trans* to the *cis* form. This is more evident for the MC in PG solution. Overall, for the investigated period of 24 h after irradiation, the mixture of *cis* and *trans* that was formed, did not revert back to its original 100% *trans* form.

Figure 6.11. Peak absorbance values as a function of time for two concentrations of 2.00 and 8.38 mM of MC in SQ and PG with path length 0.01 cm. All samples were UV irradiated (UV lamp at 7.2 cm) for 1 h as indicated by the dashed line. Beyond that point, no further irradiation occurred. For all measurements, the temperature was set at 32°C.

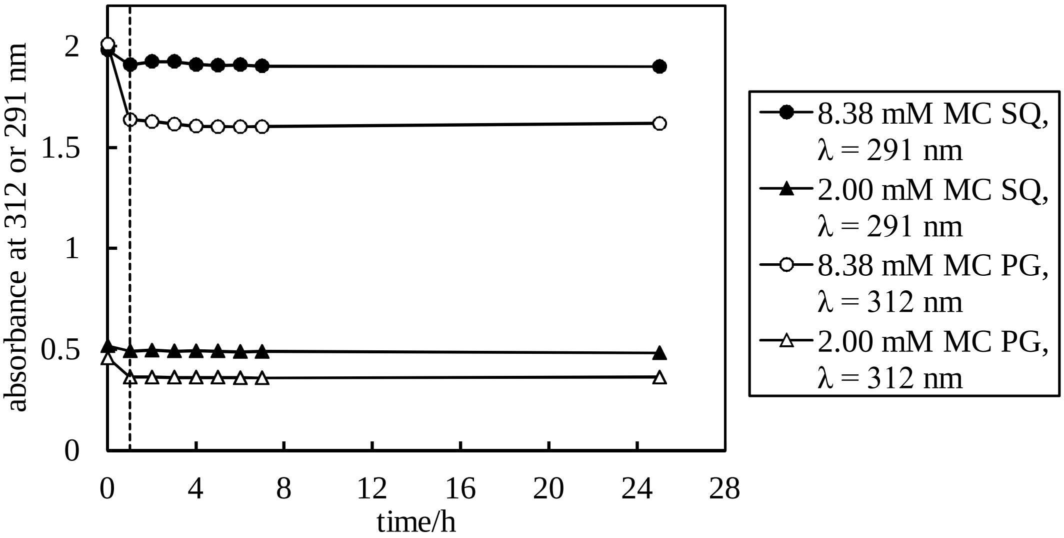

The upper plot of Figure 6.12 shows the absorbance spectra during irradiation of 0.5 mM MC in PG with path length 0.1 cm. The peak absorbance at 312 nm decreases for the first 120 min. Beyond 180 min, the peak absorbance remains constant. For the MC in PG system, it can be seen that the isosbestic points are clear and are maintained. This is a confirmation that only two absorbing species are present. For the two processes, the following quantum yields need to be determined: i) the quantum yield of the *trans* to *cis* isomerisation and ii) the quantum yield of the *cis* to *trans* isomerisation.

The middle plot of Figure 6.12 shows the fitted values of the MC species' concentrations as a function of irradiation time. Consistent with our absorbance measurements, it can be seen that beyond 180 min, both concentrations remain constant. The derived molar extinction coefficients of both the *trans* and the *cis* isomers are shown in the lower plot of Figure 6.12. The molar extinction coefficient values of the *cis* isomer are significantly lower than those of the *trans* form. This explains the loss in the absorbance and eventually in the SPF performance. Overall, the molar extinction coefficients of both species are similar to those reported for octylmethoxycinnamate in different solvents.[20,21,23]

Figure 6.12. Upper plot: Measured absorbance spectra (*versus* PG reference) during irradiation for 0.5 mM MC in PG with path length 0.1 cm. Middle plot: Species concentrations as a function of irradiation time (UV lamp at 14.4 cm) obtained by fitting the measured absorbance spectra shown above. Lower plot: Derived molar extinction coefficient spectra of the *trans* and *cis* species.

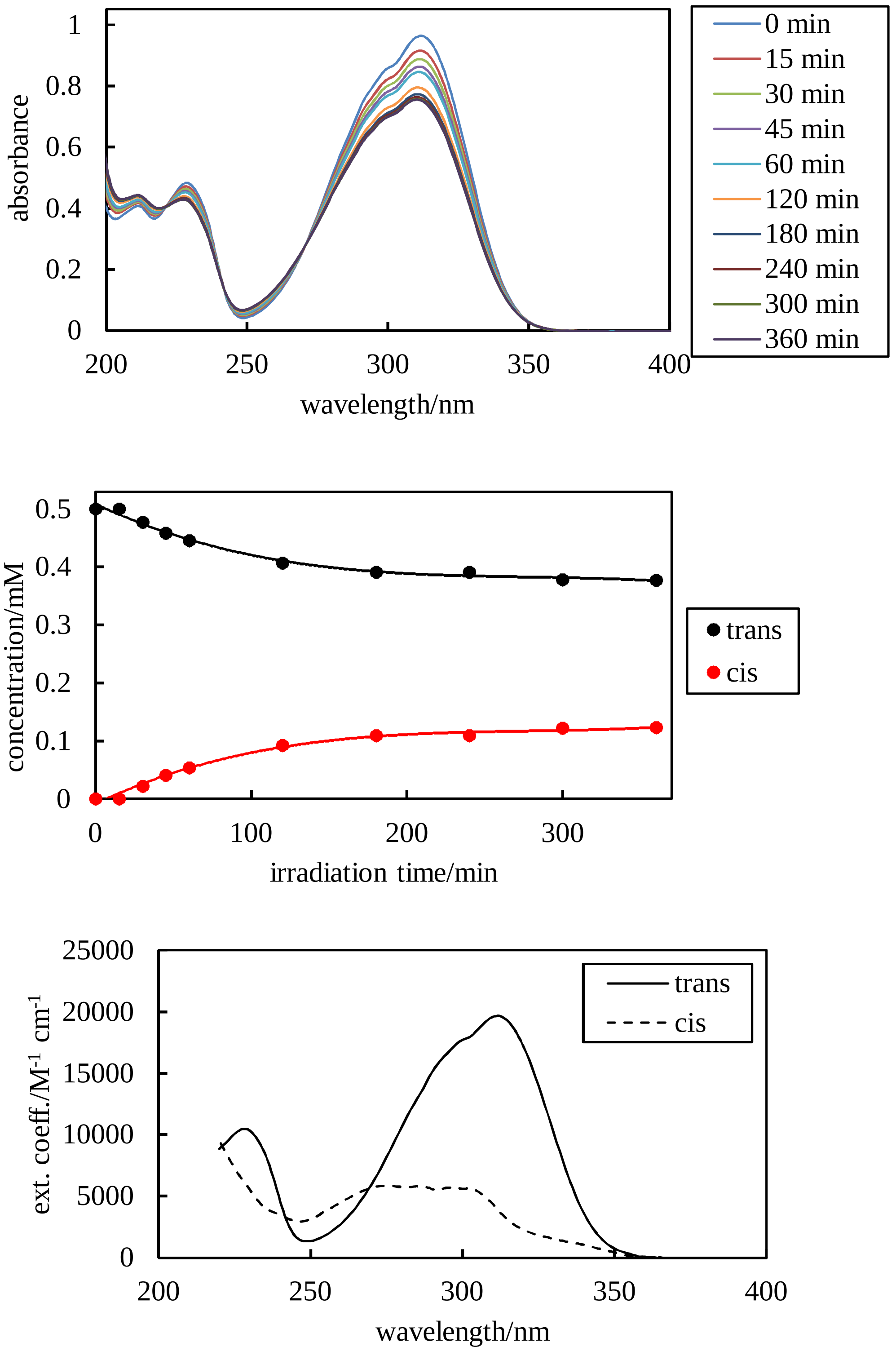

Using the fitting procedure described for AVB, the calculated absorbance spectra of MC were derived for known values of molar extinction coefficients, concentrations and guessed values of two quantum yields. Minimisation of the residual sum computed from comparison between measured and calculated spectra yielded the best-fit values of both quantum yields. As for AVB, consistent results from this fitting procedure were obtained for runs using the UV lamp at the different distances and the solar simulator and MC solutions with concentrations ranging from 0.08 to 6 mM and path lengths in the range 0.01 to 1 cm.

The upper and middle plots of Figure 6.13 show the excellent agreement between measured and calculated absorbance spectra of 6.0 mM MC in PG. This behaviour is also depicted in the lower plot of Figure 6.13, which compares both measured and calculated *in vitro* SPF values as a function of irradiation time. Overall, it can be seen that the *in vitro* SPF values show a decrease for the first 40 min during irradiation. For the SPF (290 – 320 nm) in particular, this decrease is more intense as a result of the photoisomerisation of MC, which strongly absorbs only in the UVB region of the spectrum. Beyond 60 min, however, all *in vitro* SPF values remain constant.

Our investigation was also extended to solutions of MC in non-polar solvents. The upper plot of Figure 6.14 shows the measured absorbance spectra of 6.0 mM MC in SQ with path length 0.01 cm. The peak absorbance at 291 nm progressively decreases for the investigated period of 360 min. Similar to our previous findings of MC in PG, the isosbestic points are still clear and maintained. The middle and lower plot of Figure 6.14 show the fitted values of species' concentrations and the derived molar extinction coefficients respectively.

Using the same fitting procedure, the upper and middle plots of Figures 6.15 show the excellent agreement between measured and calculated absorbance spectra for 6.0 mM MC in SQ. A further comparison between measured and calculated *in vitro* SPF values is illustrated in the lower plot of Figure 6.15. Only the SPF (290 – 320 nm) values show a decrease due to the photoisomerisation of MC. The values of the other two types of SPF are relatively low and remain constant throughout.

Figure 6.13. Comparison of measured (upper plot) and calculated (middle plot) absorbance spectra for 6.0 mM MC in PG with 0.01 cm path length. Lower plot: *in vitro* SPF values as a function of irradiation time with the UV lamp at 7.2 cm.

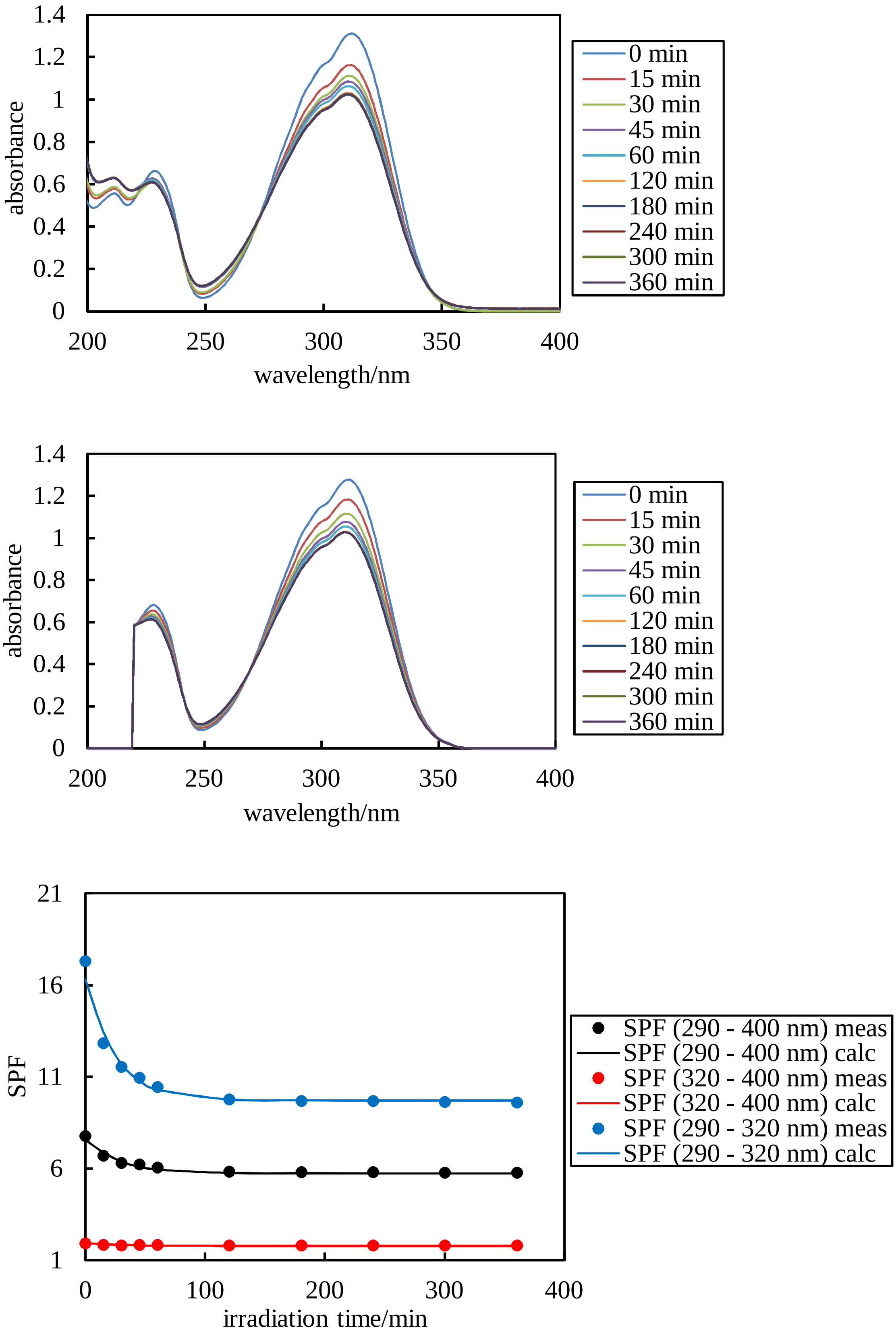

Figure 6.14. Upper plot: Measured absorbance spectra (*versus* SQ reference) for 6.0 mM MC in SQ with path length 0.01 cm. Middle plot: Species concentrations as a function of irradiation time (UV lamp at 3.6 cm) obtained by fitting the measured absorbance spectra shown above. Lower plot: Derived molar extinction coefficient spectra of the *trans* and *cis* species.

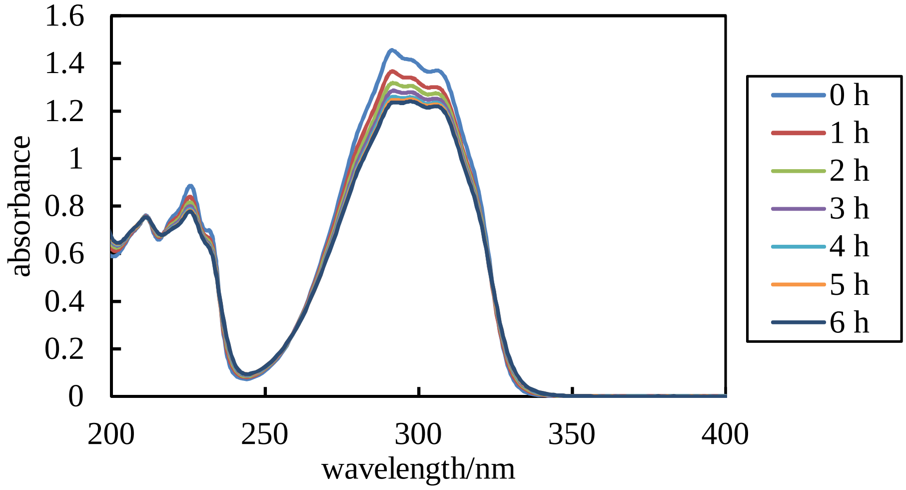

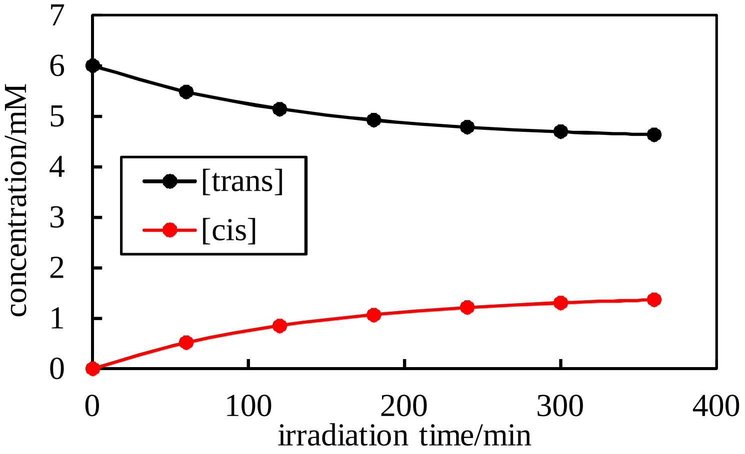

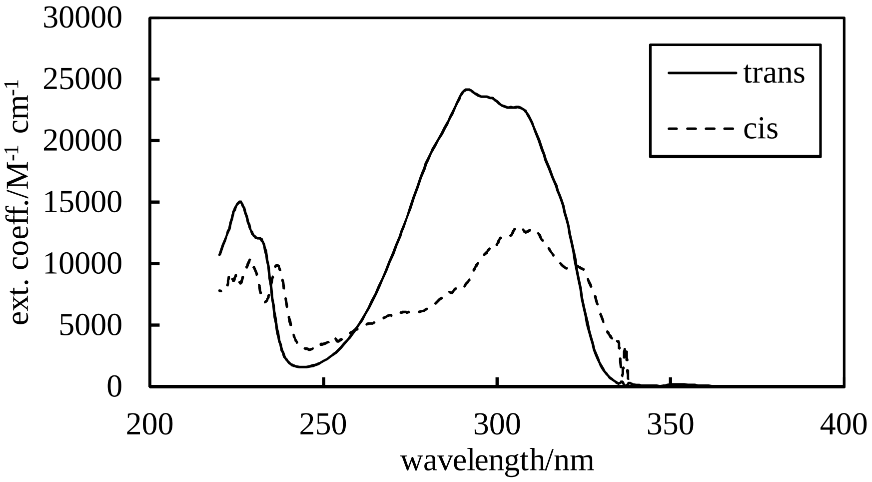

Figure 6.15. Comparison of measured (upper plot) and calculated (middle plot) absorbance spectra and *in vitro* SPF values (lower plot) for 6.0 mM MC in SQ with 0.01 cm path length as a function of irradiation time with the UV lamp set at a fixed position at 3.6 cm.

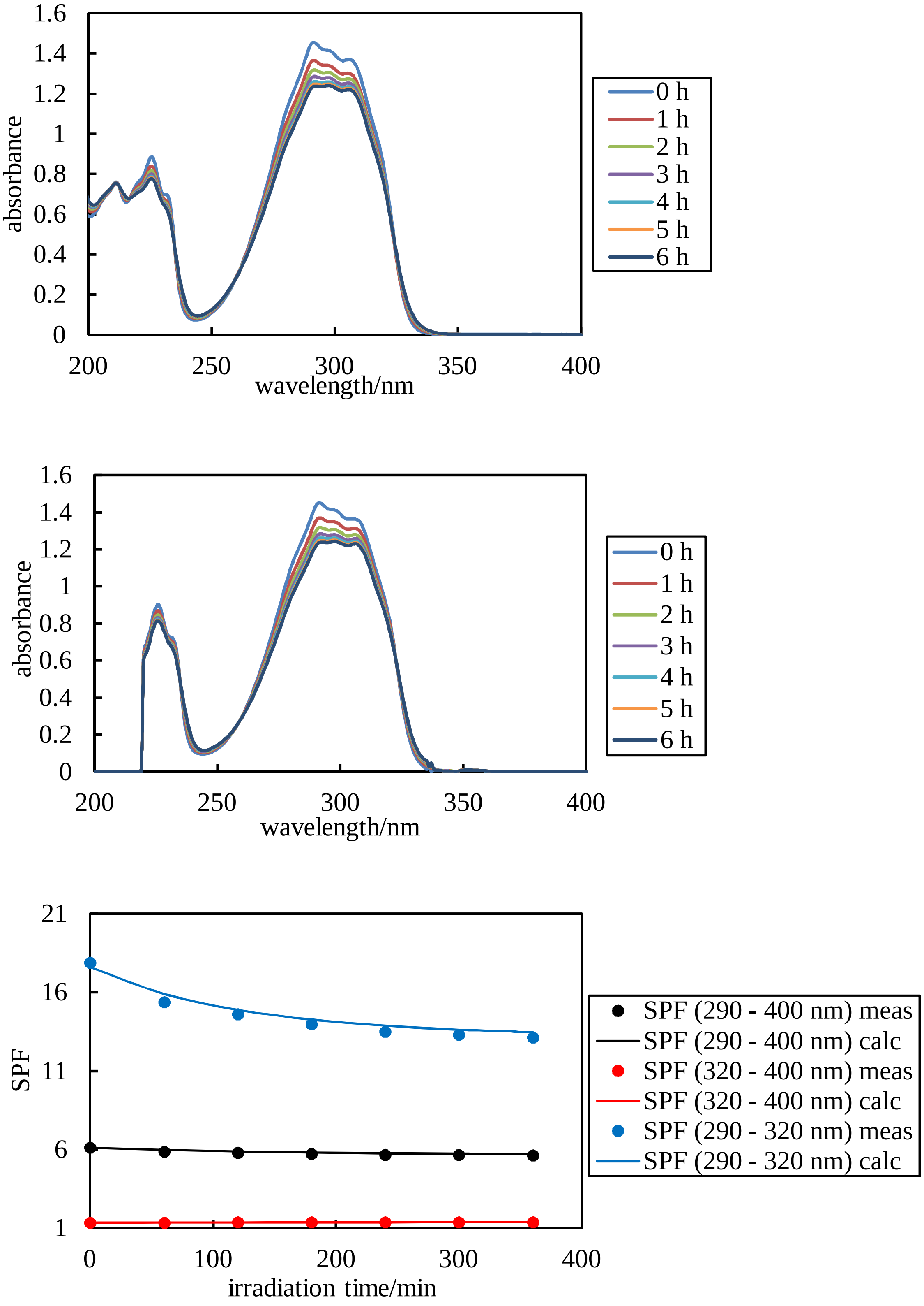

Quantum yields from all runs for AVB and MC in both solvents yield the final averaged values shown in Table 6.1. Compared with the values for AVB, the quantum yields for MC are two to three orders of magnitude larger. This implies that the photochemical rates of MC solutions are much faster when irradiated under the range of light sources used in this study. A second difference relates to the solvent dependence. For AVB, the rates are faster in SQ than in PG whereas the opposite is true for MC. Finally, we note that the two quantum yields for MC in PG add up to more than one.

For the enol to keto reaction, the quantum yields obtained were consistent within an estimated uncertainty of 50% (standard deviation/mean). Since the keto to prod reaction produces smaller changes in the spectra, the uncertainty in the quantum yield is higher and approaches 100% (standard deviation/mean).

Although the quantum yields obtained from the different runs where somewhat variable (giving the relatively high uncertainty in the final averaged values), it was checked that the values from individual runs showed no systematic trends with either solute concentration or with the irradiation light source used. We conclude that the relatively high observed uncertainties probably result from random variability in the emission outputs of the light sources used.

Table 6.1. Quantum yields for the photochemical processes of AVB and MC in SQ and PG at 32^{o}C.

System	**Quantum yield ϕ**	**Quantum yield ϕ**
	Enol to keto	Keto to prod
AVB in SQ	$2 \pm 1 \text{ x } 10^{-4}$	$\sim 2 \text{ x } 10^{-4}$
AVB in PG	$4 \pm 2 \text{ x } 10^{-5}$	$\sim 2 \text{ x } 10^{-4}$
	Trans to *cis*	*Cis* to *trans*
MC in SQ	0.028 ± 0.009	0.10 ± 0.03
MC in PG	0.16 ± 0.05	1.0 ± 0.3

6.5 Photochemical kinetics of solutions containing a combination of UV absorbers

In the previous section, the photochemical behaviour of solutions containing a single UV absorber was discussed. It is important to investigate, however, how irradiation affects a solution containing a mixture of UV absorbers. For convenience, the two UV absorbers of choice were the photolabile AVB and the photostable BEMT.

Figure 6.16 shows a comparison between measured and calculated absorbance spectra during irradiation of a mixture of 2.5 mM AVB and 2.23 mM BEMT in SQ for an investigated period of up to 48 h. The calculated absorbance values are determined based on the previously estimated molar extinction coefficients of the enol, keto and the prod species of AVB and BEMT plus the AVB quantum yield values. From Figure 6.16, it can be seen that both measured and calculated absorbance values are in excellent agreement. The photostable BEMT acts as a “spectator” species, which partially absorbs the light intensity and thus retards the two AVB photo-processes. This behaviour is depicted on the upper plot of Figure 6.17 where the derived individual species’ concentrations during irradiation of the solution containing 2.5 mM AVB and 2.23 mM BEMT are compared with those of the solution containing 2.5 mM AVB alone. The rates of loss of enol, gain of keto and gain of the final product are reduced by approximately two-fold by the addition of BEMT at the concentration used.

The lower plot of Figure 6.17 shows the three types of *in vitro* SPF as a function of irradiation time for both investigated systems. For each system, the excellent agreement between measured and calculated *in vitro* SPF values is evident. For the system containing AVB and BEMT, it can be seen that the presence of BEMT enhances the initial SPF performance compared to that of the solution containing AVB alone. In addition, the decrease in the SPF occurs at slower rate for the solution that contains the mixture of the two UV absorbers. These observations are valid for all types of *in vitro* SPF. Results for different mixtures of AVB and BEMT, though not shown here, showed similar agreement between measured and calculated spectra.

Figure 6.16. Comparison of measured (upper plot) and calculated (lower plot) absorbance spectra for 2.5 mM AVB plus 2.23 mM BEMT in SQ with 0.01 cm path length as a function of irradiation time with the UV lamp at 7.2 cm.

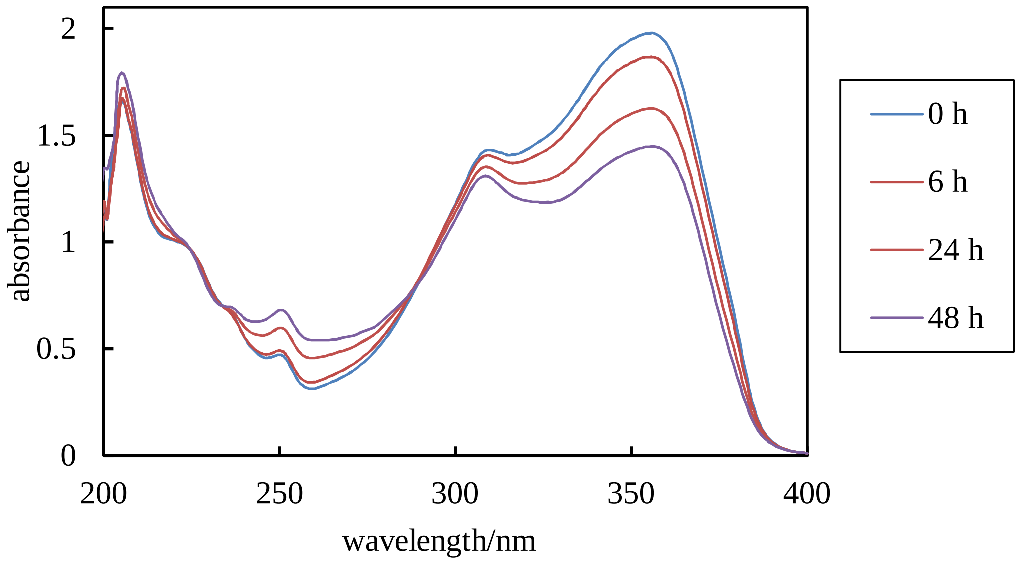

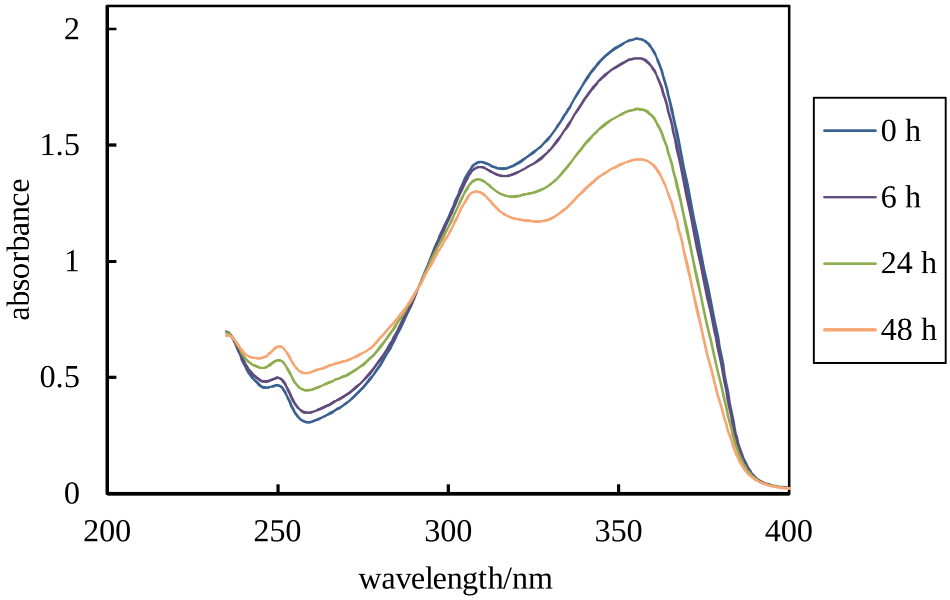

Figure 6.17. Upper plot: Variation of the concentrations of the enol, keto and product species of 2.5 mM AVB (solid lines and filled points) and 2.5 mM AVB plus 2.23 mM BEMT (dashed lines and empty points) in SQ with 0.01 cm path length as a function of irradiation time with the UV lamp at 7.2 cm. Lower plot: Comparison of calculated (lines) and measured (points) variation of *in vitro* SPF for the same systems.

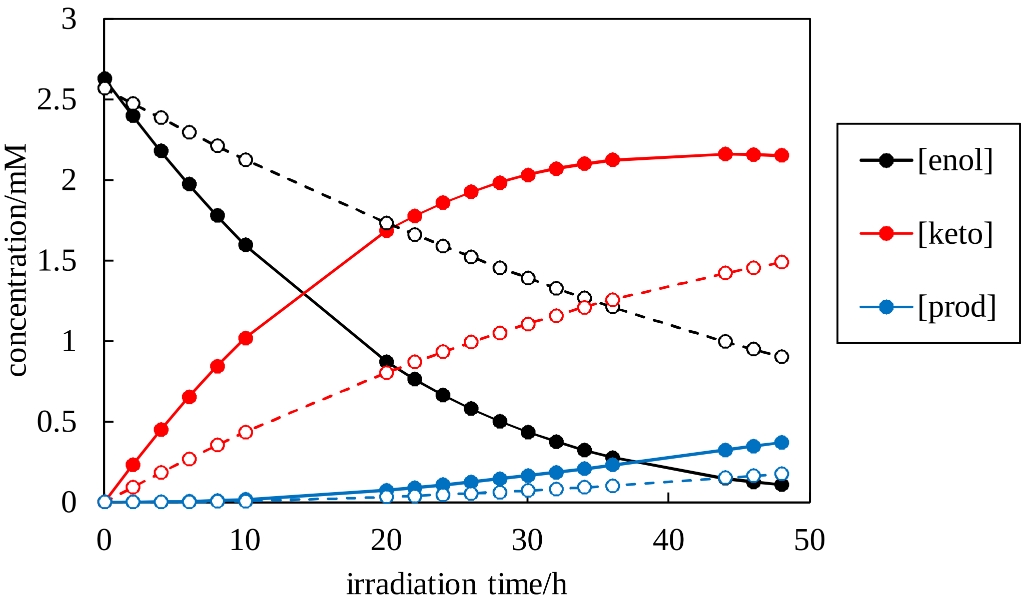

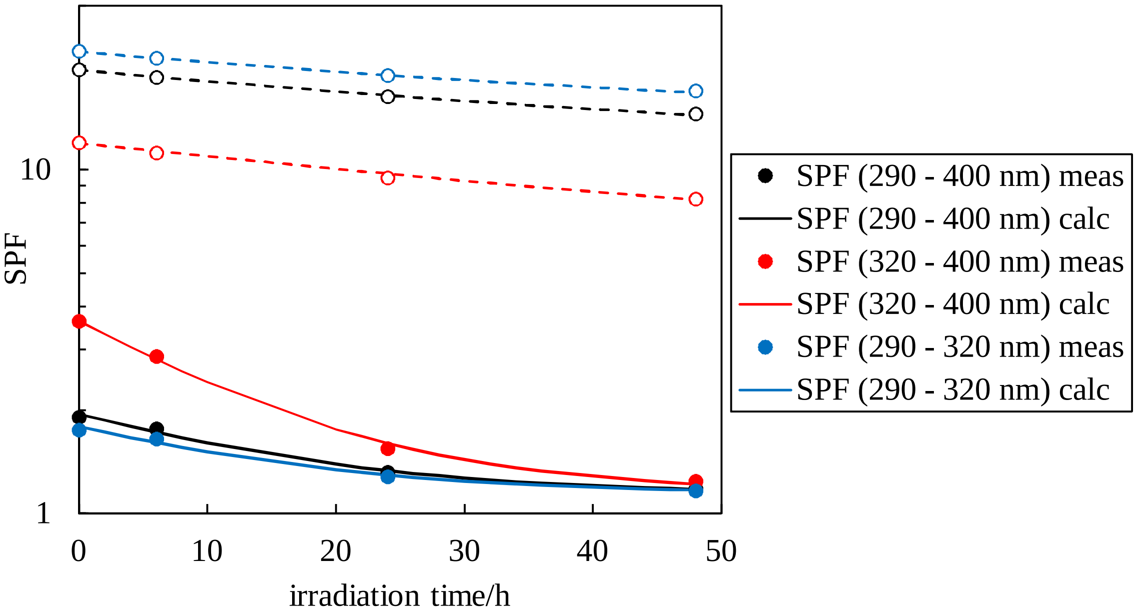

6.6 Photochemical kinetics of emulsions containing UV absorbers

Our investigation was further extended to irradiation of emulsion films consisting of equal volumes of SQ and PG and stabilised by silica particles of different degree of hydrophobicity. In these emulsions, a single UV absorber such as AVB or MC was initially dissolved in one of the phases.

Figure 6.18 shows the optical micrographs of both SQ-in-PG and PG-in-SQ emulsion types for a volume fraction of PG equal to 0.5 immediately after their emulsification. These optical micrographs correspond to emulsions without any UV absorbers present. Optical micrographs of both emulsion types with the addition of UV absorbers (either AVB or MC), though not shown here, were also taken. Our results revealed that the stability and the mean droplet sizes were neither affected by the addition of UV absorbers nor by the variation of the volume fraction of PG. The droplets of both emulsion types are polydisperse with a mean diameter of 20 and 18 μm for the SQ-in-PG and the PG-in-SQ emulsions respectively.

Figure 6.18. Optical micrographs of (left) SQ-in-PG emulsion with 50 vol.% PG, no dissolved UV filter, mean droplet diameter equal to approx. 20 μm and stabilised by 1 wt.% of 35% SiOH silica particles; (right) PG-in-SQ emulsion with 50 vol.% PG, no dissolved UV filter, mean droplet diameter equal to approx. 18 μm and stabilised by 1 wt.% of 23% SiOH silica particles.

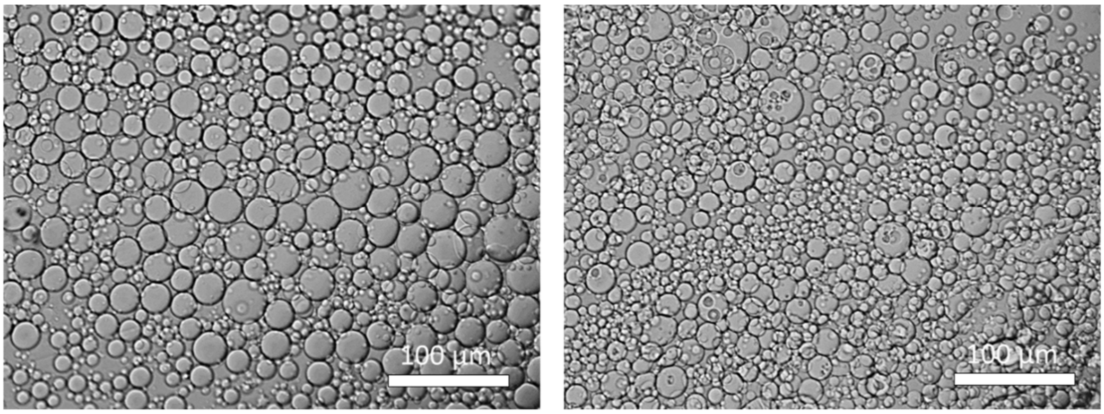

Overall, the visual appearance of both emulsion types corresponds to a greyish opaque colour. For the emulsions of interest, with a droplet size much larger than the wavelength range of the incident light, it is expected that the latter will strongly scatter within a narrow range of scattering angles in the forward direction. Figure 6.19 shows angular distribution calculations of the light scattered by a range of different droplet sizes based on Mie scattering theory.[24] For droplet sizes with a mean diameter around 20 µm, it can be seen that the light will be scattered over a small scattering angular range. This is not the case, however, for droplets with diameter below 2 µm where the light can be scattered over a large scattering angular range.

As such, for the latter case, only a small part of the scattered light is detected by the specular spectrophotometer whereas the rest is recorded as contribution to the overall absorbance. This is because the detector acceptance angular range is small in the range of ± 5°. When the same emulsion, however, is measured with the use of a diffuse spectrophotometer with an integrated sphere and with a detector acceptance angular range of ± 60°, virtually all of the scattered light is detected and hence the reported diffuse absorbance due to scattering is zero.

Figure 6.19. Calculated scattering intensity (normalised with respect to the scattering intensity at zero scattering angle) *versus* scattering angle for PG-in-SQ emulsion droplets with 30% polydispersity and the mean diameters ranging from 0.2 to 60 µm. The incident light wavelength for these calculations is 300 nm.

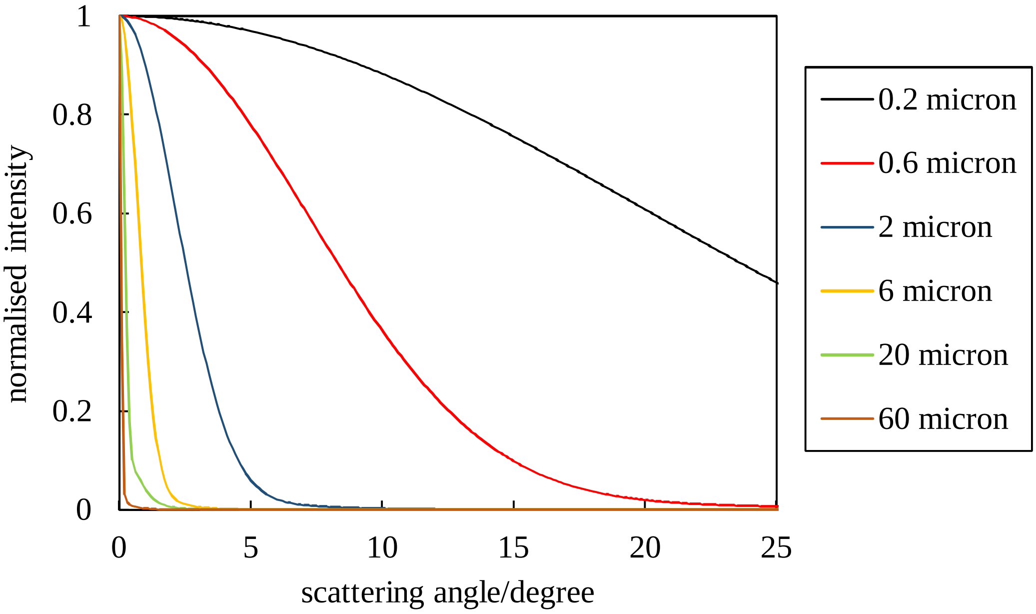

6.6.1 Photochemical kinetics of AVB in emulsions

For an emulsion containing a single UV absorber such as AVB, the volume fractions of the two immiscible liquids PG and SQ are ϕ_{PG} and $(1 - \phi_{PG})$ respectively. We discussed earlier the photochemistry of AVB in both solvents with regards to species that are present during irradiation (enol, keto and the photo-products). It is expected that within the emulsion, all three species of AVB will be distributed between the two phases (SQ and PG). As such, a total of six species are present ($enol_{PG}$, $enol_{SQ}$, $keto_{PG}$, $keto_{SQ}$, $prod_{PG}$ and $prod_{SQ}$) all of which have different extinction coefficients (ε_{enolPG}, ε_{enolSQ}, etc.) as a function of wavelength. Assuming that the species' partitioning is fast relative to the photochemical reactions, the ratio of PG and SQ concentrations of each species is maintained equal to equilibrium value of the relevant partition coefficient according to

$$P_{enol} = \frac{[enol_{SQ}]}{[enol_{PG}]} \tag{6.7}$$

where P_{enol} is the equilibrium partition coefficient for the enol species and the square brackets indicate the concentration of the species with respect to the volume of indicated liquid phase. Similar equations are valid for the keto and prod species. For each of the three species, the total concentration of each individual species with respect to the total volume of emulsion $C_{species,tot}$ is related to the concentration of the species in PG ($C_{species,PG}$) as follows

$$C_{species,tot} = \left(\phi_{PG} + (1 - \phi_{PG})P_{species}\right)C_{species,PG} \tag{6.8}$$

The concentrations with respect to the total emulsion volume (denoted using C with the appropriate subscripts) are related to the concentrations with respect to the volume of the relevant liquid phase (denoted with the square brackets) are related by the equations

$$C_{species,PG} = \phi_{PG}[species_{PG}] \; and \; C_{species,SQ} = (1 - \phi_{PG})\left[species_{SQ}\right] \tag{6.9}$$

The total of all species' concentrations is equal to initial, overall concentration of AVB. The calculated absorbance spectra and derived calculated *in vitro* SPF values during irradiation were determined using the following procedure.

1. For time zero, the six initial concentrations are entered and the absorbances due to each species are calculated using the relevant extinction coefficient spectra. Using the values of the four quantum yields (assumed to be wavelength independent) listed in Table 6.1, the spectral irradiance spectra of the light source, the value of P_{enol} derived from the ratio of solubilities and guessed values of P_{keto} and P_{prod}, the rates of the enol to keto and keto to product processes in each solvent are calculated for each wavelength and summed over wavelength to obtain the overall rates.

2. The time is incremented by a suitable time step, the overall rates from the previous time step and the relationships between the different concentrations are used to calculate the new concentrations of the enol, keto and prod species in both solvents. The individual species' absorbance values and the total absorbances (with and without addition of the specular absorbance due to the emulsion scattering) are calculated and used to derive the new values of the rates. In addition to obtaining the overall specular absorbance spectra at each time step, the *in vitro* SPF (derived from the total absorbance without the emulsion scattering contribution) is calculated according to equation 1.2.

3. Step 2 is repeated over sufficient time steps until calculated specular spectra and SPF values are obtained which cover the same irradiation times as the measured spectra. For time steps for which both measured and calculated spectra are available, the absolute differences between the measured and calculated spectra are summed. Using Solver, the two unknown partition coefficients are floated to minimise the residual sum between measured and calculated spectra as a function of irradiation time.

The upper and middle plots of Figure 6.20 show a comparison of measured and calculated absorbance spectra for a SQ-in-PG emulsion containing 5.0 mM AVB overall with respect to the entire emulsion volume and with a 0.01 cm path length. It can be seen that the agreement between the two data sets is excellent. This is also demonstrated in the lower plot of Figure 6.20 for both measured and calculated *in vitro* SPF values as a function of irradiation time. As expected, the SPF (320 – 400 nm) values progressively decrease due to the conversion of the enol to the keto and eventually to photo-products. As a reminder, the keto form absorbs in the UVC region of the electromagnetic spectrum and as such it does not contribute to the overall SPF.

Figure 6.20. Comparison of measured (upper plot) and calculated (middle plot) absorbance spectra for 5.0 mM AVB in a SQ-in-PG emulsion with 50 vol.% PG, stabilised with 1 wt.% of 35% SiOH silica particles and 0.01 cm path length as a function of irradiation time with the UV lamp at 7.2 cm. The dashed lines show the measured specular absorbance spectrum of the emulsion alone. Lower plot: Comparison of *in vitro* SPF values derived from measured and calculated spectra.

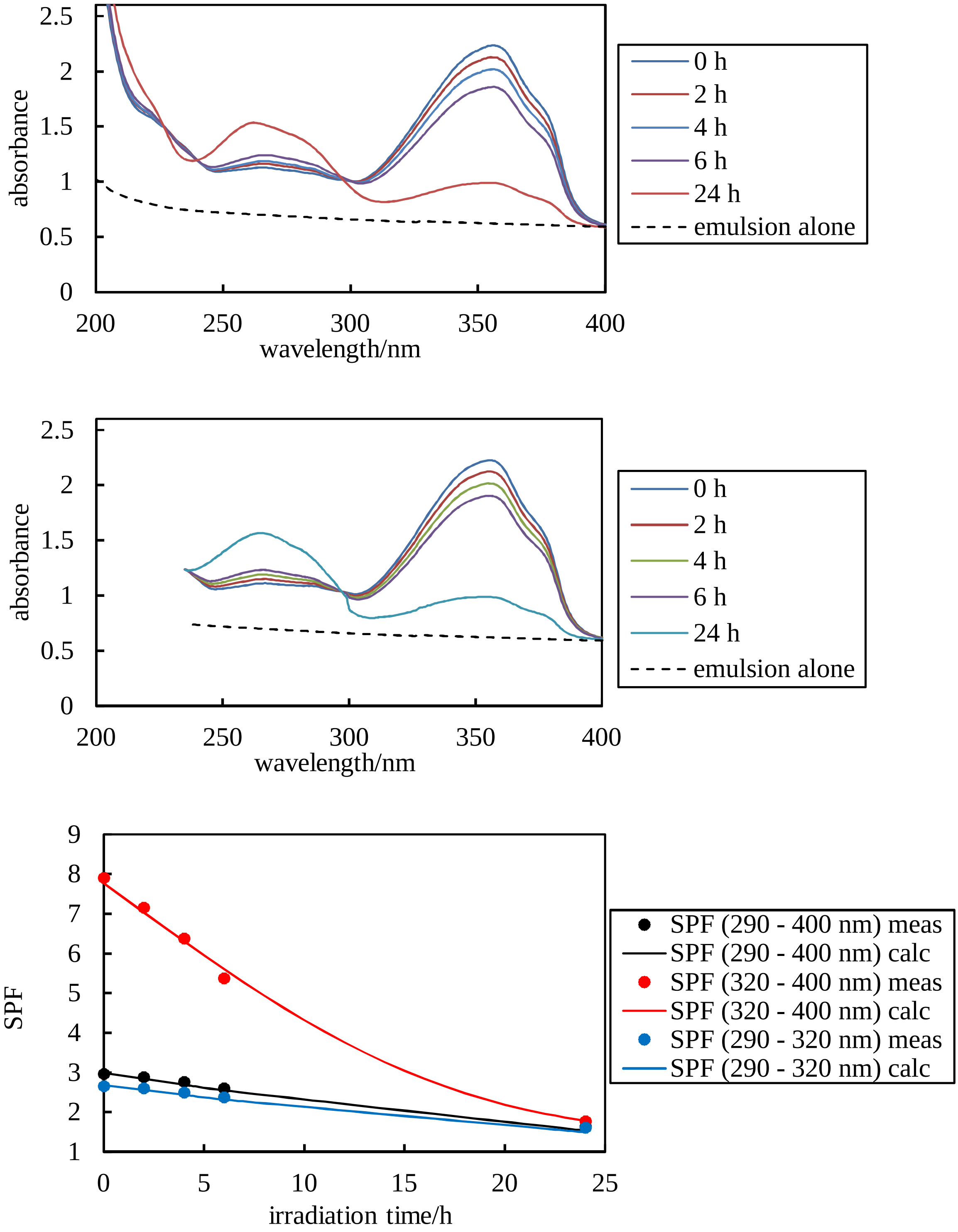

We have also investigated the photochemical behaviour of a PG-in-SQ emulsion film of 0.01 cm thickness containing 5.0 mM AVB with respect to the entire emulsion volume. Figure 6.21 shows the measured, calculated absorbance spectra and the relevant *in vitro* SPF values as a function of irradiation time respectively. Similar to our previous results, there is very good agreement between measured and calculated absorbance data. Again, this behaviour is depicted in the *in vitro* SPF values. The initial SPF (320 – 400 nm) performance is lost as a result of the two photochemical processes of AVB that occur during irradiation.

As such, the emulsion type is predicted to have no effect on the evolution of the specular absorbance spectrum due to light absorption but may have an effect on the specular absorbance “baseline” due to the emulsion scattering. Overall, the excellent agreement between the derived *in vitro* SPF values as shown in Figures 6.20 – 6.21 confirms that the photochemical behaviour of AVB in emulsions is independent of their type (either SQ-in-PG or PG-in-SQ).

Figure 6.21. Comparison of measured (upper plot) and calculated (middle) absorbance spectra for 5.0 mM AVB in a PG-in-SQ emulsion with 50 vol.% PG, stabilised with 1 wt.% of 23% SiOH silica particles and 0.01 cm path length as a function of irradiation time with the UV lamp set at 7.2 cm. The dashed lines show the measured absorbance spectrum of the emulsion alone. Lower plot: Comparison of *in vitro* SPF values derived from measured and calculated absorbance spectra.

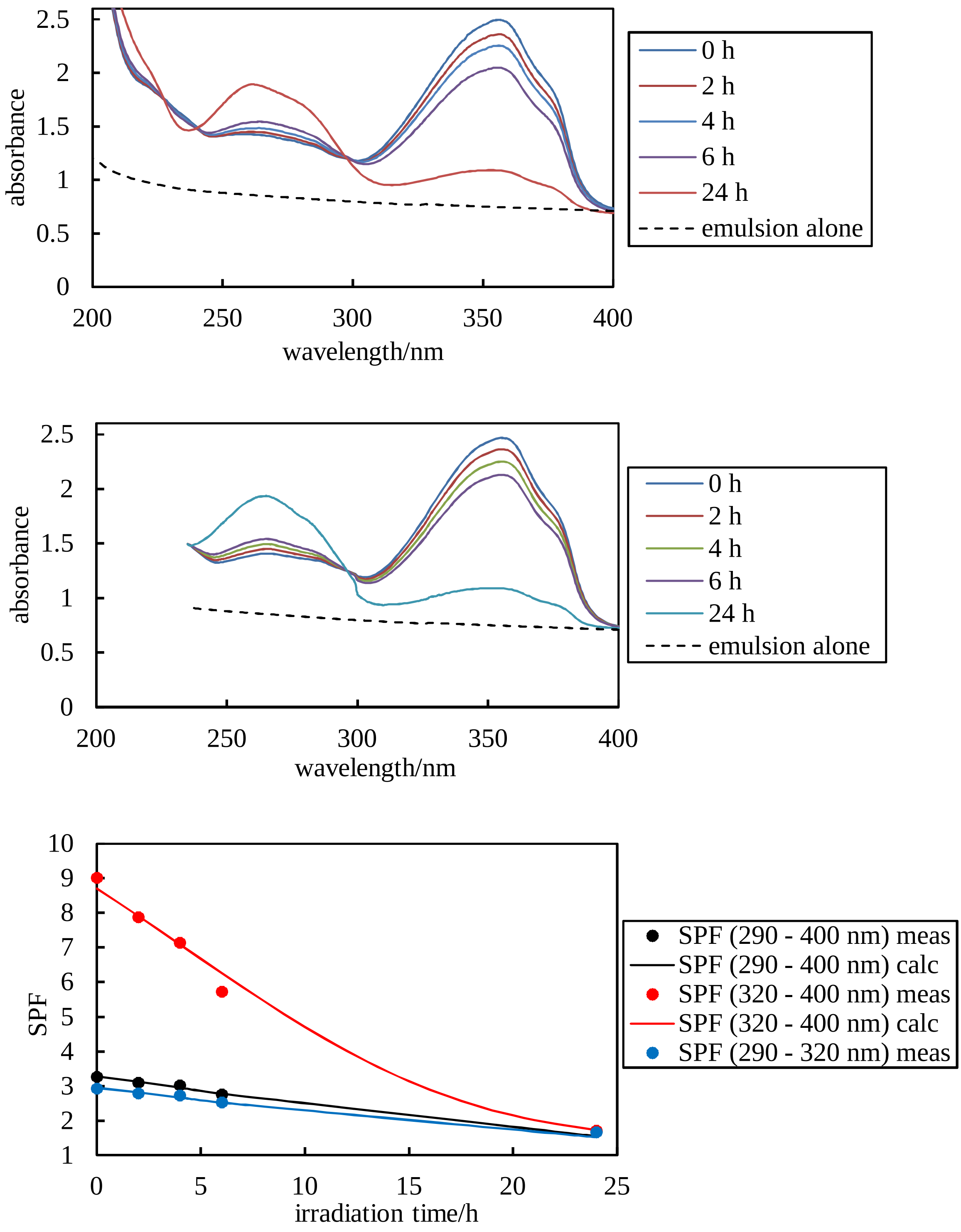

6.6.2 Photochemical kinetics of MC in emulsions

The same experimental procedure was applied for emulsions containing an alternative UV absorber such as MC. We have discussed earlier the photochemistry of MC in both solvents with regards to species that are present during irradiation (*trans* and *cis* isomers). For emulsion films containing MC with a film thickness of 0.01 cm, it is expected that within the emulsion, two species of MC will be distributed between the two phases (SQ and PG). As such, a total of four species are present, all of which have different extinction coefficients as a function of wavelength. For the simulations, the values of the four quantum yields listed in Table 6.1 were used. The partition coefficient of the *trans* species P_{trans} was taken to be approximately equal to the ratio of the solubilities of MC in the two solvents. Hence, the only unknown parameter floated in the modelling was the partition coefficient of the *cis* species P_{cis}.

Consistent with our fitting procedure, Figures 6.22 – 6.23 present measured and calculated absorbance data for both emulsion types containing MC. It is evident that there is a very good agreement between measured and calculated absorbance spectra. This is also depicted in the *in vitro* SPF values as a function of irradiation time. As expected, only the SPF (290 – 320 nm) is significantly affected showing a rapid decrease within the first 60 min irrespective of the emulsion type. Hence, the photochemical behaviour of MC in emulsions is similar in both emulsion types. Overall, the photochemistry of two different UV absorbers in emulsion films can be predicted. In addition, we show that their behaviour is not affected by the emulsion type in which they are dissolved.

Figure 6.22. Comparison of measured (upper plot) and calculated (middle plot) spectra for 8.38 mM MC in a PG-in-SQ emulsion with 50 vol.% PG, stabilised with 1 wt.% of 23% SiOH silica particles and 0.01 cm path length as a function of irradiation time with the UV lamp at 7.2 cm. The dashed line shows the measured specular absorbance spectrum of the emulsion alone. Lower plot: Comparison of *in vitro* SPF values derived from measured and calculated absorbance spectra.

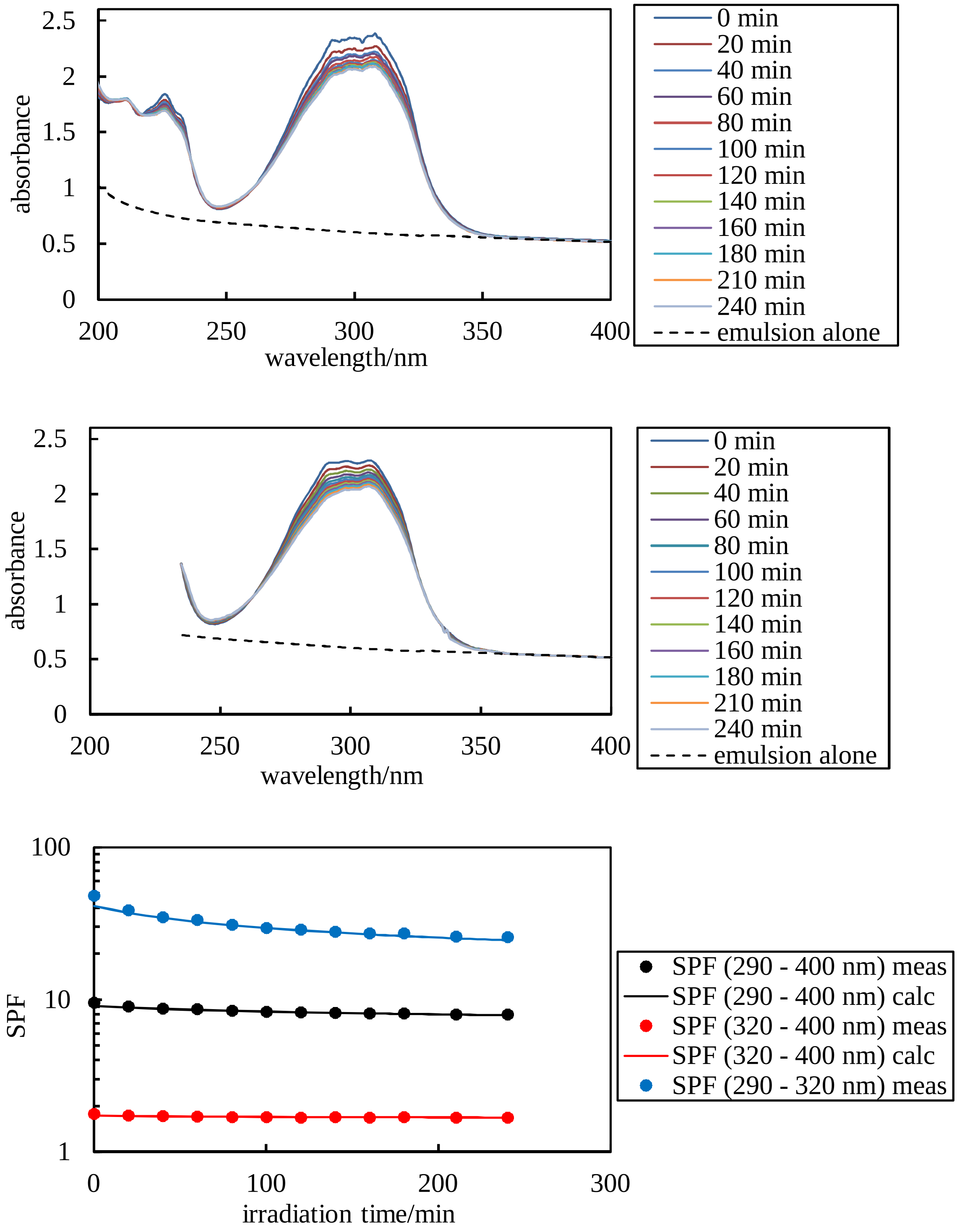

Figure 6.23. Comparison of measured (upper plot) and calculated (middle plot) spectra for 8.38 mM MC in a SQ-in-PG emulsion with 50 vol.% PG, stabilised with 1 wt.% of 35% SiOH silica particles and 0.01 cm path length as a function of irradiation time with the UV lamp at 7.2 cm. The dashed line shows the measured specular absorbance spectrum of the emulsion alone. Lower plot: Comparison of *in vitro* SPF values derived from measured and calculated absorbance spectra.

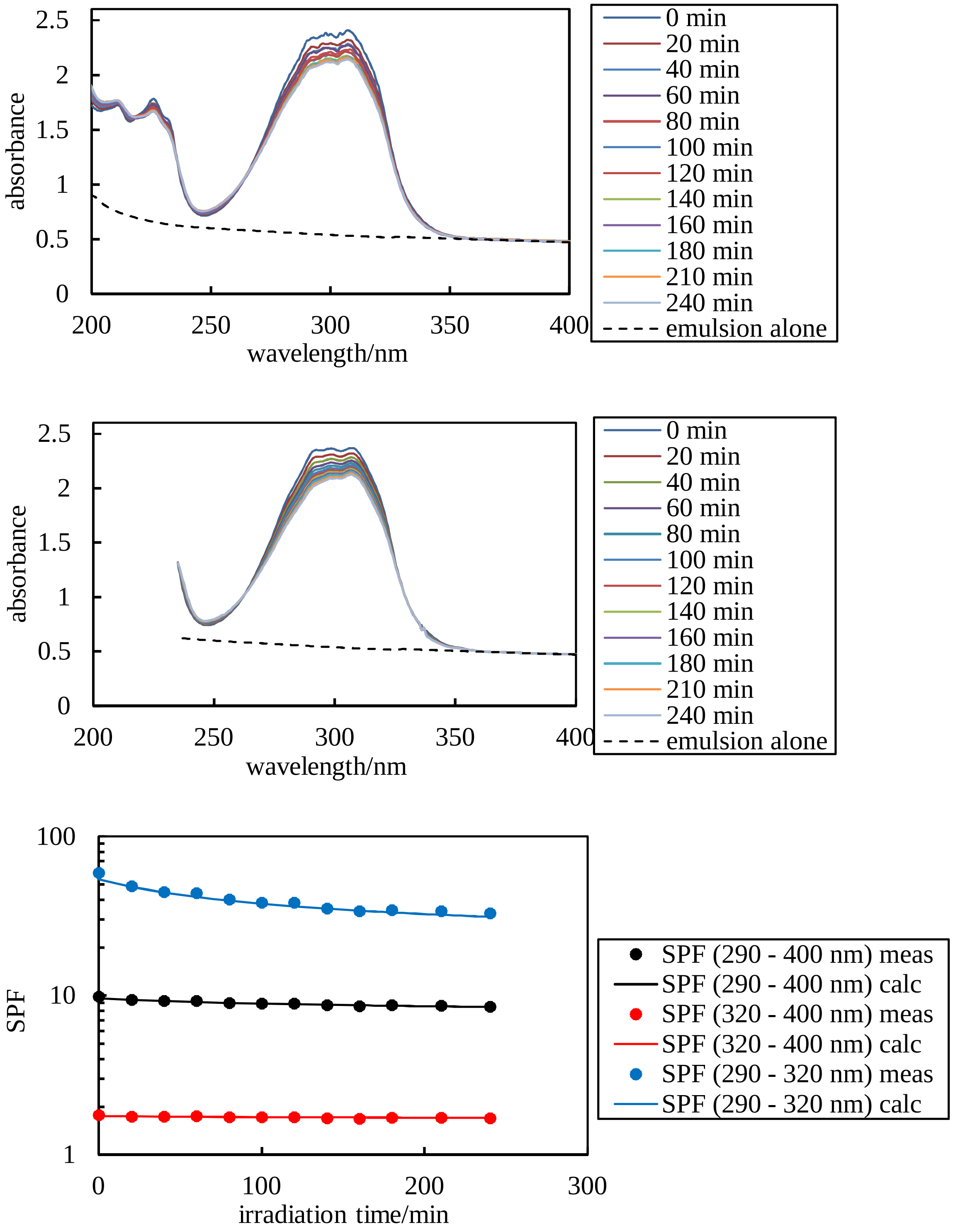

Table 6.2 shows the best-fit values of P_{trans} and P_{cis} obtained from both emulsion types containing a single UV absorber (AVB or MC). The best-fit values of P_{trans} are somewhat lower than the values corresponding to the ratio of solubilities but this may be a consequence of the high solubilities of MC in these solvents, which is likely to cause deviations from ideal solution behaviour.

Table 6.2. Fitted values of the species' partition coefficients at 32°C. The values in brackets correspond to the ratio of the equilibrium solubilities.

UV absorber/emulsion type	**Partition coefficients at 32°C**		
AVB	P_{enol}	P_{keto}	P_{prod}
5.0 mM AVB/SQ-in-PG	3.0 (2.7)	0.65	Set to 0
5.0 mM AVB/PG-in-SQ	3.0 (2.7)	1.0	Set to 0
MC	P_{trans}	P_{cis}	
8.38 mM MC/PG-in-SQ	1.4 (3.0)	5.2	
8.38 mM MC/SQ-in-PG	1.5 (3.0)	4.6	

6.6.3 Varying the volume fraction of PG

For emulsions containing equal volumes of PG and SQ, we showed that the photochemical behaviour of AVB and MC is independent of the emulsion type. The next step was to investigate whether the change in the emulsion composition will affect the photochemical processes of either AVB or MC. As such, PG-in-SQ emulsions with ϕ_{PG} in the range 0.2 – 0.6 stabilised with 1 wt.% of 23% SiOH silica particles and SQ-in-PG emulsions with ϕ_{PG} in the range 0.4 – 0.8 stabilised with 1 wt.% of 35% SiOH silica particles were prepared. These stable emulsions with droplet size of 18 – 20 μm contained a single UV absorber (either AVB or MC).

For the emulsion films containing AVB, the peak absorbance of the enol form initially decreases linearly upon UV irradiation as a result of enol to keto reaction. Hence, the initial reaction rate is proportional to enol to keto quantum yield, which is 0.4 x 10^{-4} in pure PG and 2 x 10^{-4} in pure SQ. It is expected that for the investigated emulsion films, the initial reaction rate is equal to the volume fraction weighted rates in each of the pure solvents according to

$$r = \phi_{PG} r_{PG} + (1 - \phi_{PG}) r_{SQ} \qquad (6.10)$$

where r_{PG} is the initial rate in pure PG and r_{SQ} is that for pure SQ. Hence, the initial rate for AVB is predicted to decrease approximately 5-fold as ϕ_{PG} is increased from 0 to 1.

For emulsion films containing MC, the peak absorbance decreases exponentially to a plateau value corresponding to the photo-stationary state mixture of *trans* and *cis* forms. Fitting the peak absorbance decrease to an exponential function yields a first-order rate constant k. This rate constant is proportional to the sum of the *trans*/*cis* and *cis*/*trans* quantum yields and is 0.16 + 1.0 = 1.16 for pure PG and 0.028 + 0.10 = 0.128 for pure SQ. In emulsion films, k is equal to the volume fraction weighted values in each of the pure solvents according to

$$k = \phi_{PG} k_{PG} + (1 - \phi_{PG}) k_{SQ} \qquad (6.11)$$

Hence, k for MC is predicted to increase approximately 9-fold as ϕ_{PG} is increased from 0 to 1. Figure 6.24 shows a comparison between i) the measured and the calculated AVB initial rates and ii) the k values of MC as a function of volume fraction of PG. It is important to note that the measured values are derived from both PG-in-SQ and SQ-in-PG emulsion and solution films for a range of concentrations of the UV absorber and path lengths.

Although the spread in values are fairly large (due to the variability in quantum yields noted and discussed earlier), the agreement between the measured data and the predictions is reasonably good. The plots reveal how control of the emulsion composition can be used to vary the extent of photochemical change in an emulsion sunscreen formulation.

Figure 6.24. Variation of the averaged values of initial photochemical rate for AVB (upper plot) and the measured first-order rate constant for MC photo-isomerisation in emulsions with different volume fractions of PG (lower plot). The plots refer to irradiation with the UV lamp at 7.2 cm. The solid lines are calculated as described in the text.

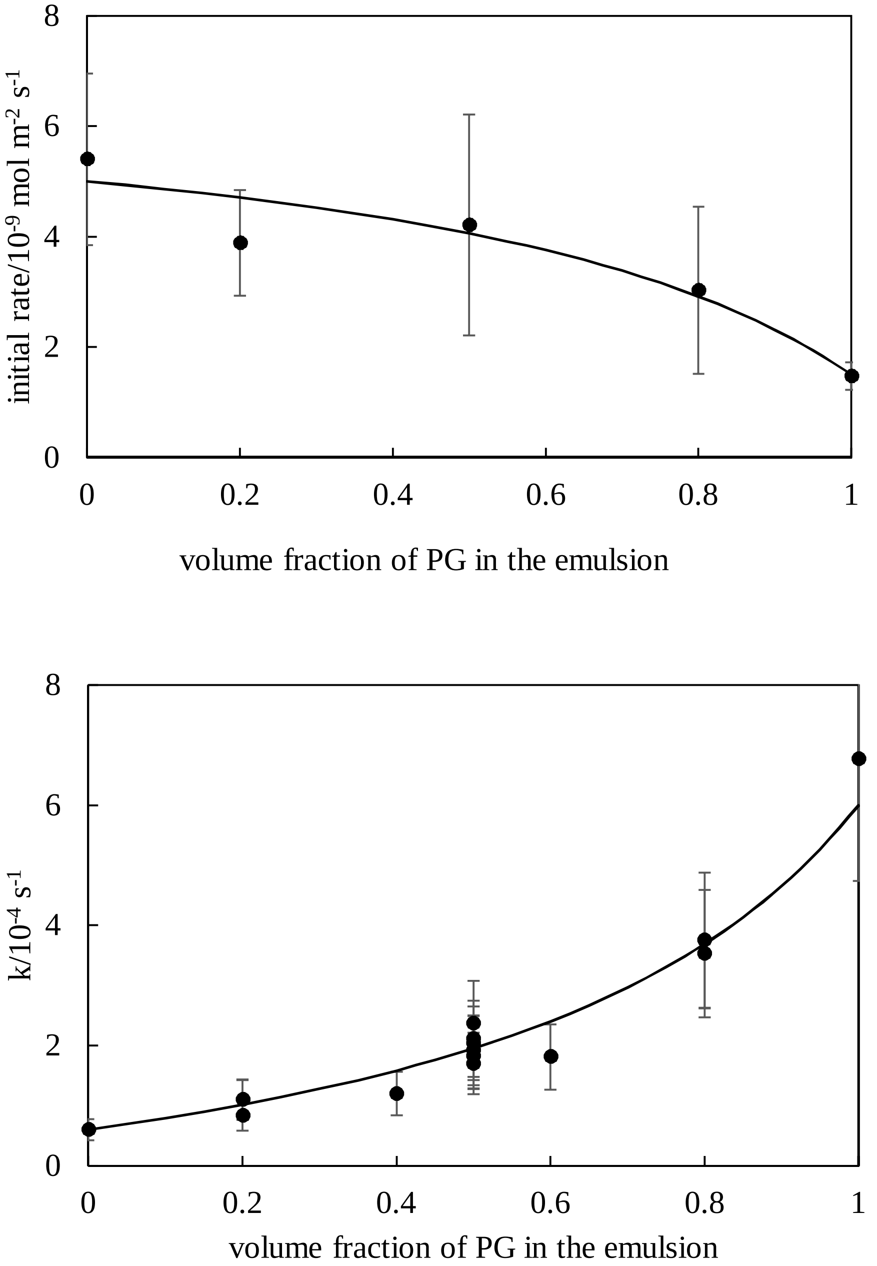

6.7 Photochemical kinetics of dispersions containing nanoparticles and a single UV absorber

Alternatively, current sunscreens can also contain a mixture of inorganic particulates and organic UV absorbers. For this reason, the photochemical behaviour of AVB was examined in the presence of a selection of metal oxide nanoparticles including TiO_2, CeO_2, ZnO and WO_3. Figure 6.25 shows the absorbance spectra of dispersions of the selected nanoparticles as a function irradiation time, which were taken at frequent timed intervals with the use of UV/vis spectrophotometer. For the irradiated period of 6 h, there is not significant change in the absorbance values.

Attempts to measure the specular absorbance of a dispersion containing 1.0 wt.% of the selected nanoparticles in 8.0 mM AVB in both SQ and PG were unsuccessful due to the strong light absorption and scattering by the particles, which exceeded the reliable range of the UV/vis spectrophotometer. As such, the absorbance of a dispersion consisting of 0.1 wt.% of nanoparticles in 8.0 mM AVB of either SQ or PG with a fixed path length 0.01 cm was investigated. Figure 6.26 shows a comparison of peak absorbance spectra at 360 nm of 8.0 mM AVB plus 0.1 wt.% of the above nanoparticles in both solvents. It can be seen that the presence of the nanoparticles at this loading does not significantly alter the rate when compared with solutions of AVB alone. As such, it is difficult to determine from these experiments whether nanoparticles contribute primarily by absorption or scattering.

We model the behaviour of these dispersions using the previously determined AVB quantum yields assuming that i) the particles only absorb and ii) the particles only scatter. For convenience, we selected the TiO_2 nanoparticles. The upper plot of Figure 6.27 shows the measured absorbance spectra of 8.0 mM AVB plus 0.1 wt.% TiO_2 nanoparticles in SQ. The middle plot of Figure 6.27 illustrates the calculated absorbance data where we assume that the TiO_2 particles only absorb light and act as "spectator" species. For the investigated period of 6 h, we would expect the calculated spectra to be slightly lower than the measured spectra. We repeat the fitting procedure based on the assumption that TiO_2 particles only scatter light and this is shown in the lower plot of Figure 6.27. This time, the calculated data are expected to be slightly higher than the measured absorbance data due to the presence of a longer effective path length. From data comparison of Figure 6.27, it is unclear as to whether the nanoparticles mostly absorb or scatter light. Due to their nature, it is expected that the nanoparticles contribute to the overall absorbance from both processes. However, it is difficult to elucidate further information from these experimental data.

Figure 6.25. Absorbance spectra of 0.10 wt.% of all nanoparticles with path length 0.01 cm in SQ (*versus* SQ reference) (upper plot) and in PG (*versus* PG reference) (lower plot). Solid lines correspond to absorbance values at UV 0 h, as opposed to dotted lines which indicate the absorbance values at UV 6 h.

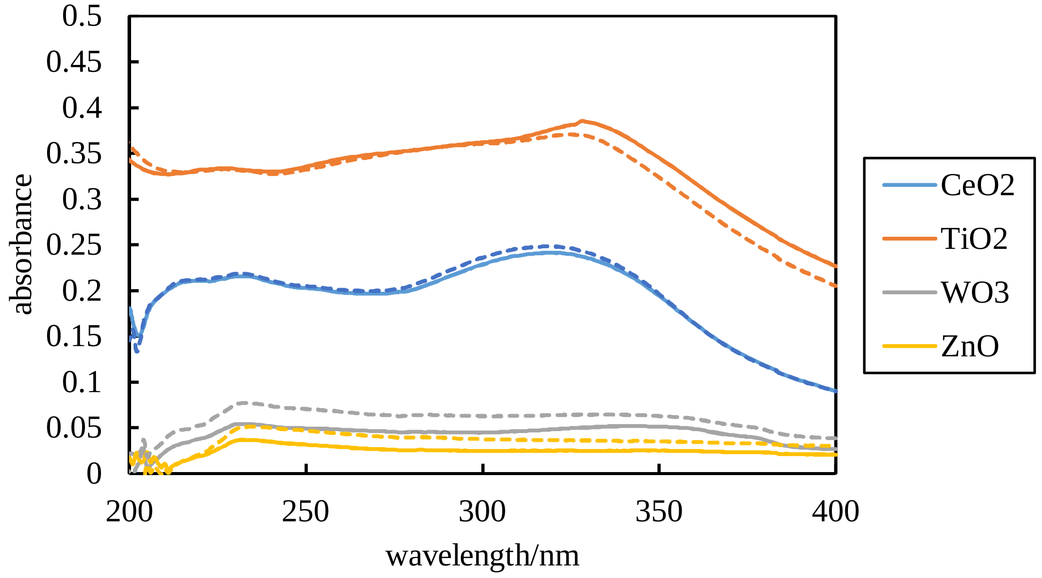

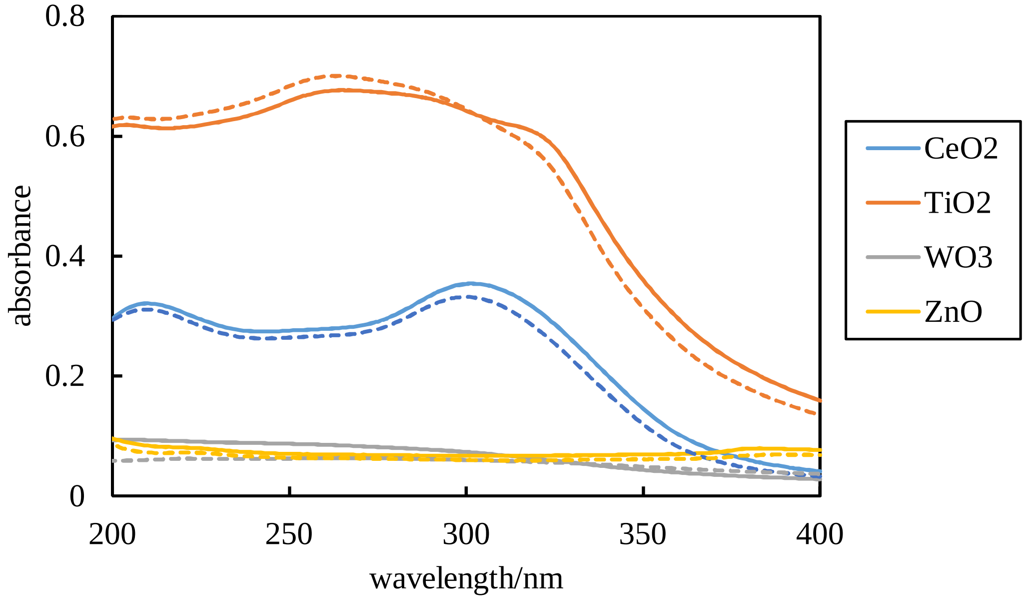

Figure 6.26. Absorbance spectra as a function of irradiation time for dispersions of 0.10 wt.% of nanoparticles plus 8.0 mM AVB in SQ (upper plot) and in PG (lower plot).

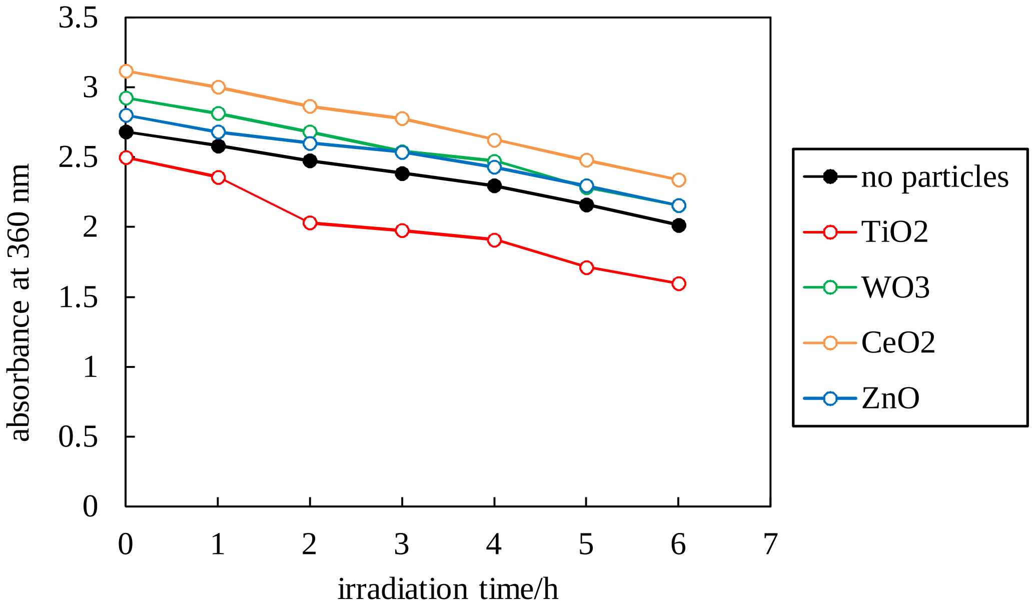

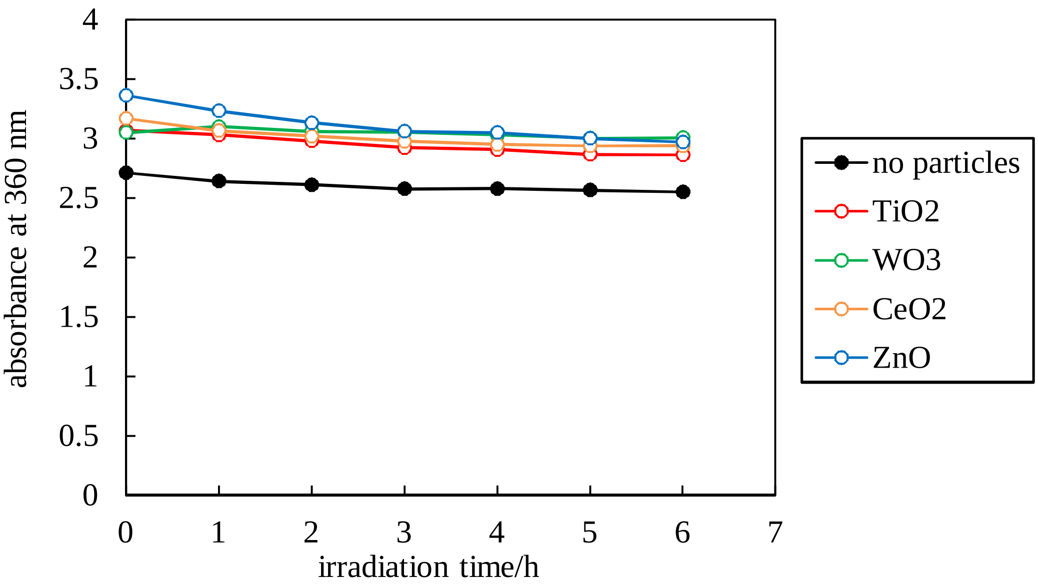

Figure 6.27. Measured (upper plot) and calculated (middle plot) absorbance spectra for 0.1 wt.% of TiO_2 nanoparticles plus 8.0 mM AVB in SQ with 0.01 cm path length (UV lamp at 7.2 cm). The calculated data were derived assuming that TiO_2 nanoparticles only absorb light. The dashed line corresponds to the absorbance spectra of 0.1 wt.% of TiO_2 nanoparticles in SQ alone. Lower plot: Calculated absorbance spectra for the same dispersion assuming that TiO_2 only scatter light.

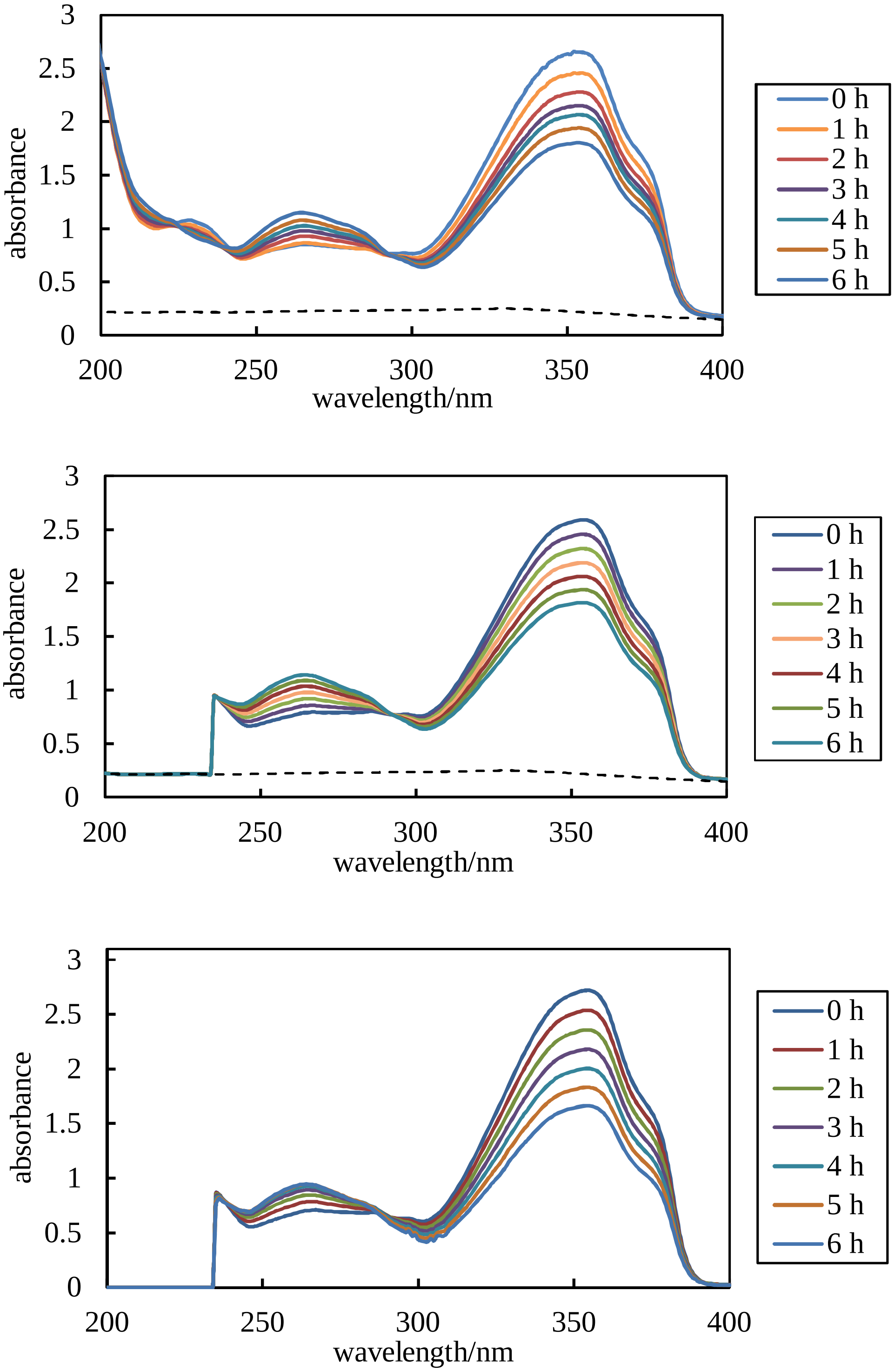

6.8 Prediction of the in vitro SPF changes during solar irradiation

The absolute spectral irradiance values of the light sources used here were determined based on actinometry measurements and they were used to estimate the quantum yields of the photochemical processes of AVB and MC in both SQ and PG. Throughout our fitting procedure, we have assumed that these quantum yields are wavelength independent (250 – 400 nm). Despite their fairly high uncertainties, we have obtained consistent values for all the possible combinations used here such as i) the use of different light sources, ii) solutions with different concentrations and path lengths, iii) solutions containing a mixture of UV absorbers, iv) solutions containing a combination of UV absorber and inorganic particulates and iii) emulsion films. These estimated values of the quantum yields will be used to predict how the spectrum of a film and the different SPF values will vary with exposure to “standard” light. By “standard” sunlight, it is implied the spectral irradiance of terrestrial sunlight under defined conditions.[10] Hence, using the estimated quantum yields and the molar extinction coefficients of the species involved, we can derive the absorbance spectra, SPF and individual species’ concentrations for any concentration and path length of solutions, dispersions and emulsions containing UV absorbers as a function of irradiation time under “standard” sunlight conditions.

The upper plot of Figure 6.28 shows the calculated spectra of a 20 μm film of 30 mM AVB in either SQ or PG for an investigated period of 4 h. As a reminder, the solubility of AVB in PG is only 14 mM. However, we retain this calculation in order to better compare AVB behaviour in the two solvents. The middle plot of Figure 6.28 shows the calculated *in vitro* SPF values as a function of irradiation time. As already discussed, the initially high SPF (320 – 400 nm) values are due to the presence of the enol form of AVB which absorbs in the UVA region of the region. The other types of SPF remain low and constant throughout. The progressive decrease in the SPF (320 – 400 nm) can be attributed to the conversion of the enol form of AVB to the keto and the photoproducts upon solar irradiation exposure. The relatively fast decrease of the values of SPF (320 – 400 nm) in SQ as opposed to that in PG is evident. The calculations also provide an estimate of the enol, keto and prod species’ concentrations during solar irradiation.

Similarly, the upper plot of Figure 6.29 shows the calculated spectra for 20 μm films of 30 mM MC in either SQ or PG for an investigated period of 20 min. The middle plot of Figure 6.29 shows the calculated *in vitro* SPF for both solvents. Relative to the photo-processes for AVB, MC reacts much faster (over minutes compared with hours for AVB) as a result of the higher quantum yields. For MC in SQ as solvent, the quantum yields are such that the photo-stationary state is achieved very fast (within 2 minutes or so) but the extent of conversion from *trans* to *cis* forms is small. As a result, the SPF (290 – 320 nm) shows a fast but small initial change. In PG as solvent, the photo-stationary state is achieved approximately ten times slower (after 20 minutes or so) but the extent of conversion from *trans* to *cis* is much greater. Thus, the SPF (290 – 320 nm) is significantly decreased over the first 20 minutes irradiation. Again, the other two types of SPF remain low and constant during irradiation irrespective of the solvent type.

Similar model calculations are possible for solution and emulsion films containing single or multiple UV filters at any set concentrations and path length (equal to the film thickness) so long as the relevant input parameters (extinction coefficient spectra and quantum yields) are known. This enables *in vitro* estimation of not only initial values of SPF but also their time dependence due to solar irradiation.

Figure 6.28. Calculated evolution of the film spectrum (upper plot) (SQ as solvent only, 20 min intervals), SPF (middle plot) and species concentrations (lower plot) during "standard" solar irradiation. The films contain 30 mM AVB in either SQ (solid lines) or PG (dashed lines) with a path length of 20 μm.

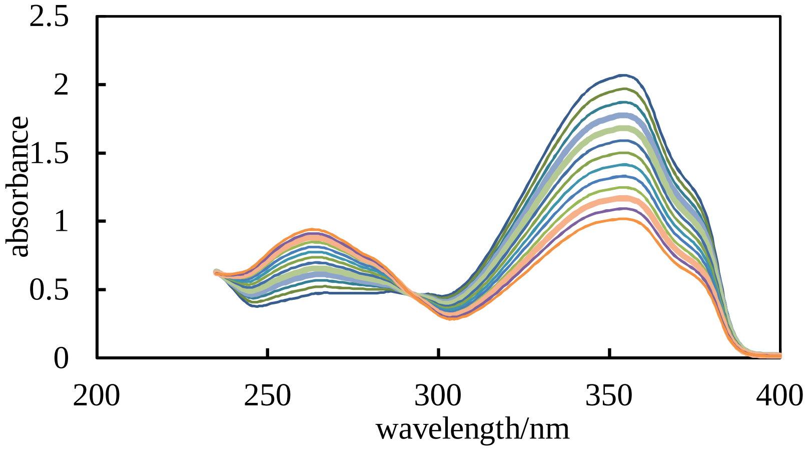

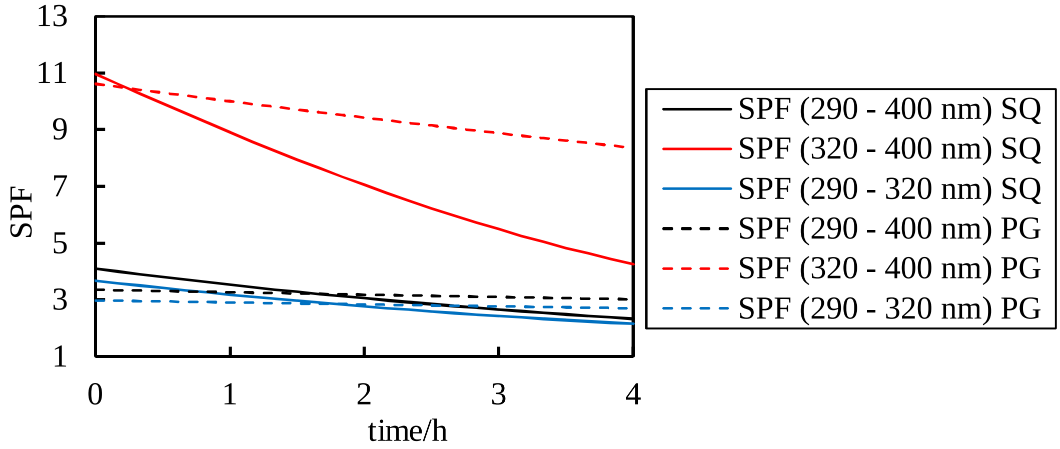

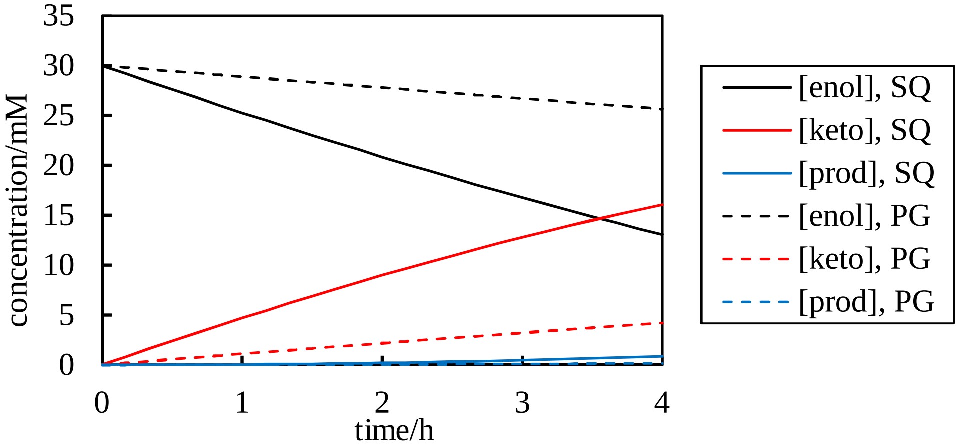

Figure 6.29. Calculated evolution of the film spectrum (upper plot) (PG as solvent only, 50 s intervals), SPF (middle plot) and species concentrations (lower plot) during “standard” solar irradiation. The films contain 30 mM MC in either SQ (dashed lines) or PG (solid lines) with a path length of 20 μm.

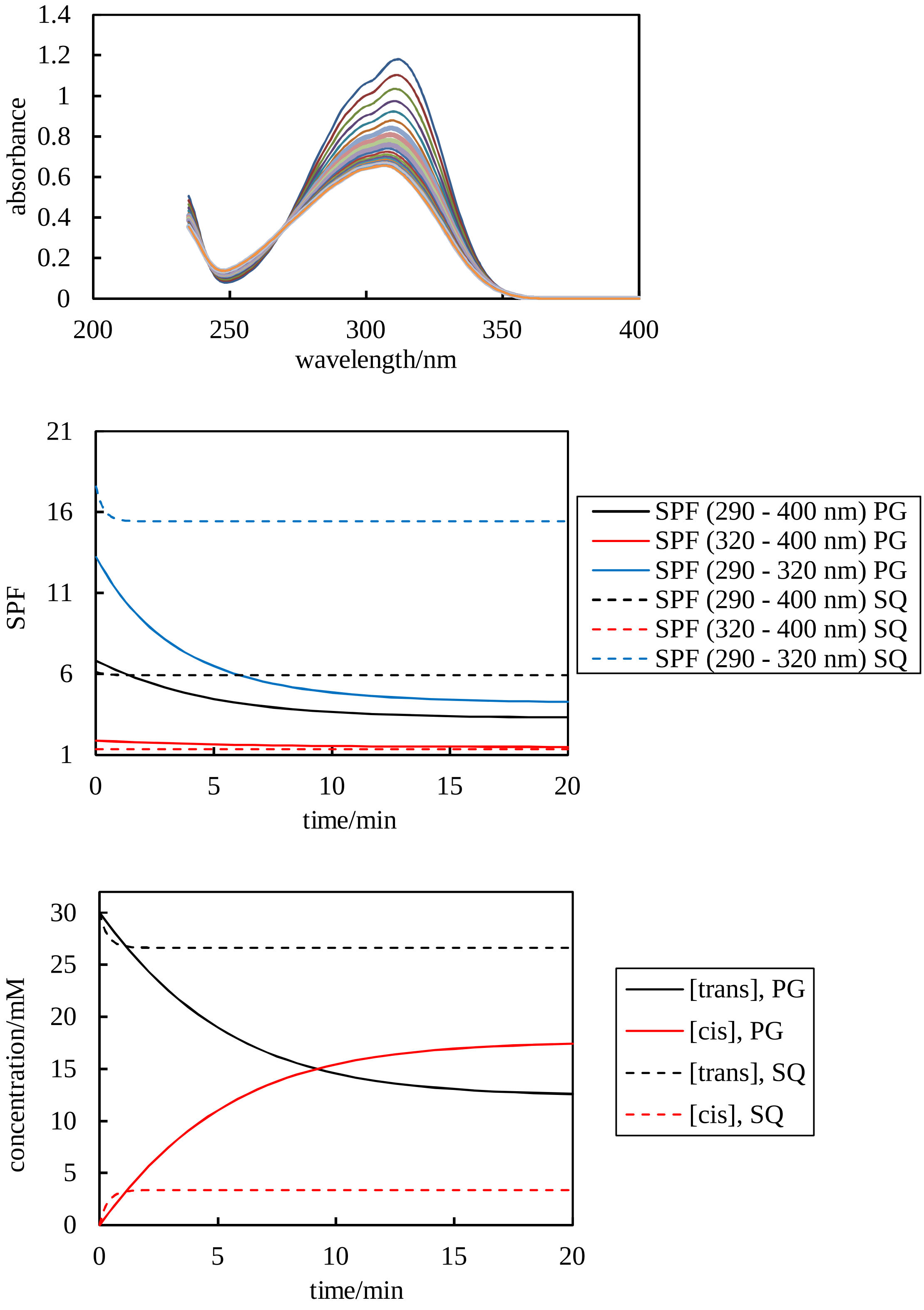

6.9 *Conclusions*

The photochemical behaviour of solutions, dispersions and emulsions containing UV absorbers such as AVB, MC, DHHB and BEMT in the polar protic PG and the non-polar SQ, was investigated. Results have confirmed the photostability of DHHB and BEMT. For the photo-unstable AVB and MC, we have also showed how the relevant photochemical processes are responsible for the spectral changes.

The measured absorbance spectra of the irradiated solutions were compared with calculated absorbance values. For the determination of the calculated absorbance values in particular, we have developed a fitting procedure that is used to estimate the molar extinction coefficients, the concentrations of each of the species involved and the relevant quantum yields of the photochemical processes. Throughout our investigation, we used different types of light sources and their absolute spectral irradiance values were determined with the use of actinometry. For each data set, we have determined both measured and calculated absorbance *in vitro* SPF values as a function of irradiation time. It is important to note, however, the fairly large uncertainties probably relevant for the estimated quantum yields that were used for our calculations.

In addition, solutions containing a mixture of UV absorbers containing AVB and the photostable BEMT were examined. It was shown that the presence of BEMT retards the photochemical processes of AVB. Similar investigation was made for dispersions containing a selection of nanoparticles. However, the presence of nanoparticles did not significantly alter the rate probably due to its very low particle loading.

Our investigation was extended to particle-stabilised emulsions containing a single UV absorber. For these systems, the spectral changes result from light absorption of the UV absorbers and a minor contribution from scattering. In addition, we are also taking into consideration the partitioning of all species' present between the immiscible liquid phases of the emulsion. As such, we were able to model the behaviour of the UV absorbers within emulsions films. Results have shown that the photochemical changes of the investigated AVB and MC when dissolved in emulsions, are not affected by the emulsion type but they are only dependent on the emulsion composition. Hence, for the emulsions that are comprised of SQ and PG phases, this corresponds to the volume fraction of PG. In the final part of this chapter, based the model developed we can predict the spectra and the SPF as a function of irradiation time for different types of sunscreen films during irradiation with “standard” sunlight.

6.10 References

1. W. A. Noyes, The photochemistry of gases, Reinhold Pub. Corp., New York, 1941.
2. J. G. Calvert and J. N. Pitts Jr., Photochemistry, Wiley and Sons, New York, 1966.
3. H. J. Kuhn, S. E. Braslavsky and R. Schmidt, *Pure Appl. Chem.*, 2004, **76**, 2105-2146.
4. H. J. Adick, R. Schmidt and H. D. Brauer, *J. Photochem. Photobiol. A*, 1988, **45**, 89-96.
5. W. Schwack and T. Rudolph, *J. Photochem. Photobiol.*, 1995, **28**, 229–234.
6. N. Tarras-Wahlberg, G. Stenhagen, O. Larko, A. Rosen, A-M Wennberg and O. Wennerstrom, *J. Inv. Dermatol.*, 1999, **113**, 547-553.
7. A. Cantrell and D. J. McGarvey, *J. Photochem. Photobiol.*, 2001, **64**, 117–122.
8. E. Chatelain and B. Gabard, *Photochem. Photobiol.*, 2001, **74**, 401–406.
9. A. Aspée, C. Aliaga and J. C. Scaiano, *Photochem. Photobiol.*, 2007, **83**, 481–485.
10. G. J. Mturi and B. S. Martincigh, *J. Photochem. Photobiol. A Chem.*, 2008, **200**, 410–420.
11. C. Paris, V. Lhiaubet-vallet, O. Jiménez, C. Trullas and M. A. Miranda, *Photochem. Photobiol.*, 2009, **85**, 178–184.
12. B. Herzog, M. Wehrle and K. Quass, *Photochem. Photobiol.*, 2009, **85**, 869-878.
13. V. Lhiaubet-Vallet, M. Marin, O. Jimenez, O. Gorchs, C. Trullas and M. A. Miranda, *Photochem. Photobiol. Sci.*, 2010, **9**, 552–558.
14. J. Zawadiak and M. Mrzyczek, *Spectrochim. Acta*, 2012, **96**, 815-819.
15. M. Yamaji and M. Kida, *J. Phys. Chem. A*, 2013, **117**, 1946-1951.
16. M. Dubois, P. Gilard, P. Tiercet, A. Deflandre and M. A. Lefebvre, *J. Chim. Phys.*, 1998, **95**, 388-394.
17. S. Tobita, J. Ohba, K. Nakagawa and H. Shizuka, *J. Photochem. Photobiol. A Chem.*, 1995, **92**, 61–67.
18. P. Morliere, O. Avice, T. S. E. Melo, L. Dubertret, M. Giraud and R. Santus, *Photochem. Photobiol.*, 1982, **36**, 395-399.

19. S. Pattanaargson, T. Munhapol, P. Hirunsupachot and P. Luangthongaram, *J. Photochem. Photobiol. A*, 2004, **161**, 269–274.
20. S. P. Huong, V Andrieu, J-P. Reynier, E. Rocher and J-D. Fourneron, *J. Photochem. Photobiol. A*, 2007, **186**, 65-70.
21. T. M. Karpkird, S. Wanichweacharungruang and B. Albinsson, *Photochem. Photobiol. Sci.*, 2009, **8**, 1455-1460.
22. L. A. MacManus-Spencer, M. L. Tse, J. L. Klein and A. E. Kracunas, *Environ. Sci. Technol.*, 2011, **45**, 3931–3937.
23. K. M. Hanson, S. Narayanan, V. M. Nichols and C. J. Bardeen, *Photochem. Photobiol. Sci.*, 2015, **14**, 1607-1616.
24. MiePlot v. 4.5.01 downloaded from http://www.philiplaven.com/mieplot.htm

CHAPTER 7 SUMMARY OF CONCLUSIONS AND FUTURE WORK

7.1 Conclusions

In this study, our primary goal is to understand and optimise sunscreen performance. For this reason, we have investigated how the UV absorption properties of sunscreen films (solutions, dispersions or emulsions containing UV absorbers) are affected when the two following processes occur: i) evaporation of the volatile components and ii) exposure to solar irradiation. In particular, we have shown that the evaporation process affects significantly the absorbance behaviour of powder UV filters, which are dissolved in volatile solvents. Hence, upon complete solvent evaporation, the presence of a film residue of precipitated crystals negligibly contributes to the overall absorbance and the SPF performance is lost. In order to tackle this problem, either liquid sunscreen UV filters or powder UV filters dissolved in involatile solvents can be used in the formulation.

In terms of investigating the photochemical behaviour of UV filters, the current *in vitro* approach is based on extrapolating data derived from solutions containing low concentrations of UV filters and long path lengths (1 cm) when exposed to an artificial source of irradiation. Our approach was to examine colloidal films containing high concentrations of UV filters and short path lengths (in the order of 100 μm) under different laboratory light sources to closely resemble “real” sunscreens. Based on our results, we can further predict how sunscreen UV filters vary with time upon exposure to “standard” sunlight. The findings presented in this study are a useful tool for formulators working primarily in the area of sunscreens. However, our results concerning the evaporation mechanism can also be extended in the area of topical medicines including creams and ointments.

As discussed, the efficiency of these formulations is measured with the use of Sun Protection Factor (SPF). The currently accepted method is the *in vivo* SPF, which is an expensive and time-consuming approach to determine the sunscreen protection against erythema/sunburn. *In vitro* SPF measurements, though rapid and inexpensive, are convenient but can only provide us with an initial SPF value relevant to the initial absorbance and composition of the investigated film. This is shown in Chapter 3, where we derive the initial *in vitro* SPF for any concentration of UV filters for a film thickness/path length of 20 μm. The latter value is approximately equal to the standard application of the *in vivo* process. The UV absorbers of choice included AVB, MC, DHHB and BEMT in both polar and apolar solvents such as PG and SQ respectively. The molar extinction coefficients were derived from absorbance measurements for a range of concentrations and path lengths. We further investigated dispersions containing a selection of metal oxide nanoparticles that are used in the sunscreen industry such as TiO_2, ZnO and CeO_2. In our study, we have also included WO_3, which is a semiconductor with a small band gap. In addition, for solutions containing a mixture of UV absorbers, we show that the calculated absorbance values agree with the measured absorbance spectra.

We demonstrate in Chapter 4, how the evaporation of thin films containing UV absorbers affects the *in vitro* SPF as a function of time. For solutions of AVB, MC and DHHB in PG, we have shown that during evaporation, the initial deposited film progressively dewets changing in both thickness and area. This behaviour results in the increase of the concentration of the UV absorbers until their solubility limit is reached. Beyond that point, solute precipitation is expected to occur. The combined film area shrinkage and solute precipitation explains the decrease in the absorbance and thus the loss in the *in vitro* SPF. We introduced a model to account for these irregularities and we have confirmed its validity by comparing the derived calculated absorbance data with the measured absorbance values. The comparison was extended to measured and calculated *in vitro* SPF. We have confirmed that the loss in the absorbance is due to combined effect of film dewetting and solute precipitation by using a fast evaporating solvent such as *n*-decane as opposed to PG.

For a thin dispersion film, however, containing metal oxide nanoparticles, we have shown that the presence of the latter suppressed dewetting. Film pinning was observed for the investigated dispersions irrespective of the particle type resulting in a fixed area until complete solvent evaporation. Throughout our investigation, a smooth quartz plate was the selected substrate. Alternative substrates, however, were also used including the commercial Vitro Skin and a keratin-lipid dispersion film. We show that both substrates aid film pinning and thus suppress dewetting. However, the solute precipitation as a result of the solvent evaporation is not inhibited.

Similarly, we have demonstrated throughout Chapter 5, how the evaporation of thin emulsion films containing UV absorbers affects the *in vitro* SPF as a function of time. For emulsions, containing equal volumes of a volatile and a non-volatile component, our findings have confirmed that the loss in the overall absorbance is due to the loss of light scattering, which is directly related to the collapse of the emulsion structure. The UV absorbers such as AVB and MC remained soluble in the involatile SQ phase maintaining their absorbance. Throughout the experimental procedure, there were no signs of dewetting due to the SQ phase. This was not the case, however, for emulsions containing equal volumes of two volatile components, such as PG and *n*-decane. The evaporation of both phases resulted in the loss of the absorbance.

In Chapter 6, we have demonstrated how the irradiation of sunscreen films affects the *in vitro* SPF as a function of time. We investigate i) the photostable DHHB and BEMT and ii) the photolabile AVB and MC UV absorbers. We show that for solutions containing the photolabile UV absorbers, the change in the absorbance resulted from the relevant photochemical processes. For the AVB in particular, it is the conversion of the enol to the keto form and eventually to photo-products responsible for the decrease in the *in vitro* SPF performance. As a reminder, the enol form absorbs exclusively in the UVA region, as opposed to the keto form which absorbs in the UVC region below 280 nm. For the MC, however, the decrease in the absorbance is related to its photoisomerisation process from *trans* to *cis* isomer.

For each system, from computer fitting data we can determine the molar extinction coefficients of all species' present, their concentrations and the relevant quantum yields that can be used for the time-dependent *in vitro* SPF estimation. For solutions containing a mixture of UV absorbers, we show that the presence of the photostable UV absorber acts as "spectator" species that retards the overall loss in the absorbance. We believe that similar behaviour is observed when inorganic particulates are present in the dispersion.

In the final part of this investigation, particular attention was given to particle-stabilised emulsions with dissolved UV absorbers. The fitting procedure has taken into consideration the partitioning of the dissolved UV absorbers within the two immiscible liquids. We show that the emulsion type did not have any effect on the photochemical behaviour of the UV absorbers of interest. However, by changing the volume fraction of the immiscible liquids, we show how the photochemical rates of both AVB and MC are varied.

All photochemical measurements were made under different light sources of irradiation. By introducing actinometry, we were able to determine the absolute spectral irradiances of all the light sources used. Based on these findings, we can now predict the *in vitro* SPF during irradiation with “standard” sunlight.

7.2 Future work

We have discussed the fairly large uncertainties in the determination of the quantum yields relevant to the photochemical processes of AVB and MC. For this reason, we need to improve the accuracy of these quantum yields and to be able to confirm whether the assumption of wavelength independent quantum yields is valid. Further investigation of a wider range of UV absorbers and/or a broader selection of solvents could also be pursued. Future work could also focus on the SPF changes of water-immersed films as a function of time. Finally, having already modelled the behaviour of films upon evaporation and irradiation, it would be interesting to investigate the combined effect of these processes.

APPENDIX A – ^{1}H-NMR DATA OF AVB AND MC

AVB: ^{1}H-NMR ($CDCl_3$): 1.36 (s, 9H), 3.88 (s, 3H), 4.55 (s, 2H), 6.78 (s, 1H), 6.98 (d, 2H), 7.50 (d, 2H), 7.91 (d, 2H), 7.97 (d, 2H).

^{1}H-NMR spectrum revealed a peak at 6.78 ppm indicative of the presence of the enol form of AVB. A peak at 4.55 ppm corresponds to the keto form of AVB. The ratio, of [enol]/[keto] based on the measured area under the peaks was 91% and 9% respectively. Data are consistent with literature values.[1]

Figure A1. Structure of avobenzone where all carbon positions are numbered.

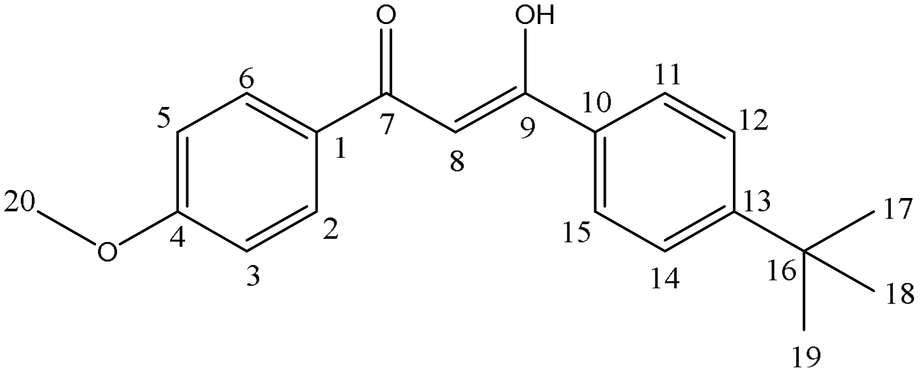

Table A1. ^{1}H-NMR data chemical shifts (in ppm) of avobenzone prior to UV irradiation.

proton	carbon position	chemical shift/ppm
CH_3	17, 18, 19	1.36 (s, 9H)
CH_3	20	3.88 (s, 3H)
CH_2	8	4.55 (s, 2H)
CH	8	6.78 (s, 1H)
CH	3, 5	6.98 (d, 2H)
CH	12, 14	7.50 (d, 2H)
CH	11, 15	7.91 (d, 2H)
CH	2, 6	7.97 (d, 2H)

MC: ^{1}H-NMR ($CDCl_3$): 0.91 (d, 6H), 1.57 (quartet, 2H), 1.71 (quintet, 1H), 3.80 (s, 3H), 4.20 (t, 2H), 6.29 (d, 1H, J = 16 Hz), 6.86 (d, 2H), 7.42 (d, 2H), 7.58 (d, 1H, J = 16 Hz).

Based on the data collected from the ^{1}H-NMR spectrum and the coupling constant J values in particular, the *trans*-MC was the starting material. Data are consistent with literature values.[2]

Figure A2. Structure of MC where all carbon positions are numbered.

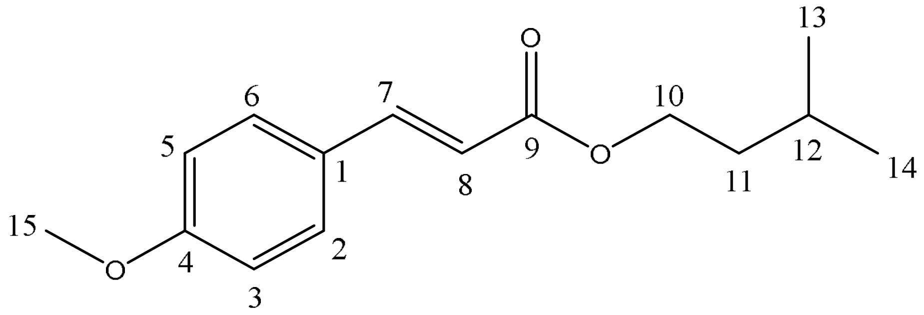

Table A2. ^{1}H-NMR data chemical shifts (in ppm) of MC prior to UV irradiation.

proton	**carbon position**	**chemical shift/ppm**
CH_3	13, 14	0.91 (d, 6H)
CH_2	11	1.57 (quartet, 2H)
CH_2	12	1.71 (quintet, 1H)
CH_3	15	3.80 (s, 3H)
CH_3	10	4.20 (t, 2H)
CH	8	6.29 (d, 1H, J = 16 Hz)
CH	3, 5	6.86 (d, 2H)
CH	2, 6	7.42 (d, 2H)
CH	7	7.58 (d, 1H, J = 16 Hz)

A1 – References

1. M. Dubois, P. Gilard, P. Tiercet, A. Deflandre and M. A. Lefebvre, *J. Chim. Phys.*, 1998, **95**, 388-394.
2. S. Pattanaargson and P. Limphong, *Int. J. Cosmet. Sci.*, 2001, **23**, 153-160.

APPENDIX B – EQUATIONS RELATED TO DETERMINING REACTION RATES

The total absorbed intensity I_α is determined by subtraction of transmitted I from incident light I_o per wavelength

$$I_\alpha(\lambda) = I_o(\lambda) - I(\lambda) \tag{B.1}$$

The relationship between transmitted and incident light is also given by the equation below

$$I(\lambda) = I_o(\lambda)10^{-(\varepsilon cl)} \tag{B.2}$$

Hence, from equations B.1 and B.2

$$I_\alpha(\lambda) = I_o(\lambda) - I_o(\lambda)10^{-(\varepsilon cl)} = I_o(\lambda)(1 - 10^{-(\varepsilon cl)}) \tag{B.3}$$

We also introduce a correction factor 0.96 in equation B.6. This is derived assuming that the reflection losses at the upper front surface of the irradiated cell will be equal to $A_{refl}/2$, where A_{refl} corresponds to the measured absorbance of reference solvent filled in a cell *versus* air and is equal to 0.035. Hence, the transmittance is expected to be

$$T = 10^{-\frac{A_{refl}}{2}} = 10^{-0.017} = 0.96 \tag{B.4}$$

Combining equations B.3 and B.4 with equation 6.1 we derived equation 6.2.

The transmitted light intensity of the spectator species within the UV irradiated sample will be dependent upon the path length l. As such, the term average light intensity <I> is introduced. For an average light intensity <I>, equation (B.2) can be applied and it follows with the aid of integration that:

$$< I > l = \int_0^l I_o(\lambda)\ 10^{(-\varepsilon c l)} dx \tag{B.5}$$

$$< I > \ l \ = \ I_o\,(\lambda) \frac{10^{(-\varepsilon c l)}}{-\varepsilon c \ ln 10} - \frac{I_o(\lambda)}{-\varepsilon c \ ln 10}$$

$$\frac{< I >}{I_o} = \frac{1}{\varepsilon c l \ ln 10}\ (1 - \ 10^{(-\varepsilon c l)}) \tag{B.6}$$

where

- $\frac{<I>}{I_o}$ is the relative average light intensity experienced by the spectator species at t = 0
- ε is the molar extinction coefficient (M^{-1} cm^{-1})
- c is the concentration of a hypothetical filter (M)
- l is the path length (cm).

Equation (B.6) can be modified as follows

$$\frac{< I >}{I_o} = \frac{1}{A_{spec} \ ln 10}\ (1 - \ 10^{(-A_{spec})}) \tag{B.7}$$

where A_{spec} is the absorbance of the “spectator” species. Hence, the number of moles of photons incident on the sample shown in equation 6.3 is reduced by a factor equal to equation B.7 due to absorption of the “spectator” species.